

# Automated Methods for Ferrocene Chemistry

Von der Naturwissenschaftlichen Fakultät der  
Gottfried Wilhelm Leibniz Universität Hannover

zur Erlangung des Grades  
Doktor der Naturwissenschaften (Dr. rer. nat.)

genehmigte Dissertation

von

Robert Gathy, M. Sc.

2022

Referent: Prof. Dr. rer. nat. Holger Butenschön

Korreferent: Prof. Dr. rer. nat. Sascha Beutel

Tag der Promotion: 04.07.2022

# Acknowledgments

Diese Arbeit wäre ohne die tatkräftige Unterstützung vieler Menschen nicht zustande gekommen. Hier sind sie\*:

Mein Dank gilt

Prof. Dr. Holger Butenschön für die hervorragende Betreuung und die Möglichkeit, völlig neue Wege zu erkunden – das ist alles andere als selbstverständlich. Prof. Dr. Sascha Beutel für die Übernahme des Korreferats als Automatisierungsexperte, und Prof. Dr. Oliver Plettenburg im Voraus für die Übernahme des Prüfungsvorsitzes, wenn ich dazu komme, ihn zu fragen.

den aktiven Mitgliedern des AK Butenschön (= Adeline) sowie allen ehemaligen Mitgliedern Winni, Geanne, Julian, Lauren, Regina, Sinem, David, Oli, Wojtek, Stephan und wen ich noch vergessen habe.\*\* Eine bessere und entspanntere Gruppe hätte ich mir nicht wünschen können, danke euch!

Meinen Praktikanten und Bacheloranden für die geile Zeit und eure Offenheit für Neues. Ihr wisst was ihr geleistet habt! Elena (wyld)! Jan (it is what it is...)! Tim (och nö...)! Felix (auch wenn du technisch gesehen gar nicht mein Praktikant warst, war trotzdem cool)! Kim (don't worry, be happy)! Unfug (bald wieder Burger?!). Nochmal Jan (er konnte es nicht lassen...)! Tom (all die Chemikalien...)! Erk (warst ja eigentlich bei Finn, aber ich zähl das)! Arend (für unzählige Lötstellen...)! Judy (soveränes BTM-handling)! Haoxuan (Nummer eins)!\*\* Außerdem allen, die sich auf die eine oder andere Art an der AG Automatisierung beteiligt haben – Veränderung kommt nicht von alleine!

Allen Co-Doktoranden und Postdocs aus OCI und BMWZ – geteiltes Leid ist halbes Leid! Viktoria, Lücki, Berit, Ardalan, Liz, Lukas, Fabi, Alex, Marius, Maik, Gö, Sherin, Lukas (und eigentlich alle "Plettis", fällt mir gerade auf) und so weiter!\*\*\*

Der NMR-Abteilung und dem Massenspektrometriezentrum, Monika, Dagmar, Sabine, Anne, Max, Jörg und Linn für den wundervollen, zuverlässigen Service und die netten Flurgepräche,

und insbesondere Gerald Dräger. Gerald, danke dir für den vertrauensvollen Support in allen Bereichen, und dass du mir die ASW anvertraut hast. Ohne dich wäre buchstäblich nichts von alledem zustande gekommen. . .

Prof. Lee Cronin und Dr. Christian Dittrich für ihren frühen Input, der mich bestätigt hat, auf dem richtigen Weg zu sein,

Den Mitarbeiterinnen des Sekretariats, Linda, Ines, Monika, Christine, Alfia und Anette für die Unterstützung in allen bürokratischen Lebenslagen,

Meinen Freunden und Boulderpartnern Cathy Kingsfield, Flo, Stephan, Sandra, Micha, McFly, Paul, Chris, nochmal Tim, Haiko (auch für die Initialzündung bezüglich PYTHON), Kathi, nochmal Winni, Maren, nochmal Unfug, Andrea, Benni, Ingo, Tobi. . . \*\*\*

und zu guter Letzt Alexey und Finn. Ohne allzu rührselig werden zu wollen, ihr wisst wofür.

---

Zitat aus Lateralus - Tool

\*Falls ihr hier nicht drinsteht, ruft mich an und ich geb euch einen aus. Das Ding hier ist um 3:50 Uhr entstanden. . .

\*\*Reihenfolge der Namen nach zeitlichem Auftreten

\*\*\*Reihenfolge der Namen per PYTHON randomisiert



*Spiral out  
Keep going.*

# Kurzfassung

Trotz zahlreicher Fortschritte während des vergangenen Jahrhunderts basiert die akademische Organische Chemie noch immer stark auf händischer Arbeit und nicht-systematischer Versuchspannung. Entdeckungs- und Optimierungsprozesse unterliegen beliebig großen *Reaktionsräumen*, welche zu einer extremen Anzahl möglicher Kombinationen aus Reagentien und Reaktionsbedingungen führen. Der praktische Aspekt beansprucht oft den größten Teil der verfügbaren Arbeitszeit, was die Möglichkeiten zur Konzeptualisierung, Planung und Analyse verringert. Folglich sind Chemiker oft mit *nicht wertschöpfenden Tätigkeiten* beschäftigt. Um diesen Flaschenhals zu beseitigen, wurden in dieser Arbeit zwei Strategien untersucht: Die Erhöhung des synthetischen Durchsatzes durch die Verwendung von Geräten, sowie die Erhöhung der Informationsdichte je Experiment durch statistische Methoden. Der Einsatz eines wiederinbetriebgenommenen Parallelsynthesizers im Zusammenspiel mit *Statistischer Versuchspannung* ermöglichte die Erzeugung reproduzierbarer, aussagekräftiger Daten im Hochdurchsatz. Durch fächerübergreifende Werkzeuge wie Programmierung, Mikrocontroller-Prototyping und 3D-Druck wurde der Anwendungsbereich der automatisierten Geräte weiter ausgebaut, beispielsweise durch die Entwicklung von automatisierter, quantitativer Dünnschichtchromatographie. Die neuen Arbeitsabläufe wurden in drei Anwendungsbeispielen um das Molekül Ferrocen demonstriert. Die Anwendungsfälle lagen im Bereich der Parameteruntersuchung in komplexen Reaktionen, der Herstellung von Substanzbibliotheken, sowie der Erkundung unbekannter Reaktionsräume.

Schlüsselwörter: Automatisierung, Statistische Versuchspannung, Python, Ferrocen, C-H-Aktivierung, Chemspeed

# Abstract

Despite numerous technical advances over the last century, the field of academic organic chemistry still relies heavily on manual labor and non-systematic experiment design. Discovery and optimization of chemical reactions are subject to arbitrarily large *reaction spaces*, leading to an extreme amount of possible combinations of reagents and reaction conditions. The practical aspect often takes up the largest portion of available working time, reducing opportunities for conceptualization, planning and analysis. Hence, chemists often find themselves performing *non-value adding activities* most of the time. To eliminate this bottleneck, two strategies were explored in this work: increasing synthetic throughput using machines, and increasing information density per experiment using statistical methods. The use of a recommissioned parallel synthesizer in synergy with *Design of Experiments* allowed for the high-throughput generation of reproducible, meaningful data. Using interdisciplinary tools such as programming, microcontroller prototyping and 3D printing, the capabilities of the automated equipment were enhanced even more, for example through the development of automated, quantitative thin-layer chromatography. The new workflows were demonstrated in three use cases based on the molecule ferrocene. The use cases were centered around parameter investigation in complex reactions, library synthesis and the exploration of unknown reaction spaces.

Keywords: Automation, Design of Experiments, Python, Ferrocene, C-H Activation, Chem-speed

# List of Abbreviations

<i>J</i>	Coupling Constant (NMR)
<i>T</i>	Temperature
<i>V</i>	Volume
$\lambda$	Wavelength (of Electromagnetic Radiation)
$\nu$	Frequency
<i>d.r.</i>	Diastereomeric Ratio
<i>m/z</i>	Mass-to-Charge-Ratio
<i>p</i>	Probability Level
<i>t</i>	Time
<b>3D</b>	Three-Dimensional
<b>AI</b>	Artificial Intelligence
<b>APCI</b>	Atmospheric Pressure Chemical Ionisation
<b>API</b>	Active Pharmaceutical Ingredient
<b>API</b>	Application-Programming Interface
<b>Ac</b>	Acetyl
<b>Ar</b>	Aryl, Aromatic
<b>Bp.</b>	Boiling Point
<b>Bu</b>	Butyl
<b>CAAC</b>	Cyclic (Alkyl)(Amino)Carbene
<b>CAS</b>	Chemical Abstracts Service
<b>CPL</b>	Circularly Polarized Light

<b>Cp</b>	Cyclopentadienyl
<b>Cp*</b>	Pentamethylcyclopentadienyl
<b>DCB</b>	2,3-Dichlorobutane
<b>DCE</b>	1,2-Dichloroethane
<b>DCM</b>	Dichloromethane
<b>DDQ</b>	2,3-Dichloro-5,6-dicyano-1,4-benzoquinone
<b>DFT</b>	Density Functional Theory
<b>DG</b>	Directing Group
<b>DIPA</b>	Diisopropylamine
<b>DIPEA</b>	Diisopropylethylamine
<b>DIY</b>	Do-It-Yourself
<b>DMSO</b>	Dimethylsulfoxide
<b>DNA</b>	Desoxyribonucleic Acid
<b>DoE</b>	Design of Experiments
<b>ESI</b>	Electrospray Ionisation
<b>Et</b>	Ethyl
<b>Fc</b>	Ferrocenyl
<b>Fp</b>	Cyclopentadienyldicarbonyliron(II)
<b>Fp*</b>	Pentamethylcyclopentadienyldicarbonyliron(II)
<b>GP</b>	General Procedure
<b>GUI</b>	Graphical User Interface
<b>HOMO</b>	Highest Occupied Molecular Orbital
<b>HPLC</b>	High-Pressure Liquid Chromatography
<b>HRMS</b>	High-Resolution Mass Spectrometry
<b>Hex</b>	<i>n</i> -Hexyl
<b>I/O</b>	Input/Output

<b>IR</b>	Infrared
<b>L</b>	Liter(s)
<b>LED</b>	Light-Emitting Diode
<b>LUMO</b>	Lowest Unoccupied Molecular Orbital
<b>M</b>	Metal
<b>Mp.</b>	Melting Point
<b>MPLC</b>	Medium-Pressure Liquid Chromatography
<b>MS</b>	Mass Spectrometry
<b>MTBE</b>	Methyl- <i>tert</i> -butyl ether
<b>MWE</b>	Minimal Working Example
<b>Me</b>	Methyl
<b>NHC</b>	<i>N</i> -Heterocyclic Carbene
<b>NLP</b>	Natural Language Processing
<b>NMR</b>	Nuclear Magnetic Resonance
<b>No.</b>	Number
<b>ODG</b>	<i>Ortho</i> -Directing Group
<b>PC</b>	Principal Component(s)
<b>PCA</b>	Principal Component Analysis
<b>Ph</b>	Phenyl
<b>Piv</b>	Pivaloyl
<b>Q</b>	Quinoyl
<b>QTLC</b>	Quantitative Thin-Layer Chromatography
<b>R<sub>f</sub></b>	Retention Factor
<b>R,G,B</b>	Red, Green, Blue
<b>SD</b>	Standard Deviation
<b>SPE</b>	Solid-Phase Extraction

<b>S<sub>N</sub></b>	Nucleophilic Substitution
<b>TFE</b>	2,2,2-Trifluoroethanol
<b>THF</b>	Tetrahydrofuran
<b>TLC</b>	Thin-Layer Chromatography
<b>TMEDA</b>	Tetramethylethylenediamine
<b>Temp.</b>	Temperature
<b>Tf</b>	Trifluoromethanesulfonyl
<b>Tol</b>	Tolyl
<b>USB</b>	Universal Serial Bus
<b>UV</b>	Ultraviolet (Part of Light Spectrum)
<b>V</b>	Volt(s)
<b>X</b>	Halide (F, Cl, Br, I)
<b>°C</b>	Degrees Centigrade
<b>Hz</b>	Hertz
<b>μ</b>	Micro (SI Prefix)
<b><i>rac</i></b>	Racemic
<b>c</b>	Centi (SI Prefix)
<b>calc.</b>	Calculated
<b>csv</b>	Comma-Separated Values (File Format)
<b>d</b>	Doublet (NMR)
<b>dd</b>	Doublet of Doublets (NMR)
<b>dppe</b>	1,2-Bis(diphenylphosphino)ethane
<b>equiv.</b>	Equivalents (molar)
<b>g</b>	Gram(s)
<b>h</b>	Hour(s)
<b>h</b>	PLANCK Constant

<b>m</b>	Meter(s)
<b>m</b>	Milli (SI prefix)
<b>m</b>	Multiplet (NMR)
<b>m</b>	Medium (IR)
<b>min</b>	Minute(s)
<b>mol</b>	Mole(s)
<b>n</b>	Molar Amount
<b>n</b>	Nano (SI Prefix)
<b>pH</b>	Potentia Hydrogenii
<b>png</b>	Portable Network Graphics (File Format)
<b>px</b>	Pixel(s)
<b>q</b>	Quartet (NMR)
<b>rpm</b>	Revolutions per Minute
<b>s</b>	Singlet (NMR)
<b>s</b>	Second(s)
<b>s</b>	Strong (IR)
<b>TRAP</b>	TLC Relative Area Percentage
<b>t</b>	Triplet (NMR)
<b>vis</b>	Visible (Part of Light Spectrum)
<b>xyl</b>	Xylenyl



# Contents

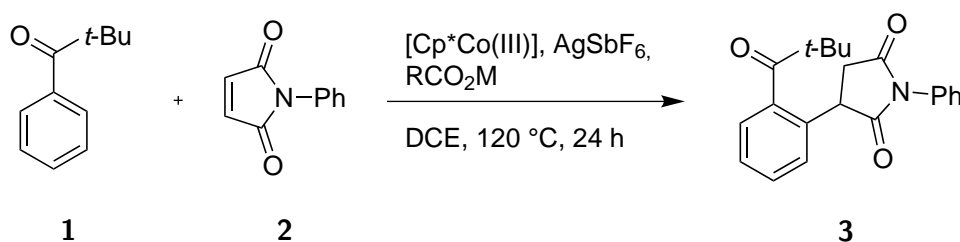
<b>Acknowledgments</b>	<b>ii</b>
<b>Quote</b>	<b>iv</b>
<b>List of Abbreviations</b>	<b>vii</b>
<b>1 Introduction</b>	<b>1</b>
1.1 Challenges and Solutions in Chemical Experimentation . . . . .	1
1.2 Objectives . . . . .	11
<b>2 Results and Discussion</b>	<b>12</b>
2.1 Development of Automated Workflows . . . . .	12
2.1.1 Parallel Synthesis and DoE . . . . .	12
2.1.2 Quantitative Thin-Layer Chromatography . . . . .	22
Idea and Concept . . . . .	22
Implementation . . . . .	24
Results and Validation . . . . .	31
Conclusion . . . . .	37
2.1.3 Custom Scripts and Tools . . . . .	37
Overview . . . . .	37
Reaction Preparation and Charge Calculation . . . . .	38
An Arduino-Based Interface for the ASW 2000P . . . . .	45
3D Printed Photoreactor Arrays . . . . .	52
2.2 Chemistry Use Cases . . . . .	57
2.2.1 Light-Controlled Functionalization of Ferrocene-Based Push-Pull Systems	57
Introduction . . . . .	57
Synthesis of a Ferrocene-based <i>Push-Pull</i> System . . . . .	60
Reactivity Screenings with Quinoylferrocene . . . . .	64
Investigations on the Reaction of Quinoylferrocene with Indole . . . . .	69
Blocking the Reactive Position . . . . .	77
Library Synthesis . . . . .	84
Conclusion and Outlook . . . . .	87

2.2.2	High-Throughput Investigations in Cp*Co(III) Catalysis . . . . .	89
	Introduction . . . . .	89
	Library Synthesis . . . . .	91
	Library Compounds in Cp*Co(III)-Catalyzed C-H Activations . . . . .	101
	Conclusion and Outlook . . . . .	109
2.2.3	Towards Fe-Catalyzed C-H Activation . . . . .	109
	Introduction . . . . .	109
	Automation/DoE Synergy for Rapid Reaction Space Exploration . . . . .	113
	Conclusion and Outlook . . . . .	127
<b>3</b>	<b>Conclusion and Outlook</b>	<b>130</b>
<b>4</b>	<b>Experimentals</b>	<b>132</b>
4.1	General Remarks . . . . .	132
4.2	Synthetic Procedures . . . . .	134
4.2.1	(Methylquinoyl)ferrocene <b>76</b> and Related Compounds . . . . .	134
4.2.2	Fractional Factorial DoE with Quinoylferrocene <b>41</b> . . . . .	136
4.2.3	Fractional Factorial DoE with (Methylquinoyl)ferrocene <b>76</b> . . . . .	140
4.2.4	((Indolyl)quinoyl)ferrocene Library . . . . .	144
4.2.5	Ferrocenylcarboxamide Library . . . . .	147
4.2.6	C-H Activation Library . . . . .	156
	<b>References</b>	<b>168</b>
	<b>Curriculum Vitae</b>	<b>177</b>

# 1 Introduction

## 1.1 Challenges and Solutions in Chemical Experimentation

The field of organic chemistry, particularly in academia, still relies heavily on manual, intuition-guided experimentation.<sup>[1]</sup> *In lieu of* appropriate general models, truly novel reactions are often discovered by chance, and reaction optimization is usually performed using a combination of *trial-and-error* and *one-factor-at-a-time* (OFAT) techniques.<sup>[2]</sup> To illustrate this, an example from the field of Cp\*Co(III)-catalyzed C-H activation is given in **Scheme 1.1**.<sup>[3]</sup> Here, phenyl ketone **1** is reacted with *N*-phenylmaleimide (**2**) to yield the alkylated species **3**.



**Scheme 1.1** Cp\*Co(III)-catalyzed reaction of *N*-phenylmaleimide (**2**) with phenyl ketone **1**.<sup>[3]</sup>

Reactions like this depend on a variety of factors, which can be of categoric or numeric nature. In this particular example, some categoric factors are the types of carboxylate, cobalt catalyst, silver salt and solvent, respectively. Typical numeric factors in chemical reactions include time, temperature, relative amounts of reagents and catalysts, addition times and stirring speeds.<sup>[4]</sup> **Table 1.1** shows an excerpt of the optimization process carried out in the given example by the authors.<sup>[3]</sup>

**Table 1.1** Exemplary OFAT optimization process taken from the chemical literature.<sup>[3]</sup> M = Na, K. R = CH<sub>3</sub>, *t*-Bu.

Entry	[Cp*Co(III)] (type)	RCO <sub>2</sub> M (type)	RCO <sub>2</sub> M (mol%)	Yield (%)
1	Cp*Co(CO)I <sub>2</sub>	NaOPiv	30	24
2	Cp*Co(CO)I <sub>2</sub>	KOAc	30	37
3	Cp*Co(CO)I <sub>2</sub>	NaOAc	30	39
4	[Cp*CoI <sub>2</sub> ] <sub>2</sub>	NaOAc	30	15
5	[Cp*CoCl <sub>2</sub> ] <sub>2</sub>	NaOAc	30	11
6	[Cp*Co(MeCN) <sub>3</sub> ](SbF <sub>6</sub> ) <sub>2</sub>	NaOAc	30	n.d.
7	Cp*Co(CO)I <sub>2</sub>	NaOAc	10	74
8	Cp*Co(CO)I <sub>2</sub>	NaOAc	0	33
9	Cp*Co(CO)I <sub>2</sub>	NaOAc	50	10

In the given table, three factors (type and amount of carboxylate salt and type of [Co] complex) were optimized against a single response (yield). First, three different carboxylates were tested, recording the yield for each reaction (**Entries 1, 2, 3**). The carboxylate giving the highest yield was then kept constant, and different [Co] complexes were investigated (**Entries 4, 5, 6**). Again, the highest yielding one was retained, and the amount of NaOAc was screened at four levels (**Entries 7, 8, 9**), giving an intermediary maximum yield of 74 % (**Entry 7**).

The aforementioned case is a typical example for OFAT optimization, where factors are investigated sequentially, one at a time. While this is common practice in many laboratories, there are some significant disadvantages. Most notably, only a narrow path within the reaction space is covered, and multifactor interactions are not registered.<sup>[5]</sup> This is illustrated in **Figure 1.1**.

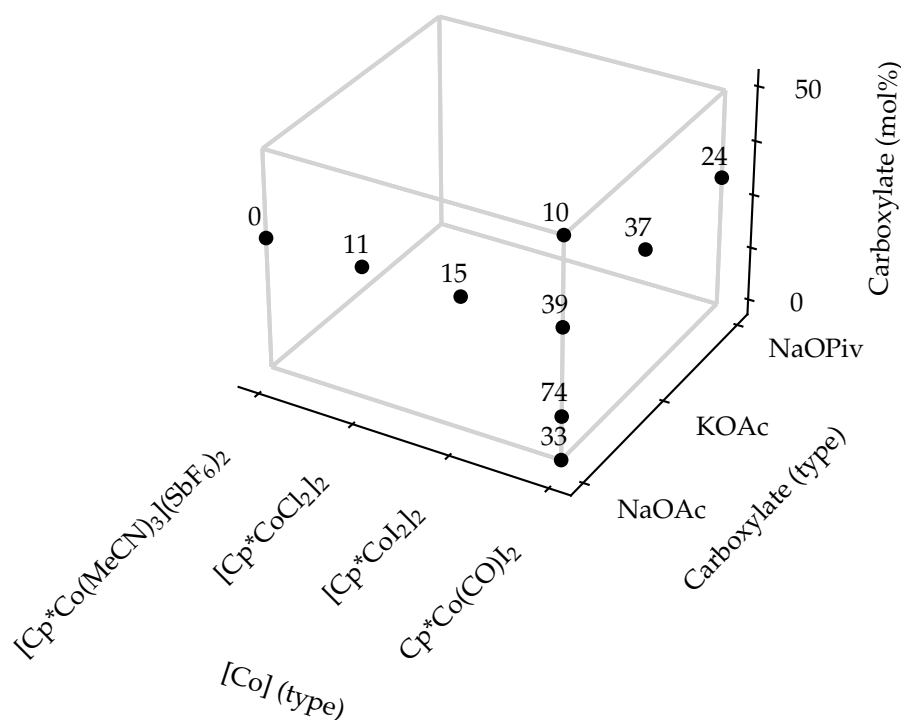


**Figure 1.1** Narrow coverage of reaction space using OFAT techniques. The arrangement of individual reagents is arbitrary.

From this visualization, it becomes apparent that no interactions between factors can be deduced, and each yield only stands isolated. Thus, no general rules about the behavior of the reaction are gained, and the only result, albeit useful, is the combination of factor settings at maximal yield.

Adding to the limited information gain using OFAT techniques, the setup of each experiment is quite costly in terms of time and human effort. Even though there is only a relatively small set of recurring unit operations necessary for reaction setup, they require a high amount of concentration and physical skill, and therefore take a lot of time to perform correctly. These operations consist mainly of gravimetric and volumetric transfer of liquids and solids, and are usually controlled visually by the operator in real time. Repeatedly handling milligram amounts of solids poses a strain on the operator, and little time is left to perform more value-adding tasks such as literature research and strategic planning.

To alleviate these issues, two main strategies exist, which are heavily used in industrial laboratories: Increasing the information density through rational experiment design, and delegating repetitive, manual labor to machines.

Laboratory automation has been developed and used in the chemical and pharmaceutical industries since the 1950s, starting with analytical devices for clinical chemistry.<sup>[6]</sup> Nowadays, leveraging the increasing availability of electrical prototyping systems such as ARDUINO and RASPBERRY PI, a small selection of academic groups is developing custom automated systems both in batch and flow.<sup>[7]</sup> The group of POLIAKOFF reported self-optimizing flow reactors for the selective synthesis of variously alkylated anilines using SIMPLEX algorithms.<sup>[8]</sup> HEIN and ASPURU-GUZIK assembled a robotic platform for the preparation, analysis and automated optimization of thin-film materials relevant for solar and electronic applications.<sup>[9]</sup> The group of COOPER has built an autonomous platform capable of driving around a laboratory and accessing various reagents, glassware and analytical equipment, while making decisions in real-time based on an optimization algorithm.<sup>[10]</sup> This “mobile robotic chemist” autonomously searched a reaction space of ten factors in 688 experiments within eight days.<sup>[11]</sup> Recognizing that most available experimental procedures assume the use of standard laboratory glassware, CRONIN built a robotic framework based on round-bottom flasks, magnetic stirrers and rotary evaporators, which are connected by a custom-made pump system. and controlled by a custom programming language<sup>[12]</sup> This *Chemputer* allows the use of standard recipes, which can be downloaded and executed even by inexperienced users. It was commercialized under the company CHEMIFY led by CRONIN.<sup>[13]</sup>

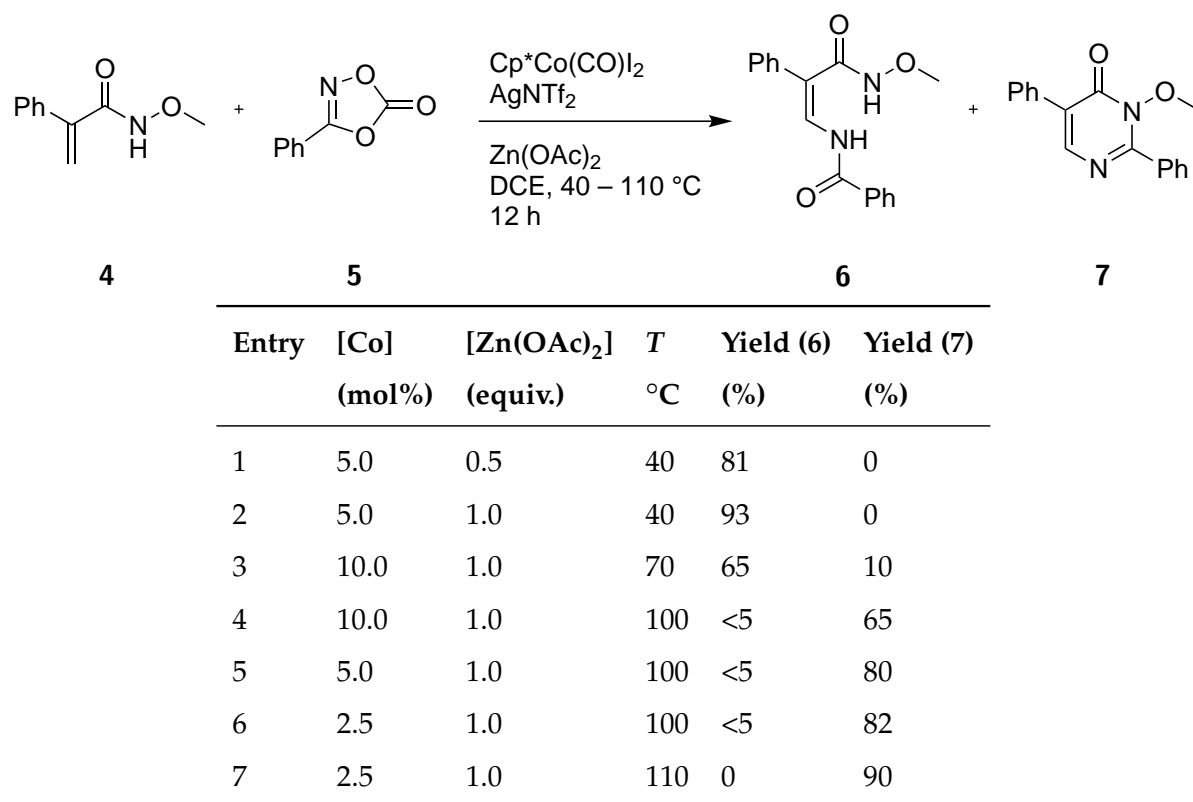
The aforementioned systems represent the frontiers of academic innovation and are thus not suitable for broad use by organic chemists. In contrast to these highly specialized custom systems, commercial solutions are available for end-users in the chemical and related industries. Besides standalone devices such as liquid handlers (GILSON, ABBOTT), some companies offer equipment suitable to conduct entire synthetic procedures automatically, including workup and sampling for characterization (UNCHAINED LABS, CHEMSPEED). These *parallel synthesizers* were first developed during the rise of combinatorial chemistry in the late 1990s,<sup>[14]</sup> and are still in continuous development. Modern equipment is not only able to handle complex operations such as solid dispensing of small (sub-milligram) to large (multigram) quantities, inert filtration and sample injection to third-party devices, but is also controllable through *application-programming interfaces* (APIs). These allow the user to control the equipment using standard programming languages such as C++ or PYTHON, which are common in the chemical automation field.<sup>[15]</sup> This feature has been exploited both in academia<sup>[16]</sup> and industry.<sup>[17]</sup> Some of these systems have been adapted by academic groups (AGGARWAL, ASPURU-GUZIK), but widespread adaptation is slow because of the high initial investment as well as a lack of necessary expertise in “traditional” chemistry laboratories.<sup>[18]</sup>

Even with state-of-the-art equipment available, the question of how to plan and conduct experiments for maximum information gain remains non-trivial. As their name suggests, the main concept of a parallel synthesizer is to conduct a large number of experiments simultaneously,

which stands in contrast to the sequential nature of OFAT experimentation. Perhaps the most widely adopted method is *Design of Experiments* (DoE).<sup>[19]</sup>

DoE is a statistical method for planning, conducting and analyzing experiments to obtain a high amount of information using the least possible amount of runs.<sup>[20]</sup> It can be applied wherever a measurable experimental outcome (*response*) is dependent on at least two process parameters (*factors*). DoE is suitable for both modelling the behavior of a system as well as optimization, both of which are routine tasks in organic chemistry.<sup>[21]</sup> While optimization relies on so-called *Response Surface* designs, modelling is often done using *2-Level Factorial* designs.<sup>[22]</sup> To illustrate how these can be created and how they compare to typical OFAT strategies, another example from Cp\*Co(III)-catalyzed C-H activation is presented. **Table 1.2** shows the formation of amidated products **6** and **7** from acrylamide analogue **4** and oxazolone **5**.<sup>[23]</sup>

**Table 1.2** Selective syntheses of enamide **6** and pyrimidone **7** as a result of a combined OFAT/*trial-and-error* optimization.



The initial conditions of the authors (**Entry 1**) provided a good yield of product **6**, which was improved by increasing the amount of Zn(OAc)<sub>2</sub> (**Entry 2**). At both a higher loading of [Co] as well as elevated temperatures (**Entry 3**), the overall yield dropped, and product **7** was obtained in small amounts. Further increasing the temperature (**Entry 4**) led to a switch of selectivity

towards product 7. The catalyst loading was then decreased in multiple steps (**Entries 5, 6**) to give even higher yields of 7. In the last step (**Entry 7**), a temperature of 110 °C gave a yield of 90 % for compound 7 with perfect selectivity.

This type of experiment design – a mixture of OFAT and *trial-and-error* – is typical for organic chemistry. In the present case, it led to very good results, represented in excellent yields and selectivities for both investigated products 6 and 7. However, looking at a visual representation of the investigated reaction space, it becomes clear that the chosen design is not the most efficient one (**Figure 1.2**).

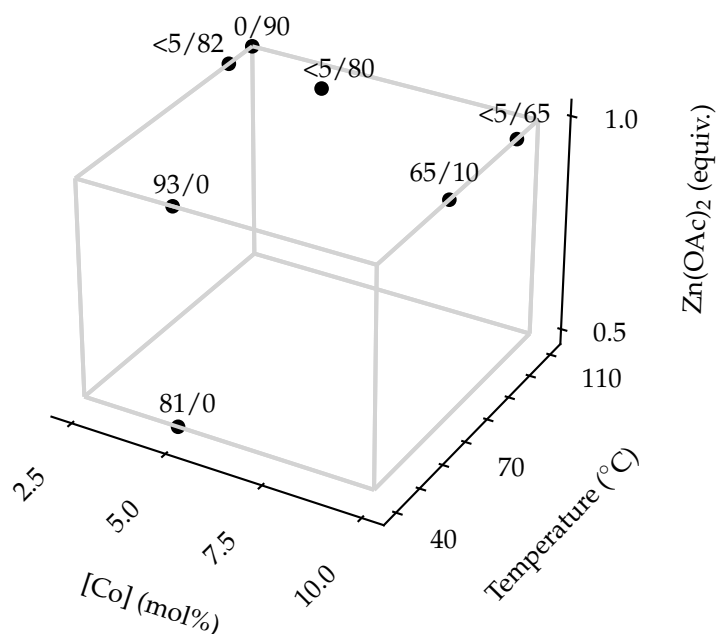


**Figure 1.2** Visualization of the reaction space covered by L1 *et al.*<sup>[23]</sup> Responses are given as yield (6)/yield (7).

Evidently, reaction space exploration is biased strongly towards high amounts of Zn(OAc)<sub>2</sub>, based on the single fact that in one case, high amounts of the zinc salt gave slightly better yields. Temperature seems to be the strongest factor in terms of selectivity, and is investigated at four levels (40, 70, 100 and 110 °C). During the investigation, the amount of [Co] was first raised to 10 mol %, then lowered again. This intuition-guided approach eventually led to excellent results, although it is not clear whether only a selection of all actually conducted experiments was shown. In addition, possible multifactor effects, especially between [Co] and temperature, were not conclusively evaluated, and the small differences in yield between **Entries 5 and 6** (**Table 1.2**) raise the question of statistical significance.



In contrast to this sequential procedure, a 2-level full factorial DoE defines all runs during the planning stage, before entering the laboratory. In such a design, each factor of interest is set to two levels, which represent the extremes of the space to be investigated. In the example shown in **Figure 1.2**, the resulting combinations would represent the vertices of the cube. In addition, a center point can be added to catch nonlinear behavior, which can point to local maxima or minima within the investigated space (**Figure 1.3**).

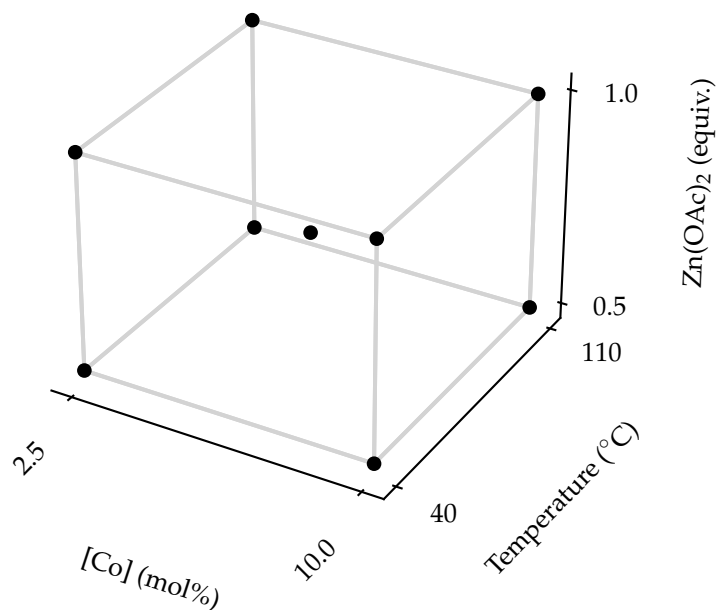


**Figure 1.3** 2-Level full factorial design inspired by the exemplary reaction space from **Table 1.2**.

After creating a design, all experimental runs are conducted either in batch or sequentially in randomized order, and the results are recorded. The process of designing and analyzing an experiment is usually done by software such as R, MODDE<sup>®</sup> or Design-Expert<sup>®</sup>. After selecting significant factors and multifactor interaction based on statistical criteria, a model equation is created that describes the response as a function of these factors. The model equation can be used both to understand the system, as well as to make predictions at specific factor settings, and to optimize the system towards a certain response, for example maximal yield or minimal impurities.<sup>[24]</sup>

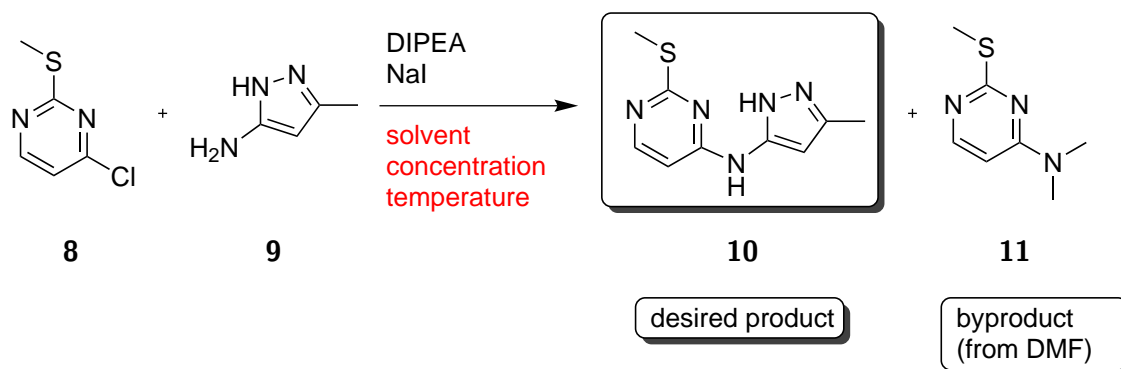
When a complex system with many factors is of interest, fractional factorial designs can be used to minimize the amount of necessary runs in exchange for the ability to capture complex multifactor interactions. By *aliasing* some of the more unlikely interactions between three or more factors among each other, thereby decreasing the *resolution*, a system with up to 16 factors can be examined in only 35 experimental runs in a *resolution IV* design (**Figure 1.4**).<sup>[4]</sup>

		Number of Factors																			
		2	3	4	5	6	7	8	9	10	11	12	13	14	15	16	17	18	19	20	21
Runs	4	$2^2$	$2^{3-1}_{III}$																		
	8		$2^3$	$2^{4-1}_{IV}$	$2^{5-2}_{III}$	$2^{6-3}_{III}$	$2^{7-4}_{III}$														
	16			$2^4$	$2^{5-1}_{IV}$	$2^{6-2}_{IV}$	$2^{7-3}_{IV}$	$2^{8-4}_{IV}$	$2^{9-5}_{III}$	$2^{10-6}_{III}$	$2^{11-7}_{III}$	$2^{12-8}_{III}$	$2^{13-9}_{III}$	$2^{14-10}_{III}$	$2^{15-11}_{III}$						
	32				$2^5$	$2^{6-1}_{VI}$	$2^{7-2}_{IV}$	$2^{8-3}_{IV}$	$2^{9-4}_{IV}$	$2^{10-5}_{IV}$	$2^{11-6}_{IV}$	$2^{12-7}_{IV}$	$2^{13-8}_{IV}$	$2^{14-9}_{IV}$	$2^{15-10}_{IV}$	$2^{16-11}_{IV}$	$2^{17-12}_{III}$	$2^{18-13}_{III}$	$2^{19-14}_{III}$	$2^{20-15}_{III}$	$2^{21-16}_{III}$
	64					$2^6$	$2^{7-1}_{VII}$	$2^{8-2}_{V}$	$2^{9-3}_{IV}$	$2^{10-4}_{IV}$	$2^{11-5}_{IV}$	$2^{12-6}_{IV}$	$2^{13-7}_{IV}$	$2^{14-8}_{IV}$	$2^{15-9}_{IV}$	$2^{16-10}_{IV}$	$2^{17-11}_{IV}$	$2^{18-12}_{IV}$	$2^{19-13}_{IV}$	$2^{20-14}_{IV}$	$2^{21-15}_{IV}$
	128						$2^7$	$2^{8-1}_{VIII}$	$2^{9-2}_{VI}$	$2^{10-3}_{V}$	$2^{11-4}_{V}$	$2^{12-5}_{IV}$	$2^{13-6}_{IV}$	$2^{14-7}_{IV}$	$2^{15-8}_{IV}$	$2^{16-9}_{IV}$	$2^{17-10}_{IV}$	$2^{18-11}_{IV}$	$2^{19-12}_{IV}$	$2^{20-13}_{IV}$	$2^{21-14}_{IV}$
	256							$2^8$	$2^{9-1}_{IX}$	$2^{10-2}_{VII}$	$2^{11-3}_{VI}$	$2^{12-4}_{VI}$	$2^{13-5}_{V}$	$2^{14-6}_{V}$	$2^{15-7}_{V}$	$2^{16-8}_{V}$	$2^{17-9}_{V}$	$2^{18-10}_{IV}$	$2^{19-11}_{IV}$	$2^{20-12}_{IV}$	$2^{21-13}_{IV}$
	512								$2^9$	$2^{10-1}_{X}$	$2^{11-2}_{VIII}$	$2^{12-3}_{VII}$	$2^{13-4}_{VI}$	$2^{14-5}_{VI}$	$2^{15-6}_{V}$	$2^{16-7}_{V}$	$2^{17-8}_{V}$	$2^{18-9}_{VI}$	$2^{19-10}_{V}$	$2^{20-11}_{V}$	$2^{21-12}_{V}$

**Figure 1.4** Obtainable resolutions for designs involving different amounts of factors depending on the number of available experimental runs. Amounts of runs given as  $2^{factors-n}$ , where  $n < factors$ . Resulting resolutions given in roman numerals. A *resolution IV* design (yellow fields) is considered to be adequate for main factor estimations.<sup>[4]</sup>

An issue arises, whenever categorical factors are of interest, a common occurrence in chemical research. Within the presented two-level designs, factors such as solvents or ligands can only be included in two levels, which is insufficient in most cases. To circumvent this, another statistical technique called *principal component analysis* (PCA) is sometimes used in combination with 2-level factorial designs.<sup>[25]</sup> PCA takes a dataset consisting of many descriptors and summarizes correlating descriptors to orthogonal *principal components* (PCs), thereby reducing the original dataset. PCA tables exist in the academic literature for various discrete factors such as solvents,<sup>[26]</sup> phosphine ligands,<sup>[27]</sup> carbenes,<sup>[28]</sup> amines<sup>[29]</sup> and aryl substituents.<sup>[30]</sup> For example, 20 properties<sup>[31]</sup> such as boiling point, dielectric constant and refractive index have been analyzed across a dataset of 136 solvents using PCA, resulting in three main PCs representing polarity, polarizability and hydrogen bonding.<sup>[26]</sup> Using principal components as factors instead of the discrete solvents, a number of  $2^f + 1$  solvents can be investigated in a single DoE, where  $f$  is the number of factors allocated for the solvents in the design. Instead of the actual values, solvents are assigned a “low” and “high” factor setting, depending on their position within the selection.

Using this technique, SHEPPARD *et al.* conducted a study on the  $S_NAr$  reaction between chloroarene **8** and pyrazolamine **9** shown in **Scheme 1.2**.<sup>[26]</sup>



**Scheme 1.2** Nucleophilic aromatic substitution between compounds **8** and **9**, leading to the formation of desired product **10** as well as byproduct **11**, which arises from the thermal decomposition of the solvent *N,N*-dimethylformamide.<sup>[26]</sup>

To avoid the formation of byproduct **11** resulting from thermal decomposition of the initial solvent dimethylformamide, a selection of five solvents chosen from a PCA dataset of 136 solvents was screened along with temperature and concentration in a  $2^{4-1}$  fractional factorial, resolution IV DoE.<sup>[26]</sup> The selection is shown in **Figure 1.5**, and their encoding for utilization in the DoE is given in **Table 1.3**.

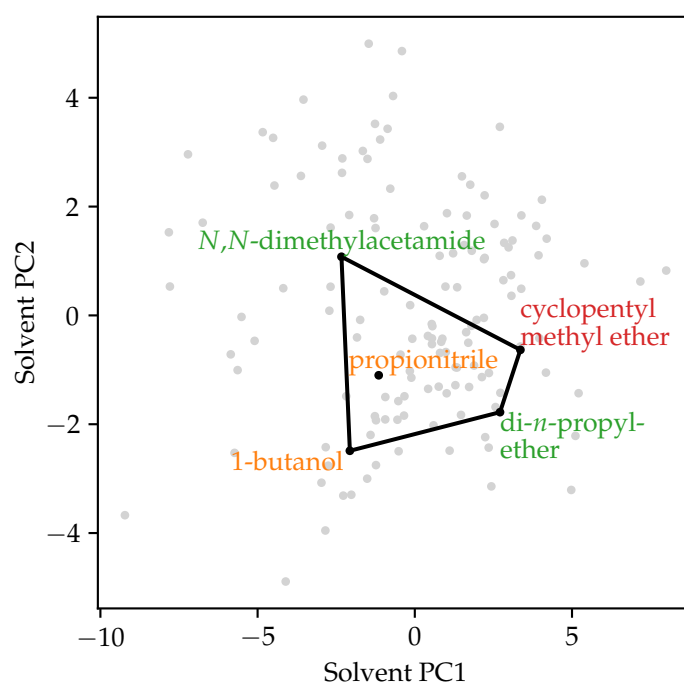


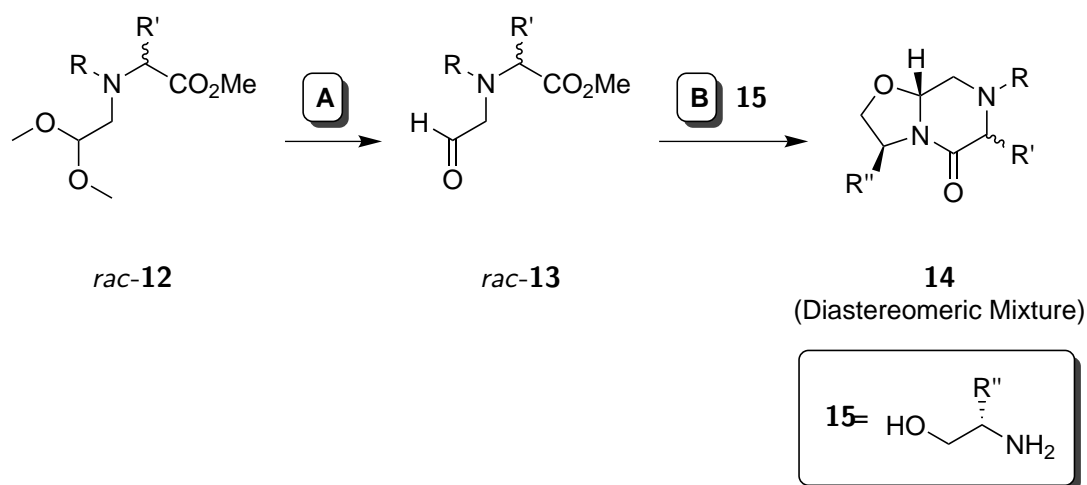
**Figure 1.5** Selection of five solvents from a 136-solvents database.<sup>[26]</sup> Colors correspond to responses in the experiment (red: low yield of **10**, orange: medium yield, green: high yield).

**Table 1.3** Encoding of five solvents by their first principal components for utilization in a fractional factorial DoE.<sup>[26]</sup> Low setting: -, high setting: +, center point: c.

Entry	PC1	PC2	Comment
1	-	-	1-butanol
2	-	+	<i>N,N</i> -dimethylacetamide
3	+	-	di- <i>n</i> -propylether
4	+	+	cyclopentyl methyl ether
5	c	c	propionitrile

As seen in **Figure 1.5**, the influence of the solvents on the yield of product **10** is non-trivial, and the chosen design allows for a clear visual interpretation of the data. Di-*n*-propyl ether, an unusual solvent for S<sub>N</sub>Ar-type reactions, was identified as the solvent of choice, and trends within the solvent space could be identified.

While in the above example, all DoE runs were conducted manually, automated equipment such as parallel synthesizers are highly suitable for DoE, as sets of runs, or even all runs of an experiment, can be conducted in parallel.<sup>[21]</sup> Consequently, this synergy has been widely exploited in the chemical and biological industries.<sup>[32]</sup> WELLS *et al.* described the optimization of the two-step synthesis of oxazolidine **14**, a late-stage API, from acetal *rac*-**12** via aldehyde *rac*-**13** using chiral amino alcohol **15** (**Scheme 1.3**).<sup>[33]</sup>



**Scheme 1.3** Two-step synthetic sequence for the generation of late-stage API **14**. **A**: MeSO<sub>3</sub>H (equiv.), AcOH (equiv.), MeCN (Volume), Temperature, Time. **B**: **15** (equiv.), temperature.<sup>[33]</sup>

Using an automated synthesis platform (UNCHAINED LABS), the authors were able to perform a  $2^{6-2}$  fractional factorial DoE in three blocks of eight automated reactions, totaling 22 runs including eight center points. Six numerical factors given in **Scheme 1.3** were investigated, and several thousand kinetic samples were automatically taken and diluted by the robotic platform, resulting in detailed, time-resolved data. Several models were generated for the formation of intermediate *rac*-**13**, product **14**, as well as various side products, and a reaction mechanism could be proposed from the findings.<sup>[33]</sup>

Synergic workflows like those mentioned above can be used for a variety of scientific problems including process development, optimization, reaction space exploration and elucidation of reaction mechanisms. In the absence of automation equipment, rational experiment planning tools such as DoE can also be used in manual workflows, lowering their entry barrier. Combining DoE with automated platforms enhances throughput even more, since robotic tools can work practically non-stop, enabling workflows such as continuous sampling over long periods of time. Therefore, the interest for such techniques has been strongly rising in both academia and industry.<sup>[34]</sup>

## 1.2 Objectives

The implementation of automated workflows can greatly assist chemists, liberating them from manual labor and allowing them to focus on the generation and investigation of hypotheses, and the analysis of data. At the same time, process development frameworks such as Design of Experiments provide an efficient way of planning and analyzing experiments in a statistically meaningful way. Combining both techniques can lead to dramatic increases in throughput, information density and reliability.

The objective of this thesis is the development and adaptation of automated workflows for ferrocene chemistry. Ideally, this goal is achieved using already available or inexpensive equipment in order to lower the entry barrier. When necessary, additional, interdisciplinary tools such as 3D printing, PYTHON programming or electrical prototyping on the ARDUINO platform will be utilized to create custom, synergistic procedures for various stages of the chemical discovery process. The feasibility of the new workflows should be tested in various use cases typical in ferrocene chemistry.

## 2 Results and Discussion

### 2.1 Development of Automated Workflows

#### 2.1.1 Parallel Synthesis and DoE

In search of useful equipment for the automation of chemical test reactions, a parallel synthesizer (ASW 2000P, CHEMSPEED TECHNOLOGIES AG) was recovered from inventory and recommissioned using a manual provided by the manufacturer, as well as reverse engineering of some components. Despite seven years of idle time, the device was found in good condition, with all parts necessary for nominal operation. An overview of the assembly is shown in **Figure 2.1**.

The parallel synthesizer is based on a main frame, which contains a vortex table, as well as adapters for reactor blocks and reagent racks. The vortex can be used for light agitation, strong stirring during reactions, and vigorous stirring for liquid-liquid extractions. All positions can be accessed using a needle head connected to a robotic arm. The needle is connected to syringe pumps and a valve system, which allows the movement of liquid from and to any position on the tray, as well as rinsing the needle. Reaction temperature is controlled by a thermostat (*Unistat*, HUBER®) in the range of  $-70\text{ }^{\circ}\text{C}$  –  $150\text{ }^{\circ}\text{C}$  using double-jacketed glass reactor arrays. An additional thermostat provides coolant for the reflux circuit, which consists of separate condensers for each reactor vial. Reactors can be put under protective atmosphere or vacuum using a valve system which mimicks the so-called SCHLENK lines known from the laboratory. Vacuum is provided by device through a membrane pump (VACUUBRAND®) controlled by the central control station of the parallel synthesizer, while inert gas can be provided through the house system. The reagent rack includes a TLC chamber, which enables the synthesizer to spot and develop 32 TLCs at once, and a *Solid Phase Extraction* (SPE) rack provides the opportunity for filtration over any filtration agent such as  $\text{MgSO}_4$  or celite. Additionally, the reactors themselves can be equipped with filter sticks, which allows for inert vacuum filtration directly from the reaction mixture. For sampling to third-party devices such as HPLC, electrically controlled 6-way valves are accessible by the needle as well.



**Figure 2.1** Photograph of the ASW 2000P parallel synthesizer. 1: Reaction thermostat. 2: Vortex table. 3: Reactor blocks. 4: Robotic arm. 5: Syringe pumps. 6: TLC chamber, reagent rack. 7: Vacuum system. 8: Reflux thermostat. 9: Control station.

Using this hardware, the device is able to perform many unit operations encountered in a traditional chemistry lab. **Table 2.1** shows a selection of those operations and compares their execution to manual workflows.

The most obvious drawback of the parallel synthesizer is its inability to handle solid reagents, as this is one of the most time-consuming tasks in the laboratory. However, conducting many reactions in parallel enables the operator to use stock solutions, which reduces the amount of necessary manual weighing operations by a factor of up to 64 (the maximum amount of concurrent reactions within the current configuration). Still, if a reagent is insoluble, it has to be weighed individually for each reaction. Additionally, only one reaction temperature can be set at a time, which makes the investigation of temperature effects in DoEs difficult. Finally, liquid handling is performed by a single needle, leading to a sequential addition of reagents. This can generate issues when time-dependent factors such as addition speeds are investigated, and when the reaction proceeds on small time scales in general.

Despite these shortcomings, the parallel synthesizer seemed to be a promising tool to accelerate research in the area of ferrocene chemistry. Some simple test experiments were conducted to observe the execution of the unit operations in **Table 2.1** in realistic scenarios. One of these experiments was a straightforward, combinatorial reactivity screening at four substituted

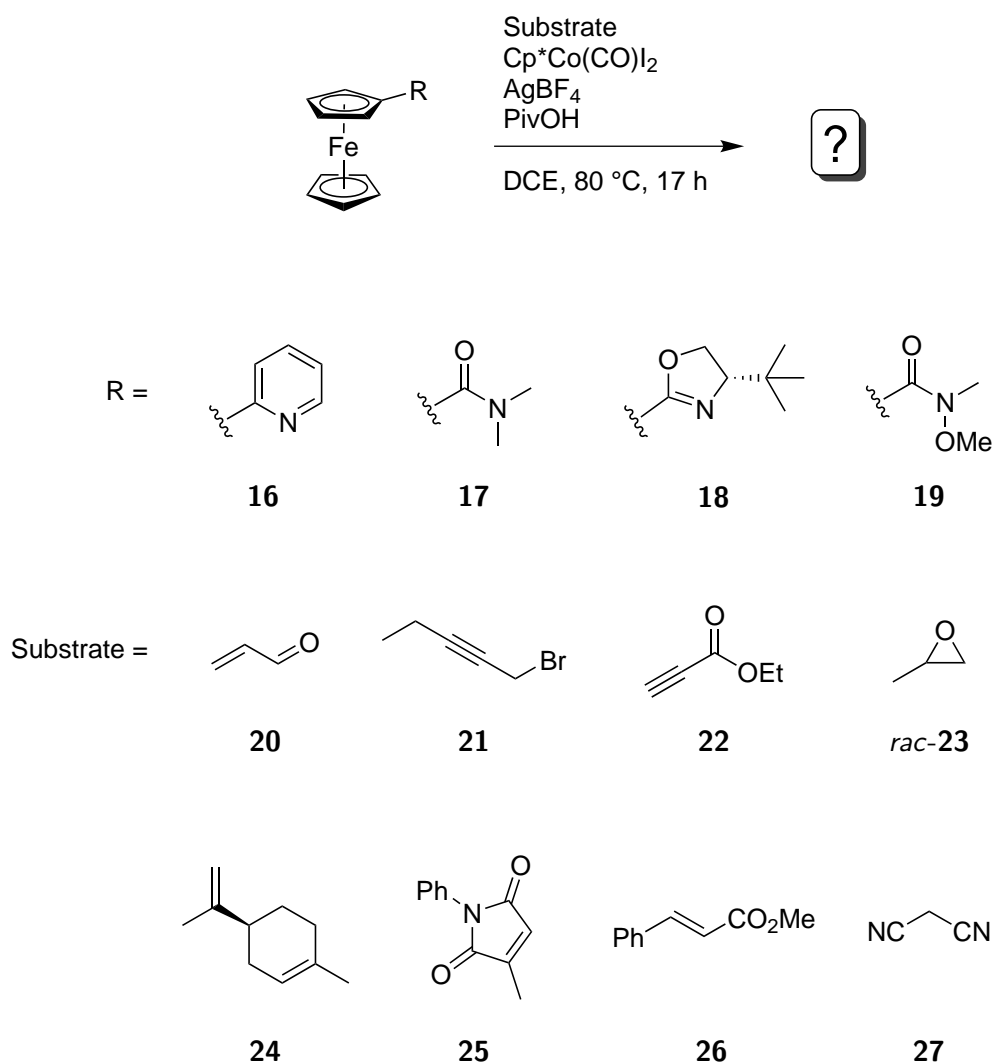
**Table 2.1** Overview of typical unit operations in the chemical laboratory, which can be executed by the ASW 2000P parallel synthesizer.

Unit Operation	ASW 2000P	Manual
Transfer of liquid (or dissolved) reagents	Robotic Arm, valve system, syringe pump (= needle system)	Pipettes, Syringes
Heating	Thermostat	Hot plates, oil baths, Heating mantles
Cooling	Thermostat	Cooling baths
Stirring	Vortex table	Magnetic stirrers, Overhead stirrers
Reflux	Reflux rack, thermostat	Reflux condensers
Inert vacuum filtration	Built-in filter sticks	Special Equipment, SCHLENK line
Filtration over agent	SPE rack	Glass frits, adapters
Evaporation of volatiles	Vacuum pump, thermostat, vortex	Rotary evaporators
Liquid-liquid extraction	Vortex table, needle system	Separatory funnels
TLC analysis	Built-in TLC rack, needle system	TLC chambers, capillaries

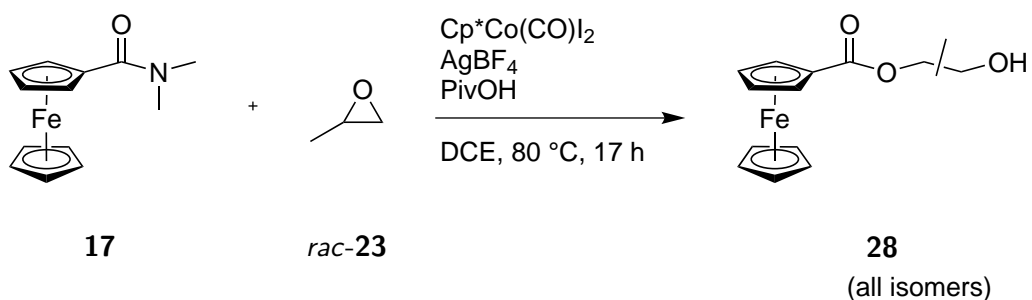
ferrocenes **16**, **17**, **18** and **19** with eight different substrates **20**, **21**, **22**, *rac*-**23**, **24**, **25**, **26** and **27** shown in **Scheme 2.1**.

All four ferrocene analogues were screened against all eight substrates under conditions typical for Cp\*Co(III)-catalyzed C-H activation,<sup>[35]</sup> resulting in a total of 32 reactions. All reagents were soluble in the reaction solvent 1,2-dichloroethane, which enabled a high degree of automation, as stock solutions could be prepared in each case. Automated TLC analysis showed some new spots, albeit none gave confirmable, new C-H activation products. The reaction of (dimethylcarbamoyl)ferrocene (**17**) and *rac*-methyloxirane (*rac*-**23**) was investigated in further studies by GERSTENBERGER, however, the product **28** showed spectroscopic signals typical for monosubstituted ferrocenes (**Scheme 2.2**).<sup>[36]</sup>





Scheme 2.1 Scheme

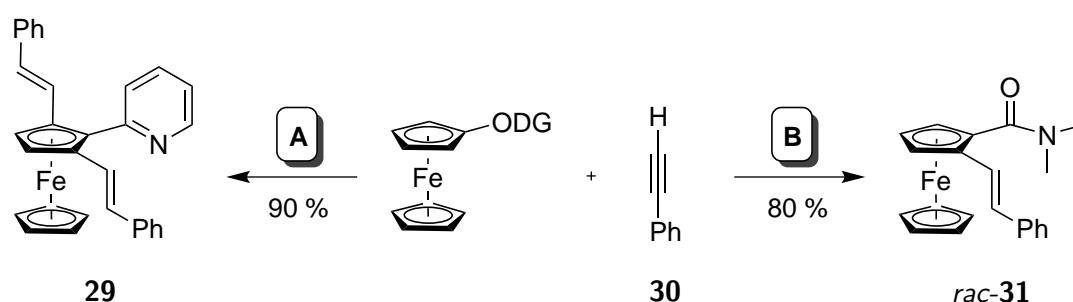


**Scheme 2.2** Suspected structure of the reaction product **28** between (dimethylcarbamoyl)ferrocene (**17**) and *rac*-methyloxirane (*rac*-**23**).<sup>[36]</sup>

This straightforward use case provided a good starting point for using the automated equipment in real-life organometallic applications. The absence of any meaningful chemical results

was expected, as the focus was placed on trying different unit operations on the hard- and software of the synthesizer. Additionally, all reagents used were either inexpensive or easy to synthesize, yet were good representatives of ferrocene-based C-H activation chemistry. All liquid transfers, incubation, solvent evaporation and redissolution as well as TLC analysis proceeded nominally, and a large amount of information could be gathered on detailed process parameters such as aspiration speeds, loop solvents and stirring speeds.

To conclusively validate the ASW 2000P for Cp\*Co(III)-catalyzed C-H activation at ferrocene, another run was set up using known chemistry published by the group of BUTENSCHÖN. Here, the catalytic alkenylation of 2-pyridyl-(**16**) and (dimethylcarbamoyl)ferrocene (**17**) with phenylethyne (**30**) was reported, with the chemoselectivity for mono- or dialkenylation strongly controlled by the *ortho*-directing group (**Scheme 2.3**).<sup>[37]</sup>



**Scheme 2.3** Influence of the *ortho*-directing group on the degree of alkenylation. ODG = 2-pyridyl: **16**. ODG = dimethylcarbamoyl: **17**. Conditions: Cp\*Co(CO)I<sub>2</sub>, AgSbF<sub>6</sub>, PivOH. **A**: PhCCH (**30**, 2.5 equiv.), DCE, 125 °C, 16 h. **B**: PhCCH (**30**, 1.0 equiv.), DCE, 100 °C, 1.5 h.<sup>[37]</sup>

In the original studies, these reactions were carried out with either directing group at various equivalents of phenylethyne (**30**). For compound **17**, both 1.0 and 2.5 equivalents of **30** exclusively led to monoalkenylation. Compound **16** on the other hand cleanly reacted to the dialkenylated product **29** with 2.5 equiv. of **30**, while 1.0 equiv. led to a mixture of starting material, mono- and dialkenylation.

To validate the parallel synthesizer for the use in Cp\*Co(III) chemistry, all four combinations were tested in a single run. Since a reactor block – the minimum unit required to run an experiment – contains 16 positions, four different addition sequences were investigated at all four combinations, fully utilizing the reactor. After several automated inert gas/vacuum cycles under strong heating, stock solutions were prepared for all reagents, which were then dispensed into the reactors in the correct order and incubated.

Automated TLC analysis performed by the synthesizer, followed by visual inspection, revealed the successful reproduction of the results obtained by manual experimentation. (Dimethylcarbamoyl)ferrocene (**17**) cleanly reacted to the monosubstituted product *rac*-**31** under all conditions given, while (2-pyridyl)ferrocene (**16**) gave mixtures with 1.0 equiv. of phenylethyne (**30**).

This proved the general feasibility of the available automation equipment for modern C-H activation chemistry at ferrocene. In addition, further inspection of the TLC plates revealed that the order of reagent addition played a role for both overall conversion as well as selectivity. Using (2-pyridyl)ferrocene (**16**) and 1.0 equiv. of phenylethyne (**30**), an early addition of PivOH led to both an increase in overall conversion of starting material, as well as an increase of selectivity for the dialkenylated product **29** over the monoalkenylated one. Similarly, when PivOH was added after the ferrocene compound, overall conversion sank and the monoalkenylated product was favored over dialkenylation. It should be noted that these results were obtained practically without any additional effort.

As the now fully operational parallel synthesizer would generate a high amount of crude samples in short periods of time, the purification and analysis of those samples was anticipated to become the next bottleneck. Ideally, it would be possible to use automated solutions for those tasks as well. Conveniently, from the same inventory, a *medium pressure liquid chromatography* (MPLC) device, as well as a parallel evaporator (BUECHI Syncore<sup>®</sup>), were recovered. The MPLC device allowed for automated, unattended column chromatography including fraction separation for one sample at a time, while the BUECHI Syncore<sup>®</sup> enabled the parallel evaporation of up to 24 samples. Together, both devices promised to alleviate the purification bottleneck which would be caused by the high throughput of the ASW 2000P.

As the equipment necessary for the automated execution and workup of ferrocene-based reactions was fully set up, the focus was placed on *Design of Experiments* (DoE). While statistical designs are perfectly compatible with automated execution in batch, they can also be used in the context of sequential, manual experimentation. To eliminate possible additional sources of error stemming from automation, the first trial DoE was conducted manually. As mentioned in **Scheme 2.2**, the reaction of (dimethylcarbamoyl)ferrocene (**17**) with *rac*-methyloxirane (*rac*-**23**) under Cp\*Co(III) catalytic conditions led to the formation of ester mixture **28**. To improve yield, the influence of solvent, time and catalyst amount was investigated in a straightforward 2<sup>3</sup> full factorial DoE (**Table 2.2**). Each reaction was set up manually, and isolated yields were determined after automated column chromatography.<sup>[36]</sup>

**Table 2.2** Factors investigated during the first exploratory DoE intended to increase the yield of product mixture **28**.<sup>[36]</sup>

Factor	Description	Type	Level -1	Level +1
A	Solvent	Categorical	Acetone	1,2-DCE
B	Time	Numeric	2 h	17 h
C	Catalyst Amount	Numeric	2.5 mol %	10 mol %

Yields were recorded in the range of 1 % – 17 %, and a significant model could be built using the factors solvent, catalyst amount as well as their interaction. The terms were selected according to their *p*-values, and in total contributed 94 % to the observed variance in the dataset. A summary is given in **Table 2.3**.<sup>[36]</sup>

**Table 2.3** Selected terms for modelling influences on the formation of **28**.<sup>[36]</sup>

<b>Term</b>	<b><i>p</i>-Value</b>	<b>% Contribution</b>
Model	0.0064	–
A (Solvent)	0.0125	27.6
C (Catalyst Amount)	0.0033	58.3
AC	0.0782	8.2

*Per* convention, terms with a *p*-Value below 0.05 are considered significant, meaning there is below 5 % chance that the observation was caused by noise. In the present case, both solvent and catalyst amount fulfill this criterium, while their interaction AC lies slightly above the threshold. The term was still included for three reasons: With 0.0782, its *p*-value was only slightly above the threshold, it showed a significant contribution of 8.2 %, and its underlying main factors were already significant parts of the model. The overall adjusted  $R^2$  value was 0.8964, which points to a good modelling of the observed results.

The main result of the investigation was that high catalyst amounts led to better yields, just as 1,2-dichloroethane was favorable over acetone. The AC multifactor interaction provided a more detailed picture, as it showed a dependency of the solvent-induced yield variation on the amount of catalyst present. More precisely, the yield improvement observed when using 1,2-dichloroethane over acetone was less pronounced at high catalyst loadings (**Figure 2.2**).

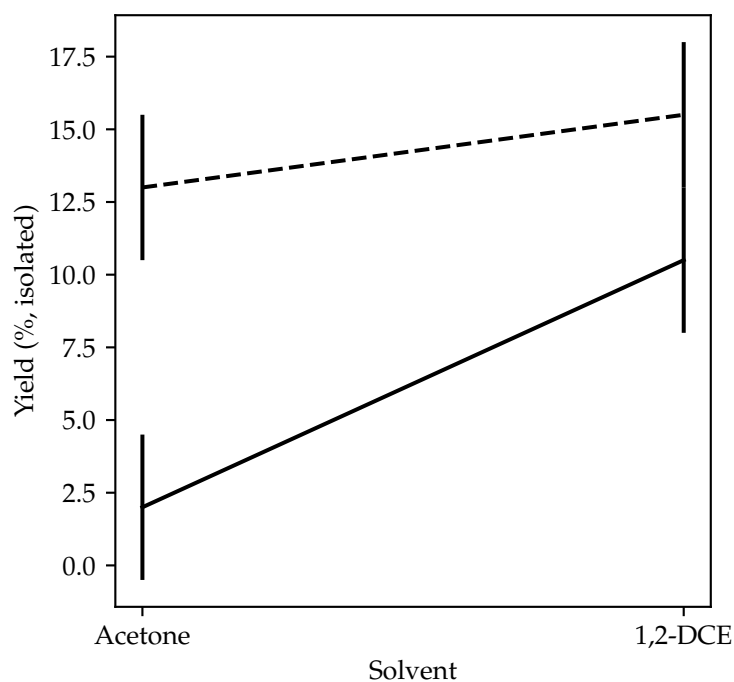


**Figure 2.2** Two-factor effects plot showing the interaction between solvent and catalyst amount. Solid line: 2.5 mol % catalyst. Dashed line: 10 mol % catalyst.

While almost no product formation occurs with acetone at low catalyst loadings, the difference between both solvents almost disappears at catalyst loadings of 10 mol %. Considering that 1,2-dichloroethane is a highly toxic, cancerogenic solvent banned for commercial use in the European Union,<sup>[38]</sup> this result is highly relevant, as in the present case it can be substituted with acetone, given higher catalyst loadings.

To gain some more experience, another DoE was prepared and manually executed, this time in the field of carbene synthesis. Besides the widely applied *N*-heterocyclic carbenes, which are known for their use as ligands in GRUBBS-type complexes,<sup>[39]</sup> a less known group of *cyclic (alkyl)(amino)carbenes* (CAAC) has been reported in 2005.<sup>[40]</sup> Their structure is shown in **Figure 2.3**.

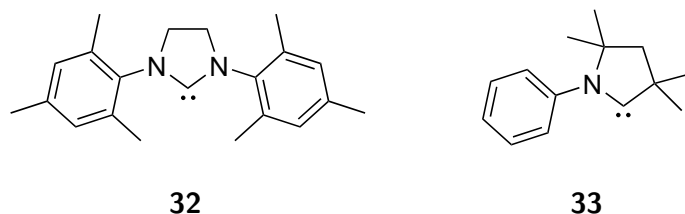
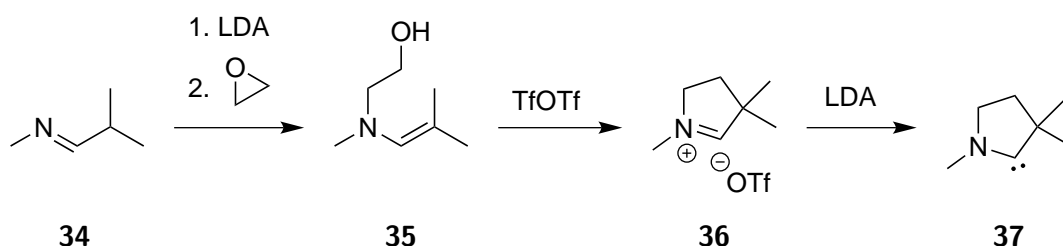


**Figure 2.3** A typical *N*-heterocyclic carbene **32**, as used in the second generation GRUBBS catalyst, next to a cyclic (alkyl)(amino)carbene **33**.<sup>[39,40]</sup>

In the context of a project utilizing a PCA table of various carbenes, CAACs became of interest, as they were located in the database in a position favorable for inclusion in another DoE. The particular CAAC of interest **37** as well as its envisioned synthesis<sup>[40]</sup> are shown in **Scheme 2.4**.



**Scheme 2.4** One-pot, multi-step sequence to cyclic (alkyl)(amino)carbene **37** investigated by DoE.

The hypothetical CAAC **37** deviated from the literature-known structures in having an *N*-methyl- instead of an *N*-phenyl substituent, as well as missing the *gem*-dimethyl group adjacent to the nitrogen atom. Unfortunately, exactly these two structural motifs were reported to be crucial for the formation of both the cationic precursor, as well as the free carbene.<sup>[41]</sup> Nonetheless, the synthesis of **37** was attempted using a fractional factorial  $2^{(4-1)}$  design. Factors investigated were the nitrogen substituent, addition temperature and -time of the epoxide, as well as the stirring time before triflic anhydride addition. These process parameters were chosen since the literature reaction involved short reaction times and low temperatures, hinting at kinetic reaction products. The list of all experiments is given in **Table 2.4**.

**Table 2.4**  $2^{(4-1)}$  fractional factorial design for the attempted formation of carbene **37**.

Experiment (No.)	<i>N</i> Substituent	Addition Temp. (°C)	Addition Time (min)	Stirring Time (min)
1	Me	23	1	15
2	Me	0	5	15
3	Me	23	5	1
4	Me	0	1	1
5	Ph	0	1	15
6	Ph	23	1	1
7	Ph	23	5	15
8	Ph	0	5	1

Since there was a high probability of no product formation at all, mass spectra of various intermediate stages of the reaction were taken, and the presence or absence of the expected intermediate signals were chosen as responses. Within a single DoE, any desired number of responses can be analyzed, further increasing the potential information gain.

For all responses, models were either barely significant, or not at all. Besides the fact that a fractional factorial design has limited resolution, binary responses (yes/no) were given instead of continuous numeric ones, which further limited the predictive capabilities of the generated models. Nonetheless, some trends were observed. The formation of intermediate **35** was favored by a fast addition of the epoxide at low temperature. The correct  $m/z$  for the triflate addition product was only observed in one case, where again low settings for all times and temperatures had been applied.

Although models were barely significant, if at all, some trends could be derived. All observable formation of intermediates took place at low temperatures and short reaction times. While the synthesis could be attempted at even lower temperatures and shorter times as a follow-up, the findings confirmed the literature,<sup>[41]</sup> and no stable product could be isolated.

An interesting observation was made, when the reaction flasks were visually inspected after completion of all runs. In the cases of phenyl as the *N* substituent, the appearances of the reaction mixtures dramatically differed from each other (**Figure 2.4**).

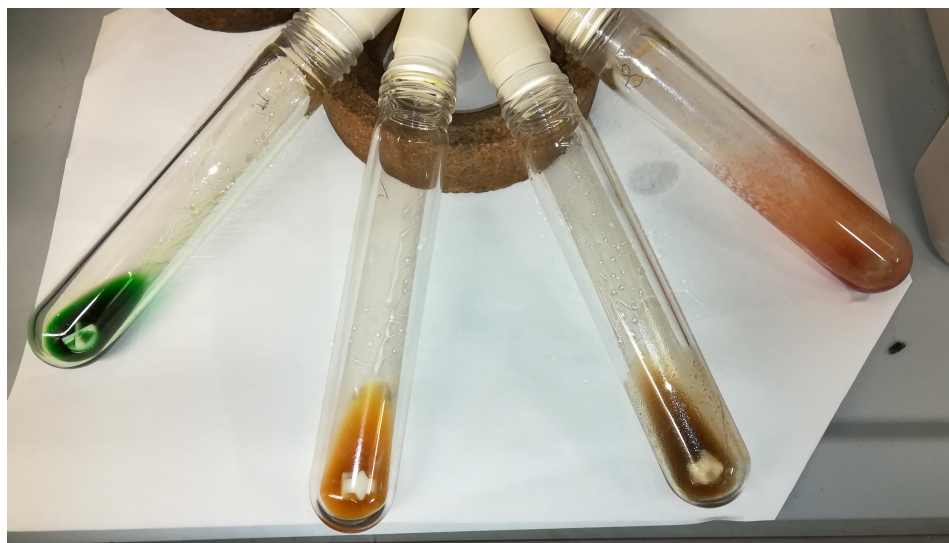


**Figure 2.4** Different visual appearances of reactions with *N*-phenyl substituents.

Even though no product was isolated, the different conditions seemed to have a strong impact on the behavior of the reaction mixtures. All reagents within the four flasks shown in **Figure 2.4** were exactly the same, yet still the products – although not characterized – were vastly different,

at least visually. Upon reducing the number of experiments, fractional factorial design select conditions that are “most different” from each other to ensure an even coverage of a wide reaction space. Thus, the lack of product formation was seen as conclusive, and no further investigation on this reaction seemed necessary.

The presented use cases both in automation and DoE served as a good starting point to understand and gain experience with these tools. The obtained knowledge was then used in further applications, which are discussed in detail in **Section 2.2**.

## 2.1.2 Quantitative Thin-Layer Chromatography

### Idea and Concept

One of the recurring themes of this thesis is the elimination of bottlenecks by leveraging synergies between available equipment, or creating custom additional features if necessary. As mentioned in **Section 2.1.1**, the ASW 2000P parallel synthesizer has the capability of spotting and developing up to 32 TLCs in an automated fashion. As this thesis deals mostly with non-polar ferrocene chemistry, standard normal-phase thin-layer chromatography was already the method of choice for quick reaction progress monitoring. More sophisticated chromatographic methods such as *high performance liquid chromatography* (HPLC) provide the user with both structural (if coupled with a mass detector) and qualitative (peak integrals) data. In contrast, TLC plates are usually only inspected visually to estimate reaction progress, leading to suboptimal exploitation of the potential of this technique. Because of the now automated nature of TLC sampling, the high number of parallel samples possible as well as the high degree of standardization, the question was raised whether more information could be extracted from the automatically generated TLC plates (**Table 2.5**).

**Table 2.5** Comparison of HPLC-MS and TLC.

HPLC-MS	TLC
Quantitative	Semi-Quantitative
Peak Integrals	Approximate Spot Sizes
$m/z$ , Atomic Formulas	Spot colors
Complex Setup	Simple Setup
Expensive	Inexpensive
Automated	(Typically) Manual



Retrieving structural information from the TLC plates became straightforward when an expression<sup>®</sup> compact mass spectrometer by ADVION was purchased by a collaborating group in combination with the plate express<sup>®</sup> add-on. This benchtop device designed for chemist end-users is advertised to be capable of extracting spots directly from TLC plates and generating mass spectra using an APCI or ESI ionization source, a technique which will be called TLC-MS within the scope of this thesis. This claim was confirmed with manually generated TLC plates in earlier studies, with the APCI source practicably returning the molecular ion peaks exclusively in most cases. Applying this technology in combination with the automatically generated TLC plates from the parallel synthesizer was trivial, as the plate express<sup>®</sup> module accepts any TLC plate, and spots are extracted selectively by alignment with a built-in laser pointer. Thus, molecular identities of compounds generated in the parallel synthesizer could easily be confirmed or at least estimated using the synergy between ASW 2000P and ADVION expression<sup>®</sup>. Conveniently, no dedicated hardware connection had to be made to the parallel synthesizer, allowing the mass spectrometer to be used in manual workflows as well (Figure 2.5).

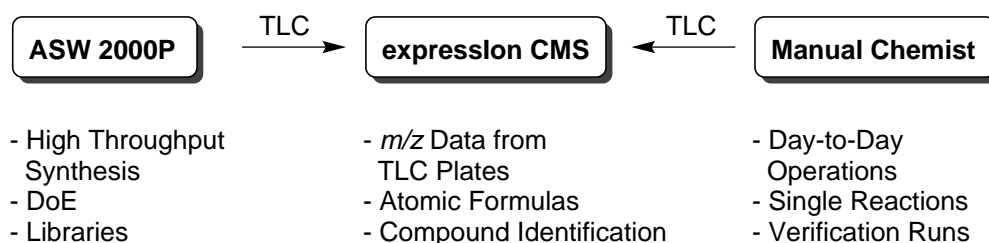


**Figure 2.5** TLC-MS workflow between ASW 2000P and ADVION expression<sup>®</sup>.

The combination of parallel synthesis and semi-automated TLC-MS presented a significant advantage in the everyday laboratory work during this thesis, and some thought was put into further capitalizing on the automated TLC feature. Obtaining quantitative data is one of the key tasks of an organic chemist, as the yield of a reaction is probably the single most important response metric in optimization and synthesis. It was reasoned that quantitative data should be obtainable from automatically generated TLC plates, similar to gel documentation systems in biochemistry. These systems are typically used to quantify biomolecules after gel electrophoresis, a process much similar to TLC in that molecules are separated across a simplified two-dimensional surface and detected visually. Consequently, such devices have also been manufactured specifically for TLC applications and are called TLC densitometers, the most notable example being the CAMAG<sup>®</sup> TLC Scanner 4 (Figure 2.6).



**Figure 2.6** TLC Scanner 4, a popular, optical TLC densitometer by CAMAG® (Image modified).

The idea of extracting quantitative data from thin layer chromatograms is almost as old as the method itself, dating back to 1953.<sup>[42]</sup> While early attempts focused on scraping spots of interest off the plates, extracting the analyte and weighing the residue after evaporation,<sup>[43]</sup> reflection-based methods soon emerged and became popular due to their non-destructive nature.<sup>[44]</sup> The first commercial densitometer was available as early as 1964 by CAMAG®, and the devices were constantly upgraded according to available technology such as digital cameras and image processing software.<sup>[45]</sup> For the projects in this thesis, this professional equipment was unavailable due to the high risk/reward ratio associated with the cost of the devices. For this reason, a low-cost, DIY system was designed and implemented using a common smartphone, 3D printing and PYTHON programming.

## Implementation

The development process was divided into two parts, consisting of 1) the hardware-based process of obtaining standardized photographs of chromatograms, and 2) the software-based process of analyzing those photographs to obtain one-dimensional densitograms and, eventually, usable peak integrals (**Figure 2.7**).

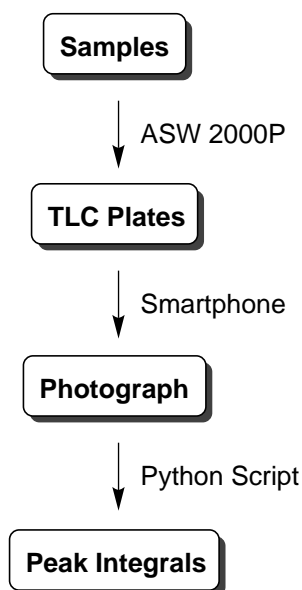


**Figure 2.7** Envisioned process for obtaining quantitative data from automated TLC.

For the hardware side, some type of rack was necessary to contain the TLC plate, the camera and a light source, preferably both in UV and vis wavelengths, respectively. As the camera, a smartphone was chosen for convenience. To construct the rack, the proper distance between smartphone and tlc plate had to be found to ensure optimal use of the resolution of the camera. A first rough prototype was built out of Lego<sup>®</sup>, and all necessary measurements were taken. Next, a 3D model was designed using AUTODESK Inventor Professional<sup>®</sup> (**Figure 2.8a**), and successively 3D printed using polylactic acid (PLA) filament. The prototype had a removable compartment to accomodate a standard TLC plate from the ASW 2000P. In the correct distance, a cutout for a Honor 6X smartphone was made so that its camera was placed in the center of the TLC plate, while the plate covered the entire image field of the smartphone. To the side, another diagonal cutout could take a standard UV/vis lamp so that it covered the entire opening, sealing the TLC plate inside from daylight and thus providing a standardized illumination. The full assembly is shown in **Figure 2.8b**.

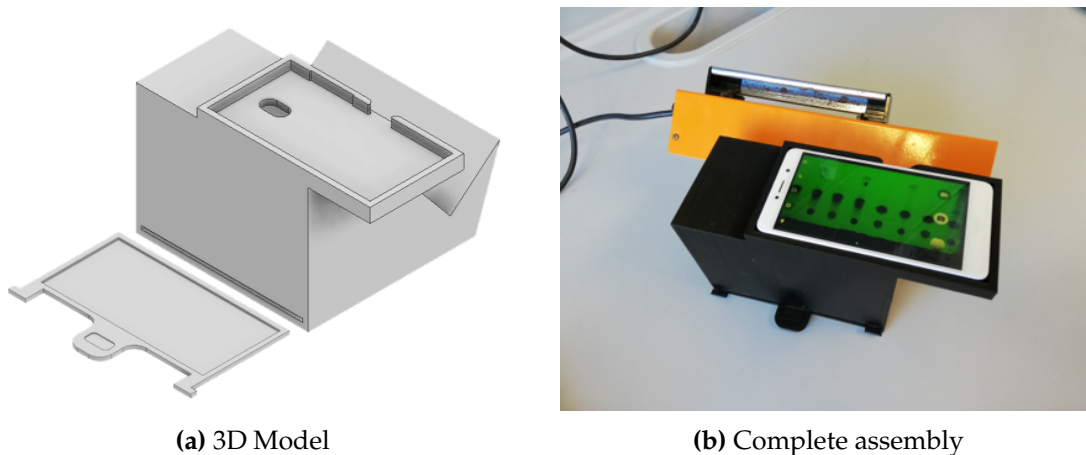


**Figure 2.8** TLC Chamber for the repeatable generation of standardized TLC plate photographs. Size of main chamber: 218 mm × 129 mm × 178 mm.

With standardized photographs of TLC plates available, the next task was to design and implement the image processing algorithm. The general idea with its top-level tasks is shown in **Figure 2.9**.

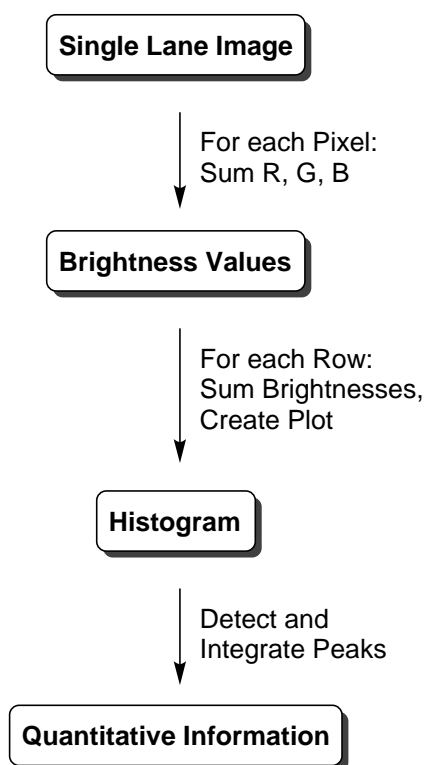


**Figure 2.9** Concept for obtaining peak integrals from photographs of automatically generated TLC plates using a PYTHON algorithm.

After reading the image, the single lanes have to be separated and analyzed individually. For each lane, pixel brightnesses per row must be summed up, and their values plotted against distance, creating a histogram which is equivalent to a chromatogram in HPLC. After peak detection, the area of each peak has to be determined and returned to the user, optimally in a standard file format such as csv.

The \*.jpg image is taken with the smartphone and transferred to a laptop using a cloud service. In the first steps of the PYTHON algorithm, the image is read, inverted and sliced into the areas that make up the eight lanes created by the parallel synthesizer. Due to the high degree of standardization provided by both the ASW 2000P and the 3D printed TLC chamber, the lane areas could be determined empirically once, and then hard-coded. To ensure proper execution, separate images of all lane selections can be stored during each run of the software. Inversion was carried out to obtain positive peaks. All image manipulation steps were carried out using the PIL imaging library (Figure 2.10).<sup>[46]</sup>

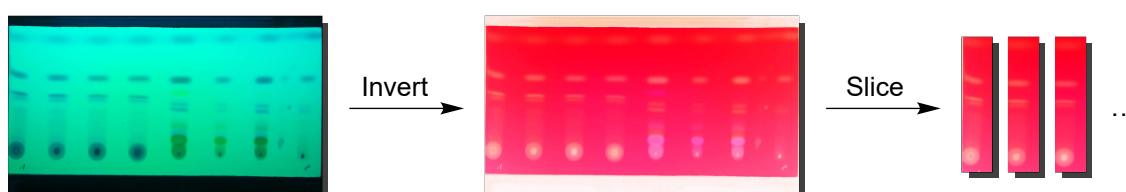


Figure 2.10 Image manipulation preceding quantitative analysis.

Next, each lane had to be processed to obtain a 1D densitogram. Every lane was stored as a  $3 * 360 * 1700$  array, representing the R, G, B values for each pixel, multiplied by the amount of pixels. First, each pixel was converted to a “brightness” value by taking the average of the (R,G,B) tuple. For each row representing a certain elution distance, the average of all 360 brightness values was taken, resulting in a single value per distance (Figure 2.11).

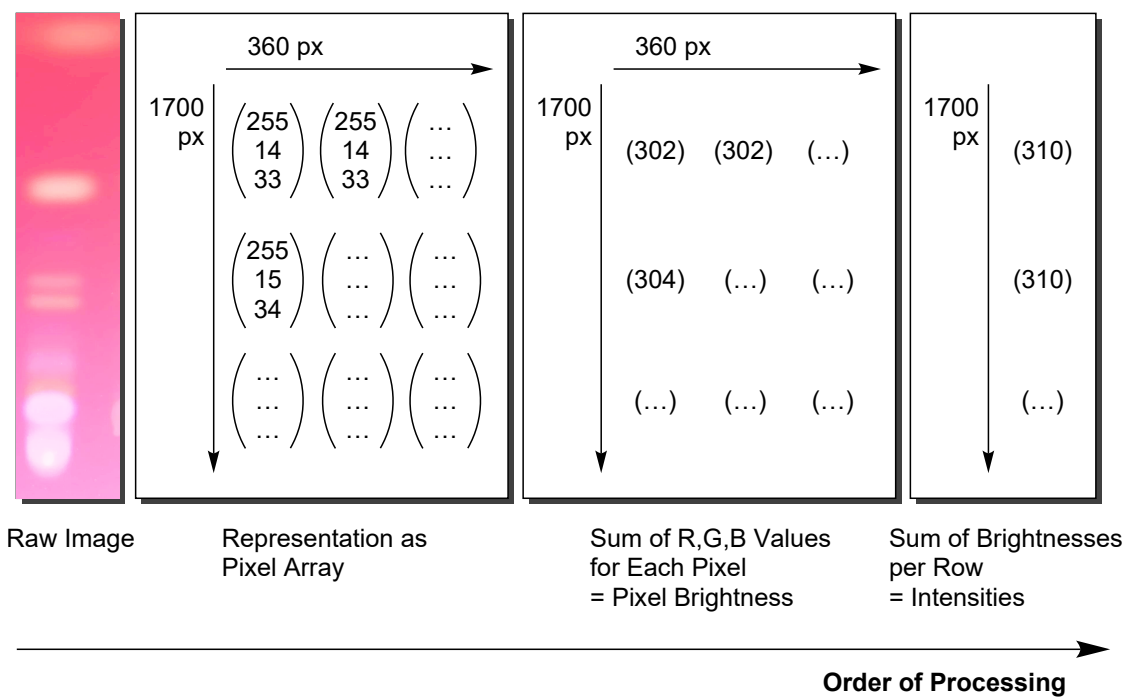


Figure 2.11 Obtaining densitograms from pre-defined lanes.

Plotting these “total intensity” values across the 1700 distance values results in the desired raw densitogram as shown in Figure 2.12.

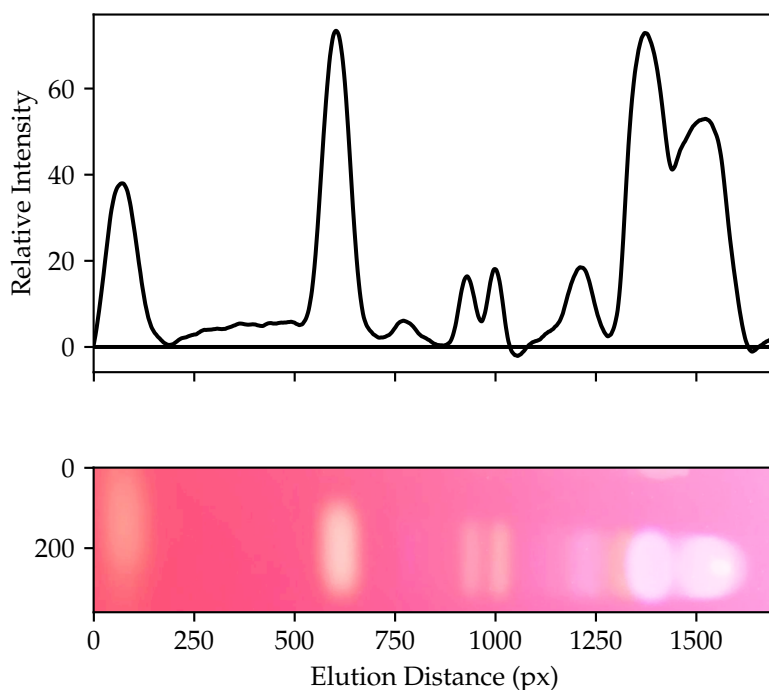
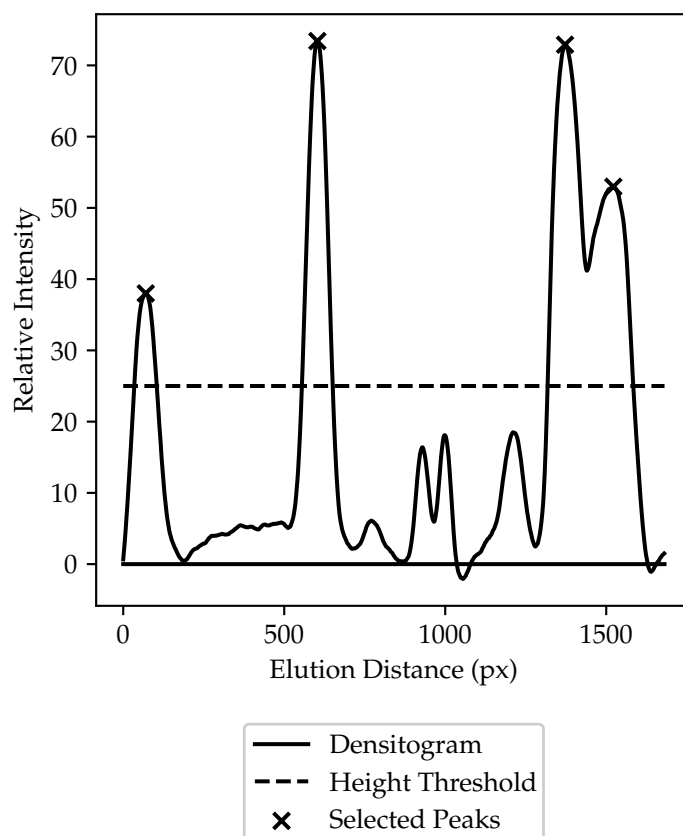


Figure 2.12 Exemplary QTLC densitogram with the underlying TLC lane image.

To eliminate noise, the raw data was first baseline corrected, and then moving average smoothing (window size = 20 px) was applied. Many PYTHON libraries with peak detection features exist, *scipy*<sup>[47]</sup> and *peakutils*<sup>[48]</sup> being two examples. Within this project however, these libraries gave inconsistent results while being somewhat intransparent in their functionalities, leading to overcomplication. Instead, peaks were selected by a simple height threshold criterium, which worked well especially for densitograms with little noise caused by decomposition of analytes (**Figure 2.13**).



**Figure 2.13** Simple peak selection using a height threshold criterium.

The integration of chromatographic peaks is a non-trivial subject, and many different methods have been developed in this area.<sup>[49]</sup> Among those using “traditional” maths,<sup>[50,51]</sup> some recent developments have been made using machine learning to detect and integrate peaks.<sup>[52]</sup> The main challenge arises with overlapping peaks, where some sort of deconvolution has to take place in order to estimate all areas correctly. Some methods investigated in this thesis are shown in **Figure 2.14**.

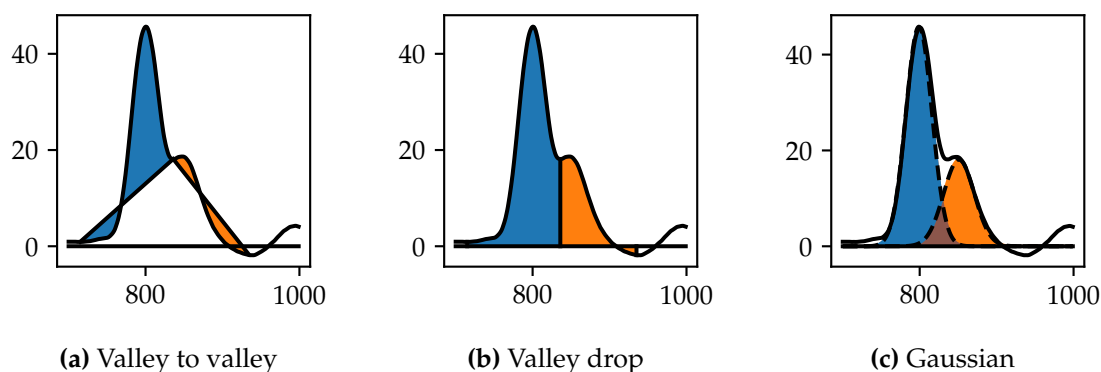


**Figure 2.14** Different QTL peak integration methods and their performance with overlapping peaks.

The first proof of concept was given using a valley-to-valley method. This is appropriate for well-separated peaks, but lacks with overlapping peaks, as areas are drastically underestimated. In severe cases such as in **Figure 2.14a**, baselines can even be above the sample curve, leading to negative integrals. The valley drop method is more appropriate, but problems arise with overlapping peaks of significantly different sizes, as the smaller peak is usually overestimated (**Figure 2.14b**). The final method of choice was a GAUSS fitting of all detected peaks, performing well in most situations encountered within the chemistry projects in this thesis (**Figure 2.14c**). After detection of all peaks in a lane, a model for the entire densitogram is created using a sum of as many GAUSS curves as there are detected peaks, according to **Equation 2.1**.

$$f(x) = \sum_{i=1}^n \alpha_i \frac{1}{\sigma_i \sqrt{2\pi}} e^{-\frac{1}{2} \left( \frac{x-c_i}{\sigma_i} \right)^2} \quad (2.1)$$

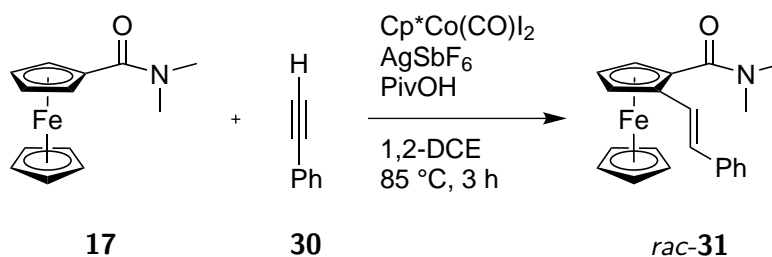
This sum of GAUSS curves is then optimized at once to fit the original data using a LEVENBERG-MARQUARDT algorithm<sup>[53,54]</sup> implemented in the PYTHON library *scipy*. The optimized parameters  $\alpha_i$ ,  $\sigma_i$ ,  $c_i$  for each summand  $i$  are then used to calculate the area of each contributing peak by taking the sum of its function values across the entire range. Optimizing all peaks at once prevents overestimation at regions of overlap, and provides good overall results.

The entire process is repeated for each lane, and results are stored in multiple ways. For quick visual inspection, the processed densitograms are stored as \*.png files, with all integrated areas colored. Additionally, for each TLC plate, a \*.csv file is created storing position and integral values for each peak, sorted by lane. These files can be processed further manually, or machine-read by other applications, and provide an easy way to use the obtained data without any additional, proprietary software. For example, peak areas were routinely divided by each other directly within the \*.csv file using a spreadsheet software, and the results directly copied into STAT-EASE Design-Expert<sup>®</sup> for creating DoE models.



## Results and Validation

Before applying the technology in actual use cases, its accuracy and reproducibility had to be validated. As a first benchmark, the reaction of (dimethylcarbamoyl)ferrocene (**17**) with phenyl ethyne (**30**) was chosen, since it had been well investigated in the group before (Scheme 2.5).<sup>[37]</sup>



Scheme 2.5 Test reaction for the validation of the QTLC methodology.<sup>[37]</sup>

Similar amounts of all reagents were added to the 16 reaction vials of a single reactor block and incubated according to protocol. Due to an unknown handling error, the anticipated reaction did not take place. However, samples of the crude reaction mixtures containing all starting materials were still subjected to automated TLC, and spots for both the ferrocene compound **17** as well as the alkyne **30** could be observed. Since the same amounts were aliquoted to all vials, similar peak sizes were expected between reactions. The first analysis was carried out using the valley to valley integration method, and the results for both compounds are shown in Figure 2.15.

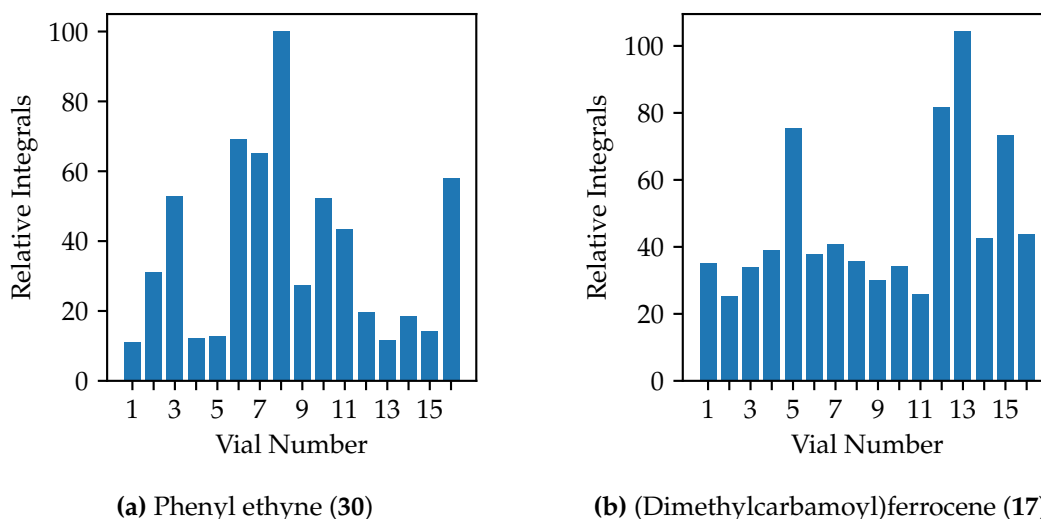
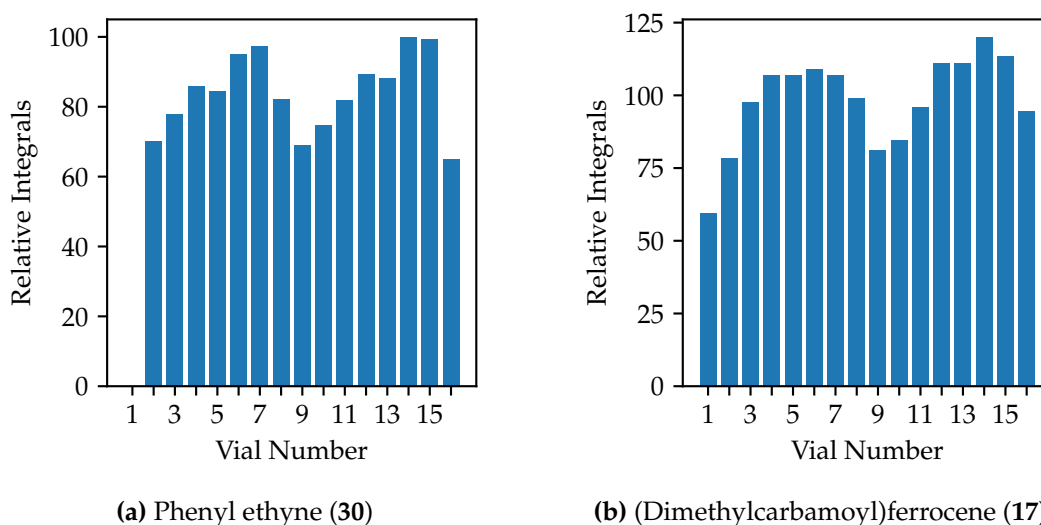


Figure 2.15 QTLC analysis of 16 samples of equimolar amounts of compounds **30** and **17** using simple valley-to-valley integration. Peak integrals are vastly different between samples, and do not correlate to each other. Relative Integrals: Highest value arbitrarily set to 100 for easier readability.

Peak integrals varied significantly between samples, with some examples being almost an order of magnitude apart (samples 5 and 8, phenyl ethyne (**30**), **Figure 2.15a**). It was unclear whether this was due to severe liquid handling errors or a lacking integration algorithm, or both. To exclude a faulty algorithm, integrals were compared between compounds **30** and **17** across all vials. Comparing vials among each other, no correlation could be observed, pointing towards grave errors during peak integration.

After development of the GAUSS integration method, the raw data stored in the form of photographs of the TLC plates was revisited. GAUSS integration was applied, and the results were collected and graphed as before (**Figure 2.16**).



**Figure 2.16** QTLC analysis using GAUSS integration. The deviation between vials is significantly smaller than with the valley-to-valley method, and a correlation between both compounds across all vials is visible. Relative Integrals: Highest value arbitrarily set to 100 for easier readability.

Using the refined GAUSS integration method, the variance across vials is significantly reduced compared to the results obtained from the valley-to-valley method in **Figure 2.15**. Additionally, there is a clear correlation across vials between both compounds, which points to the errors now originating more from liquid handling errors, or uneven consumption of starting materials, which can be expected. To emphasize the correlation, the quotients between peak integrals of compounds **30** and **17** were plotted (**Figure 2.17**).

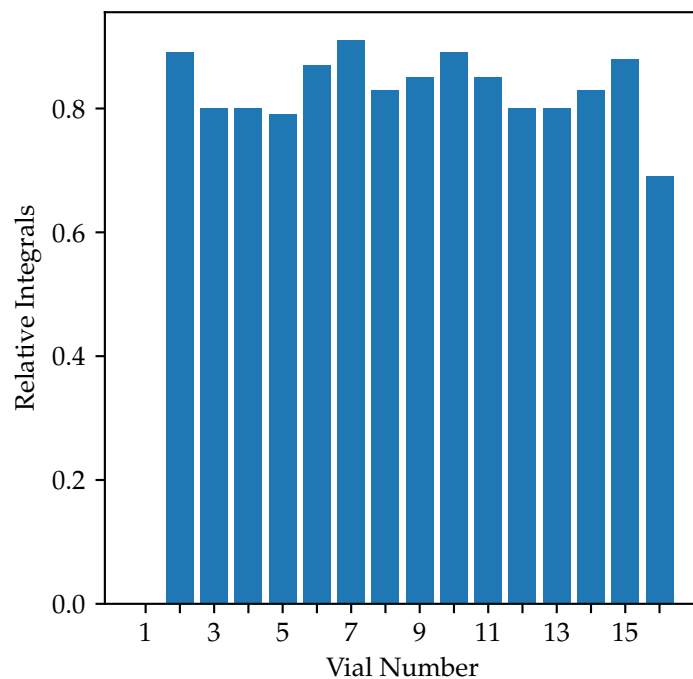


**Figure 2.17** Quotients between peak integrals of compounds 30 and 17.

Dividing the peaks of compounds 30 and 17 by each other, a more random distribution emerges, with an even smaller standard deviation than that of standalone compound integrals. In this case, where no conversion took place, this is akin to referencing against an internal standard. Generally, comparing two compounds from a single run by dividing their integrals yields more reliable values than taking single compound integrals. In later applications of the QTLC method, product integrals were often divided by integrals of leftover starting material *in lieu* of an internal standard. This carries the underlying assumption that no major decomposition pathways exist for the starting material other than formation of product, which is not always the case. Nevertheless, good DoE models were usually obtained from responses obtained in this fashion.

To compare both integration methods more directly, mean values and their standard deviations for the 30/17 quotients were plotted for both integration methods (**Figure 2.18**).

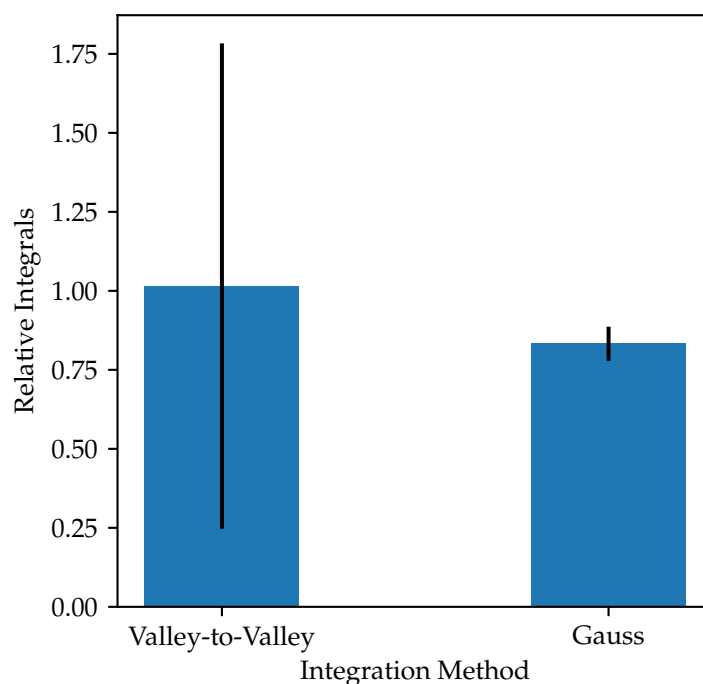


**Figure 2.18** Comparison of mean values and their standard deviations for both integration methods. The outlier in vial 1 (no phenyl ethyne (**30**) detected) was omitted from the calculations. Error bars represent two standard deviations ( $\pm SD$ ).

The estimated mean value obtained by the valley-to-valley method is higher than that obtained using GAUSS integration. More importantly, the standard deviation is much smaller in relation to the absolute value using GAUSS integration, confirming the trend observed in **Figure 2.16**. Considering the somewhat undefined behavior of the reaction mixture in this example, the obtained values indicated a good usability of the QTLC method, assuming compound referencing and GAUSS integration.

To further confirm the stability of the method, some calibration curves were created using different ferrocene-based compounds used in this thesis. As a first example, a dilution series of acetylferrocene (**38**) against a constant amount of 1,1'-diacetylferrocene (**39**) was made automatically using the ASW 2000P (**Figure 2.19**).

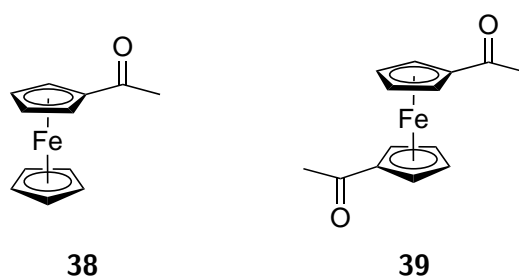


**Figure 2.19** Structures of acetylferrocene (**38**) and 1,1'-diacetylferrocene (**39**).

Starting from a stock solution concentration of  $0.5 \text{ mmol mL}^{-1}$ , a total of eight samples were created with a dilution factor of two. Concentrations were chosen so that typical reaction concentrations ( $10 \text{ mg mL}^{-1} - 20 \text{ mg mL}^{-1}$ ,  $0.1 \text{ mmol mL}^{-1}$ ) were included, as well as some higher concentrations to test the limits of the method. The calibration plot obtained from dividing integrals of acetylferrocene (**38**) against the internal standard is shown in **Figure 2.20**.

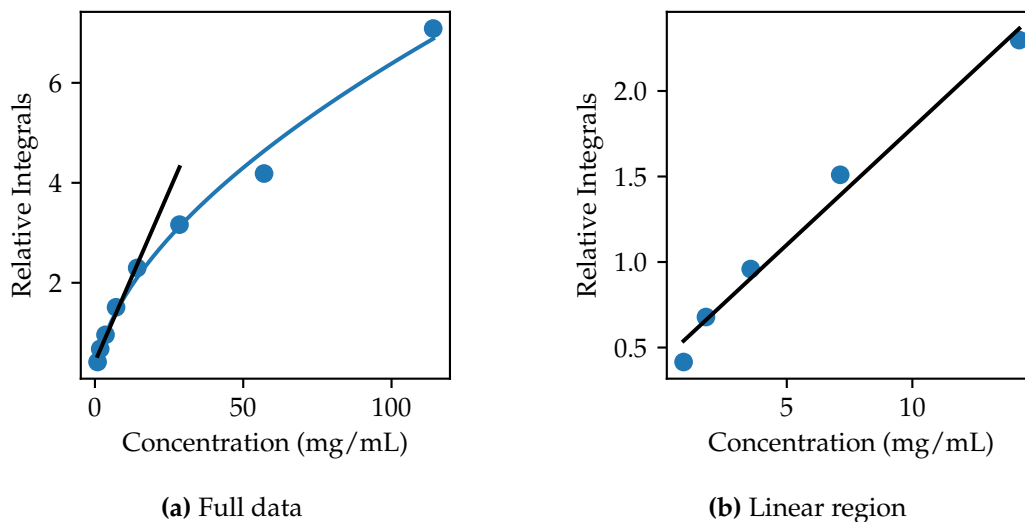
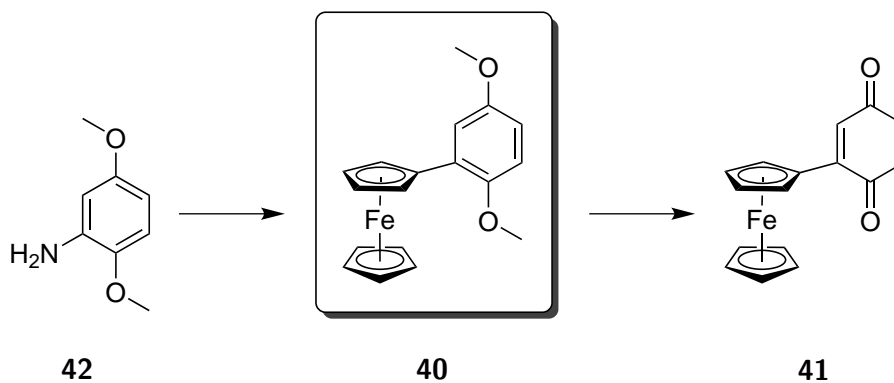


**Figure 2.20** Calibration curve for dilution series of acetylferrocene (**38**) against 1,1'-diacetylferrocene (**39**) as internal standard. Black lines: linear regression over the concentration range of  $0.89 \text{ mg mL}^{-1} - 14.25 \text{ mg mL}^{-1}$  (first five values),  $y = 0.1366x + 0.4173$ ,  $R^2 = 0.9834$ . Blue line: power regression over entire dataset,  $y = 0.4631x^{0.5698}$ .

The overall data follows a non-linear trend and is best approximated using a power function, which resembles a square root approximation ( $y = a \cdot x^b$ ,  $b \approx 0.5$ , **Figure 2.20a**). As the concentration range was chosen to include exceedingly high concentrations of analyte, this was to be expected, as a saturation range was reached due to intermolecular interactions. Nonetheless, the five lowest-concentration values gave a good linear fit. acetylferrocene (**38**), within typical reaction concentrations, can be analyzed using QTLC and shows a linear correlation between concentration and referenced sample integrals.

To confirm these findings, another compound relevant to this thesis was investigated in a similar way. (2,5-dimethoxyphenyl)ferrocene (**40**) is an intermediate compound in the synthesis of quinoylferrocene (**41**) from 2,5-dimethoxyaniline (**42**) (**Scheme 2.6**).



**Scheme 2.6** (2,5-dimethoxyphenyl)ferrocene (**40**) as an intermediate in the synthesis of quinoylferrocene (**41**) from 2,5-dimethoxyaniline (**42**).

Its synthesis *via* a GOMBERG-BACHMANN reaction was subject to a DoE analysis for yield optimization, which is thoroughly investigated in **Section 2.2.1**. As such, it provided a real-world example for validation of the automated QTLC method. The calibration plot is given in **Figure 2.21**.

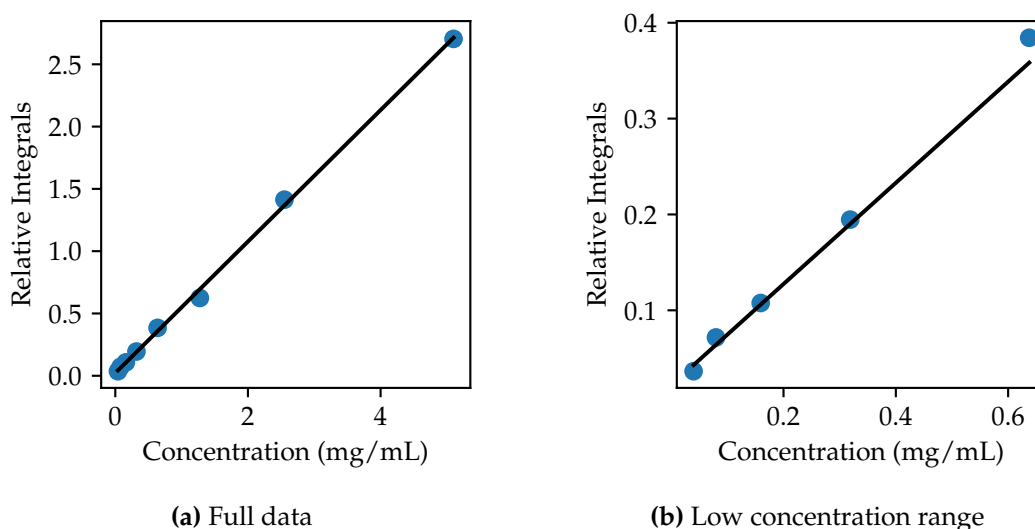


**Figure 2.21** Calibration curve for dilution series of compound (**40**) against acetylferrocene (**38**) as internal standard. Black lines: linear regression,  $y = 0.5277x + 0.0219$ ,  $R^2 = 0.9987$ .

Compound (**40**) was diluted starting from a stock solution of  $5.1 \text{ mg mL}^{-1}$ , a range which was previously determined to show linear correlation. This finding was verified, with the entire range being represented well by a linear regression function (**Figure 2.21a**). Values of low concentration still lie in the linear range, down to values of  $0.04 \text{ mg mL}^{-1}$ , or over two orders of magnitude in total (**Figure 2.21b**). As an example, if compound **40** was investigated

as a reaction product, yields from 1 % – 100 % could safely be determined using automated QTLC.

## Conclusion

In order to optimally leverage the automated TLC feature of the parallel synthesizer, methods for obtaining both structural and quantitative data from TLC plates were developed. Mass spectra of separated TLC spots were easily obtained from an ADVION expression<sup>®</sup> mass spectrometer with the plate express<sup>®</sup> module. To obtain quantitative data, a methodology based on standardized photographs of TLC plates obtained from the ASW 2000P and subsequent peak integration using PYTHON was designed and implemented. After introducing GAUSS fitting and peak referencing, the method gave linear correlations for two ferrocene-based examples in concentration ranges typical in organic chemistry.

Further improvements could include a more stable GAUSS fitting algorithm, as sometimes peak fitting is inaccurate with high amounts of noise present. In these cases, fitting the broad noise can give a better fit when unconstrained functions are used. Additionally, peak detection currently relies on a simple height threshold, which can become problematic again when excessive noise is present. In these cases, important peaks are either not selected, or a multitude of noise peaks is selected together with the actual analyte peaks, leading to unnecessarily long fitting times, and sometimes errors. This could be improved by selecting peaks according to additional criteria such as width and prominence. Moreover, peak shoulders are currently not detected, which limits the applicability of the method when strong peak overlapping is present in the data. This issue could be remedied by looking at zero-crossings of second derivatives of the densitograms.

After its development, automated QTLC was used routinely within all chemistry examples in this thesis due to its robustness against unpurified samples and low manual effort, as well as high reliability and speed. Responses from QTLC were used to generate various DoE models (**Sections 2.2.1**) as well as time-resolved decomposition analyses (**Section 2.2.3**).

## 2.1.3 Custom Scripts and Tools

### Overview

One of the aims of this thesis was to acquire industry-relevant skills in some modern prototyping tools such as 3D printing, PYTHON programming and building electrical circuits on the ARDUINO platform. These skills were then used to create both hardware- and software-based, custom scripts and tools to help the chemist with their daily routine. Some selected

examples, namely an automated charge calculation tool, a communication interface for the parallel synthesizer, and a photoreactor for the high throughput screening of photoreactions, are showcased in this section.

## Reaction Preparation and Charge Calculation

One of the recurring tasks of chemists is the calculation of reaction charges, i.e. the amounts of reactants and reagents needed for each chemical transformation. In our group, this is usually done by manual lookup of reagent properties online, or drawing structures using software such as CHEMDRAW and extracting molar masses from there. This information is then transferred to paper journals, where charges are calculated using physical calculators. Other groups use EXCEL sheets that function both as databases as well as digital laboratory journals. After each new calculation, it is checked whether some of the required reagents are available in-house. The remaining chemicals are ordered using a standardized EXCEL sheet, where the user has to fill in details such as order number, vendor and price (Figure 2.22).

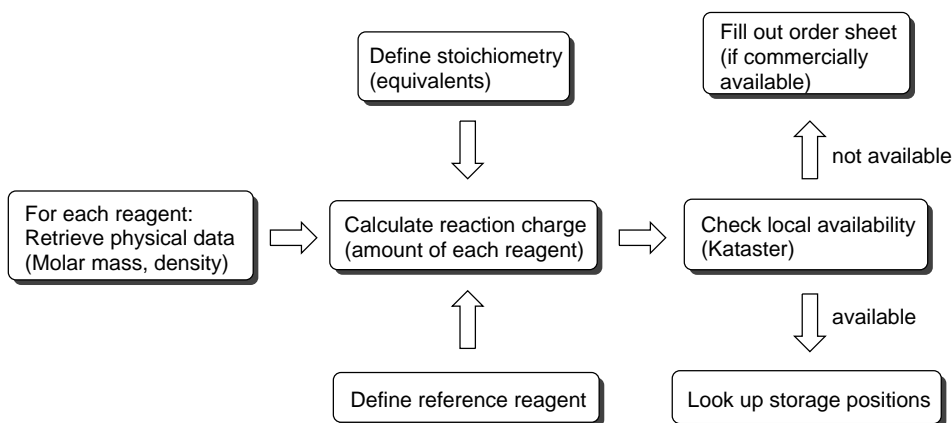


Figure 2.22 Standard manual workflow for charge calculation and reaction preparation.

As the main task of traditional chemists is synthesis, these operations are often performed multiple times per day, each time taking up to 10 min depending on the complexity of the reaction. To alleviate this issue, a project was launched to design a PYTHON script to handle all of the above tasks. Besides the obvious positive effects on chemistry-related workflows, this was seen as a good opportunity to train coding, as it combines concepts such as webscraping, basic mathematical operations, file handling and a *Graphical User Interface* (GUI). The script named *Genesis Lab Journal* was developed starting from a *minimal working example* (MWE) and gradually built upon using *git* version control. The resulting product handles each of the steps mentioned above automatically, creating a standardized folder structure which can be used as a digital laboratory journal. It must be noted that some commercial systems exist, such



as LABFOLDER, ELABJOURNAL and SCINOTE, however, most of them are not free of charge. FINDMOLECULE came closest to the actual needs in the laboratory while being free of charge for academic institutions, but would have required the integration of the chemical inventory of the institute into the software, which was not an option. Therefore, a custom solution was built around the existing infrastructure.

Upon starting, the user is prompted the GUI shown in **Figure 2.23**.

	CAS or name	amount	unit	Conc.	unit	moles	equivs
1.	<input type="text"/>	<input type="text"/>	mg	<input type="text"/>	mol/L	<input type="text"/>	<input type="text"/>
2.	<input type="text"/>	<input type="text"/>	mg	<input type="text"/>	mol/L	<input type="text"/>	<input type="text"/>
3.	<input type="text"/>	<input type="text"/>	mg	<input type="text"/>	mol/L	<input type="text"/>	<input type="text"/>
4.	<input type="text"/>	<input type="text"/>	mg	<input type="text"/>	mol/L	<input type="text"/>	<input type="text"/>
5.	<input type="text"/>	<input type="text"/>	mg	<input type="text"/>	mol/L	<input type="text"/>	<input type="text"/>
6.	<input type="text"/>	<input type="text"/>	mg	<input type="text"/>	mol/L	<input type="text"/>	<input type="text"/>
7.	<input type="text"/>	<input type="text"/>	mg	<input type="text"/>	mol/L	<input type="text"/>	<input type="text"/>
8.	<input type="text"/>	<input type="text"/>	mg	<input type="text"/>	mol/L	<input type="text"/>	<input type="text"/>
9.	<input type="text"/>	<input type="text"/>	mg	<input type="text"/>	mol/L	<input type="text"/>	<input type="text"/>
10.	<input type="text"/>	<input type="text"/>	mg	<input type="text"/>	mol/L	<input type="text"/>	<input type="text"/>
11.	<input type="text"/>	<input type="text"/>	mg	<input type="text"/>	mol/L	<input type="text"/>	<input type="text"/>
12.	<input type="text"/>	<input type="text"/>	mg	<input type="text"/>	mol/L	<input type="text"/>	<input type="text"/>
13.	<input type="text"/>	<input type="text"/>	mg	<input type="text"/>	mol/L	<input type="text"/>	<input type="text"/>
14.	<input type="text"/>	<input type="text"/>	mg	<input type="text"/>	mol/L	<input type="text"/>	<input type="text"/>
15.	<input type="text"/>	<input type="text"/>	mg	<input type="text"/>	mol/L	<input type="text"/>	<input type="text"/>

**Figure 2.23** GUI prompt at startup of *Genesis Lab Journal*. Software written in PYTHON, GUI made using the *PySimpleGUI* library.

After entering a unique reaction identifier as well as a user shorthand (e.g. RG for Robert Gathy), the user is able to enter names and amounts for up to 15 reagents. When the script is used for the first time, an empty substance database file (\*.csv) is created, where data for all used reagents will be stored. During following program starts, this database will be loaded, allowing the user to directly select previously used reagents from the dropdown menus in the “CAS or Name” column.

Having provided names (systematic or trivial, or CAS numbers) and amounts for all reagents, the script will begin retrieving information either from the local database or from internet sources (*ChemIDplus* or Wikipedia). First, a standard name for the reagent along with its CAS number and molar mass is retrieved from *ChemIDplus*, which has a large collection of

common and specialty chemicals. For positive hits, a lookup on Wikipedia is attempted to obtain further physical data (melting and boiling points, densities).

The stoichiometry for a reaction is either derived from literature precedent or, in the case of own research, from individual experiment designs such as *one-factor-at-a-time* (OFAT) or *design of experiments* (DoE). In the latter case, relative reagent amounts will simply be provided as equivalents. In the case of repeating a literature-known reaction, relative amounts are often given in a non-standard format, especially in older procedures.<sup>[55]</sup> Error handling was implemented for cases where reagents are not found, or the provided name is ambiguous. In the worst case, the user is asked to manually enter the molecular weight for the reagent. An example for a medium-complex procedure from the literature<sup>[55]</sup> is given below:

“To a three-necked flask with stirring equipment and thermometer, aromatic amine (0.1 mol), H<sub>2</sub>O (30 mL) and concentrated HCl aqueous (30 mL) were added. The solution was heated to dissolve the aromatic amine, then cooled to 0 °C – 5 °C. While maintaining the temperature of the solution below 5 °C, NaNO<sub>2</sub> aqueous (7 g NaNO<sub>2</sub> in 20 mL H<sub>2</sub>O) was added dropwise. After the addition, the mixture was stirred for 1 h – 1.5 h at the same temperature. Adequate urea was added to decompose the surplus HNO<sub>2</sub>. C<sub>16</sub>H<sub>33</sub>N(CH<sub>3</sub>)<sub>3</sub>Br (0.5 g) was used as catalyst. Then, keeping the temperature below 5 °C, the solution of ferrocene (0.01 mol ferrocene in 20 mL ether) and 0.5 g C<sub>16</sub>H<sub>33</sub>N(CH<sub>3</sub>)<sub>3</sub>Br was added dropwise over 0.5 h – 1 h under stirring.”<sup>[55]</sup>

In the above example, reagent quantities are given as substance amounts, volumes and masses. **Figure 2.24** shows the GUI with information for the above procedure entered by the user.

Genesis Automated Lab Journal

Enter CAS numbers or names, amounts OR equivalents, and (if reagent is a solution), conc.:

Experiment Identifier: ferrocene\_diazotization

	CAS or name	amount	unit	Conc.	unit	moles	equivs
1.	2,5-Dimethoxyaniline		mg		mol/L	0.1	
2.	Water	30	mL		mol/L		
3.	Hydrochloric acid	30	mL	30	%		
4.	Sodium nitrite	7000	mg		mol/L		
5.	Water	20	mL		mol/L		
6.	Cetrimonium bromide	500	mg		mol/L		
7.	Ferrocene		mg		mol/L	0.01	
8.	Ether	20	mL		mol/L		
9.			mg		mol/L		
10.			mg		mol/L		
11.			mg		mol/L		
12.			mg		mol/L		
13.			mg		mol/L		
14.			mg		mol/L		
15.			mg		mol/L		

Submit Cancel

**Figure 2.24** GUI with information entered by the user, ready for submitting. The software is able to handle substances and calculate the correct amounts even when reagent amounts are provided in a mixed, non-standard way.

The script was constructed in a way that handles all possible cases including solutions. First, a reference reagent is defined, and its substance amount calculated. Quantities of each reagent relative to the reference reagent are then calculated individually using standard stoichiometry mathematics. Each case is handled individually according to the information provided by the user. In the following, an exemplary workflow for  $\text{NaNO}_2$  in the above procedure is described. First, the reference reagent is determined from the first entry, and its values are calculated (**Figure 2.25**)

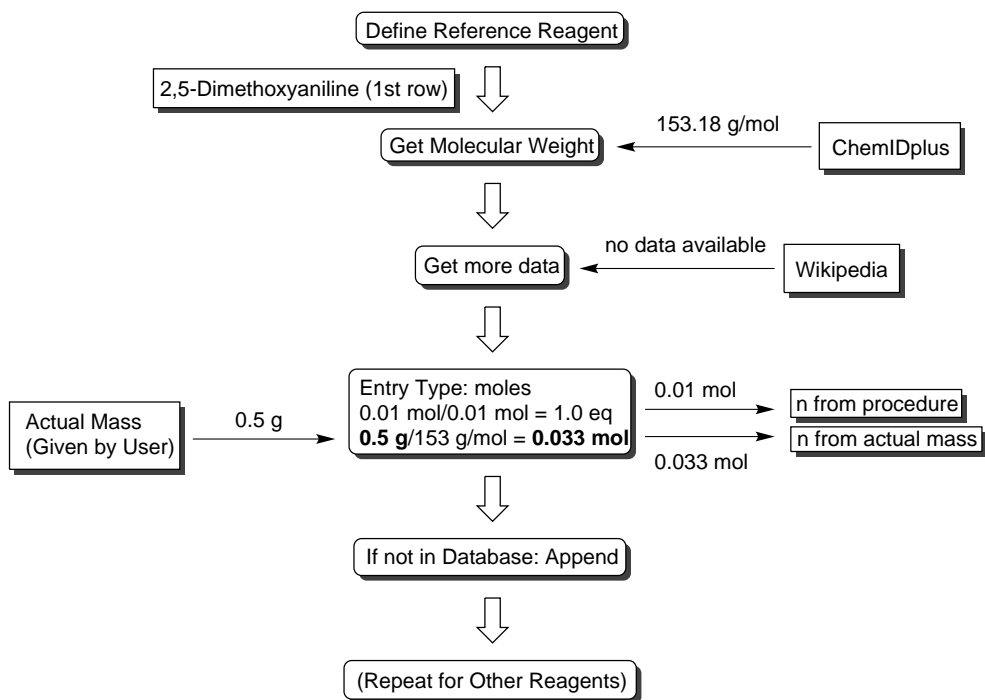


**Figure 2.25** Exemplary calculation for 2,5-dimethoxyaniline.

It must be noted that the substance amount from the procedure is used to calculate the equivalents (here: 1.0 equiv.). This is followed by calculation of the actual substance amount, which is derived from the starting mass provided by the user (here: 500 mg). The actual substance amount will be used to determine all amounts of following reagents. The subsequent calculation for  $\text{NaNO}_2$  is shown in **Figure 2.26**.

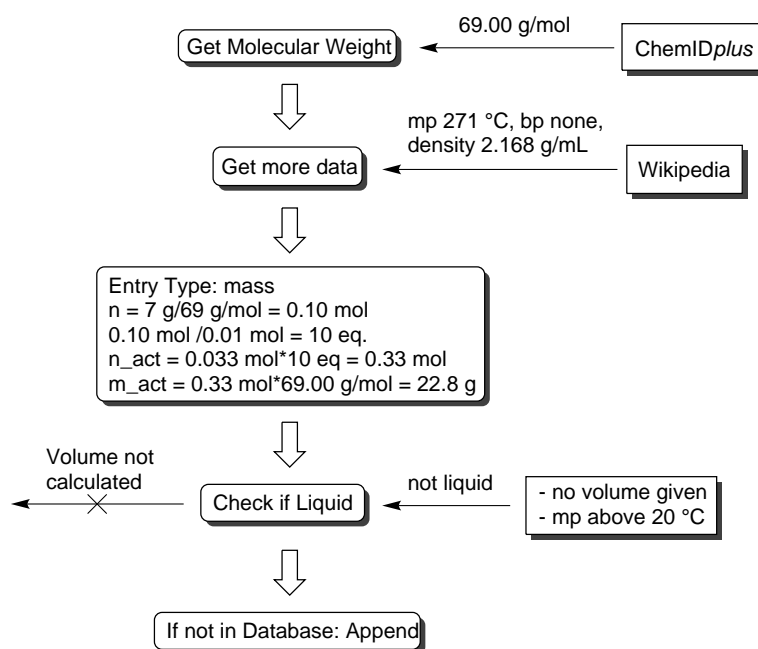


Figure 2.26 Subsequent calculation for  $\text{NaNO}_2$ .

In this case, the relative amount is given as a mass (7 g). After retrieving reagent information from internet sources, this mass is used to calculate the substance amount (0.10 mol) and, using the original reference substance amount, the molar equivalents (10.0 equiv.). These are then multiplied by the actual molar amount (0.033 mol) to yield 0.33 mol. Multiplying this result with the molar mass of  $\text{NaNO}_2$  retrieved from the internet gives an actual mass of 22.8 g. The physical state of the substance is then determined to be “solid” by its melting point, thus no volume is calculated despite a density value being available. As usual, the substance is appended to the central database if not already present.

All other reagents are then calculated in a similar way using the data available. In addition to the pure calculations, substances are also looked up at the chemical database of the institute (Chemikalienkataster). In the absence of an accessible API, the database was downloaded using a PYTHON script which grabbed all entries manually from the corresponding website, storing them in a CSV file (oci\_kataster.csv). Each reagent is looked up *via* its CAS number retrieved from ChemIDplus, and all its occurrences are written into a dedicated file (<user shorthand><serial number>\_kataster\_<substance name>.csv) for convenient lookup.

Whenever a chemical is not present at the institute, the user might desire to order it from a vendor. Typically, the ordering is carried out by the purchasing department of an institute, to which the end user provides the list of chemicals to be ordered. At our institute, for example, a standard EXCEL sheet (Chemikalienbestellung\_<user name>.xlsx) must be filled out using substance name, vendor, CAS number, order number and price, which have to be researched

manually. Hence, a function was implemented which automatically looked up these data for each reagent available at TCI Chemicals Europe and wrote them into an order sheet as described below.

Upon finishing all calculations, data is stored in several files for convenience. The file and folder structure for the present example is depicted in **Figure 2.27**.

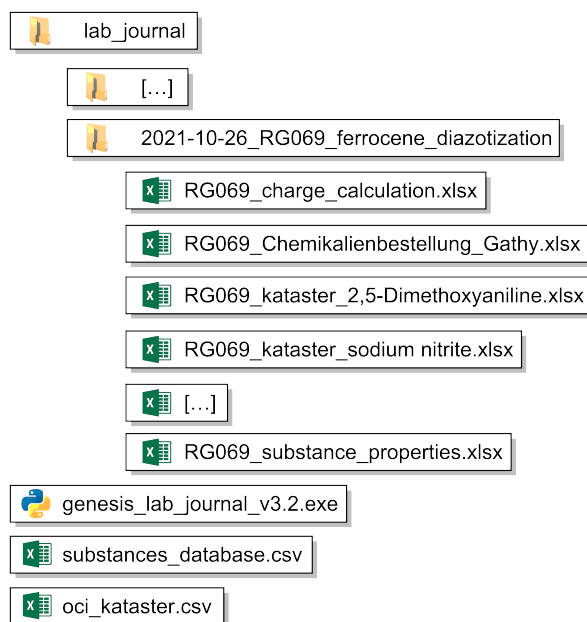


**Figure 2.27** Standard file and folder structure for *Genesis Lab Journal*.

The executable should be placed in a folder which will serve as the digital laboratory journal. This folder also contains the reaction database, as well as the chemical database for the institute. For each experiment, a folder in the general format <current date>\_<user shorthand><serial number>\_<experiment identifier> will be automatically created, which will contain files with the charge calculation, physical properties of all used substances, their entries in the substance database of the institute, as well as a chemical order sheet for the current reaction.

One of the main drawbacks of the script is the need to enter all reagent information manually. Methods to translate literature procedures directly to machine-readable code using *natural language processing* (NLP) have been published,<sup>[56]</sup> however, these would have been difficult to implement and showed unsatisfactory results after some own experimentation with procedures relevant to this thesis. The present workflow of entering names and numbers proved to be a good compromise between development difficulty, reliability and user-friendliness. For future versions, automated methods of reagent information transfer could be investigated.

Since the completion of *Genesis Lab Journal*, the OCI chemicals database has been moved to a new architecture (DAMARIS<sup>[57]</sup>). In contrast to the previous system, DAMARIS contains not only reagent names, CAS numbers and storage positions, but also physical data and safety information. Future versions of *Genesis Lab Journal* could be based on this single database for both physical data as well as storage position retrieval. The order sheet generation could be enhanced to incorporate more vendors than just TCI chemicals. In this regard, the script would have to be regularly maintained, as web sites are frequently edited, requiring adaptation of the web scraping algorithms.

In conclusion, *Genesis Lab Journal* provides a straightforward, user-friendly way of planning own reactions or adjusting literature procedures to desired amounts. The script automates all parts of reaction planning, from retrieving reagent information, calculating and adjusting amounts, creating an order sheet, finding local storage positions and organizing the output in a structure, which can serve as a digital laboratory journal. After its successful development, *Genesis Lab Journal* was used for all chemistry-related calculations in this thesis.

### **An Arduino-Based Interface for the ASW 2000P**

The parallel synthesizer in its standard configuration takes over a majority of repetitive tasks concerning reaction preparation, execution and workup as well as sample preparation for analysis or purification. One of its drawbacks, however, is the lack of remote communication with the user, requiring personal presence during large parts of reaction sequences to ensure proper execution.

This problem extends in the opposite direction as well: The ASW 2000P is equipped with a "Wait for Input"-task, which allows a reaction sequence to be paused and resumed upon a signal provided by the operator. Still, without a way to access this command remotely, its usefulness is greatly diminished, as the operator again has to be physically present. With external communications, the synthesizer could set up a run overnight while the operator receives progress messages on their way home. The following morning, a user input signal sent from home could stop the incubation process and initiate a preprogrammed purification or sampling method, which would then be finished upon arrival of the operator at the lab. This could reduce waiting times for monitoring both reaction setup and sampling (**Figure 2.28**).

input signals) is labeled 1. At first, the behavior of the ASW 2000P was investigated by executing different series of “Set Electrical Contact” tasks and monitoring the readings of the microcontroller. A pin can either be switched on or off permanently, or a pulse with defined length (min. 100 ms) can be sent. Importantly, multiple pulses from the same pin cannot be sent directly after another, as they will instead be joined to a single pulse, creating erratic behavior at the recipient (**Figure 2.30**).

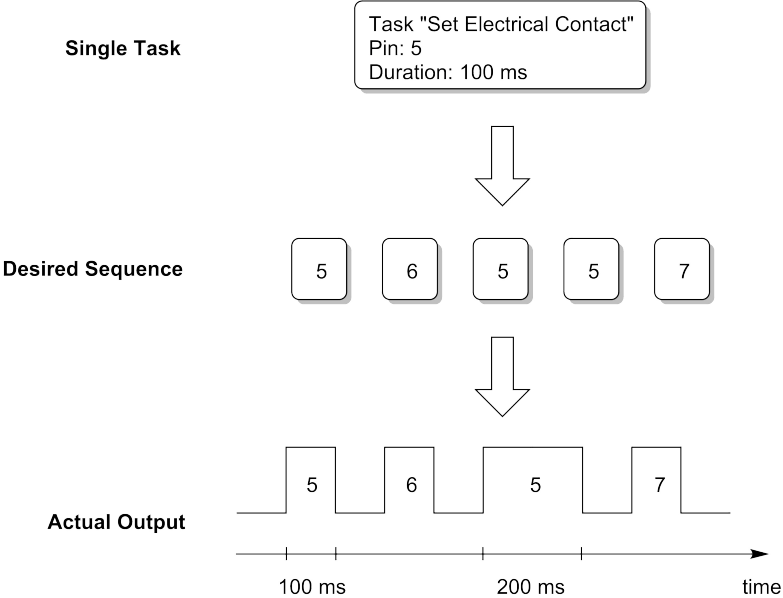


**Figure 2.30** Unexpected signal concatenation within the 735 Sampler Software.

In a first basic idea, signals were encoded using three data pins and a “clock” pin. Data pins were set to either 0 or 1, and the state was recorded using the clock pin, resulting in  $2^3 = 8$  possible combinations. This served as a proof of concept, but was deemed too inefficient for practical use. Instead, a protocol using a fixed number of contact switches per signal was developed. Signals were first initiated using an “init message” pin. With the remaining three data pins, considering the concatenation constraint mentioned above, four different states could be encoded into binary numbers, which are shown in **Table 2.6**.



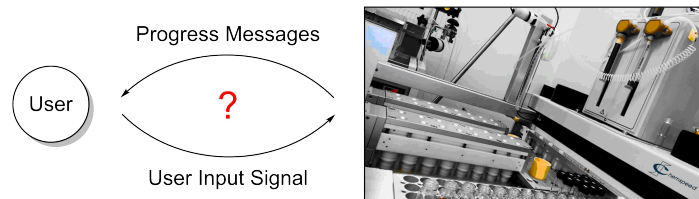


**Figure 2.28** Desired communication features between Chemspeed ASW 2000P and user.

To tackle this issue, communication ports on the ASW 2000P were investigated. The device is equipped with a GILSON control box, providing serial communication ports in the standard D-sub 9 format. At the time, only little personal knowledge was present on serial communication, and parameters such as baud rate and parity were not available for the device. For these reasons, other possibilities had to be considered. In addition to the serial ports, the parallel synthesizer has an array of digital and analog I/O pins, which can be switched using the “Set Electrical Contact” task within the 735 Sampler Software. With some ARDUINO experience from previous hobby projects, it was decided to connect these pins to a microcontroller and write a custom communication algorithm (**Figure 2.29**). An additional advantage would be that the ARDUINO could also be used to control other machines and circuits, providing some flexibility for future upgrades.

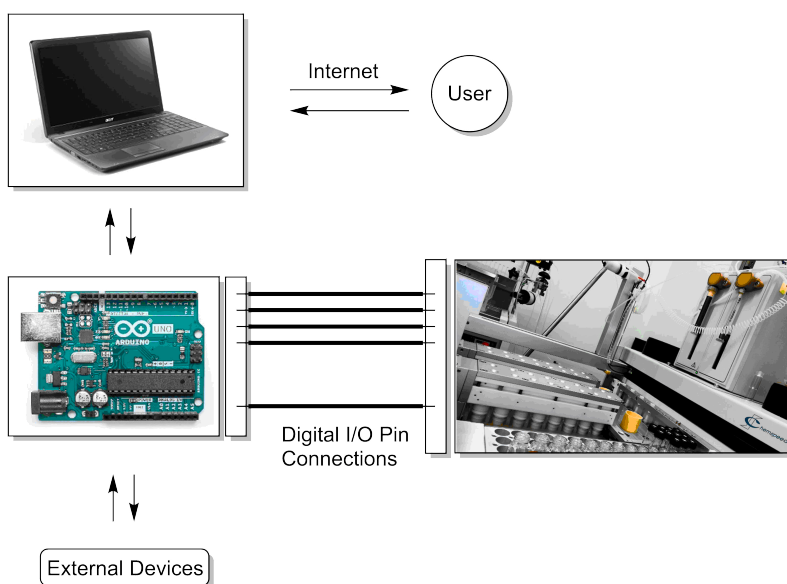


**Figure 2.29** General concept for an ARDUINO-based communication protocol between Chemspeed ASW 2000P and user.

The ASW 2000P digital pins operate on a 5 V logic similar to the ARDUINO platform. Thus, both were connected directly to one another as well as to common ground. The output pins of the ASW 2000P are numbered 4, 5, 6 and 7, whereas its digital input pin (to receive user

**Table 2.6** Different possible states encoded by three data pins.

Sequence	Data 1	Data 2	Data 3	Result
6-5-6	high	low	low	00
7-5-7	low	high	low	01
7-6-7	low	low	high	10
7-6-5	low	low	low	11

The ARDUINO was used to detect events (pulsed switchings to ground) from the data pins, recording their state as “low”. Pin states without events during recording were noted as “high”. By always using three events per state, these could easily be counted by the ARDUINO to ensure a correct alignment between ASW 2000P and microcontroller. After each state recording, the encoded binary number was stored in an array.

The sequences described above resulted from the unwanted concatenation of adjacent events from the same pin. For example, in principle, the combination low-high-high would be possible as well, using the sequence 7-7-7. In practice however, this sequence would be concatenated by the ASW 2000P to a single 7-, resulting in only one event instead of the desired three.

For each signal, four states (groups of three events) were recorded, resulting in a total of 256 possible signals. This number could easily be augmented by a factor of  $2^2 = 4$  per additionally recorded state. In the present application however, 256 seemed sufficient. An additional challenge arose when multiple states were recorded next to each other, again due to the concatenation constraint. For example, to send the two-state combination “01-10”, a data sequence of “7-6-7-7-5-7” would be necessary. Evidently however, this results in two adjacent events on data pin 7, again leading to unwanted concatenation. To circumvent this, a simple reshuffling algorithm was created, detecting such occurrences and resorting the affected sequences until all problems were resolved. The issue as well as the solution are shown in **Figure 2.31**.

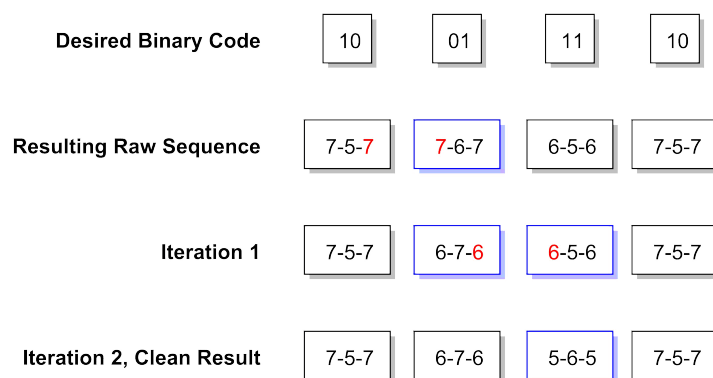


**Figure 2.31** An exemplary signal containing adjacent events with the same pin, resolved by a reshuffling algorithm.

Using the clean sequences, each signal was encoded to an 8-digit binary number (= 1 byte), which was converted to its decimal analogue and sent to a PYTHON script via serial communication. In a dictionary, those numbers were assigned a message such as “Start aliquoting next reagent”, “Priming pump finished” or “Waiting for User Input”. These messages were then sent to the user *via* a TELEGRAM bot directly through PYTHON (**Figure 2.32**).

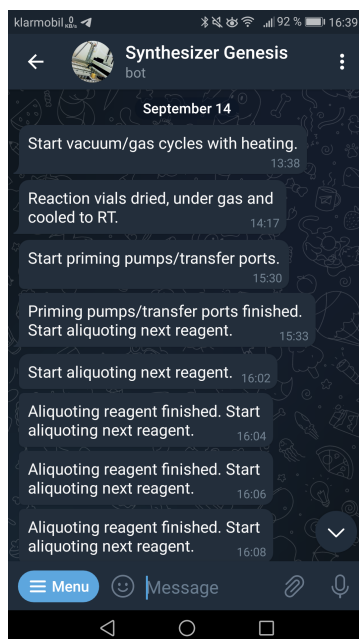


**Figure 2.32** Screenshot of TELEGRAM user interface for communication with the ASW 2000P.

A complete exemplary workflow for sending the message “Waiting for user input to continue” is shown in **Figure 2.33**.



so that adjacent messages would be concatenated into a single one to further enhance user experience. For example, **Figure 2.32** shows the combined message “Priming pumps/transfer ports finished. Start aliquoting next reagent.”.

The ARDUINO platform is not only capable of reading, but also writing signals. With the established interface between smartphone and ARDUINO, additional functionalities were added to the TELEGRAM bot to enable active user commands. Most notably, the ASW 2000P possesses a user input function **Section 2.1.1**, which is triggered by a digital input pin on the synthesizer. This pin was connected to the ARDUINO, and the algorithm was expanded to include a user input command which could be triggered by the user *via* smartphone. This enabled the unattended triggering of events such as workup sequences on the parallel synthesizer, as seen in **Table 2.7**.

**Table 2.7** Exemplary, partly remote workflow using the new TELEGRAM bot user input command.

Time	User Location	Communication	ASW 2000P Action
↓	Laboratory	← Message	Start Reaction Preparation
	On Way Home	← Message	Finish Reaction Preparation
	Home	← Message	Incubation Over Night
	Home	→ User Input Signal	Start Workup
	On Way to Laboratory	← Message	TLC Preparation
	Laboratory	–	Finished TLC Plates

The remote triggering function allowed the user to pre-program a workup, purification or analysis sequence which would be executed upon a user input signal sent remotely. Upon arrival at the laboratory, the sequence was finished and the samples ready for further processing. A typical application was incubation over night, triggering of a TLC spotting and development sequence (approx. 45 min for 32 samples), and immediate TLC-MS or QTLC analysis at the start of the actual workday.

Since the electrical circuitry was built on a component level, a multitude of different possibilities for further remotely triggered applications exist. Some of these applications that were explored within this thesis were an HPLC device connected directly to the 6-way injection valve of the ASW 2000P to serve as an autosampler, as well as the custom photoreactor arrays described in this section, which could be triggered both from within an ASW 2000P application as well as remotely by the user. Thus, the communication platform proved to be an easily extendable, robust feature which greatly improved day-to-day operations.

In hindsight, more effort could have been placed on finding the serial communication parameters for the GILSON interface, which would have avoided the necessity to create the custom communication protocol described above. These parameters could possibly have been obtained from the CHEMSPEED customer service. In terms of speed, the protocol is obviously seriously lacking compared to established protocols such as USB, with its speed of transmission of  $0.67 \text{ b s}^{-1}$ . This is largely attributed to the constraints regarding the switching of the digital output pins of the synthesizer, and does not interfere with regular operation, as the time to send one message (1.5 s) is still orders of magnitude smaller than typical physical actions of the synthesizer (minutes to days). For a more concise approach, a follow-up version could be implemented on a RASPBERRY PI, which would combine all electrical as well as software aspects into a single, portable device which could be attached directly to the frame of the parallel synthesizer, thus providing an even closer integration to the standard hardware.

In summary, a device for external communication with the ASW 2000P based on inexpensive hardware has been developed. The message function greatly enhances user experience, allowing the operator to monitor progress even when not physically present. User input signals given via the TELEGRAM messenger allowed the operator to start e.g. TLC spotting procedures from home, giving finished plates ready for manual inspection upon arrival in the lab. Connecting the HPLC enables the ASW 2000P to be used as an autosampler directly from reactions. The nature of the ARDUINO provides virtually unlimited possibilities for further expansion to more third-party equipment, integration into other communication channels or algorithmic processing of data.

### 3D Printed Photoreactor Arrays

A majority of chemical use cases in this thesis involved visible-light assisted steps, creating the need for a suitable light source. Photochemistry has been a growing field since the mid-twentieth century (**Figure 2.34**), and is in high demand for applications such as photoredox catalysis.<sup>[58]</sup> While mercury lamps are still frequently used, they have some disadvantages including high heat dissipation, which often requires complicated setups. LED-based photoreactors have seen a rise in organic chemistry, particularly due to their low cost and high efficiencies, which eliminates the requirement for extensive cooling.<sup>[59]</sup>

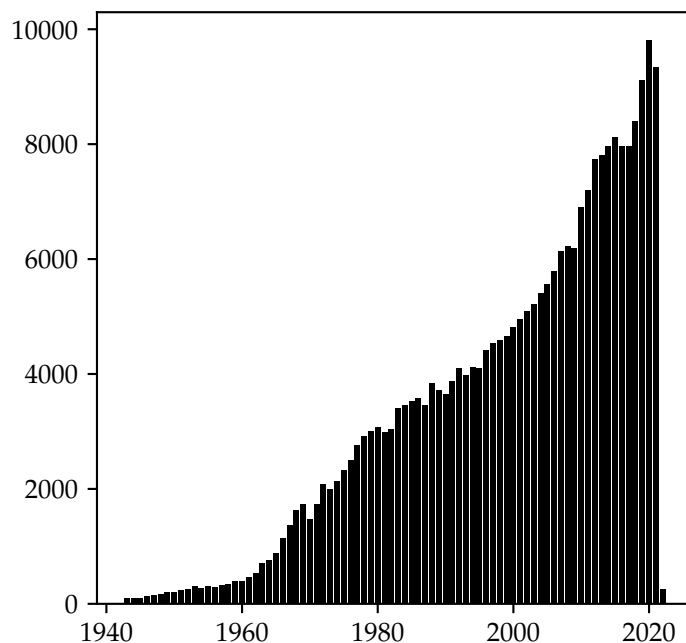


**Figure 2.34** Search results for the query 'photochemistry OR photochemical' on the SciFinder-n database, date of access: 2021-12-23.

During some chemical investigations within this thesis, the need for a source of light ( $\lambda = 730 \text{ nm}$ ) emerged. The use of mercury lamps was neglected due to their emission in a multitude of other wavelengths including UV, which could easily have led to decomposition of the highly photoactive quinoylferrocene molecule, necessitating the use of filters. Additionally, the emission intensity of such lamps in the desired region is usually rather low. For these reasons, including the disadvantages mentioned above, LEDs were chosen as the light source in this case. Despite the growing popularity of photochemistry, corresponding systems today often still consist of self-constructed setups with a low grade of standardization.<sup>[60]</sup> Some commercial systems are available, but often only offer wavelengths around UV or blue light. Additionally, they were unavailable for this project due to cost constraints. Previously, a photoreactor had been designed and 3D printed within the AG AUTOMATISIERUNG as a service for a cooperating research group using inspiration from the literature.<sup>[61]</sup> This design was modified to accommodate eight test tube-like reactor vials, and 3D printed using an ANET A8 printer (**Figure 2.35**). An LED strip ( $\lambda_{max} = 730 \text{ nm}$ ) was purchased, its emission spectrum confirmed and mounted into the photoreactor. Using this setup, eight different substrates were screened and indole was determined as a promising candidate for further studies (**Section 2.2.1**).

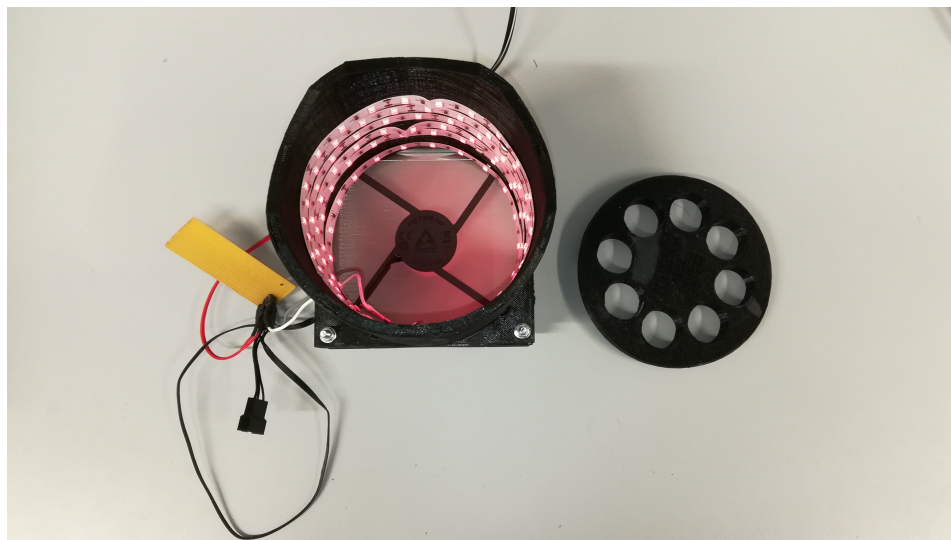


**Figure 2.35** Self-designed, 3D printed photoreactor for manual execution of eight reactions. Diameter of the reactor = 12 cm.

In a later stage of the project, a photoreactor for high-throughput experimentation was required to facilitate the execution of DoE-assisted investigations. To reduce experimental effort and time, the design and reaction sequence were arranged to accommodate the parallel synthesizer. In order to enable the investigation of the influence of light, a new photoreactor array had to be designed around the reactor arrays of the ASW 2000P.

Some initial considerations were the ease of assembly of the photoreactor, its mechanical stability during strong vortexing and even distribution of light to all vials. The array was envisioned as a casing, which would wrap around the reactors. The inner walls of the casing would be supplied with pieces of the LED strip in a way that each vial is exposed to the same number of light sources. The reactor arrays of the parallel synthesizer were measured and roughly modelled in AUTODESK Inventor. Based on this model, a casing was designed around this, which consisted of two equal halves, which would be connected using wires (**Figure 2.36**).



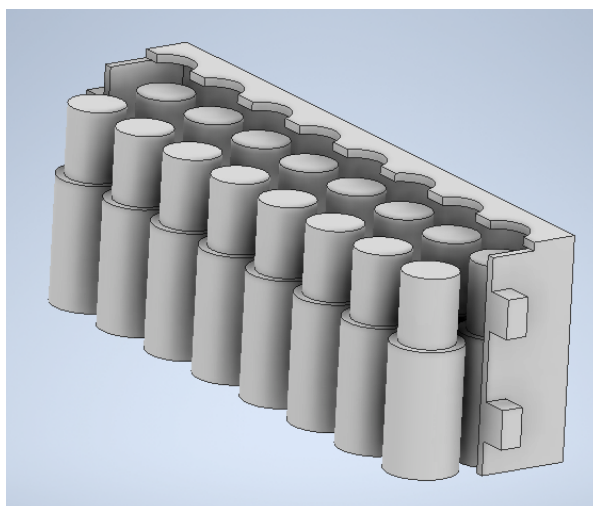


**Figure 2.36** 3D model of a photoreactor array for the ASW 2000P, based on a rough model of the original reactors. Photoreactor size: 248 mm × 80 mm × 33 mm

The casings were 3D printed, and a template was designed in excel to ensure proper alignment of the LED strips during assembly. Next, pieces of 5 cm were glued onto the printed template, and the entire assembly was placed into the casing. The strips were aligned so that each reactor was exposed to  $2 \cdot 3 = 6$  LEDs. Holes were drilled using a handheld drill, and wires were soldered in parallel to the LED strips (**Figure 2.37**).

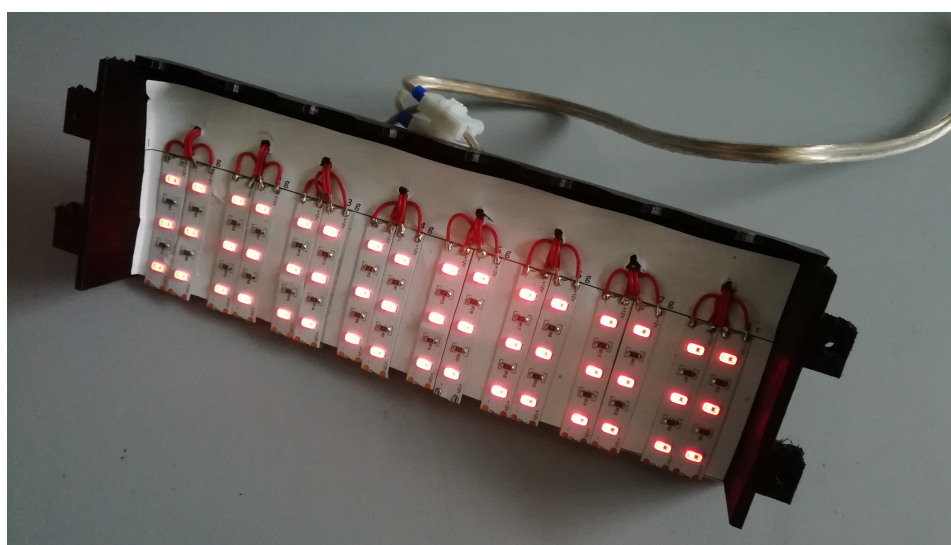


**Figure 2.37** One half of the photoreactor array with assembled LEDs.

The above procedure was performed twice, and the two halves were connected using a central power line made from 4-wire telephone cable. To ensure a smooth assembly, the power wire was equipped with a standard 2-pole connector, and its counterpart was installed permanently

to one of the free reagent vial cutouts of the ASW 2000P. In addition, the photoreactor was integrated into the previously discussed ARDUINO interface, enabling its activation through both the ASW 2000P as well as by a user input signal given *via* smartphone. The finished product on a reactor array is shown in **Figure 2.38**.



**Figure 2.38** Reactor array of the ASW 2000P with one half of the photoreactor array installed.

Using this design, the influence of light on the reaction between quinoylferrocene (**41**) and indole (**43**) was successfully investigated using automated DoE (**Section 2.2.1**). In another project (**Section 2.2.3**), reactions under blue light catalysis ( $\lambda = 450 \text{ nm}$ ) were investigated. Due to all template files being available from the initial design, two more photoreactor arrays were easily 3D printed and assembled using LEDs in the desired 450 nm range within days. Thus, 32 blue light-catalyzed reactions could be investigated at once, greatly improving the speed of research in that area.

To summarize, 3D modelling and -printing were used to quickly design and construct prototypes of photoreactors, which enabled the investigation of light-assisted reactions on the ASW 2000P parallel synthesizer. This feature greatly extended the range of applications for automation in the scope of this thesis, and can serve as an additional, useful tool for high-throughput experimentation using the CHEMSPEED equipment.

## 2.2 Chemistry Use Cases

### 2.2.1 Light-Controlled Functionalization of Ferrocene-Based Push-Pull Systems

#### Introduction

One of the best-known properties of ferrocene is its electron donor behavior in redox reactions.<sup>[62]</sup> By covalently attaching electron accepting groups, this behavior can be observed intramolecularly as well.<sup>[63]</sup> These structures are known as *push-pull* systems and are of special interest in the fields of organic chromophores<sup>[64]</sup> and molecular electronics<sup>[65]</sup> (**Figure 2.39**).

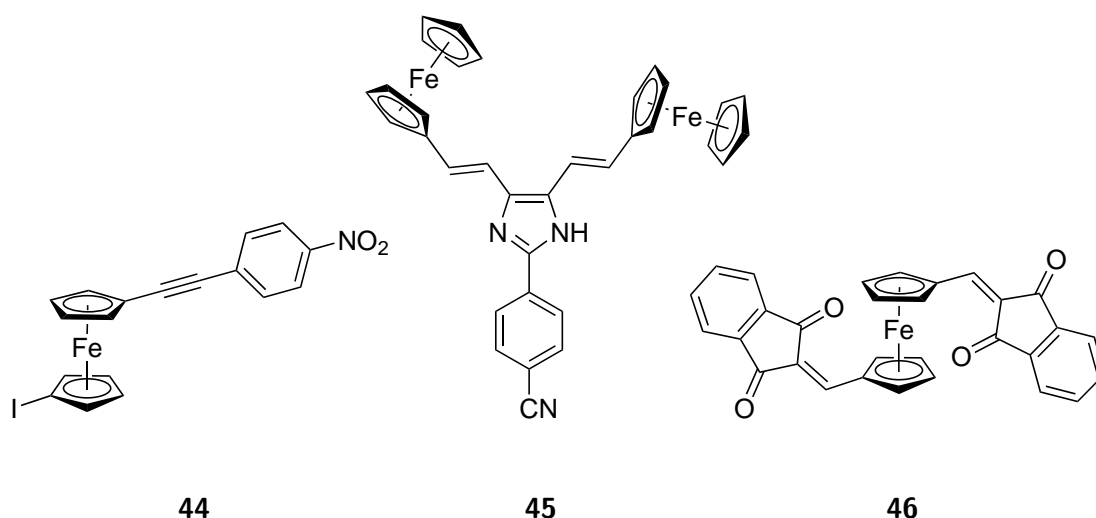


**Figure 2.39** Examples for ferrocene-based push-pull systems. **44**: A building block for molecular wires, consisting of a ferrocene donor and nitroaryl acceptor.<sup>[65]</sup> **45**, **46**: Ferrocene-based chromophors with cyanoaryl<sup>[63]</sup> and indene<sup>[64]</sup> acceptors.

Catalytic C-H activation usually relies on the presence of directing groups at the substrate, with some exceptions.<sup>[66]</sup> These groups are often electron-withdrawing groups such as carbonyls or *N*-heterocycles such as 2-pyridyl (**Figure 2.40**).<sup>[67]</sup>

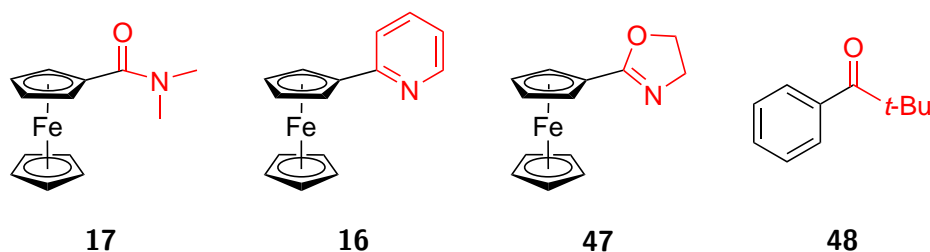
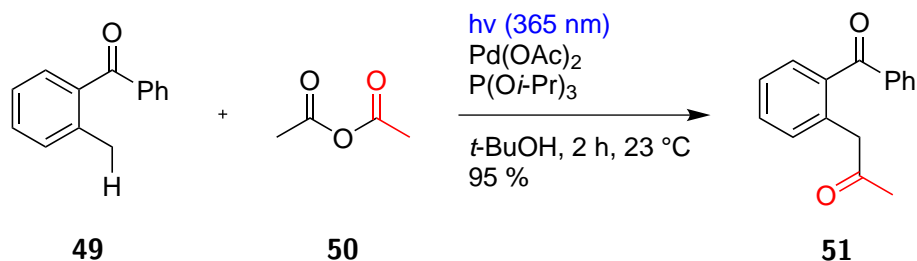


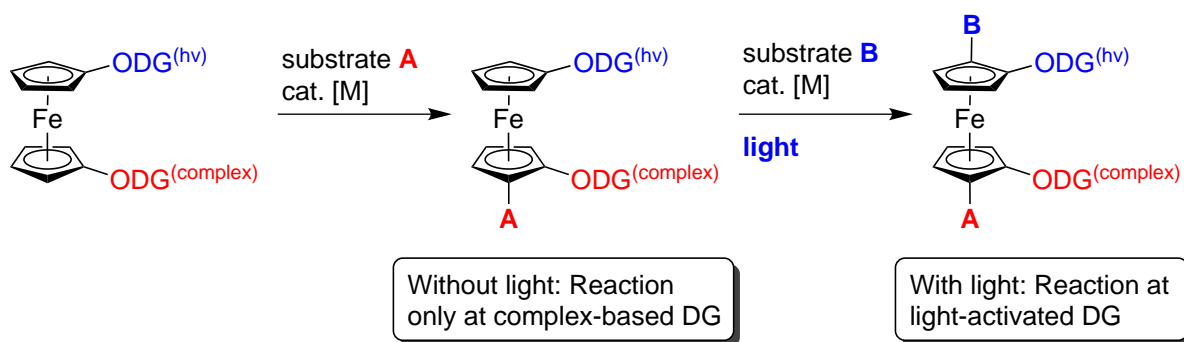
**Figure 2.40** Typical *ortho* directing groups (marked red) used for catalytic C-H activation.<sup>[3,37,68,69]</sup>

During activation of a *push-pull* system by irradiation with the appropriate wavelength of light, electron density is shifted from the HOMO of the molecule (located around the donor) into its LUMO (located around the acceptor).<sup>[70]</sup> Since the first step in directed C-H activation – the complexation of the metal catalyst by the directing group – is dependent on the nucleophilicity of the directing group, the question arose whether a light-activated directing group could be found. In such a system, the C-H activation reaction would take place preferably under irradiation, potentially opening some possibilities for selectivity. One literature example is the benzylic C-H acetylation of 2-methylphenyl ketone **49** with acetic anhydride (**50**) yielding compound **51**, proposed by MURAKAMI *et al.* (**scheme 2.7**).<sup>[71]</sup>



**Scheme 2.7** Light-activated benzylic C-H acetylation using a carbonyl directing group.<sup>[71]</sup>

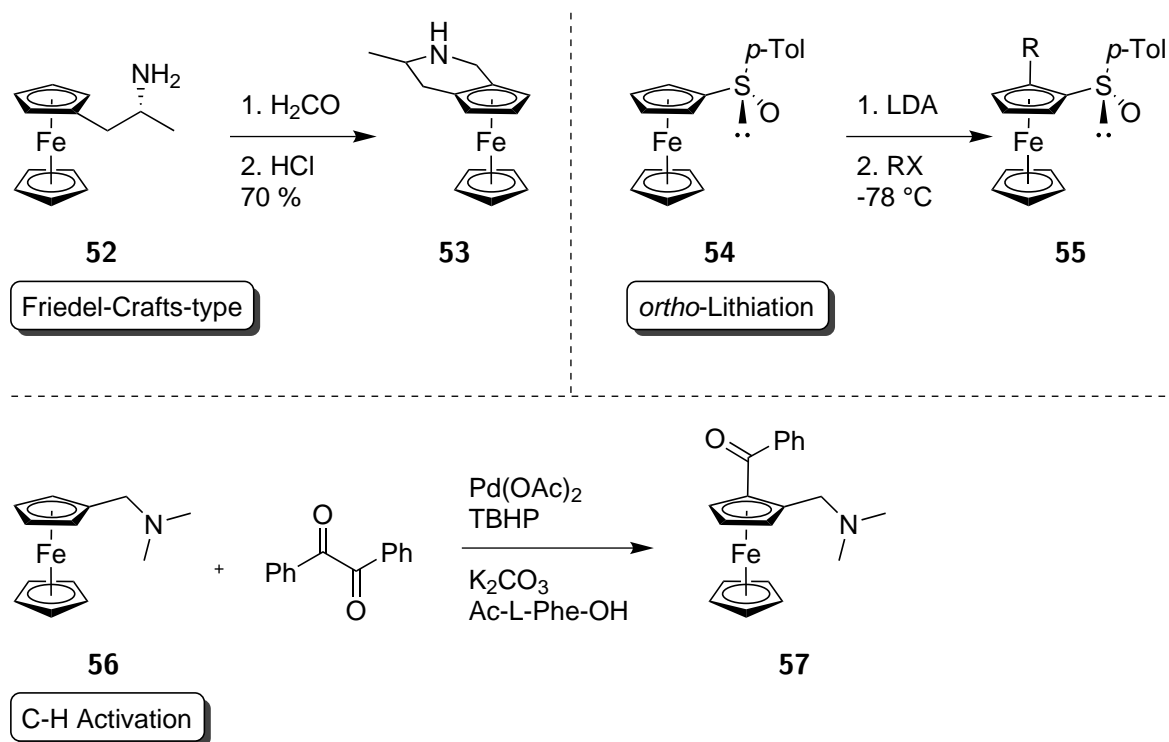
These systems would show a significant difference to other light-activated C-H activation systems, as in most cases the metal complex is activated instead of the directing group. By utilizing a light-activated DG next to a non light-activated one, divergent synthetic strategies could emerge (**scheme 2.8**).



**Scheme 2.8** Divergent strategies using a hypothetical light-activated directing group next to a classical, complexation-based directing group. In the dark, a reaction only takes place at the latter, while under irradiation, a reaction would occur at the light-activated directing group.

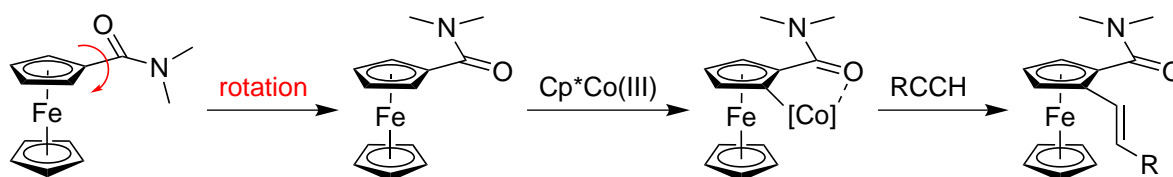
Another interesting property specific to ferrocene is its ability to have planar chirality introduced by unsymmetric disubstitution at one ring.<sup>[72,73]</sup> Among other procedures, these systems have been generated by intramolecular FRIEDEL-CRAFTS-type transformations, forming annelated rings, such as the transformation of **52** to **53**.<sup>[74]</sup> More modern methods include

*ortho*-lithiation of compound **54** yielding **55**, and catalytic *ortho*-C-H-activation, for example at compound **56**, giving structure **57** (scheme 2.9).<sup>[75,76]</sup>



**Scheme 2.9** Overview of different synthetic methods for the generation of planar chiral ferrocenes.<sup>[74–76]</sup>

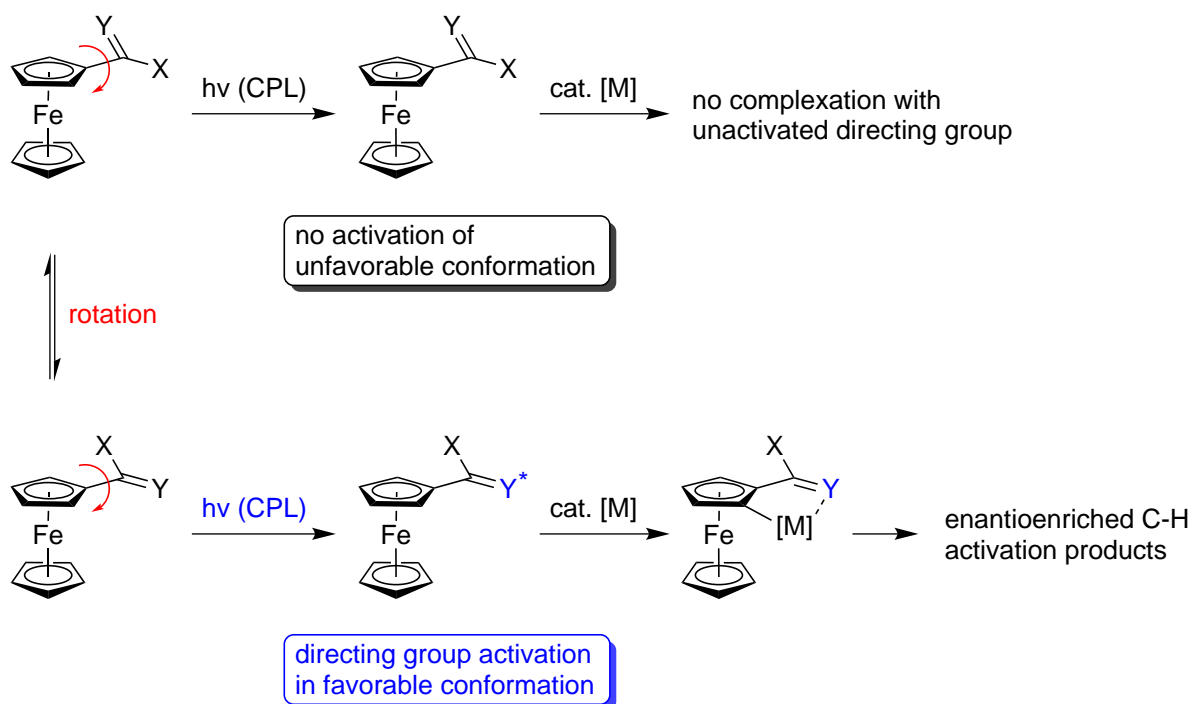
Most typical directing groups are not symmetrical across the axis of the C-C bond between Cp ring and directing group. This leads to the generation of enantiomeric conformers, depending on the orientation of the DG. In a C-H activation reaction, the configuration of the C-H activation product depends on the orientation of the DG-metal complex at the moment of the C-H insertion step (scheme 2.10).



**Scheme 2.10** Different enantiomeric conformations of a prototypical ODG (here: *N,N*-dimethylcarbamoyl, DMC), dictating the configuration of C-H activation products at the Cp ring.

With a light-dependent directing group, the question could be raised whether the use of circularly polarized light (CPL), which can very briefly be described as helically chiral photons,

could lead to a preferred orientation of the DG and thus to some enantioselectivity during C-H activation (**scheme 2.11**).



**Scheme 2.11** Possible enantioselectivity in C-H activation reactions by using a light-activated directing group and activating with circularly polarized light. Using “chiral photons”, one of the possible enantiomeric conformations could be favored over the other, which would lead to enantiomerically enriched product.

The main disadvantage of this strategy could be that CPL usually shows only weak chiral induction when applied to molecular transformations. Therefore, most strategies thus far rely on CPL-assisted generation of enantioenriched photodecomposition products followed by autocatalysis.<sup>[77,78]</sup> The amplification of enantioselectivity then happens during the autocatalysis step, not directly through CPL irradiation. It is thus to be anticipated that any effect on the orientation of a DG by CPL would be quite small. Nevertheless, if a proof of concept were successful, one could think of further strategies to amplify this effect.

### Synthesis of a Ferrocene-based *Push-Pull* System

The project was started by selecting an appropriate *push-pull* system to test for any light-dependent reactivity, more specifically in C-H activations. As an initial test substrate, quinoylferrocene (**41**) was chosen. This compound has been synthesized and characterized by Colbran *et al.*,<sup>[79]</sup> and its *push-pull* properties have been confirmed by UV-vis spectroscopy. The molecule shows a broad, solvatochromic absorption band at around 730 nm, which was assigned to the HOMO(Fc)-LUMO(Q) transition (**Figure 2.41**).

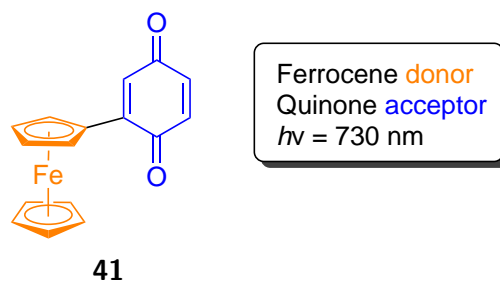
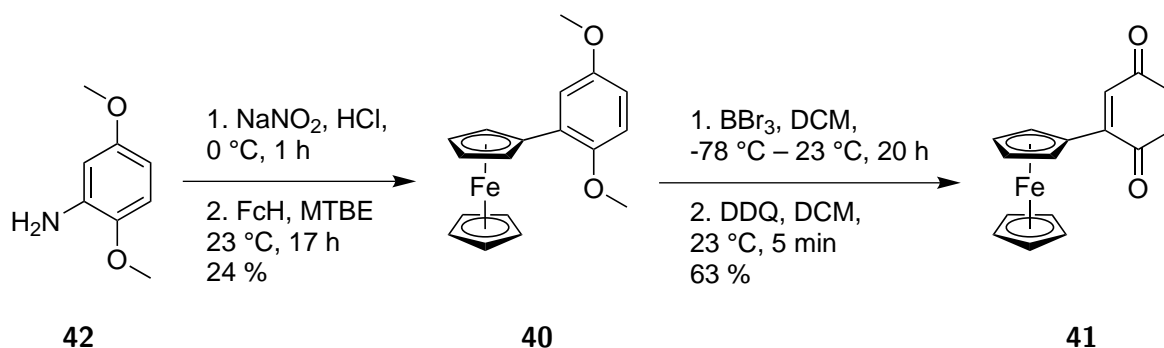


**Figure 2.41** Quinoylferrocene (Fcq, **41**) as a model substrate for a ferrocene-based *push-pull* system with potential ODG functionality.

The proposed synthesis starts with the GOMBERG-BACHMANN reaction of ferrocene (**58**) with diazotized 2,5-dimethoxyaniline (**42**). The product **40** is demethylated with  $\text{BBr}_3$  and oxidized to the quinone form **41** using DDQ.<sup>[79]</sup>

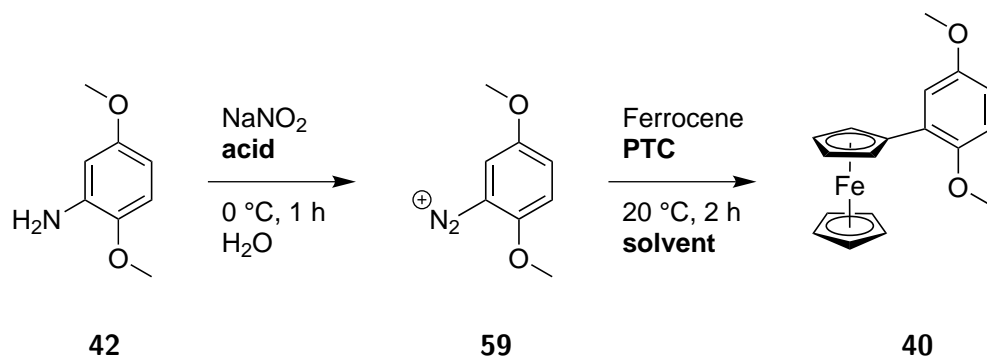


**Scheme 2.12** Synthesis of quinoylferrocene (**41**) according to COLBRAN *et al.*<sup>[79]</sup>

Due to the first low yield of the first step, some effort was spent in optimizing the conditions. This was taken as an opportunity to explore some new DoE strategies. During this process, it became clear that simplified protocols can provide an overall benefit in the sense that the probability for critical errors is kept low, increasing the chances for a successful execution of the experiment. Therefore, the following run was designed as a multilevel categorical DoE with only three factors, while the basic reaction protocol would be kept constant (**Table 2.8**). Multilevel Categorical designs are useful if more than two levels of categorical factors are of interest, which cannot be fit into a factorial design, e.g. by using PCA modelling. They are also one of the most efficient ways to load the parallel synthesizer, as only relatively few reagents need to be prepared to give many possible runs. The response was to be measured using the *quantitative thin-layer chromatography* (QTLC) protocol developed in this thesis (**Section 2.1.2**).



**Table 2.8** Multilevel categorical design for the optimization of the synthesis of compound (40) from 42 via diazotized intermediate 59.



Factor	Level 1	Level 2	Level 3	Level 4
Acid	H <sub>2</sub> SO <sub>4</sub>	HBF <sub>4</sub>	HCl	<i>p</i> -TsOH
Solvent	AcOH	MTBE	MeCN	acetone
PTC	yes	no		

As seen in **Table 2.8**, the factors “solvent” and “acid” were investigated with four settings each. For the third factor, the absence or presence of a phase transfer catalyst was chosen, giving a total of 32 runs.

Due to a false amount of internal standard stock caused by human error, 9 of the 32 reactions could not be analyzed properly, preventing a successful response collection in these cases. The remaining 23 reactions were analyzed against acetylferrocene as internal standard. The response was obtained by division of the product integrals by the respective internal standard integrals. Under these conditions, a significant model using solvent and mineral acid could be generated. The presence or absence of phase transfer catalyst was not a significant model term. This may however result from the combinations of MTBE/PTC being among the erroneous runs, and is therefore not a conclusive result. A graph summarizing the results is shown in **Figure 2.42**.



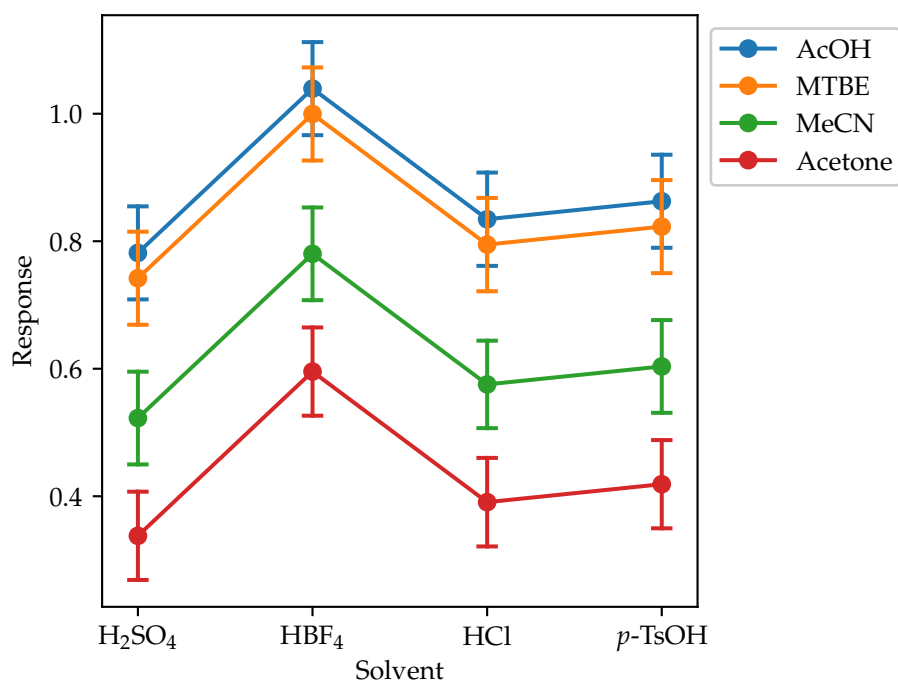


**Figure 2.42** Results for multilevel categorical screening of the GOMBERG-BACHMANN reaction between 2,5-dimethoxyaniline (**42**) and ferrocene (**58**). Responses are QTLC integrals of product divided by the internal standard acetylferrocene (**38**).

The model suggests AcOH or MTBE as good solvents. For increased ease of workup, MTBE is chosen for further reproductions. Additionally, HBF<sub>4</sub> was identified as a possible alternative for HCl or H<sub>2</sub>SO<sub>4</sub>. This is in accordance with the literature,<sup>[80]</sup> which mentions a stabilizing effect of the BF<sub>4</sub><sup>-</sup> anion on diazonium salts. However, an upscaled manual run using MTBE and HBF<sub>4</sub> resulted in an isolated yield of 17%, compared to 12% – 24% with HCl, providing no further improvement. This finding again reflects the suboptimal result quality obtained in this run. With as many as 11 runs omitted from model building – corresponding to roughly a third of the entire design – it is expected that the resulting model will not accurately reflect reality. The experiment would have to be repeated with correct reagent amounts to obtain a clearer picture. However, since with the available data no breakthrough in terms of product yield seemed probable, the investigation was continued at this point using MTBE and HCl as sufficiently suitable reagents.

The following demethylation and oxidation steps were carried out without modifications, resulting in a total yield of 15% over 3 steps, in accordance with the literature (14%).<sup>[79]</sup>

## Reactivity Screenings with Quinoylferrocene

With quinoylferrocene (**41**) in hand, the next step was to identify whether the molecule could undergo reactions with any substrate under conditions of catalytic C-H activation, and whether those reactions would be dependent on irradiation. As the catalyst system, Cp\*Co(III) was chosen, as it provides an alternative to noble metals, and some experience was already available in the group.

For experimental convenience, a photoreactor was designed and 3D printed (for details see **Section 2.1.3**). The literature stated a broad absorption band of the compound in the region of 730 nm.<sup>[79]</sup> Since this wavelength lies outside that of common commercial LEDs, special far red-emitting LEDs had to be sourced and imported from a Chinese manufacturer.

To quickly gain an overview of the existing literature on Cp\*Co(III)-based C-H activation, a python script was built to download all corresponding pdf files using the query "35886-64-7", the CAS identifier of Cp\*Co(CO)I<sub>2</sub>, and merge them into a single file. Using the resulting 1296 page document, frequently used reagents and substrates were swiftly identified. Eight different substrates were chosen for an initial screening under typical Cp\*Co(III) standard conditions for a first proof of concept (**Table 2.9**).

**Table 2.9** Layout for the initial substrate screening for Cp\*Co(III)-catalyzed reactions at quinoylferrocene (**41**). Run 5 with additional Ag<sub>2</sub>O (2 equiv.). Expected structures according to the provided literature.

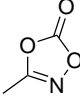
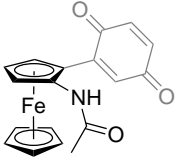
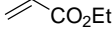
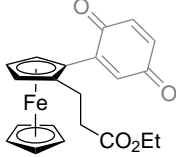
Entry	Substrate	Expected Product
1 <sup>[68]</sup>	 <b>60</b>	 <b>61</b>
2 <sup>[81]</sup>	 <b>62</b>	 <b>63</b>

Table 2.9 (continued)

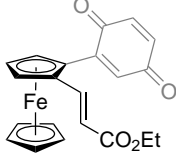
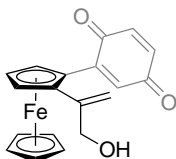
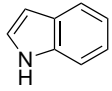
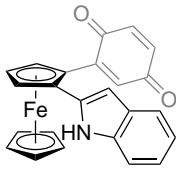
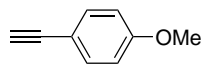
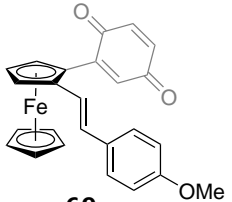
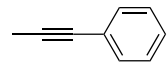
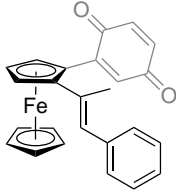
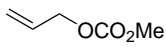
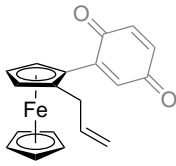
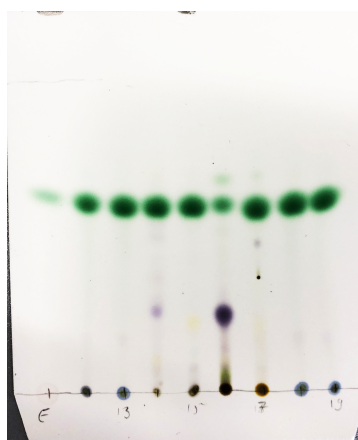
Entry	Substrate	Expected Product
3[82]	$\text{≡-CO}_2\text{Et}$ <b>22</b>	 <b>64</b>
4[83]	$\text{≡-CH}_2\text{OH}$ <b>65</b>	 <b>66</b>
5[84]	 <b>43</b>	 <b>67</b>
6[37]	 <b>68</b>	 <b>69</b>
7[85]	 <b>70</b>	 <b>71</b>

Table 2.9 (continued)

Entry	Substrate	Expected Product
8[86]	 <b>72</b>	 <b>73</b>

Most reactions showed no formation of any defined product. With indole (**43**) and Ag<sub>2</sub>O however, a new, deep violet spot was observed on the TLC, a mass spectrum of which returned a correct  $m/z$  of 407.1 (**scheme 2.43**). Other reactions showed some faint spots, most of which were not unique to any one reaction, and were therefore assumed to be unspecific decomposition products. Reaction 3 (ethyl propiolate, **22**) showed a faint violet spot, which did not give conclusive results in TLC-MS and was therefore ignored. Elongating reaction times up to 48 h did not lead to any significant changes. All further efforts were hence concentrated on the successful transformation with indole (**43**).



**Figure 2.43** TLC analysis of initial substrate screenings with quinoylferrocene (**41**).

In contrast to the expected constitution **67**, <sup>1</sup>H-NMR analysis showed a monosubstituted ferrocene system as the single product, while the signal of one of the quinone protons was no longer observable. It was concluded that the reaction had actually taken place at the quinone system, yielding structure **74** (**Figure 2.44**).

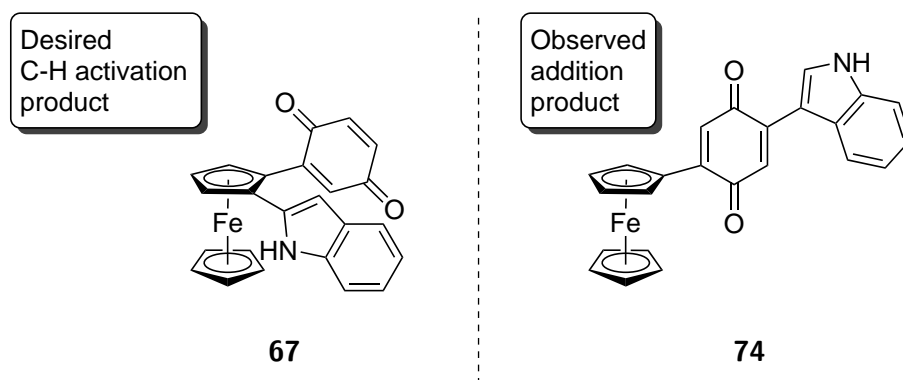


Figure 2.44 Expected and obtained structures.

The working hypothesis was that the quinoylferrocene donor-acceptor system would exhibit increased reactivity under irradiation. To quickly test the dependency on light of the observed reaction, temperature and  $\text{Ag}_2\text{O}$ , four parallel reactions were conducted manually in an OFAT fashion (Table 2.10).

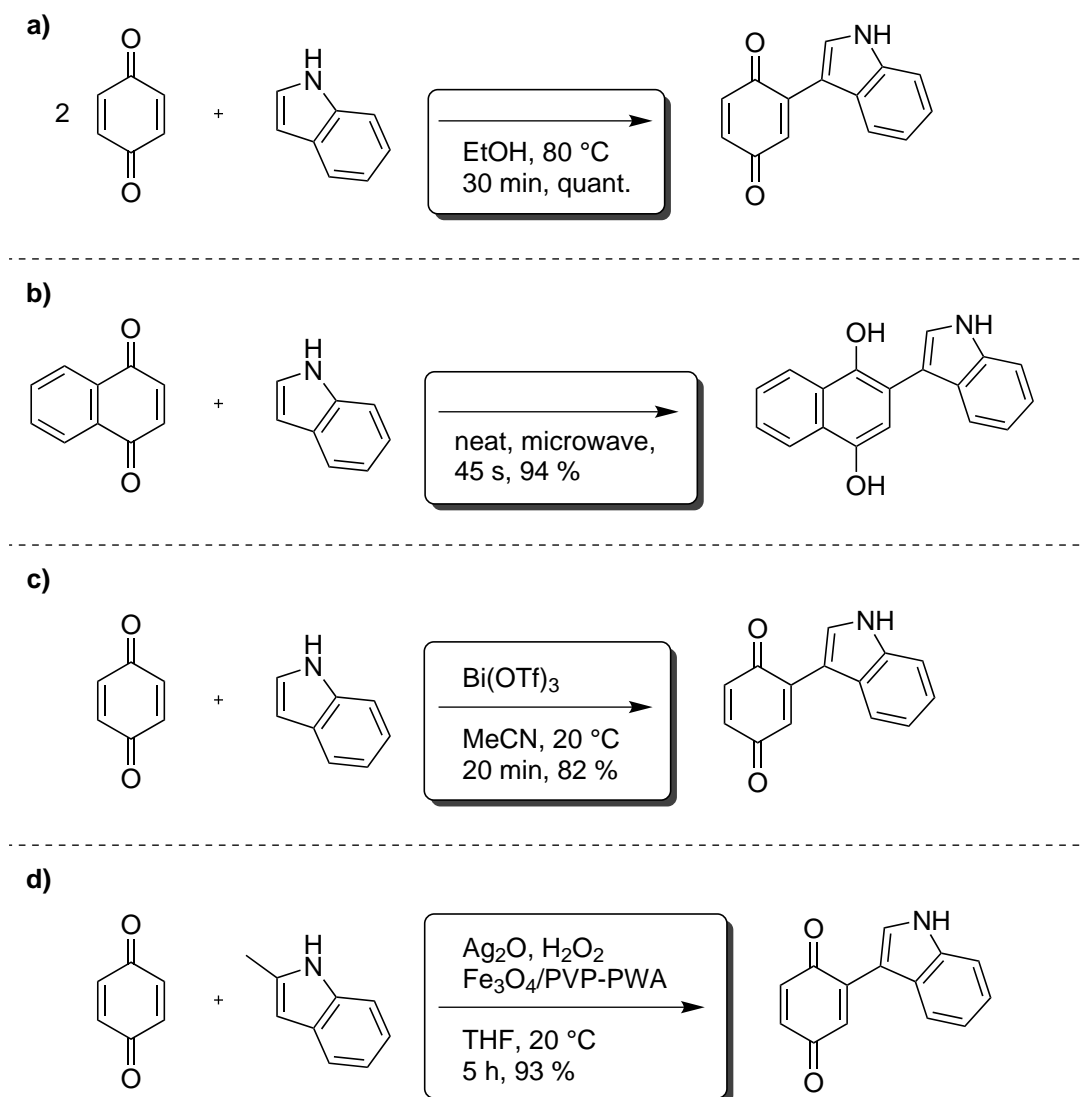
Table 2.10 OFAT screening for the influence of light, temperature and  $\text{Ag}_2\text{O}$ .

No.	Light (730 nm)	$T$ (°C)	$\text{Ag}_2\text{O}$ (2 equiv.)	Yield (%)	Yield (brsm) (%)
1	yes	20	yes	36	54
2	no	20	yes	0	0
3	no	85	yes	4	5
4	yes	20	no	0	0

The reaction under standard conditions (20 °C, irradiation, with  $\text{Ag}_2\text{O}$ ) gave an unoptimized yield of 36 % (54 % brsm, **entry 1**). The absence of light led to a loss of product formation (**entry 2**), which remained even at reflux temperatures (85 °C, 4 %, 5 % brsm, **entry 3**). Moreso, at elevated temperature even the starting material **41** was almost completely decomposed. Silver oxide seemed to be just as crucial for a successful reaction, with no detectable product formed in its absence (**entry 4**).

The resulting compound **74** is part of a larger class of indolylquinones. Their straightforward synthesis from the corresponding quinone and indole, respectively, has been mentioned in 1911 by MÖHLAU and REDLICH.<sup>[87]</sup> Since then, some refined methods have been developed using microwave irradiation<sup>[88]</sup> and LEWIS acid catalysis.<sup>[89]</sup> More recent methods employ

heterogenous catalysis using complex  $\text{Fe}_3\text{O}_4$ -povidone-phosphotungstic acid/ $\text{Ag}_2\text{O}$ -based systems (scheme 2.13).<sup>[90]</sup>



**Scheme 2.13** Known synthetic routes to indolylquinones.<sup>[87-90]</sup>

The indolylquinone structural motif is represented in a class of fungi metabolites called asterriquinones (**Figure 2.45**).<sup>[91]</sup> These compounds have been investigated for their widespread biological – including anti-tumor – activity.<sup>[92]</sup> Complementarily, ferrocenes are sometimes used as bioisosteres for planar aryl groups in medicinal chemistry.<sup>[93,94]</sup> The obtained structure **74** could therefore be an interesting starting point for research on ferrocene analogues of asterriquinones.

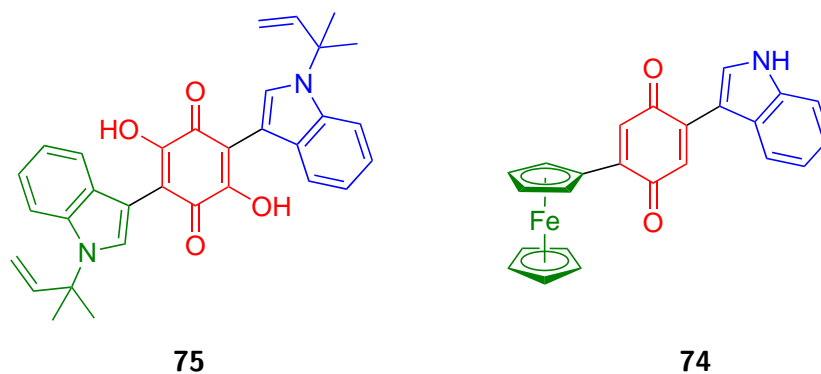


**Figure 2.45** Structure of asterriquinone A1 (**75**)<sup>[89]</sup> next to structure **74** obtained from quinoylferrocene (**41**) and indole (**43**). Ferrocene could act as a bioisostere for one of the indole units of asterriquinones.<sup>[93,94]</sup>

### Investigations on the Reaction of Quinoylferrocene with Indole

With these encouraging results in hand, the next step was to determine the effects of all reagents in order to obtain a deeper understanding of the reaction. The Cp\*Co(III)/AgSbF<sub>6</sub> system was joined into a single factor. Special attention was given to the role of light, due to its interesting mechanistical implications. To enable automated, light-dependent screenings, yet another photoreactor array was designed, 3D printed and connected to the GENESIS interface to enable both automated and remote control. The screening was attempted as a fractional factorial 2<sup>(7-2)</sup>, Resolution IV categorical DoE, where each reagent was either added to (level +1) or omitted from (level -1) the reaction (**Table 2.11**). In addition, four solvents were investigated using the *principal component analysis* (PCA)-based methodology described in **Section 1.1**. This represents a negative control for all factors, while simultaneously investigating their interactions. All reactions were carried out at once in the parallel synthesizer. It must be noted that addition sequences deviated between the original manual runs and the automated ones for technical reasons. This has to be considered when later results are compared to those shown in **Table 2.10**

**Table 2.12** Selected Solvents and their properties.<sup>[26]</sup> PC = Principal Component.

Solvent	Mp. (°C)	Bp. (°C)	Density (g mL <sup>-1</sup> )	PC1	PC2	PC3
Acetonitrile	-46	81	0.776	-2.18	-1.49	-0.25
Pyridine	-41	115	0.982	-1.25	1.61	-1.75
2-Methyltetrahydrofuran	-136	80	0.854	1.73	-1.32	-0.91
1,2-Dichloroethane	-35	84	1.253	0.79	1.10	1.34
Dichloromethane	-96	39	1.327	0.54	-0.42	1.45

**Table 2.11** Factors for the negative control categorical DoE.

ID	Factor	Low	High
A	Cp*Co(III)	0 equiv.	0.1 equiv.
B	PivOH	0 equiv.	0.5 equiv.
C	Ag <sub>2</sub> O	0 equiv.	2.0 equiv.
D	NaOAc	0 equiv.	1.0 equiv.
E	Light (730 nm)	off	on
F	Solvent PC1	-1	+1
G	Solvent PC2	-1	+1

Solvents were selected mainly by their PC1 and PC2 values, respectively.<sup>[26]</sup> Additionally, their availability as well as physical properties were considered, ultimately leading to the selection shown in **Table 2.12**. Dichloromethane was used as solvent for all stock solutions, and was conveniently located in the center of the actual reaction solvents (**Figure 2.46**). It must be noted that within the chosen selection, the solvents' PC1 values (polarity) strongly correlate with their respective PC3 values (hydrogen bonding). Therefore, any effect observed for PC1 may as well be due to an acid-base interaction instead. This can theoretically create issues, should PC1 and PC3 have opposing effects. After careful consideration, it was decided to accept this risk as a tradeoff for convenient executability.



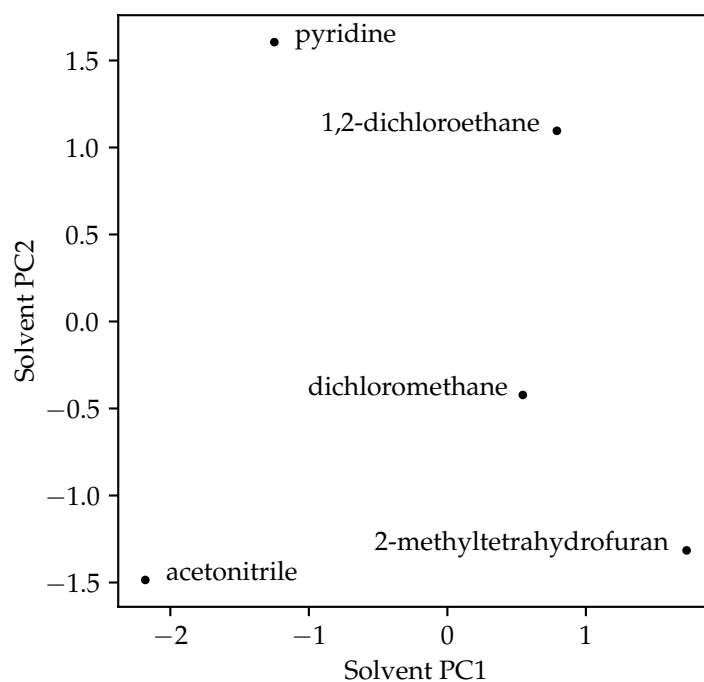


**Figure 2.46** PC plot for selected solvents.

Reactions were analyzed using automated QTLC. As a measure of reaction yield, product integrals were divided by the respective starting material integrals for each reaction (*TLC Relative Area Percentages, TRAP*).<sup>[95]</sup> These values were recorded at three time steps (3 h, 35 h, 51 h). Additionally, a binary decomposition metric was introduced by visual inspection of the TLC plates. Its value was defined positive if the corresponding reaction showed a brown-colored spot at the baseline, or any side product spots besides starting material and desired product. A response containing the time steps with the highest TRAP per reaction was also considered but ultimately rejected. Around half the reactions showed no product formation at any time step. For these cases, the “optimal time” metric would be undefined due to division by zero, leading to a skewed model.

Five of the 32 reactions showed no leftover starting material at one or more time steps. In these cases, the respective reaction was omitted from model building, since the response was undefined due to division by zero. Using the remaining runs, significant models could be created for all responses. An excerpt of the raw data is shown in **Table 2.13**.

**Table 2.13** Excerpt of raw result data for the fractional factorial DoE.

Run	Decomp.	TRAP ( $t_1$ )	TRAP ( $t_2$ )	TRAP ( $t_3$ )
1	1	0.00	0.00	0.00
2	0	0.12	0.45	0.52
3	0	0.11	0.00	0.00
...	...	...	...	...
13	1	0.37	0.80	0.86
14	1	0.00	0.85	1.38
15	0	0.00	0.00	0.00
...	...	...	...	...
32	1	n. def.	n. def.	n. def.

Around half the reactions showed no conversion at any time step. To gain a first overview, the TRAPs of some successful reactions were plotted against time. Additionally, *in lieu* of the “optimal time” metric described above, the average TRAP for each time step was calculated and plotted as well, using only those reactions with some conversion at any time step (Figure 2.47).

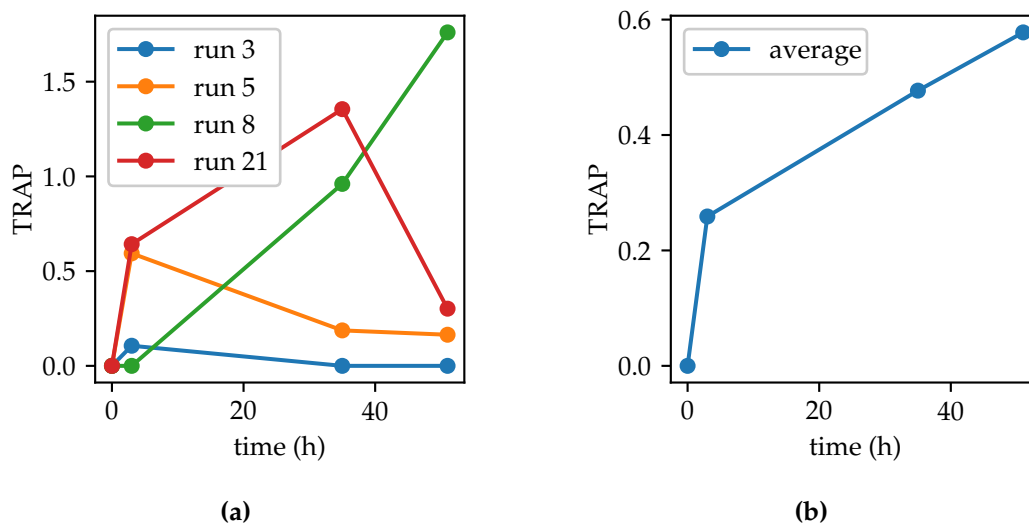


**Figure 2.47** TLC relative area percentages (TRAPs) for some selected reactions (2.47a), as well as the average TRAP per time step for runs with measurable conversion (2.47b).

The kinetic profiles of the reactions varied significantly (**Figure 2.47a**). The product to starting material ratio for runs 3 and 5 peaked at 3 h and decayed throughout the following time period. In contrast, run 21 showed its highest TRAP value at the second time step (35 h), dropping sharply at 51 h. Lastly, run 8 only showed any conversion from 35 h, still increasing after the maximum observed time period of 51 h. This vastly different behavior is attributed to the nature of fractional factorial designs, which aim to select the “most different” reaction conditions within the given factor ranges. On average, longer reaction times led to higher yields, as shown in **Figure 2.47b**.

Next, the decomposition response was analyzed using a model with logistic regression transformation. Since the response was binary, only main effects were investigated. Using “Solvent PC1” and “Solvent PC2” as the only factors, a good model ( $p = 0.0041$ ) was obtained. Both a high PC1 value, as well as a low PC2 value lead to a low probability of decomposition. This combination of values corresponds to 2-Methyltetrahydrofuran, which was thus unambiguously identified as the preferable solvent for obtaining a clean reaction mixture. Accordingly, the highest probability of decomposition was assigned to pyridine (PC1  $-1$ , PC2  $+1$ ). These findings can be important in further automated syntheses, where a low amount of side products can greatly simplify column chromatography, possibly even enabling column reuse. The effects plot for both PC1 and PC2 is shown in **Figure 2.48**

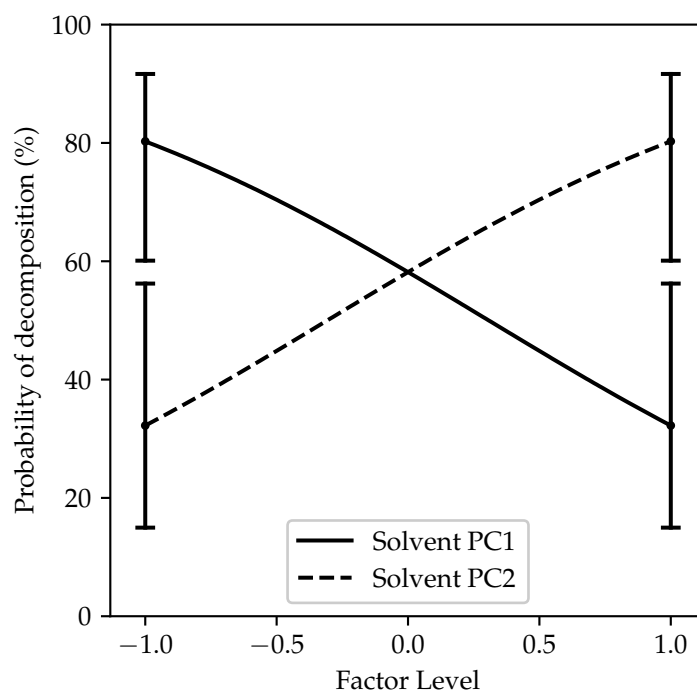


**Figure 2.48** Plot of the probability of decomposition in dependency of the solvent.

Following up, the TRAP responses were investigated to obtain some insight into the reaction mechanism. It should be noted that in 2013, a DoE-based technique for analyzing time-resolved responses was presented by GEORGAKIS.<sup>[96]</sup> Within this advanced technique named *Design of Dynamic Experiments*, additional time-dependent dynamic subfactors are introduced directly into the model. For simplicity, this approach was not taken in this work. Instead, separate models were created for each time step, and analyzed independently. As a tradeoff, the actual significance of time cannot be determined. Still, the varying importance of *all other factors across time* is observed, while no additional experimental effort is required due to the automated nature of TLC sampling and analysis. Importantly, time must not be included as a separate factor, if – as in this experiment – samples of *the same run* are simply taken at different time intervals. This would lead to a propagation of systematic errors throughout the model, rendering it useless for any educated decision making.

For the first two time steps (3 h and 35 h), good models were easily generated by manual selection of significant terms. The *Box-Cox* plot, which is a measure to determine the appropriate transformation for the data, called for an inverse square root transformation. Applying this, however, led to a large difference between predicted and adjusted  $R^2$  for both time steps and was therefore rejected. For time step three (51 h), model building was not as straightforward, as many combinations gave either strong overfit or unsatisfactory diagnostics metrics. In the end, an inverse square root-transformed model with only three factors was chosen, giving the best overall results. It is unknown why the last time step was more difficult to analyze than the previous two. The reaction might simply become less predictable over time, as lurking variables could take control. Further efforts were therefore concentrated on the first two, more reliable time steps.

To obtain a first, rough summary, the main effects' influences across time were compiled in **Table 2.14**.

**Table 2.14** Summary of main effects' contribution over time. n.e. = no (significant) effect

Factor	Decomposition	TRAP ( $t_1$ )	TRAP ( $t_2$ )	TRAP ( $t_3$ )
Ag <sub>2</sub> O	n.e.	↑	↑	↑
Cp*Co(III)	n.e.	↑	n.e.	n.e.
NaOAc	n.e.	↑	n.e.	n.e.
Solvent PC1	↓	n.e.	n.e.	↑
Solvent PC2	↑	n.e.	↓	↓

As explained above, decomposition was modeled to be dependent only on the solvent, being favored by low PC1 and high PC2 values, respectively. For the TRAP responses,  $\text{Ag}_2\text{O}$  was by far the most significant factor in all observed time steps, contributing positively to product/starting material ratios.  $\text{Cp}^*\text{Co(III)}$  and NaOAc both showed a positive effect in the early stage of the reaction (3 h), which was not observed in the following measurements at 35 h and 51 h. The effect of the solvent on the other hand was not significant during the first 3 h, but became so at 35 h (PC2) and even more so at 51 h (both PC1 and PC2). Interestingly, the same solvent principal component combination that suppressed decomposition (+1/−1, 2-Methyltetrahydrofuran) was also beneficial to reaction yield, underlining the importance of careful solvent selection. Both pivalic acid and light were not significant factors on their own, although light was part of some important multifactor effects, which will be discussed later.

In addition to these main effects, some two-factor interactions were found for the first two time steps. All of those interactions consisted of  $\text{Ag}_2\text{O}$  and another significant main effect, stressing its impact on reaction yields. Put simply, the presence of  $\text{Ag}_2\text{O}$  increased the effects of  $\text{Cp}^*\text{Co(III)}$  and NaOAc at 3 h, as well as that of solvent PC2 at 35 h. The average effects of these factors were already significant according to **Table 2.14**, however their actual contribution strongly depended on their combination with silver(I) oxide. As an example, an representative plot of the  $\text{Ag}_2\text{O}$ /NaOAc interaction for time step one is shown in **Figure 2.49**.

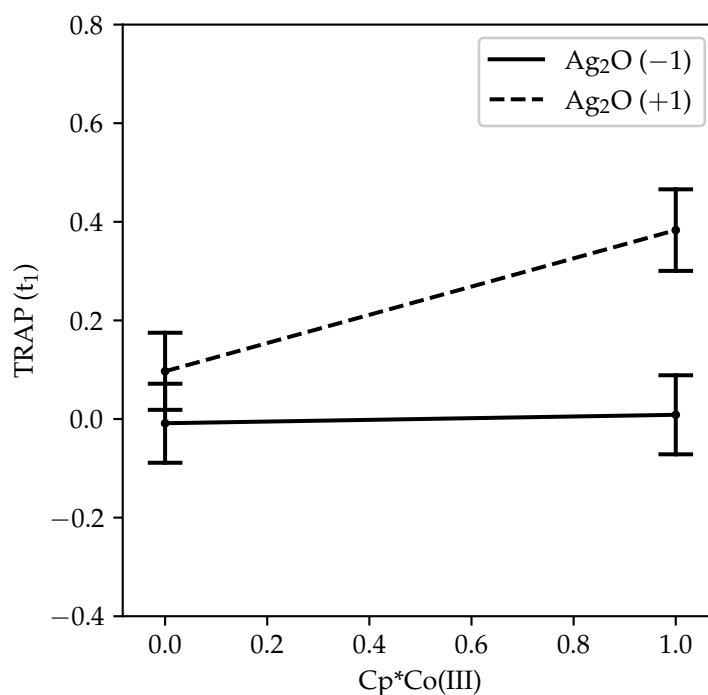


**Figure 2.49** Two-factor interaction between  $\text{Ag}_2\text{O}$  and  $\text{Cp}^*\text{Co(III)}$ . Solid line: Without  $\text{Ag}_2\text{O}$ . Dashed line: With  $\text{Ag}_2\text{O}$ .

As seen above, in the absence of  $\text{Ag}_2\text{O}$  (solid line),  $\text{Cp}^*\text{Co(III)}$  does not have a noticeable effect on the TRAP response at  $t_1$  (y axis). However, with  $\text{Ag}_2\text{O}$  present (dashed line), adding  $\text{Cp}^*\text{Co(III)}$  to the reaction leads to a large increase in product to starting material ratio.

Arguably the most interesting observation made during this investigation was a complex three-factor interaction between silver oxide, sodium acetate and light during the first two time steps. This interaction is visualized in **Figure 2.50**.

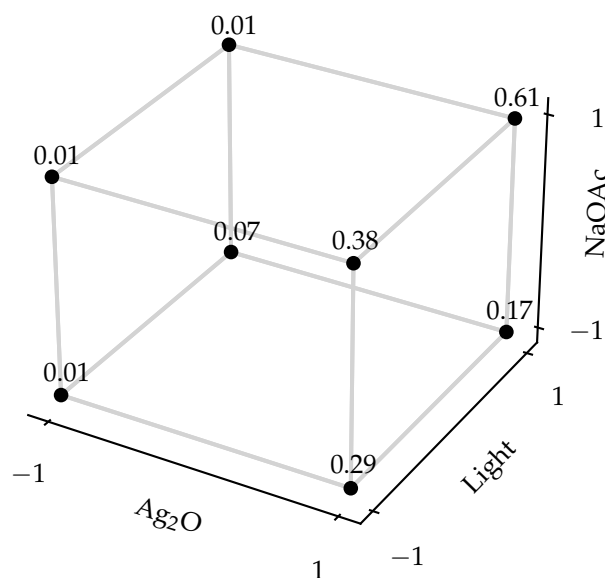


**Figure 2.50** Three-factor interaction between  $\text{Ag}_2\text{O}$ , NaOAc and Light at  $t_1$ . Vertex values are predicted TRAPs at  $\text{Cp}^*\text{Co(III)}$  (+1), PivOH (+1), solvent PC1 (+1), solvent PC2 (-1).

Expectedly, all values without  $\text{Ag}_2\text{O}$  show low TRAP values, with only the combination light +1/NaOAc +1 showing any measurable response at all. The highest overall response is obtained with both NaOAc and light at their high levels. Interestingly, when NaOAc is not present, TRAP responses are higher when light is switched off as well. This observation is a testament to the versatile behavior of quinoylferrocene (**41**) with its reported redox-, acid/base- and light-absorbing properties (**Figure 2.51**).<sup>[79]</sup> Notably, this detailed model is in contrast to the simple *one-factor-at-a-time* (OFAT) experimentation given in **Table 2.10**. The initial assumption was that both  $\text{Ag}_2\text{O}$  and light had the same influence on yield. The fractional factorial DoE revealed a more complex situation which would have been more difficult to find using traditional experimentation.

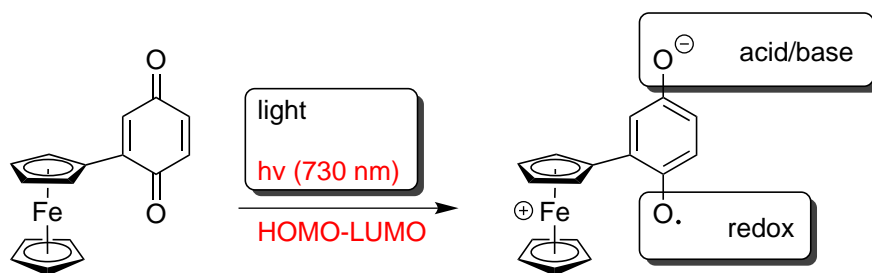


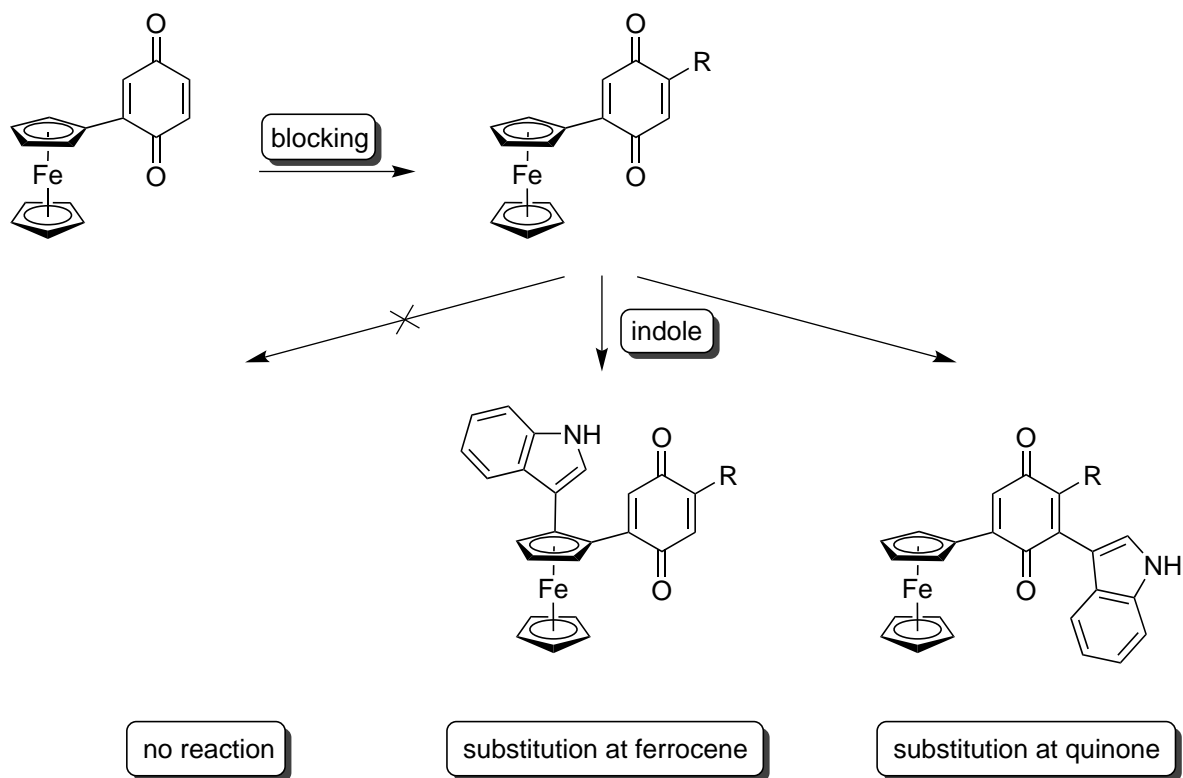
**Figure 2.51** Complex behavior of quinoylferrocene **41** showing light-, acid/base- and redox chemistry.

To confirm the results obtained above, a follow-up, full factorial  $2^3$  DoE was performed manually, again using the 3D printed photoreactor. Product integrals obtained from automated QTLC were compared to both starting material as well as an internal standard consisting of acetylferrocene **38**. A valid model was obtained, showing silver(I) oxide, NaOAc and their interaction as significant factors, but not light. As fewer experiments had been carried out in this validation, it was expected that not all interactions would be revealed. On the contrary, including the interaction between  $\text{Ag}_2\text{O}$ , NaOAc and light would automatically lead to the selection of all investigated factors, leading to a perfect-fit model which has no statistical use. The observed interaction, however, matched the one observed in the automated 32-experiment run carried out before.

It is noteworthy that the inclusion of the aforementioned three-factor interaction was only possible because it was not aliased in the chosen design. In fractional factorial designs, most three-factor-, and even two-factor interactions are more or less heavily confounded with each other, preventing their inclusion in the design model. The  $\text{Ag}_2\text{O}$ -NaOAc-light interaction not being aliased in this design was a mere coincidence, as the generator of DESIGN EXPERT automatically creates the design model, and the assignment of factors to their terms was not systematic. If such an interaction is anticipated before design generation, factors can be assigned in a way that interesting multifactor interaction will definitely be considered in the model.

### Blocking the Reactive Position

The results obtained thus far showed a different substitution at quinoylferrocene (**41**) than originally desired. Instead of indole being attached at the *ortho* position at the ferrocene ring of **41**, the addition took place at the quinone moiety. With this observation, the question arose what would happen if the reactive position of the quinoyl moiety were blocked by an inert group. Possible outcomes were a reaction at the desired position at ferrocene, a reaction at another quinone position, or complete quenching of any reactivity (**scheme 2.14**).

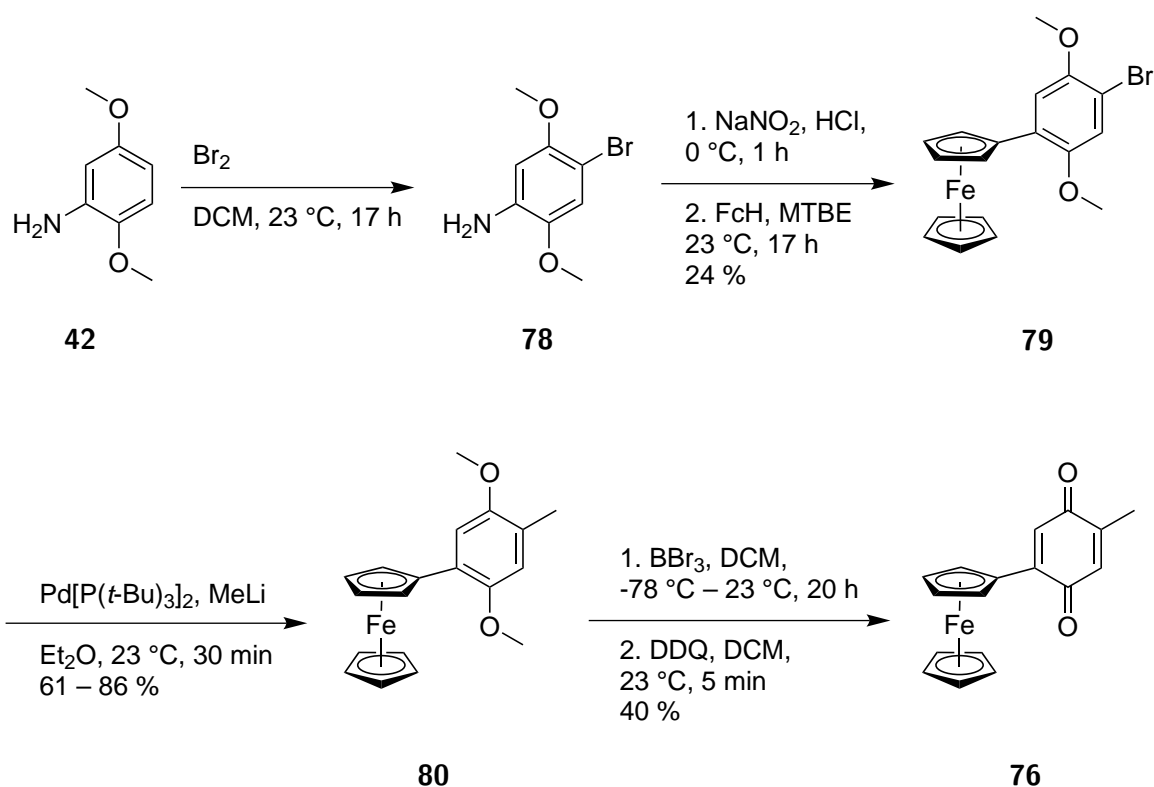


**Scheme 2.14** Possible outcomes of reacting a blocked derivative of quinoylferrocene with indole.

To prevent a significant shift in the absorption spectrum of the substrate, which would necessitate the use of different wavelength LEDs and therefore a reassembly of the photoreactor, the methyl group was chosen as a simple blocking group. It was assumed that with its small inductive but lacking mesomeric effects, the HOMO-LUMO gap of the corresponding substrate **76** should stay roughly the same as in its parent compound **41**.

The most straightforward way of synthesizing the unknown (methylquinoyl)ferrocene (**76**) with regard to the base procedure (**scheme 2.12**) would be obtained by simply changing 2,5-dimethoxyaniline (**42**) for 2,5-dimethoxy-4-methylaniline (**77**) and keeping the rest constant. Due to its lacking commercial availability, the methyl group was instead to be introduced by methylation of a previously introduced bromide group. The resulting forward synthesis is shown in **scheme 2.15**.





Scheme 2.15 Synthesis of (methylquinoyl)ferrocene (76).

After bromination of 2,5-dimethoxyaniline (**42**) using a known procedure,<sup>[97]</sup> the resulting 2,5-dimethoxy-4-bromoaniline (**81**) was subjected to the usual GOMBERG-BACHMANN conditions already applied for the synthesis of (**41**). As expected, the bromide group did not interfere, and the product **79** was obtained in 23% yield. With the nucleophilic amino group now gone, subsequent methylation using a palladium-based procedure by FERINGA *et al.*<sup>[98]</sup> gave compound **80** in 61% – 86% yield. The final demethylation/oxidation step produced the desired (methylquinoyl)ferrocene **76** in 40% yield.

With the target compound **76** in hand, its reaction with indole was to be tested. Leveraging the pre-programmed synthesis sequence in the ASW 2000P as well as the pre-designed DoE from the previous run with quinoylferrocene (**41**), (methylquinoyl)ferrocene (**76**) was subjected to those same conditions. With protocols already in place, the preparation for this 32-experiment run took only a single day. Reagents were loaded as usual, and the reaction was executed over night. This time, samples were only taken once at 2 h, and automated TLCs were made.

At first glance, the present run optically resembled the previous one with unblocked quinoylferrocene **41**. While in some of the runs apparently no reaction had occurred, many TLC lanes showed a new, purple spot below the green starting material (**Figure 2.52**). Generally, yields appeared to be higher than with **41**, as many products spots appeared much more intense. A

TLC-MS analysis revealed  $m/z = 422.5$  for the new violet spots, which corresponds to the expected  $[M + H]^+$  peak.

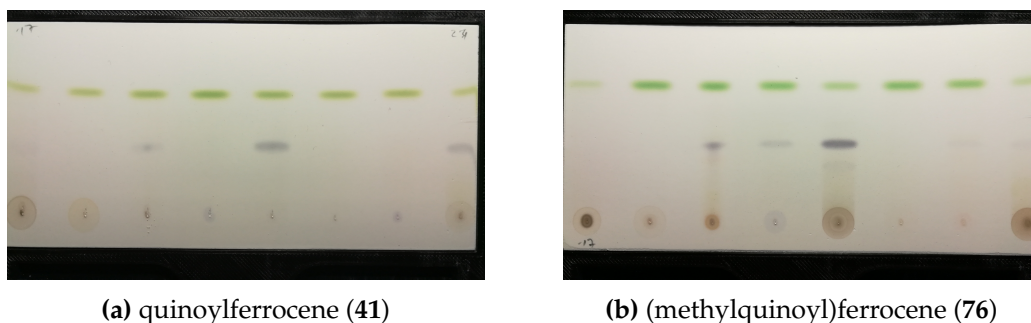


**Figure 2.52** Comparison of screening results with quinoylferrocene (41) and (methylquinoyl)ferrocene (76). TLC plates of runs 1 – 8 shown for both experiments.

Using the automatically generated TLC plates, DoE responses were generated using the established PYTHON QTLC algorithm. Eliminating one outlier (run 5) and applying a natural log transformation, a model with very good overall metrics was obtained. Many factors were at a significance level of  $p < 0.0001$ , with the adjusted  $R^2$  and predicted  $R^2$  of the model being 0.9861 and 0.9687, respectively. **Table 2.15** shows an overview of all factors included in the model.

**Table 2.15** Significant factors for the reaction of (methylquinoyl)ferrocene (**76**) and indole (**43**) with p-values and contributions.

Factor	p-value	Contribution (%)
Model	< 0.0001	
A-Cp*Co(III)/AgSbF <sub>6</sub>	< 0.0001	6.6
B-PivOH	0.145	0.1
C-Ag <sub>2</sub> O	< 0.0001	27.0
D-NaOAc	0.838	0.0
E-Light	0.0631	0.2
F-Solvent PC1	< 0.0001	21.1
G-Solvent PC2	< 0.0001	4.8
AC	< 0.0001	4.1
AF	< 0.0001	5.9
BD	< 0.0001	4.6
CD	0.039	0.3
CE	0.0115	0.4
CG	< 0.0001	5.5
DE	< 0.0001	9.9
CDE	< 0.0001	8.9

In comparison to quinoylferrocene (**41**), a much more detailed and smooth model was generated. Besides (methylquinoyl)ferrocene (**76**) actually showing different reaction behavior, this might also simply be attributed to the higher amount of usable data points in the present run (15 non-zero responses as opposed to 10 with quinoylferrocene (**41**)). Multifactor interactions were also more sophisticated, involving factors other than Ag<sub>2</sub>O in this instance.

Just as with quinoylferrocene (**41**), silver(I) oxide was the most significant factor, contributing 27% to the overall model. Interestingly, solvent PC1 was identified as the second most important factor, a high polarity being beneficial to product formation. The interaction between NaOAc and light, as well as Ag<sub>2</sub>O, NaOAc and light were next, contributing 16% in total. Without silver(I) oxide, responses are generally low. With it present, sodium acetate and light should either both be present or absent to yield high responses. Both NaOAc or light alone, without the other one present, lead to a significant decrease in yield (**Figure 2.53**).

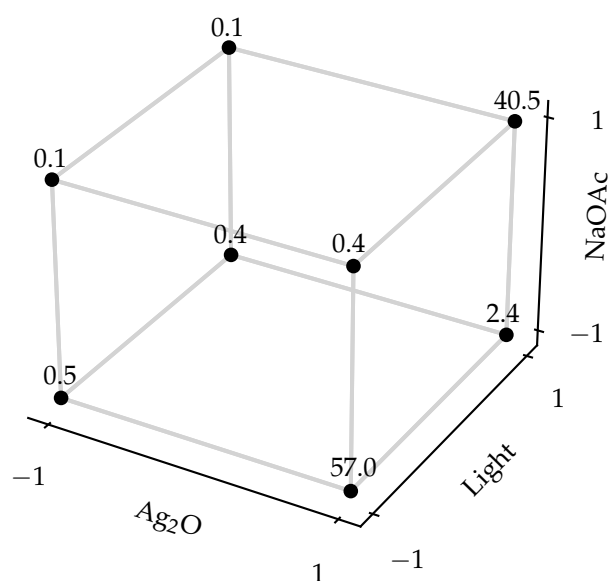
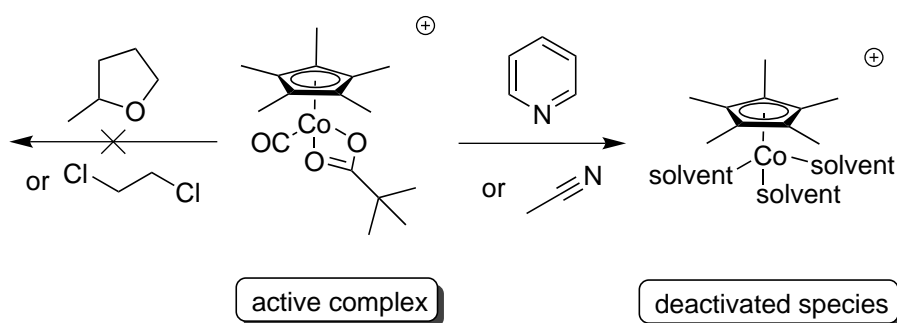


**Figure 2.53** Three-factor interaction between  $\text{Ag}_2\text{O}$ , NaOAc and Light at  $t_1$ . Vertex values are predicted TRAPs at  $\text{Cp}^*\text{Co(III)}$  (+1), PivOH (+1), solvent PC1 (+1), solvent PC2 (-1).

Like in the previous experiment,  $\text{Cp}^*\text{Co(III)}$  was determined to be a significant factor as well. However, it was also involved in a two-factor interaction with solvent PC1 (polarity). The  $\text{Cp}^*\text{Co(III)}$  complex was only beneficial in combination with a low polarity solvent. This seemed counterintuitive, as the complex is positively charged and should dissolve better in polar solvents. Upon closer inspection, the "polar" solvents (PC1 -1) chosen in this experiment were acetonitrile and pyridine, both nitrogen-based and nucleophilic. As cobalt shows a high affinity to nitrogen, it seems likely that in these solvents, the complex was deactivated and therefore no longer participated in the reaction. The "non-polar" solvents (PC1 +1) were 2-methyltetrahydrofuran and dichloroethane, both of which should not be strong ligands for the cobalt complex and therefore not hinder its reactivity (**scheme 2.16**).



**Scheme 2.16** Possible deactivation of  $\text{Cp}^*\text{Co(III)}$  complexes by nitrogen-bearing solvents, explaining the multifactor interaction between  $\text{Cp}^*\text{Co(III)}$  and solvent polarity.

Besides solvent polarity, polarizability (PC2) also played a significant, albeit smaller role, both on its own and in an interaction with silver(I) oxide. Straightforwardly, more polarizable solvents were advantageous for product formation. Interestingly, both pivalic acid and sodium acetate were not significant factors on their own, but were part of a two-factor interaction with one another. DoE responses were higher if exactly one of both was present in the reaction. This may point to the reaction being able to use both acid and base catalysis, as both NaOAc and PivOH can lead to yield increase. With both reagents present however, they might neutralize each other, weakening the effect of pH catalysis. The same should apply if neither base nor acid are present. Lastly, Cp\*Co(III) and Ag<sub>2</sub>O participated in a curious two-factor interaction. Although both were on average positively correlated with high responses, in some cases the presence of one actually inversed the effect of the other. The exact reason for this remains inconclusive.

The reaction with methylated quinoylferrocene **76** proceeding in almost the same way as with the parent compound **41** was an unexpected result, which raised the question whether the originally assigned structure of product **74** was correct. To obtain a more conclusive answer, considerable efforts were put into obtaining single crystals of **74**, which were eventually successful. The resulting X-ray diffractograms showed a structure significantly different from the one originally assigned by NMR (Figure 2.54).

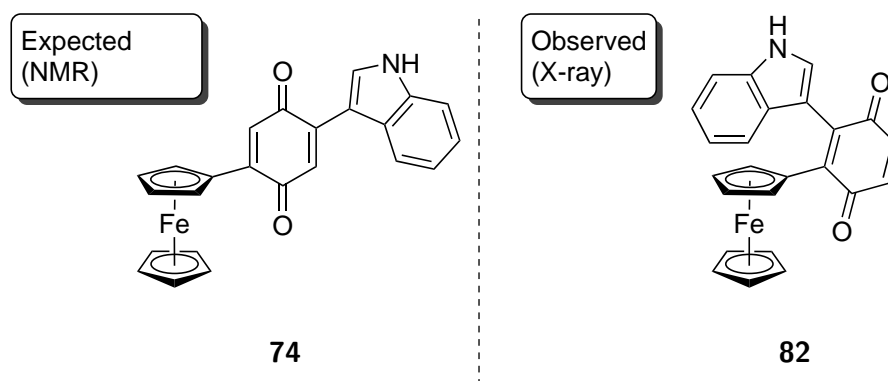


**Figure 2.54** Structure obtained from literature precedent<sup>[89]</sup> and NMR assignment, against actual structure obtained from X-ray crystallography.

Despite literature precedent,<sup>[89]</sup> as well as comprehensive NMR analysis and comparison with simulated data, the actual structure of the product was proven to be that of **82** instead of **74**. The indolyl motif, instead of being attached to quinone at the position opposing the ferrocenyl moiety, was found directly next to it. This was a surprise because the quinone moiety was expected to be both less electrophilic and more sterically hindered at this position. The exact reason for this regioselectivity could not be investigated within the scope of this thesis, and therefore remains unknown.

The observed structure **82** showed some interesting properties. A single molecule from the X-ray analysis is shown in **Figure 2.55**.

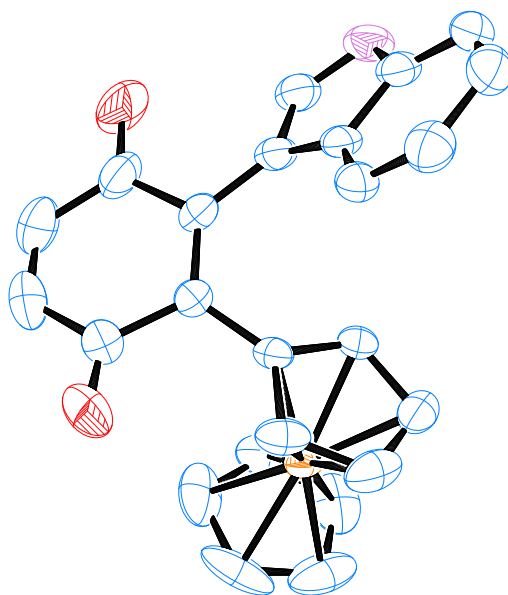


**Figure 2.55** Structure of a single molecule of **82** as obtained by X-ray crystallography.

Due to the close proximity of the ferrocenyl- and indolyl moieties, significant steric hindrance is introduced, which leads to considerable twisting and bending within the molecule of **82**. Not only is there a strong twist across the ferrocenyl-quinoyl and quinoyl-indolyl axes, but the quinoyl moiety is also twisted in itself, leading to a non-planar geometry. This twisting leads to the stable conformation seen in **Figure 2.55**, which also exists in the crystal as its mirror image in a ratio of 50/50. Although the molecule in its solid state shows a helical twist resembling the structure of DNA, it would have to be called axially chiral, if the barrier of rotation were high enough for both conformers to be stable in solution. This barrier is unknown at this point, but could be calculated using *density functional theory* (DFT) methods.

### Library Synthesis

With the reaction now investigated in good detail, different indoles were reacted with both quinoylferrocene (**41**) and (methylquinoyl)ferrocene (**76**) to test the reaction scope. Reaction conditions were developed from previous DoEs. The investigation with quinoylferrocene (**41**) showed that longer reaction times generally lead to higher responses (**Figure 2.47**), but also to diminished predictability. General trends were the same for all time steps however, and conditions favorable for yield simultaneously predicted low decomposition (2-Me-THF as solvent, Ag<sub>2</sub>O) present. A reaction time of 17 h was chosen, representing a time point between

the two first time steps investigated in the quinoylferrocene model (**Section 2.2.1**). A numerical optimization performed within the DESIGN EXPERT software returned  $\text{Ag}_2\text{O}$  and  $\text{NaOAc}$  in 2-Me-THF as the optimal conditions. These were consequently chosen for both library syntheses.

The reaction was designed as a  $2 * 8$  synthesis using 8 different indoles on both quinoylferrocene (**41**) and (methylquinoyl)ferrocene (**76**), yielding a total of 16 reactions. Selected indole derivatives are shown in **Figure 2.56**.

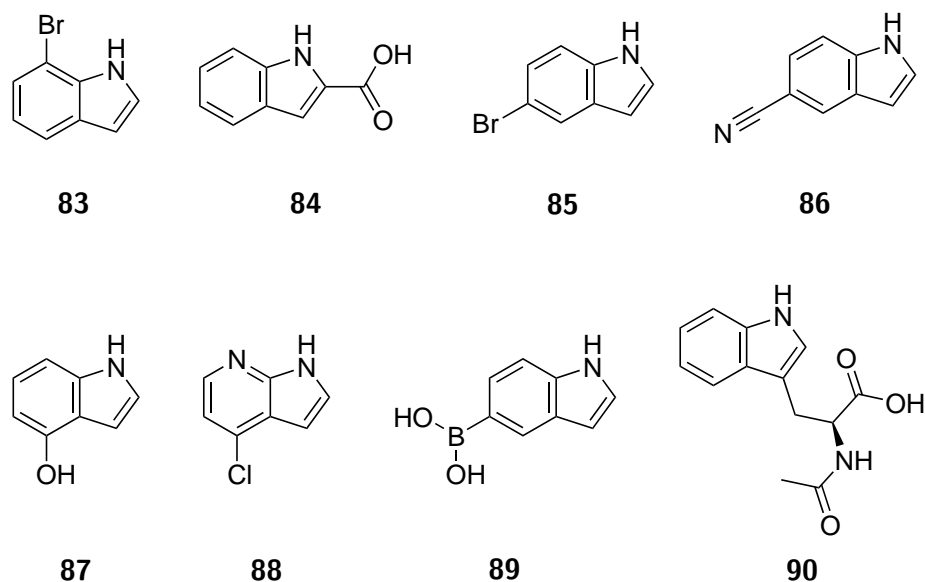


**Figure 2.56** Indole derivatives chosen for scope testing and library synthesis.

As shown above, some straightforward derivatives (**83**, **85**, **86**) were chosen besides some more challenging ones (**84**, **87**, **88**, **89**, **90**) with higher probability of functional group interference to fully investigate the potential of the reaction.

The syntheses were carried out in the parallel synthesizer as usual. During sequence planning however, it became obvious that major manual efforts would be necessary in comparison to previous runs. Both  $\text{Ag}_2\text{O}$  and  $\text{NaOAc}$  had to be added as solids, and since no automated gravimetric dispensing module was available, this was done manually. Furthermore, the indoles' solubility in 2-Me-THF was unclear, leading to their manual weighing and addition as well. Even in dissolved form, stock solutions would have contained only two aliquots, leading to low efficiency. In the end, the only automated tasks were dispensing of both ferrocene derivatives pre-dissolved in reaction solvent, incubation including the photoreactor, and TLC preparation. Even with this strongly diminished efficiency however, having 16 parallel reactors available was a great advantage.

Because at the time of execution not enough (methylquinoyl)ferrocene (**76**) was available, library synthesis was started with only quinoylferrocene (**41**) at first. Automated TLCs revealed dark violet spots for reactions with both bromo- as well as the cyano derivatives (**Figure 2.58a**). TLC-MS confirmed the expected product  $m/z$  values, and reactions were retrieved, subjected to automated column chromatography and characterized (**Figure 2.57**).

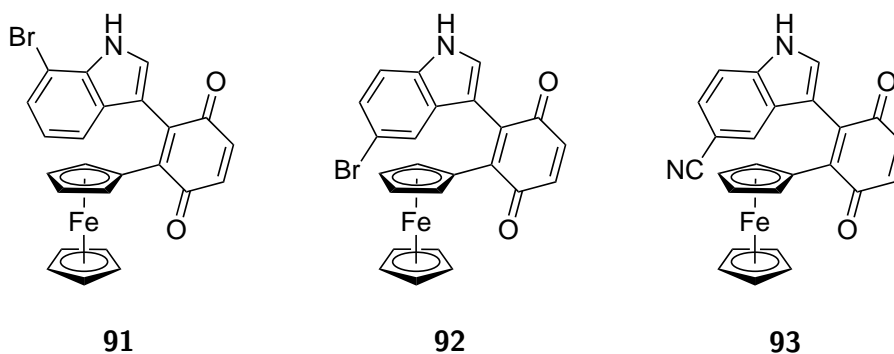


**Figure 2.57** Indoles obtained from library synthesis with quinoylferrocene (**41**).

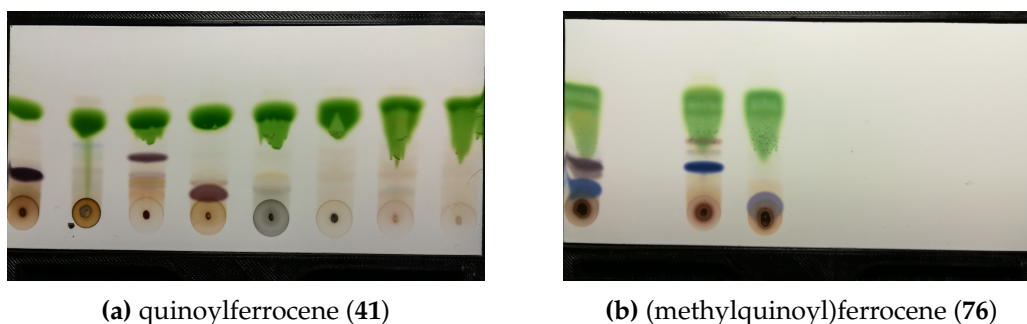


**Figure 2.58** Results from library syntheses. quinoylferrocene (**41**) showed formation of expected violet products in three cases (left), whereas with (methylquinoyl)ferrocene (**76**) unexpected blue products were formed due to a photoreactor malfunction (right).

(methylquinoyl)ferrocene was synthesized from previously made batches of precursor **80**. As only a limited quantity was available, only those indoles leading to isolable products with quinoylferrocene (**41**) were used in this run, leading to three reactions. Due to a computer malfunction over night, the photoreactor was erroneously switched off after an unknown amount of time. Since light is crucial in a multifactor interaction with sodium acetate, its unplanned absence lead to unpredicted behavior. Most notably, only reactions with indoles **94** and **95** lead to formation of a violet product. Unexpectedly, in all three reactions a new, deep blue product was formed (**Figure 2.58b**), the identity of which could not be determined due to decomposition upon purification. They might have been analogues of indigo formed from dimerization of two molecules of indole followed by oxidation *via*  $\text{Ag}_2\text{O}$  (**Figure 2.59**).



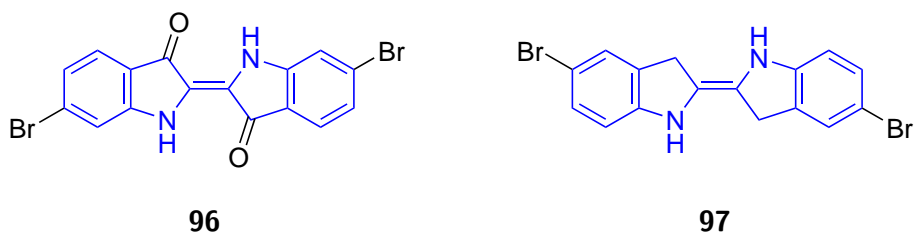


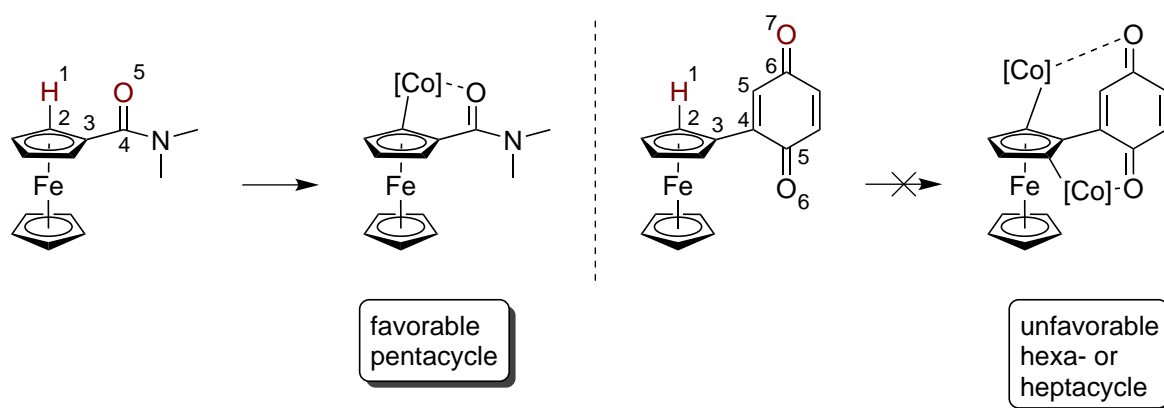
**Figure 2.59** Structure of Tyrian purple (**96**),<sup>[99]</sup> a prototypical derivative of the indigo dye class, and suspected structure **97** of unexpected blue derivatives formed during library synthesis at absence of light.

Due to the aforementioned events, only the 7-bromo derivative **98** could be isolated. Despite this apparent failure, the delicate balance between reagents predicted by DoE was showcased. As described earlier **Figure 2.53**, the simultaneous presence of both light and sodium acetate is favorable for product formation, whereas the sole absence of either one strongly diminishes yields. Due to the failure of the photoreactor, only sodium acetate was present in the reactions, leading not only to decreased product formation but to the formation of new side products.

## Conclusion and Outlook

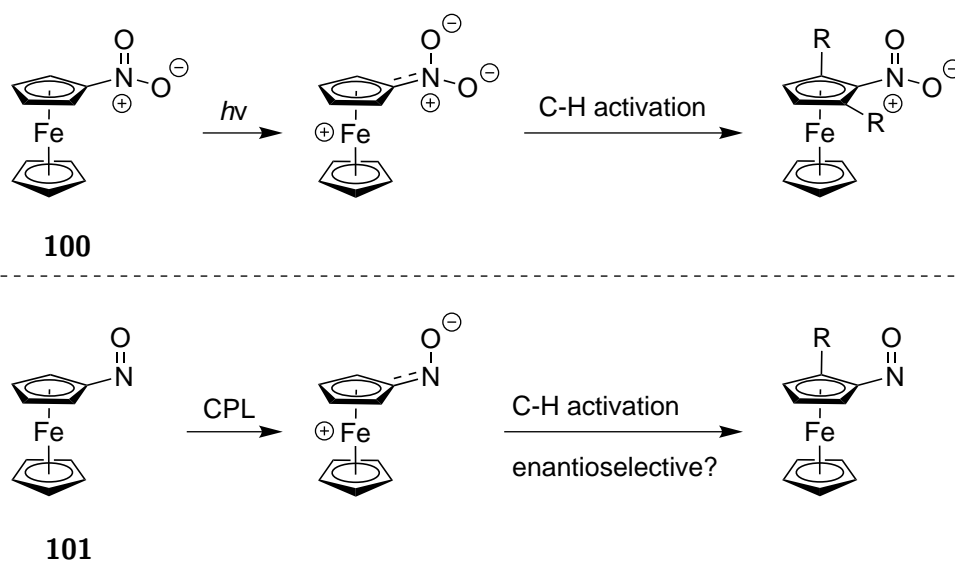
In summary, a method for the synthesis of new ferrocene analogues of asterriquinone (**99**) was found. The influence of reaction parameters on product formation were investigated using parallel synthesis-enabled DoE, and complex multifactor interactions involving light were found. Solvent screenings were included in the fractional factorial designs using PCA tables from the literature.<sup>[26]</sup> Responses were collected using the PYTHON-based quantitative TLC methodology developed in this thesis, which gave results sufficient for generating significant models.

The reactions did not lead to desired C-H activation products, but to substitution at the quinone moieties instead. Blocking this reactive quinone position did not lead to C-H activation at ferrocene either, but rather to reaction at a different site on the quinone moiety. Further approaches could include blocking all quinone-H positions, for example with methyl groups. However, since during all tests the desired Fc substituted products were not observed even in trace quantities, quinone might not be suitable as an ODG for C-H activations. Besides its own high reactivity towards radicals and nucleophiles, the angle of both carbonyl groups is not optimal due to an unfavorable atom distance between the Fc *ortho* protons and the oxygen atoms (**scheme 2.17**).



**Scheme 2.17** Unfavorable properties of the quinone group, preventing its use as an *ortho*-directing group in C-H activation chemistry.

In further studies, a different ODG with electron-accepting properties should be found. A simpler molecule which has been synthesized<sup>[100]</sup> but not well investigated is nitroferrocene (**100**). The nitro group is a prototypical acceptor group in *push-pull* systems, should be less prone to side reactions and possesses the optimal atomic distance typical for Cp\*Co(III)-catalyzed C-H activations. Pre-chiral analogues could be obtained from nitrosoferrocene (**101**), possibly providing a means of enantiomeric selectivity during an activation with circularly polarized light (**scheme 2.18**). Comparable N-nitroso compounds have recently been used as directing groups in various late transition metal-catalyzed C-H activations.<sup>[101]</sup>



**Scheme 2.18** Nitro-(**100**) and nitrosoferrocene (**101**) as possible *push-pull* systems for light-dependent C-H activation.

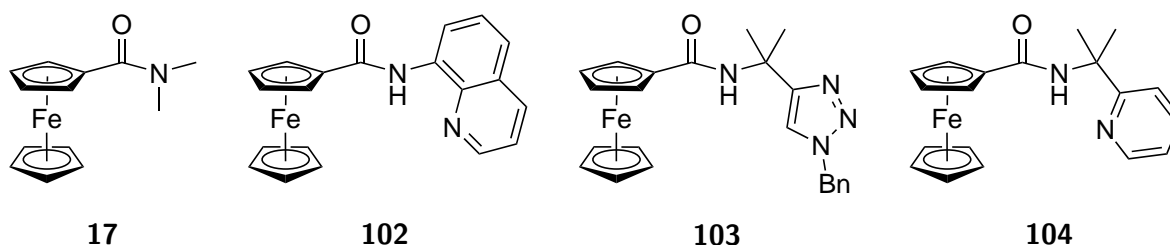
This project was meant to explore one of the major potentials of the ASW 2000P in organic chemistry – rapid reaction optimization and characterization. It was the first use case where all

developed tools were utilized at once, namely automated charge calculation (**Section 2.1.3**), reaction planning using fractional factorial, multi-time step DoE coupled with PCA (**Section 1.1**), 3D printed photoreactors (**Section 2.1.3**) controlled by the ARDUINO interface (**Section 2.1.3**), QTLC for response generation (**Section 2.1.2**) and parallel synthesis (**Section 2.1.1**), making a strong case for the usability of these tools in real-life, academic organometallic chemistry.

## 2.2.2 High-Throughput Investigations in Cp\*Co(III) Catalysis

### Introduction

As mentioned briefly in **Section 2.2.1**, amide-based *ortho*-directing groups (ODGs) are regularly utilized in metal-catalyzed C-H activation reactions.<sup>[67]</sup> In the group of BUTENSCHÖN, various ferrocene-containing amides such as **17**, **102**, **103** and **104** have been investigated in both Fe- and Co-catalyzed transformations (**Scheme 2.19**).<sup>[37,69,102]</sup>



**Scheme 2.19** Some known amide-based *ortho*-directing groups in C-H activation at ferrocene.<sup>[37,69,102]</sup>

Carbamides are usually stable compounds, which are easily synthesized by reaction of the corresponding acyl chlorides with amines. This sequence can be applied to ferrocene as well,<sup>[103]</sup> with ferrocenoyl chloride (**105**) being an isolable, crystalline solid. With its easily available starting materials, the reaction can be applied to a large scope of acyl chlorides and amines to produce a wide range of carbamides. In C-H activations, amides are relatively weakly coordinating groups, but are transformed to strong DGs by deprotonation at nitrogen.<sup>[104]</sup> This mechanism can be used to selectively tune reactivity, when carbamides with multiple aryl groups are used.<sup>[105]</sup> In contrast to *N*-heterocyclic ODGs, which facilitate disubstitution, carbamide-based ODGs often selectively lead to 2-monosubstituted products as a result of steric hindrance **Figure 2.60**.<sup>[37,106]</sup>

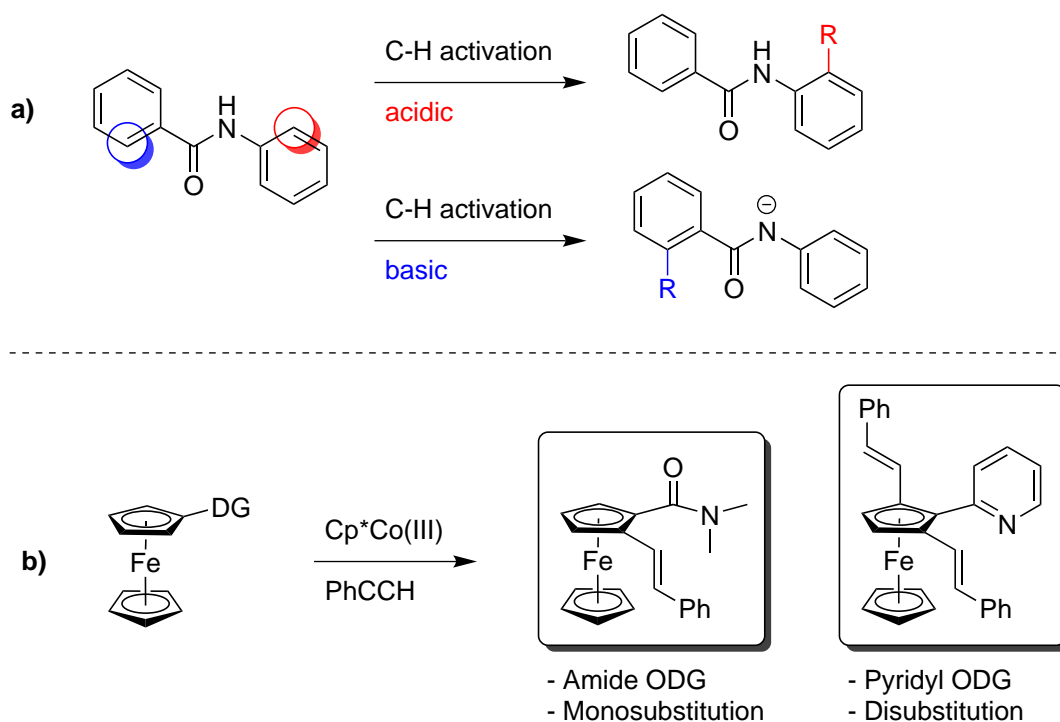
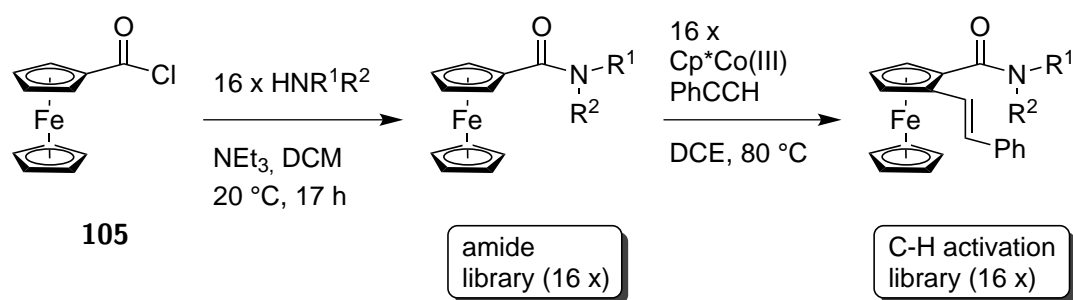


**Figure 2.60** Selected properties of amides as *ortho*-directing groups. a) Site selectivity based on pH.<sup>[104]</sup> b) Selectivity of amide directing group for monosubstitution.<sup>[37]</sup>

Due to their straightforward synthetic protocol as well as their extensive use in contemporary C-H activations, one of the first projects with the parallel synthesizer was the transformation of ferrocenoyl chloride **105** with 16 different amines available from the inventory of the institute. The main purpose of this experiment was to investigate the behavior of different solutions and liquids in the synthesizer, as well as to test basic functionalities such as evaporation, inert vacuum filtration and the automated TLC-MS workflow described in **Section 2.1.1**. Products were not recovered from those initial experiments.

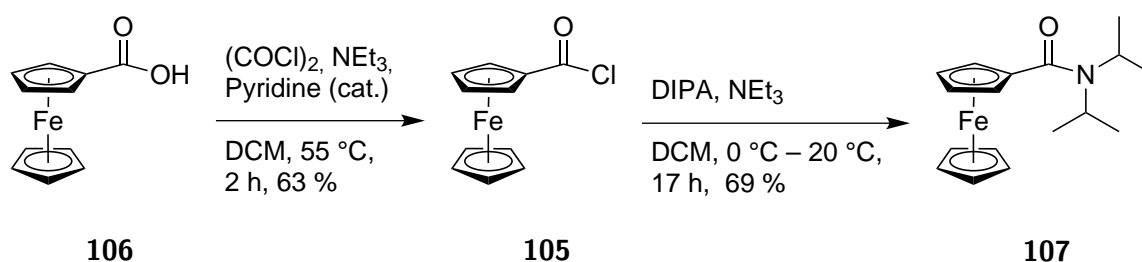
At a later stage, when workflows were stable, the idea of a ferrocenyl carbamide library was brought up again, and it was decided to repeat the experiments with the aim of isolation and characterization of all products. Furthermore, it was decided to subject all ferrocenyl carbamide products to the C-H activation conditions developed in a previous publication **Scheme 2.20**.<sup>[37]</sup> With such a library, the influence of different nitrogen substituents on reactivity and selectivity would be investigated in detail. The use of enantiopure chiral amides was expected to lead to diastereomeric products, with selectivities to be investigated. Using aryl-based substituents, the question of site selectivity may arise, as discussed above. With the completed workflow based on parallel synthesis and sample preparation, TLC-MS, automated MPLC and parallel sample evaporation, this would additionally become an interesting case study with regards to synthetic throughput compared to traditional experimentation.



**Scheme 2.20** Project layout for generation of a ferrocenyl carbamide library, and subsequent test reactions under typical catalytic C-H activation conditions.

## Library Synthesis

To start, a 4 g batch of ferrocenoyl chloride (**105**) was synthesized straightforwardly according to a known procedure from ferrocenylcarboxylic acid (**106**) and oxalyl chloride (**Scheme 2.21**).<sup>[107]</sup> Before the actual 16-reaction run, a single experiment with diisopropylamine (DIPA) was carried out manually to become familiar with reaction conditions and material properties.<sup>[108]</sup>



**Scheme 2.21** Synthesis of ferrocenoyl chloride (**105**)<sup>[107]</sup> and subsequent, single test reaction with diisopropylamine (**108**).<sup>[108]</sup>

Next, 16 different amines were sourced from the electronic inventory database of the institute using the search query "amin". Their choice – aside from availability – was mainly based on structural diversity. Notably, PCA tables for amines exist in the literature, potentially providing a means for their rational selection based on overall diversity of properties.<sup>[29]</sup> However, a PCA-based approach always carries a tradeoff with reagent availability. Since the main focus of this study was the generation of an automated library synthesis use case rather than structural investigations, and as not all available amines were listed in the PCA tables, this approach was not taken. The final selection (compounds **109** – **123**) is shown in **Figure 2.61**.

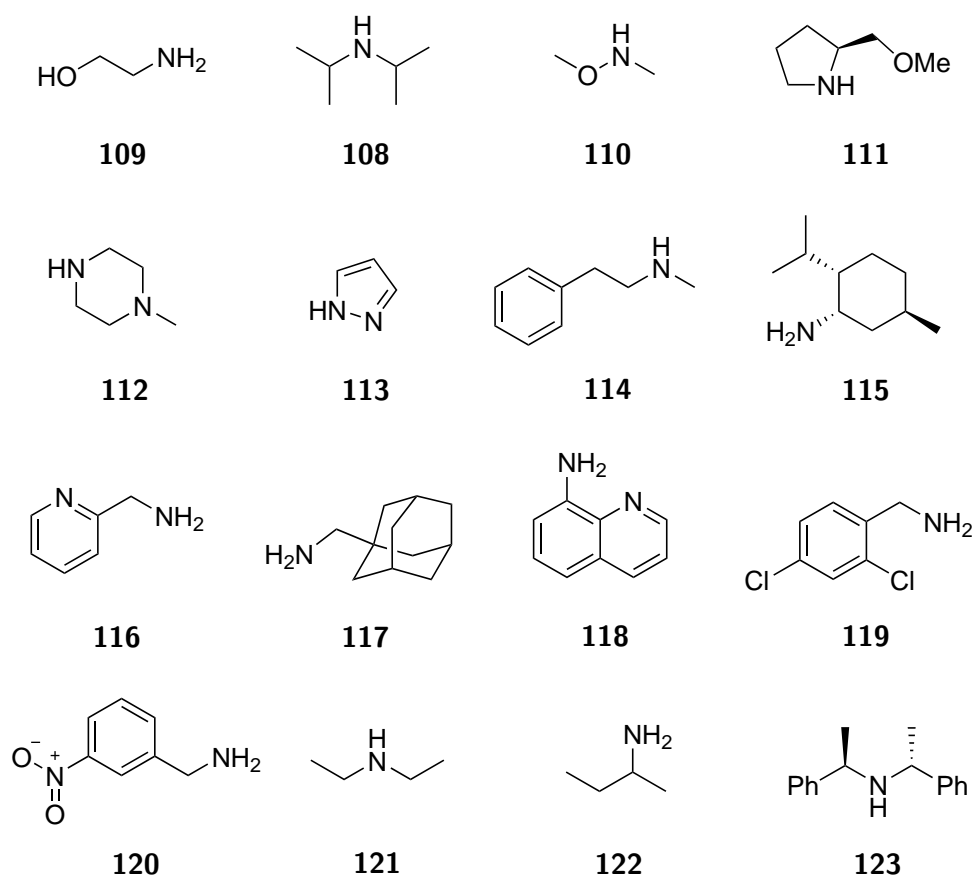


**Figure 2.61** Selection of amines for the reaction with ferrocenyl chloride (**105**).

In the original work,<sup>[37]</sup> *N,N*-(dimethylcarbamoyl)ferrocene was investigated in Cp\*Co(III)-catalyzed alkenylations. To extend on this, three other simple alkyl amines (**108**, **121** and **122**) were chosen for the amide library. Some (alkyl)aryl ODGs could be formed from amines (**114**, **119** and **120**). The use of amines **109**, **113**, **116** and **118** could lead to multidentate directing groups, which have been shown to be effective in Cp\*Co(III)-catalyzed transformations.<sup>[109]</sup> An easily functionalizable Cp\*Co(III) directing group<sup>[110]</sup> is the WEINREB amide formed from amine **110**. Some structural motifs commonly found in drugs are provided in amines **112** and **117**. Finally, some chiral amines were employed to test for diastereoselectivity during the following C-H activation trials. These include compounds **111**, **115** (both providing centric chirality) and compound **123**, forming an ODG with axial chirality.

For the charge calculation, the automated script described in **Section 2.1.3** was used. 14 of the desired 16 amines were found automatically, leading of all reagent amounts being finished in about two minutes.

After calculating appropriate dilutions for all starting materials, the desired reaction sequence was programmed into the parallel synthesizer. All 16 reactors were heated and flushed with

argon automatically, and starting materials were distributed to 8 mL reagent vials. Equimolar solutions were created for all 16 amines, enabling the use of a single dispense task in the synthesizer. With all starting materials provided, the automated sequence was started. Ferrocenoyl chloride (**105**) in dichloromethane was distributed to the reactors. The solutions were cooled to 0 °C and triethylamine (**124**) was added. Then, all 16 amines were added dropwise to their respective reactor vials. Upon completed amine addition, the reactors were warmed to 20 °C and the reactions were stirred over night for 25 h.

Upon an external user signal *via* smartphone, an automated TLC screening was performed to estimate the completeness of the reaction as well as eluting properties of all products for subsequent purification by column chromatography. Different compositions of petroleum ether and ethyl acetate were provided to the synthesizer along with fresh, pre-cut TLC plates. An automated sequence sampled spots directly from all reactor vials, primed the solvent lines with the current solvent mixture, developed the TLCs by dispensing and aspirating a preset amount of mobile phase to the TLC chamber, and sent a message at the end. Most reactions were spot-to-spot conversions, with some brown residue at the baseline typical for ferrocene chemistry (**Figure 2.62**). Additionally, the question arose whether the crude mixtures could be applied to a silica column directly as DCM solutions. However, a TLC developed in pure DCM as the mobile phase showed high  $R_f$  values for most reactions, leading to rejection of this approach. Instead, the crude mixtures were to be adsorbed on silica, or suspended in starting eluent by sonication.

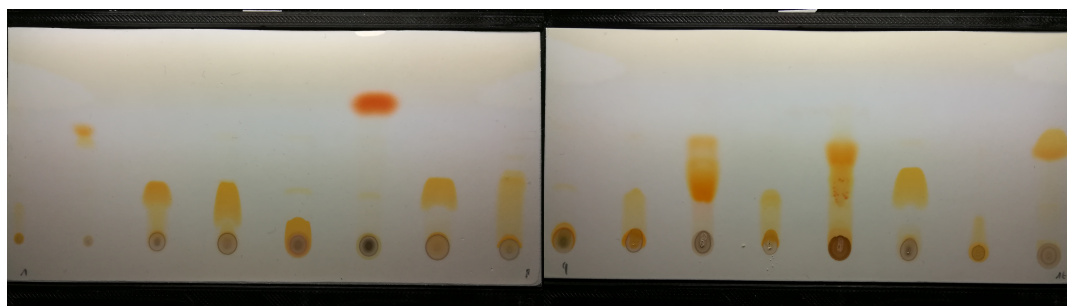


**Figure 2.62** Automated thin layer chromatograms of reactions between ferrocenoyl chloride (**105**) and amines **109** to **123**. Using automated sampling, optimal gradients for subsequent automated column chromatography could easily be determined.

To quickly confirm product formation, a TLC plate with good separation (PE/EA 4:1) was subjected to TLC-MS analysis. The expected products are shown in **Figure 2.63**, For all but one reaction (amine **120**), the correct  $m/z$  values were found (**Table 2.16**), providing a level of confirmation for the upcoming MPLC gradient programming.

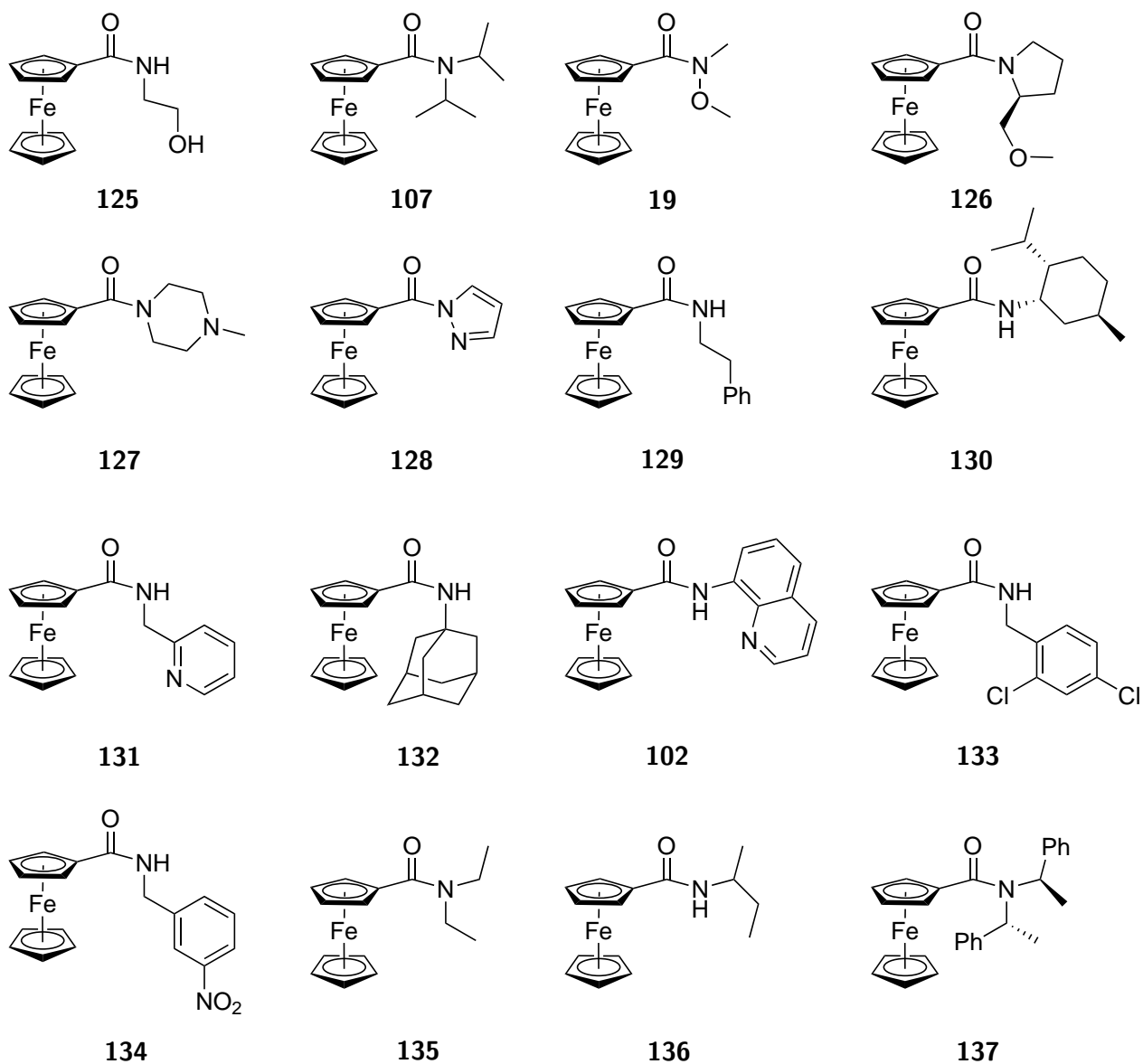


**Figure 2.63** Expected amide products, later confirmed by TLC-MS from automatically generated thin-layer chromatograms.



**Table 2.16** Semi-automated TLC-MS analysis of crude reaction mixtures.

Rxn ID	Product	M (g mol <sup>-1</sup> )	m/z (APCI+)	Interpretation
alr_01	125	273.1	274.5	[M+H] <sup>+</sup>
alr_02	107	313.2	314.7	[M+H] <sup>+</sup>
alr_03	19	273.1	274.6	[M+H] <sup>+</sup>
alr_04	126	327.2	328.7	[M+H] <sup>+</sup>
alr_05	127	312.2	313.7, 354.8	[M+H] <sup>+</sup> , [M+MeCN+H] <sup>+</sup>
alr_06	128	280.2	281.5	[M+H] <sup>+</sup>
alr_07	129	347.3	348.8	[M+H] <sup>+</sup>
alr_08	130	367.4	368.8	[M+H] <sup>+</sup>
alr_09	131	320.3	321.7	[M+H] <sup>+</sup>
alr_10	132	377.4	378.8	[M+H] <sup>+</sup>
alr_11	102	356.3	357.8	[M+H] <sup>+</sup>
alr_12	133	388.2	388.7, 390.7	[M+H] <sup>+</sup> (Cl isotopes)
alr_13	134	364.3	272.5	[FcCOOH+MeCN+H] <sup>+</sup>
alr_14	135	285.3	286.7	[M+H] <sup>+</sup>
alr_15	136	285.3	286.6	[M+H] <sup>+</sup>
alr_16	137	437.5	438.9	[M+H] <sup>+</sup>

In the original run, prepurification was carried out by precipitation of ammonium chlorides (mainly triethylammonium chloride) using ethyl acetate, followed by automated vacuum filtration under protective atmosphere. Since liquid-liquid extraction is a common method in synthetic organic chemistry, it was decided to test the capability of the ASW 2000P to perform this operation on the crude mixtures obtained in the present run. As explained in **Section 2.1.1**, this workflow is in principle enabled by strong vortex mixing in combination with dispense/aspiration cycles using pre-set needle heights. After extraction, an automated filtration step over MgSO<sub>4</sub> was envisaged for all reactions, testing the *solid phase extraction* (SPE) functionality of the synthesizer.

To obtain constant layer heights throughout all vials, crude reaction mixtures were first evaporated to dryness, and 2 mL of dichloromethane were then added to each vial. The needle height for phase separation was pre-programmed using a calibration table provided by CHEMSPEED within the user manual of the parallel synthesizer (**Figure 2.64**).

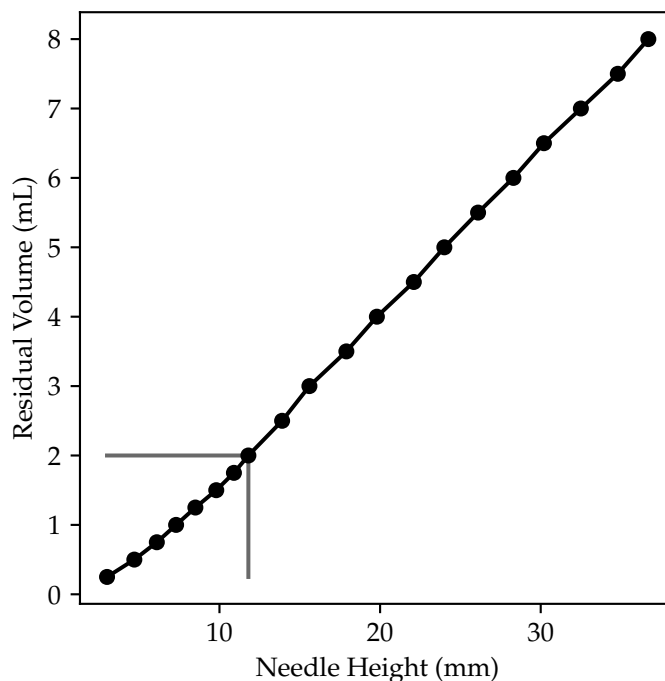


**Figure 2.64** Plot of residual volume vs. needle height in the parallel synthesizer. In the current run, the phase boundary was expected at 11.8 mm, corresponding to 2 mL DCM in the lower phase.

After initial DCM addition, hydrochloric acid ( $1 \text{ mol L}^{-1}$ ) was added and reactors were vortexed vigorously at 1000 rpm for 1 min. After a 5 min phase separation, mixtures were inspected visually. Unexpectedly, phase boundary locations differed significantly throughout reaction vials. Additionally, in two cases strong coloration was observed in the upper layer instead of the lower one. In run **alr16\_06**, the organic phase containing the product unexpectedly separated above the aqueous one. In run **alr16\_09** on the other hand, the product had migrated to the upper aqueous phase. This is explained by the product **131** bearing a basic pyridyl group which was likely protonated after acidic workup (**Figure 2.65**). Both cases required manual intervention.

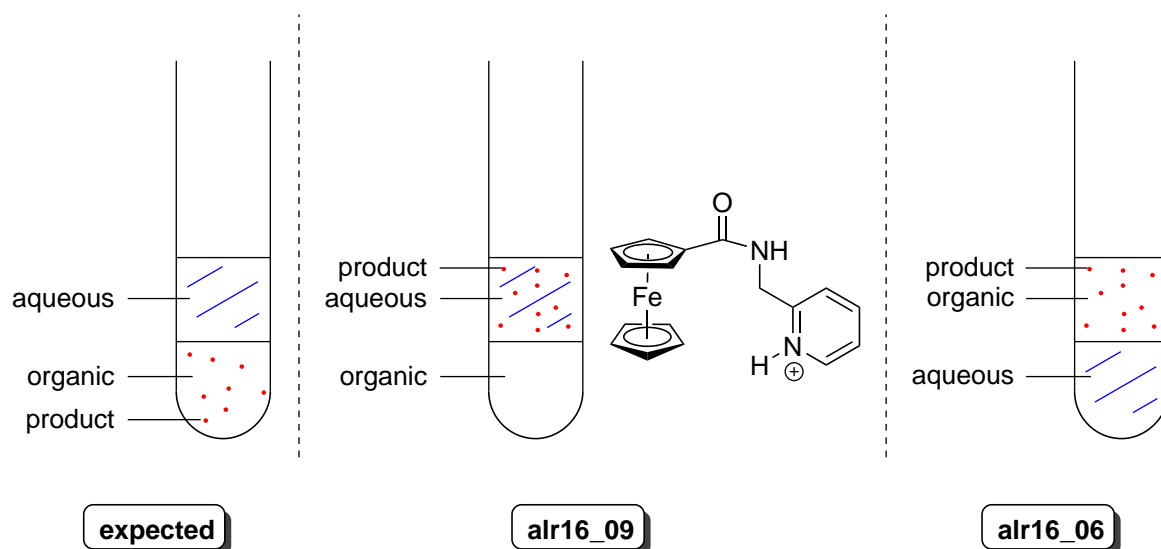


**Figure 2.65** Expected behavior of reaction mixtures during liquid-liquid extraction, and unexpected behavior in the cases of **alr16\_09** (product migration into upper aqueous phase) and **alr16\_06** (organic phase above aqueous).

Subsequent aspiration of aqueous phases was not trivial, due to differing layer heights as mentioned above. As a result, some of the organic layer was lost in most cases. In future runs, an additional safety margin for needle heights and solvent amounts should be considered to avoid unnecessary waste of product. Similarly, aspiration speeds need to be low to prevent unwanted organic phase aspiration. Separated phases should be stored in designated intermediary vials in case of malfunction. The following washing steps with  $\text{NaHCO}_3$  and brine proceeded smoothly.

The last automated purification step consisted of filtration over  $\text{MgSO}_4$  using the SPE rack of the synthesizer. 1 mL cartridges were filled with approx. 200 mg of  $\text{MgSO}_4$  and placed into the rack. A sequence was programmed to first prime the cartridges with DCM, discarding the eluate. This was followed by application of products and an elution/washing step with pure DCM. Again, differing layer heights became an issue. If only a small amount of water was aspirated, this was dispensed first onto the  $\text{MgSO}_4$  cartridges, immediately clogging the filter and not allowing any DCM solution to pass through. It is crucial to observe actual layer heights and to program large safety margins in order to avoid such errors. Resulting inaccuracies can be compensated for by adding more washing steps to recover most of the products. In this run, clogged  $\text{MgSO}_4$  suspensions were broken up manually with a spatula. When only organic phase was dispensed to the cartridges, filtration proceeded as expected without issues.

Filtrates were collected automatically in 8 mL vials and directly evaporated in parallel using a BUECHI Syncore. Vials were gently placed into 50 mL collection tubes and heated to  $40^\circ\text{C}$ . A vacuum gradient was programmed to slowly evaporate the bulk DCM and then completely dry the crude products.

Next, crude products were subjected to automated MPLC purification. From automated TLC runs at different polarities, two standard gradients (“non-polar”, “polar”) were programmed. Crude products were suspended in starting eluent by sonication, applied to a 10 mL loop and injected onto the column. After automated product separation using UV detection, product solutions were concentrated, transferred to 8 mL sample vials and concentrated again to dryness. After treating the first few samples classically on the rotary evaporator, the last evaporation step became a serious bottleneck, which is shown in **Figure 2.66**.

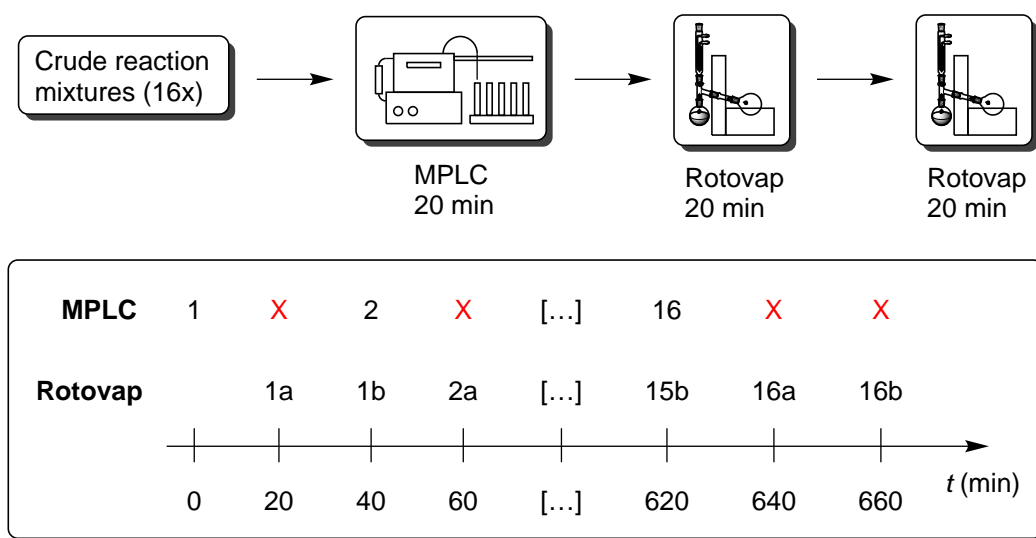


**Figure 2.66** Single evaporation workflow for the purification of amide reaction products. Sample numbers at each time step are shown for both MPLC and rotovap (a: concentration step, b: evaporation to dryness in storage vials). The involvement of the rotary evaporator in two separate steps creates a serious bottleneck.

Crude mixtures were subjected to automated chromatography, which yielded a single fraction of clean product. The product solution was concentrated on the rotary evaporator, transferred to a storage vial and then evaporated to dryness, again on the rotary evaporator. Each step took about 20 min to complete, and with only a single rotary evaporator available, throughput was seriously hindered.

To alleviate this bottleneck, the capabilities of the BUECHI Syncore were again leveraged, and a new workflow was designed (**Figure 2.67**).

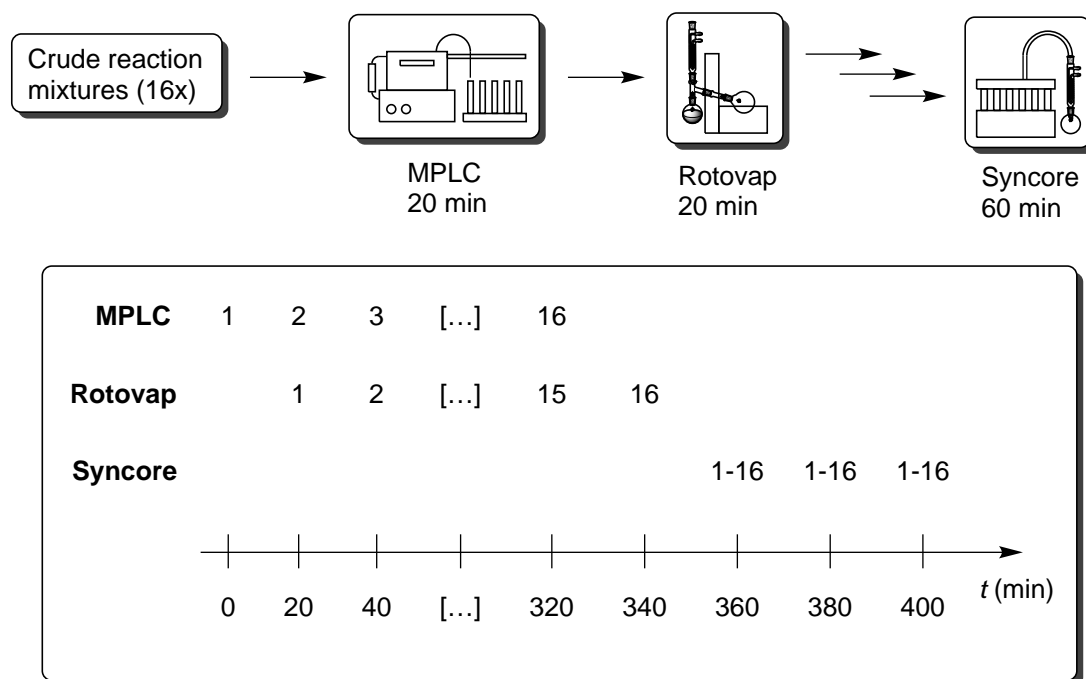


**Figure 2.67** Improved workflow based on the BUECHI Syncore. Samples are chromatographed and concentrated first, and then evaporated in batch.

Instead of evaporating samples to dryness right after concentration, they were only concentrated at first, transferred to storage vials and left to stand. The viability of this decision was supported by the stability of almost all compounds even on TLC plates over night. At the end, all vials were placed into the BUECHI Syncore, and evaporated in parallel.

The duration of the original procedure was calculated as

$$20 \text{ min} + 15 \cdot 40 \text{ min} + 40 \text{ min} = 660 \text{ min.}$$

With the new workflow, the duration was determined as

$$20 \text{ min} + 15 \cdot 20 \text{ min} + 20 \text{ min} + 60 \text{ min} = 400 \text{ min,}$$

resulting in a time saving of 39 %, or 4 h 20 min.

Using the second approach, all samples were isolated in three days, including training of a student on the MPLC device. All products were characterized using standard techniques such as NMR, HRMS and IR. Isolated yields are shown in **Table 2.17**.

**Table 2.17** Summary for reaction products of ferrocenyl amide library synthesis.

Reaction ID	Group	New	Yield (%)	Mass (g)
alr16_01	multidentate	–	0	0
alr16_02	simple alkyl	no <sup>[111]</sup>	12	15
alr16_03	functionalizable	no <sup>[112]</sup>	18	20
alr16_04	chiral	yes	50	65
alr16_05	drug-like	no <sup>[113]</sup>	19	24
alr16_06	multidentate	yes	47	53
alr16_07	alkylaryl	no <sup>[114]</sup>	38	53
alr16_08	chiral	yes	26	38
alr16_09	multidentate	no <sup>[115]</sup>	13	17
alr16_10	drug-like	no <sup>[116]</sup>	35	53
alr16_11	multidentate	no <sup>[102]</sup>	41	58
alr16_12	alkylaryl	yes	35	54
alr16_13	alkylaryl	yes	22	32
alr16_14	simple alkyl	no <sup>[117]</sup>	42	60
alr16_15	simple alkyl	yes	41	63
alr16_16	chiral	yes	67	97

Except for one reaction (**alr16\_01**, ethanolamine (**109**)), all runs gave the expected products in reasonable quantities for the following C-H activation step, albeit yields were generally moderate (12% – 67%, 15 mg – 97 mg). In order to find trends in reactivity, group yields were plotted and are shown in **Figure 2.68**.

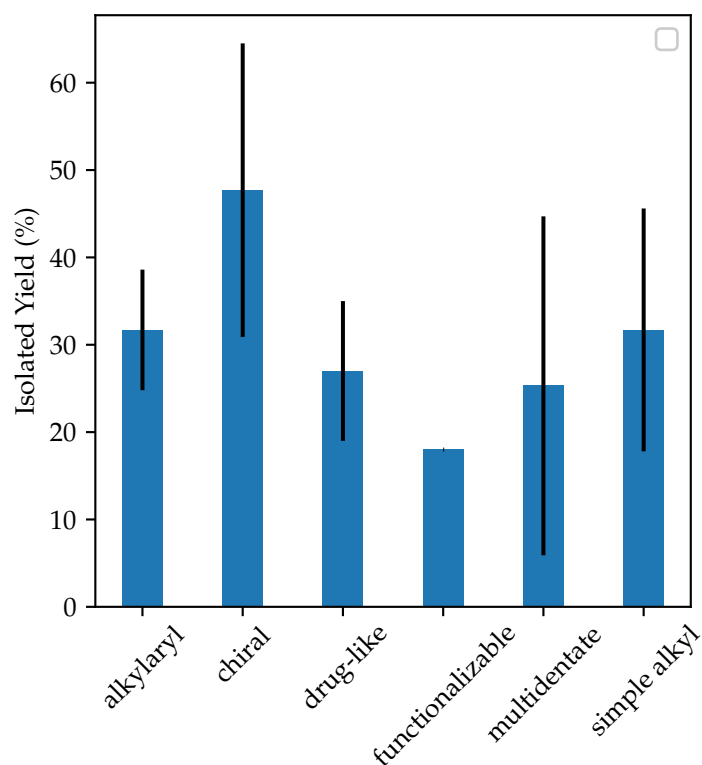
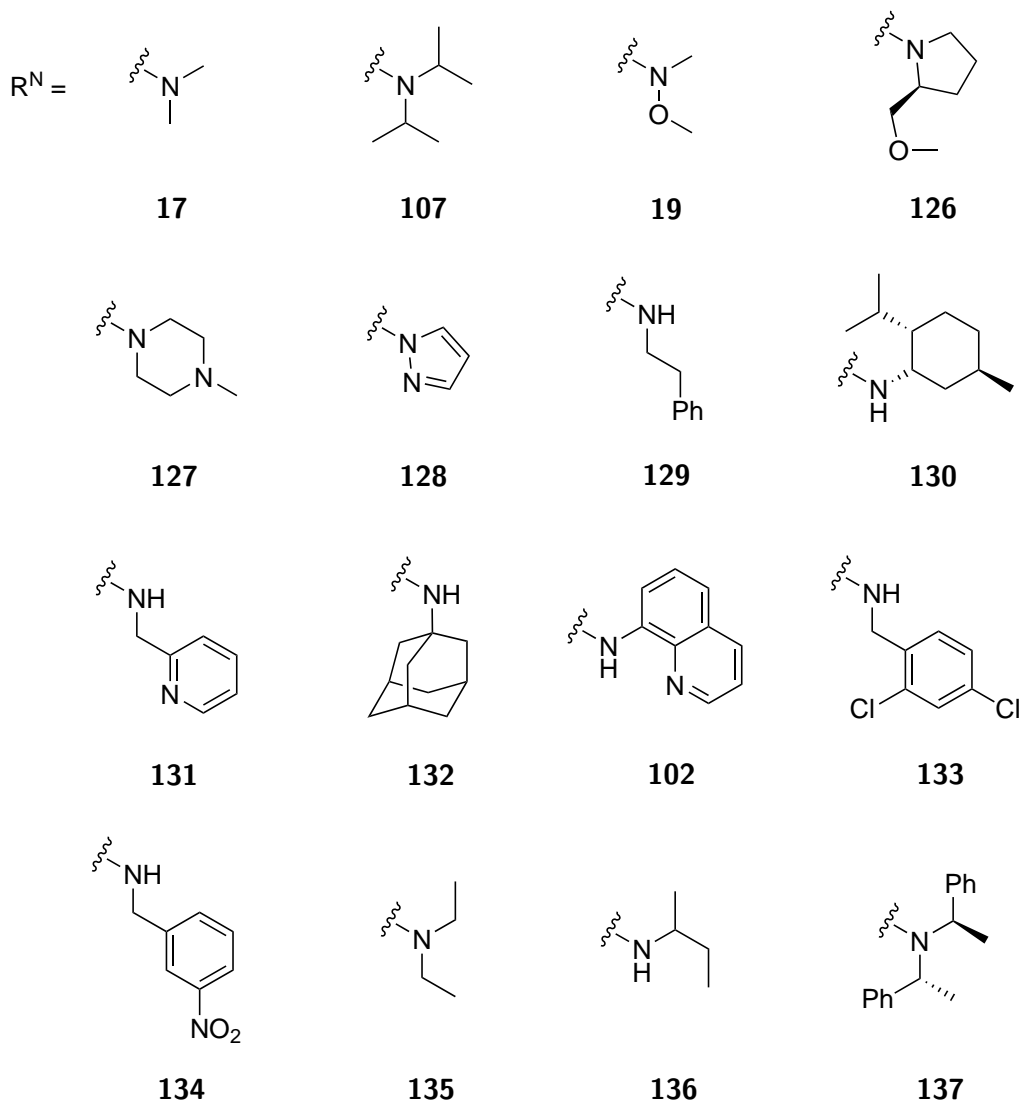
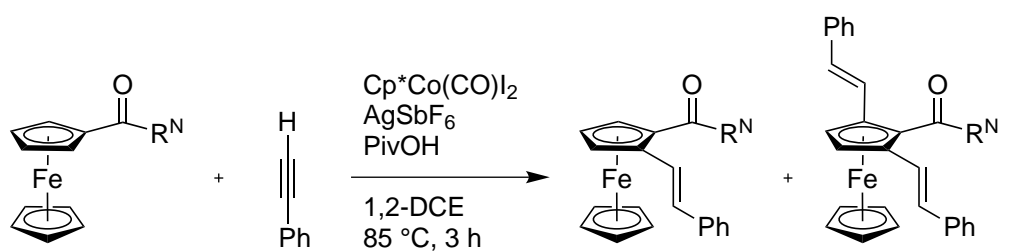


**Figure 2.68** Group yields for ferrocenyl amide library synthesis with standard deviations.

Chiral amines gave the highest group yields, followed by simple alkyl- and alkylaryl amines. The low yield of the functionalizable WEINREB amide was accompanied by a large amount of leftover starting material as well as some demethylated side products. The large variance in the multidentate group arises from the difficulties during workup described in **Figure 2.65**. Of the 15 successfully synthesized ferrocenyl amides, 7 were new compounds, which were fully characterized.

### Library Compounds in Cp\*Co(III)-Catalyzed C-H Activations

Following their synthesis described above, all ferrocenyl amides were tested for their reactivity in Cp\*Co(III) catalyzed C-H activations. The missing derivative **125** was replaced with *N,N*-(dimethylcarbamoyl)ferrocene (**17**), which had successfully been applied in our group<sup>[37]</sup> and served as a reference substrate. Standard conditions were taken from the same publication, and the resulting reaction design is shown in **Scheme 2.22**. It must be noted that the original heating medium temperature was lowered from 100 °C to 85 °C to account for the lower reflux capacities of the ASW 2000P. The full selection of ferrocenyl carbamides included compounds **17**, **19**, **102**, **107**, **126**, **127**, **128**, **129**, **130**, **131**, **132**, **133**, **134**, **135**, **136** and **137**.



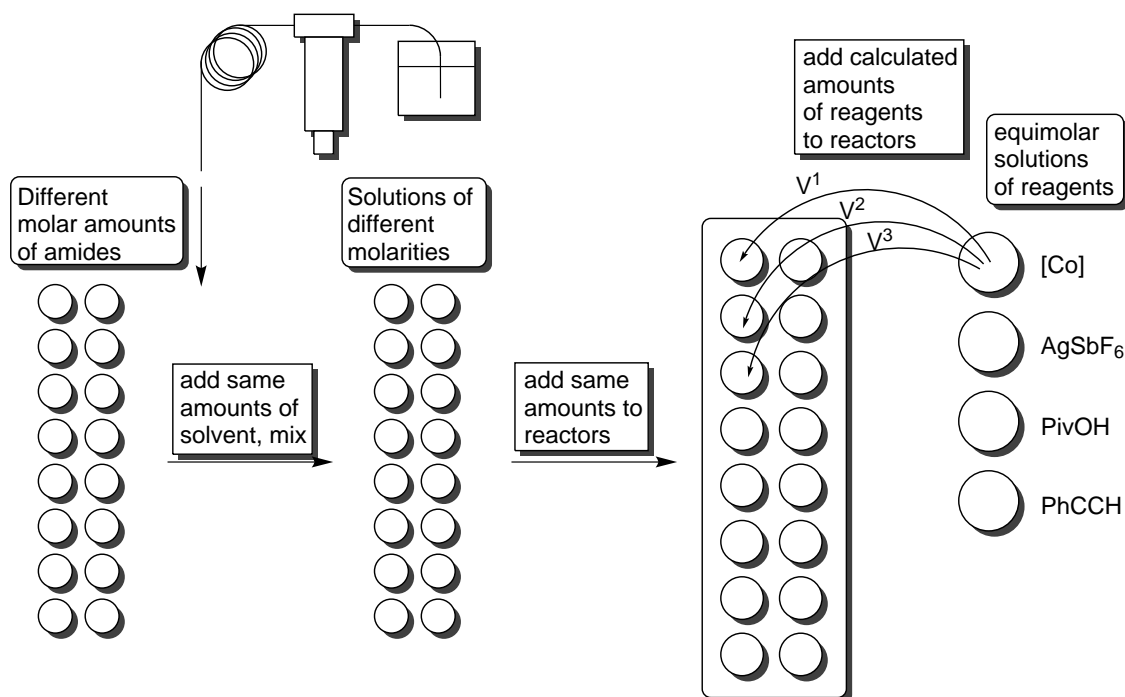
**Scheme 2.22** Reaction design for C-H activation screening of ferrocenyl amide library.

The library of starting materials was available in solid (or oil) form in 8 mL vials after evaporation on the SYNCORE (**Figure 2.67**). Preparing the following screening, the question arose how to optimally design the experiment in a way that would require minimal handling of substances as well as minimal programming effort. As shown in **Table 2.17**, starting materials



were available in significantly differing amounts. The main priority was to avoid an extra weighing step of the starting materials, which would not only be unnecessary since the vials were already compatible with the synthesizer, but also difficult in case of oily substances or those available only in small amounts.

One possible solution would have been to dilute all amides in different amounts of solvent to create equimolar solutions, then add different volumes to the reactors so that each amide is present in the same molar amount. This has the obvious disadvantage of creating large amounts of solutions that will later have to be evaporated again, as well as constraining everything to the amide available in the lowest quantity. Instead, it was decided to dilute all amides in the same amount of solvent (1000  $\mu\text{L}$ ) and add the entire amount to the reactors, providing different molar amounts for each amide. Amounts of all other reagents were calculated so that 1) the correct relative amounts would be dispensed to each amide and 2) the same amounts could be used across all reagents according to their stoichiometries. Actual diluent volumes were chosen so that total reaction volumes would be within the usable range of the ASW 2000P (approx. 500  $\mu\text{L}$  – 5000  $\mu\text{L}$ ). The workflow is shown in **Scheme 2.23**.



**Scheme 2.23** Concept for reagent dilution and addition.

Choosing the above sequence provided several advantages over other alternatives. From a programming standpoint, amides could be added in a single *aliquot* task, while only a single *aliquot different volumes to zone* task had to be created for all other reagents, since the method could be copy-pasted after entering the correct volumes once. Additionally, an extra

weighing step was avoided and all amides were used according to their available quantities. The necessary inclusion of a safety volume, which remains in the stock vials, facilitated the generation of reserve samples for later comparative analysis.

Having established this procedure, all amides in **Scheme 2.22** were subjected to Cp\*Co(III)-catalyzed C-H activation conditions using an excess of 2.5 equiv. of phenyl ethyne (**30**). Amide storage vials were placed into the tray, and DCE was aliquoted automatically in two steps to allow for dissolution. All vials were inspected visually and sonicated manually if necessary. Amide solutions were placed back into the ASW 2000P, and reagents were added in the correct order to ensure catalyst pre-formation. Samples were incubated over night, after which automated TLC sampling was carried out (**Figure 2.69**). TLC plates were then subjected to TLC-MS analysis for quick identification of starting materials and different products.

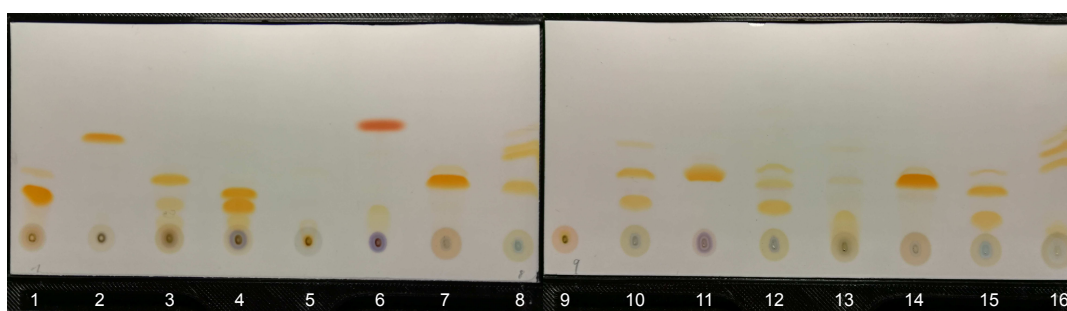


**Figure 2.69** Automated TLC plates for C-H activation screening. New products visible on lanes 1, 2, 3, 4, 7, 8, 10, 12, 14, 15 and 16.

Of all 16 reactions, 11 showed the formation of at least one new compound, the  $m/z$  values of which pointed to the expected C-H activation products in different degrees of substitution. Reaction mixtures were recovered by the parallel synthesizer and evaporated in parallel using the *Syncore*. Again, a standard gradient for automated flash chromatography was developed, and samples were treated directly with the newly developed workflow for parallel chromatography and evaporation (**Figure 2.67**). In total, 14 fractions were collected from all reactions (**Table 2.18**).

**Table 2.18** Overview of C-H activation screening results.

No.	Compound	Yield (%)	Identity
cal16_01-1	<i>rac</i> - <b>31</b>	79	Monosubstituted
cal16_02-1	<i>rac</i> - <b>138</b>	51	Monosubstituted
cal16_03-1	<i>rac</i> - <b>139</b>	45	Monosubstituted
cal16_03-3	<b>140</b>	9	Monosubstituted, Demethylated
cal16_04-1	<b>141</b>	21	Monosubstituted, Single Diastereomer
cal16_04-2	<b>142</b>	27	Monosubstituted, Single Diastereomer
cal16_07-1	<i>rac</i> - <b>143</b>	48	Monosubstituted
cal16_08-1	<b>144</b>	52	Monosubstituted, Mix of Diastereomers
cal16_10-1	<b>145</b>	2	Disubstituted
cal16_10-2	<i>rac</i> - <b>146</b>	16	Monosubstituted
cal16_12-2	<i>rac</i> - <b>147</b>	5	Monosubstituted
cal16_14-1	<i>rac</i> - <b>148</b>	85	Monosubstituted
cal16_15-1	<i>rac</i> - <b>149</b>	21	Monosubstituted
cal16_16-1	<b>150</b>	21	Monosubstituted, Mix of Diastereomers

The vast majority of successful reactions selectively led to the formation of racemic monosubstituted products. The isolated yield of *rac*-**31** from reference reaction **cal16\_01-1** corresponds well to those obtained manually,<sup>[37]</sup> hinting towards a good transferability of these reactions from manual to automated. Disubstituted product could only be isolated in the case of compound **151**, although they have been observed in multiple cases on TLC. Reactions with chiral ODGs (**cal16\_04**, **08** and **16**) led to the formation of diastereomeric mixtures, and in the case of **cal16\_04** they could be separated directly during the first automated chromatography. All isolated products are new compound and are shown in **Figure 2.70**.

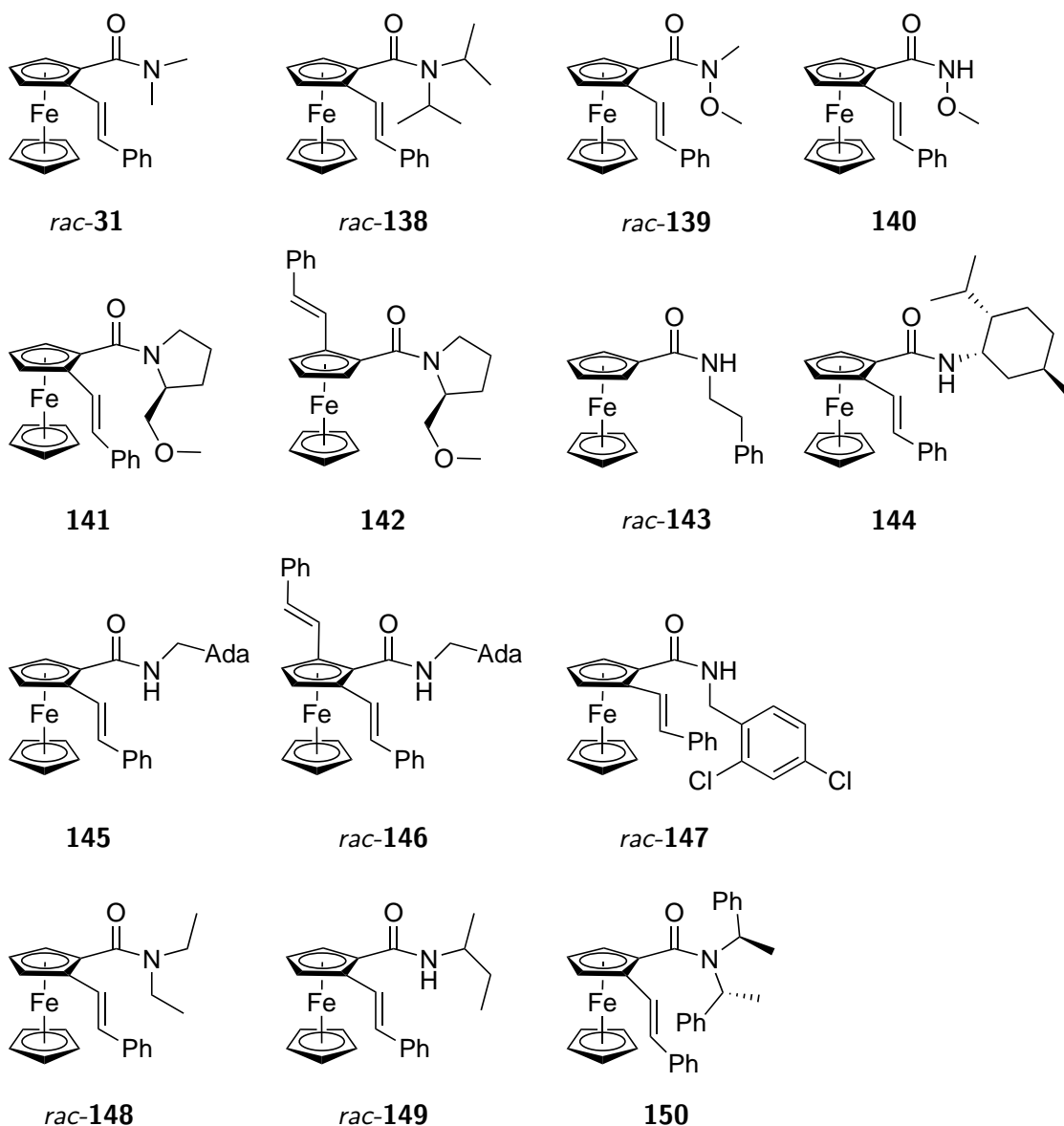


**Figure 2.70** Isolated products obtained in C-H activation screening. Exact identity of products **141** and **142** not known.

To gain a more detailed overview, yields were again plotted against the different ODG groups. The plot is shown in **Figure 2.71**.

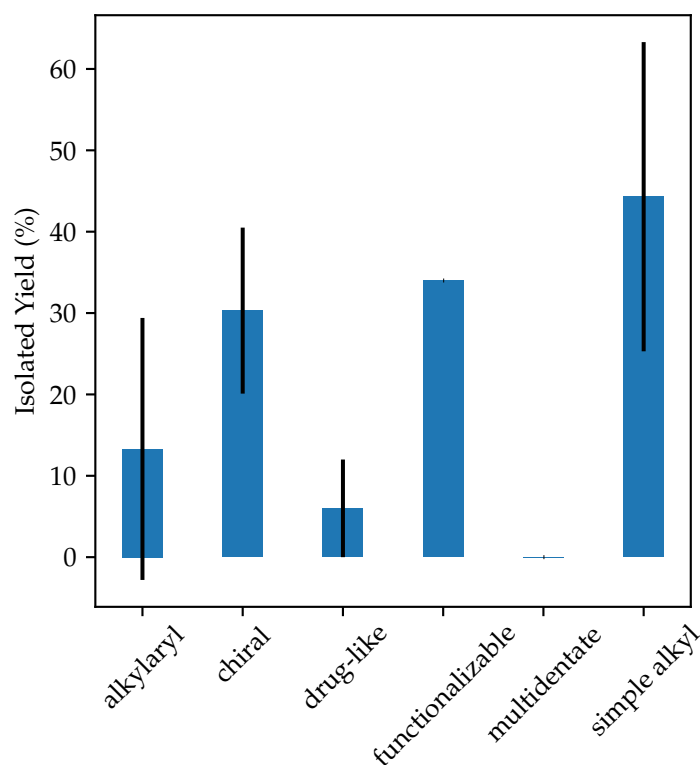


**Figure 2.71** Group yields for C-H activation screening. Only yields for monoalkenylated main products were considered.

While amide yields were more or less consistent throughout the different groups, their behavior in C-H activations depended strongly on the nature of the ODG. Evidently, simple alkyl derivatives showed the highest overall conversion, followed by chiral ODGs which are also unfunctionalized in most cases. As expected,<sup>[112]</sup> the functionalizable compound **19** was formed in relatively high yield, too. Alkylaryl ODGs gave mixed results, which may be due to suboptimal solubilities of some of these compounds. Yields for drug-like ODGs were generally low, likely reasons being the extra coordinating nitrogen atom of compound **127** and the large steric demand of compound **132**. Finally, none of the multidentate directing groups led to the formation of any product at all. This was surprising, as the reaction of compound **102** under similar conditions in moderate yield had been reported before in the group of BUTENSCHÖN,<sup>[37]</sup> albeit at higher temperatures (**Figure 2.72**). Within those studies, it had already been found that increasing the oil bath temperatures well above the boiling point of the solvent can lead to dramatic increases in yield. In the present, automated example, lowering reaction temperatures according to the limits of the equipment lead to the complete absence of product.

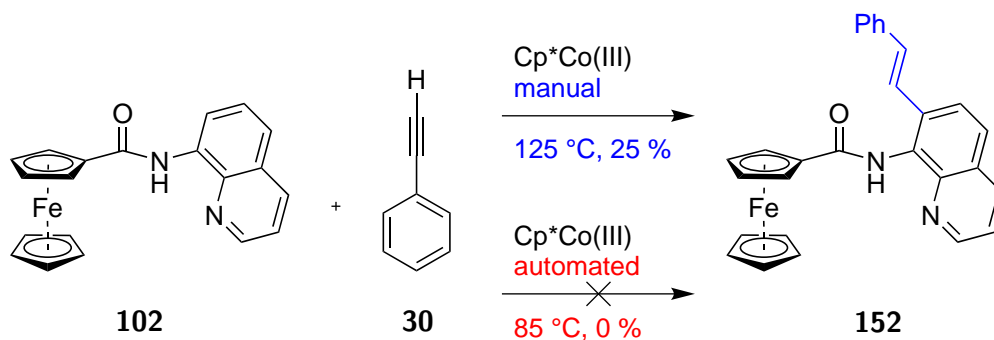


**Figure 2.72** Absence of reaction at lower temperatures due to a constraint of the automated equipment.

In discussions on whether to implement automated methods or not, edge cases like the present one are sometimes used as evidence against automation. However, the main takeaway should be that more robust and versatile equipment must be developed in order to enable conditions like efficient condensation even at reaction temperatures well above the boiling point of the solvent.

Within the group of ferrocenes bearing chiral ODGs, possible diastereoselectivities were investigated. Compound **126** gave the diastereomers **141** and **142** in 21% and 27% yield, respectively, corresponding to *d.r.* = 1.3 : 1. Given the low substance quantities, this low selectivity might well be within the range of error and is not deemed significant. The reaction of compound **130** gave a mixture only partly separable by column chromatography. Again, no significant diastereoselectivity was observed in this case.

The diastereomers resulting from the transformation of amide **137** were first submitted to QTLC for determination of diastereoselectivity. Although this method is not strictly suitable due to possible differences in extinction coefficients, similar techniques such as HPLC are sometimes used as a first, crude estimate. A sample of crude reaction mixture was provided to the ASW 2000P, and automated QTLC was performed. Using triple determination, the diastereomeric ratio was estimated as *d.r.* =  $2.0 \pm 0.1$  : 1. After a first column chromatography, the purified mixture of diastereomers was investigated by HNMR. Interestingly, integration of cyclopentadienyl protons pointed to *d.r.* =  $5.4 \pm 0.3$  : 1. After two more chromatographic runs in an attempt to isolate the pure diastereomers, only one was left due to decomposition on silica. This explains the increasing *d.r.* values obtained at different points during purification, pointing to a similar decomposition rate for both isomers. The initially obtained value of 66.2% seems to best reflect reality in this instance. For further separation attempts, it may be necessary to determine the *d.r.* value directly from the crude mixture *via* HNMR analysis.

## Conclusion and Outlook

Using the automated workflows described above, the entire synthetic part of the investigation was carried out in 16 workdays, mostly by a single student. This included training of the student on all technical devices, manual synthesis of FcCOCl (**105**), a single manual test run, all planning, starting material selection and sourcing, charge calculation, robot programming, execution, workup, MPLC purification and sample preparation for full characterization, for both the library synthesis and the C-H activation test runs. 15 out of 16 ferrocenyl amides were synthesized in reasonable quantities for the following C-H activation step despite testing new unit operations such as liquid-liquid extraction and filtration on the SPE rack. Of those 15 compounds, 7 were literature-unknown and fully characterized. C-H activations gave 14 additional new compounds, most of which were expected products of a single *ortho*-alkenylation. Trends in reactivity based on ODG substitution were investigated, and some diastereoselectivity was observed within the reaction of amide **137**.

Further investigations should extend not only to different directing groups, but catalysts, additives, solvents and even substrates. By leveraging statistical methods such as PCA combined with DoE, highly efficient designs could be generated to comprehensively examine reaction spaces and derive generalized theories on reactivities and selectivities within this field.

This investigation highlights the capability of the parallel synthesizer for organometallic library synthesis. By optimally combining the ASW 2000P, the ADVION TLC-MS plate express and the BUECHI Syncore, a streamlined workflow for synthesis, analysis and purification was established, enabling the generation of large numbers of derivatives suitable for systematic observations.

### 2.2.3 Towards Fe-Catalyzed C-H Activation

#### Introduction

While C-H activation using noble metals continues to be an increasingly important field, considerable effort is being put into developing first row transition metal-based transformations due to their decreased cost and toxicity.<sup>[118,119]</sup> The Cp\*Co(III)-catalyzed reactions discussed in this thesis are one example of first row transition metal cyclopentadienyl complexes being used as catalyst in these reactions.<sup>[120]</sup> With the parent compound Cp\*Co(CO)I<sub>2</sub> (**153**) showing a great substrate scope, its iron-based analogues CpFe(CO)<sub>2</sub>I (**154**) and Cp\*Fe(CO)<sub>2</sub>I (**155**) became of interest (**Figure 2.73**).

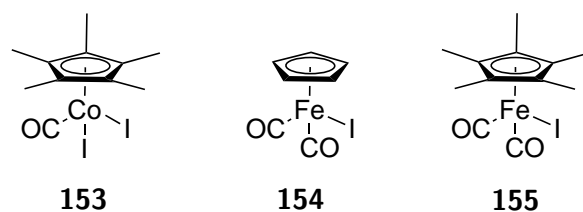
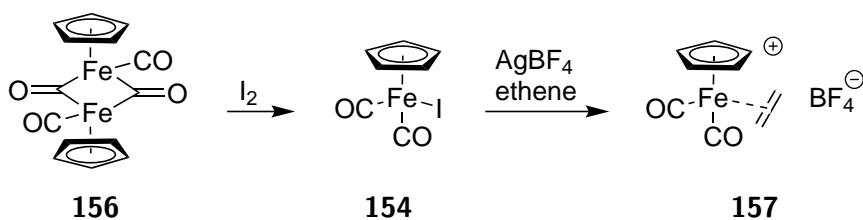


**Figure 2.73** Known C-H activation precatalyst **153**, and its iron-based analogues **154** and **155**.

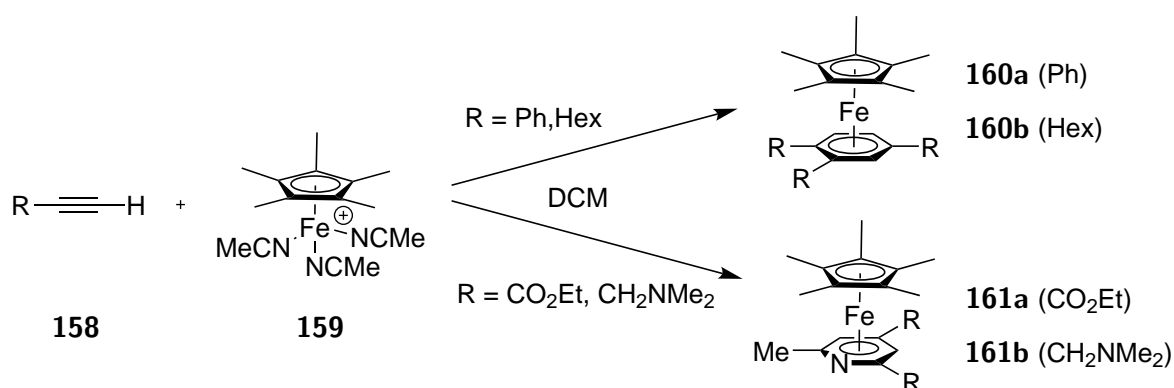
The CpFe system has been well investigated in the past, and the CpFe(CO)<sub>2</sub> group is so stable and well-defined in its reaction behavior, that it is usually abbreviated as Fp.<sup>[121]</sup> Starting from [CpFe(CO)<sub>2</sub>]<sub>2</sub> (Fp<sub>2</sub>, **156**), which is accessible from iron pentacarbonyl and cyclopentadienyl dimer, a large amount of various Fp<sup>-</sup> and Fp<sup>+</sup> species are accessible.<sup>[122]</sup> Of specific interest for this work is the ability of Fp<sub>2</sub> (**156**) to undergo oxidative cleavage to afford the halide derivative **154**, which can then undergo a LEWIS acid- or silver(I) mediated ligand exchange, yielding alkene complexes like **157** (**Scheme 2.24**).<sup>[121]</sup> The complexation of alkenes and alkynes by a cationic Cp<sup>\*</sup>M (M = transition metal) species is a key step in the catalytic cycle of Cp<sup>\*</sup>Co(III)-catalyzed C-H activations.<sup>[123]</sup>



**Scheme 2.24** FpI can undergo LEWIS acid or silver(I) mediated ligand exchange to afford alkene complexes,<sup>[124]</sup> which are key steps in Cp<sup>\*</sup>Co(III)-catalyzed C-H activation.<sup>[121,123]</sup>

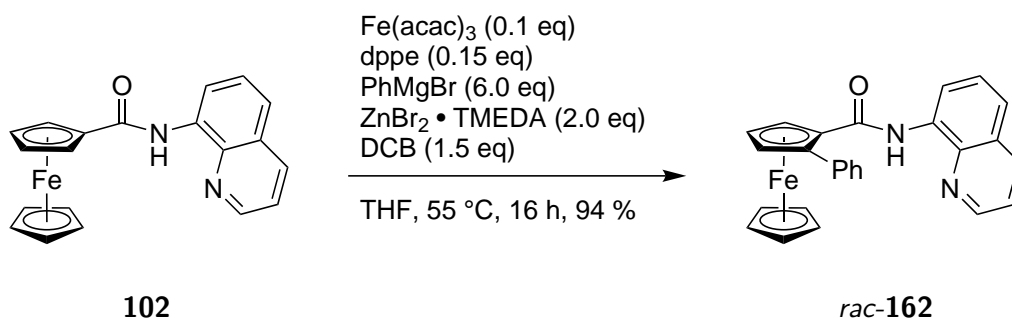
The chemistry of the Fp moiety has been extended to its pentamethylcyclopentadienyl analogue, Fp<sup>\*</sup>, as well.<sup>[124]</sup> It consists mainly of ligand exchange reactions at the free coordination site, often using phosphine<sup>[125]</sup> or coordinating solvent ligands.<sup>[126]</sup> Building on this, stoichiometric cyclotrimerizations of alkynes and metal-bound nitriles to benzenes and pyridines have been developed,<sup>[127]</sup> and extended to tandem Cp<sup>\*</sup>Fe/Cp<sup>\*</sup>Co cocatalyst systems (**Scheme 2.25**).<sup>[128]</sup>





**Scheme 2.25** Selective cyclotrimerization of alkynes **158a** – **158d** and metal-bound nitriles to complexed benzenes **160a**, **160b** and pyridines **161a**, **161b** using stoichiometric  $\text{Fp}^*$  systems.<sup>[127]</sup>

While a number of iron-catalyzed C-H activation reactions have been reported, the field is by far not as developed as that of noble metal catalysis, and suitable, general ligand systems are still to be discovered.<sup>[129]</sup> Often,  $\text{FeCl}_3$  or  $\text{Fe}(\text{acac})_3$  are used as catalysts, and some examples for directed *ortho* functionalizations similar to those with  $\text{Cp}^*\text{Co}(\text{III})$  have been reported,<sup>[130]</sup> one from the group of BUTENSCHÖN.<sup>[102]</sup> Here, a bidentate ODG-bearing ferrocene **102** is reacted with an *in situ*-generated zinc-organic reagent to yield the racemic, *ortho*-functionalized derivative *rac*-**162** (Scheme 2.26).



**Scheme 2.26** Iron-catalyzed, *ortho*-directed C-H activation at ODG-bearing ferrocene **102** using *in situ*-generated zinc GRIGNARD reagents.<sup>[102]</sup>

In contrast to this,  $\text{Fp}$ - and  $\text{Fp}^*$ -based systems (compounds **163** and **164**) often exhibit C-H activation behavior at ligands previously bound to the iron center. These ligands can be phosphites or even *N*-heterocyclic carbenes (NHCs), and C-H activation can occur at  $\text{sp}^2$ -<sup>[131]</sup> or  $\text{sp}^3$  centers,<sup>[132]</sup> leading to products such as **165** and **166** (Figure 2.74).

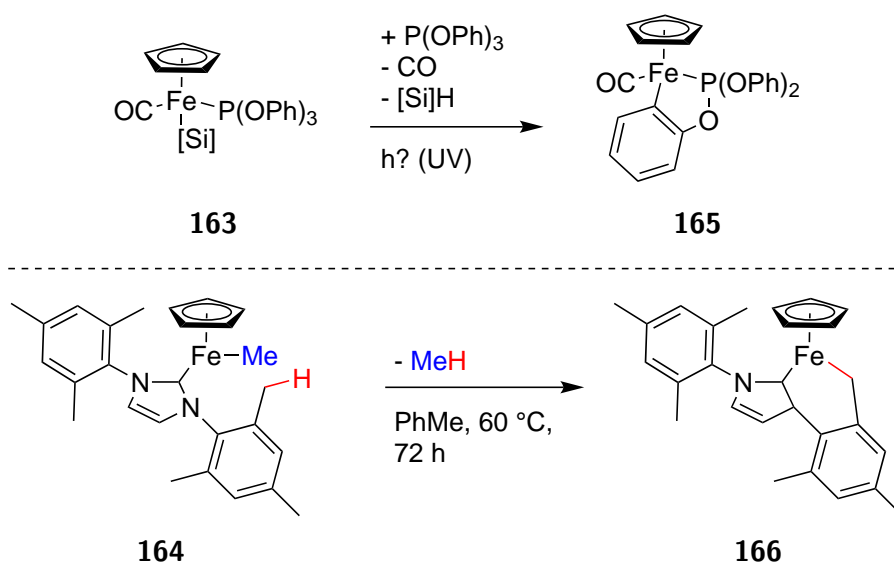
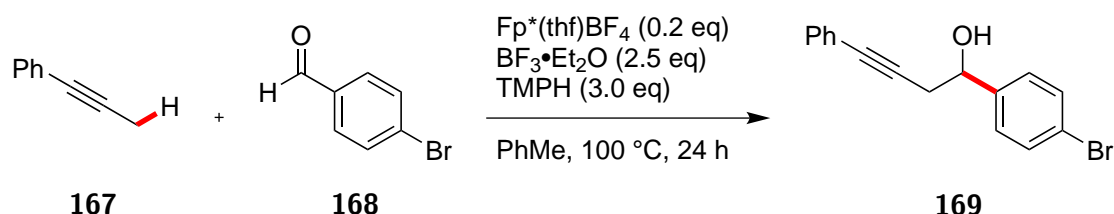


**Figure 2.74** Intramolecular C-H activation at ligands bound to the Fp and Fp\* center, respectively.<sup>[131,132]</sup>

Some recent, catalytic examples of Fp\*-based C-H activation have been reported by WANG *et al.* Using the cationic complex Fp\*(thf)BF<sub>4</sub>, alkynes have been functionalized at the propargylic position and coupled with aldehydes<sup>[133]</sup> and tetrahydroisoquinolines.<sup>[134]</sup> Again, the reaction relies on the complexation of alkynes by the free coordination site of the Fp\* moiety. For example, alkyne **167** is reacted with aldehyde **168** to yield product **169** through Fp\*-catalyzed sp<sup>3</sup> C-H activation (**Scheme 2.27**).

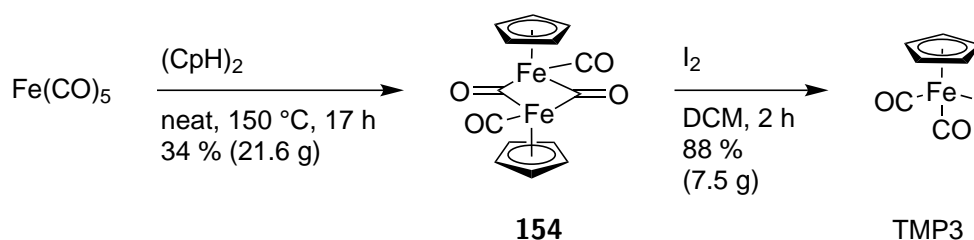


**Scheme 2.27** Recent examples of Fp\*-catalyzed C-H activation at propargyls..<sup>[133,134]</sup>

The literature precedent pointed to some trends, including an affinity of the Fp complex to alkenes and alkynes, which are typical substrates in Cp\*Co(III) chemistry. Since for CpFe-based systems, no general reaction conditions for *ortho*-directed C-H activation seemed available, this was seen as a good opportunity to explore another strength of a combined automation/DoE approach, which is the rapid navigation of unknown reaction spaces in search of new reactivities. Hence, the goal was set to investigate the behavior of the CpFe moiety in *ortho*-directed C-H activation reactions similar to those observed with Cp\*Co(III) systems.

## Automation/DoE Synergy for Rapid Reaction Space Exploration

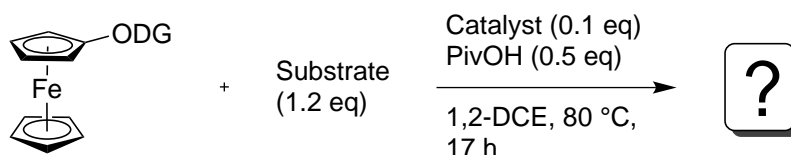
To begin, strong inspiration was taken from typical Cp\*Co(III) chemistry,<sup>[35]</sup> and it was decided to start with the CpFe analogue **154** of the well-known complex Cp\*Co(CO)I<sub>2</sub> (**153**). Investigations were started with the basic, unmethylated cyclopentadienyl group due to its significantly lower cost and availability. The complexes **156** and **154** were synthesized straightforwardly in multigram quantities using literature procedures **Scheme 2.28**.<sup>[135,136]</sup>



**Scheme 2.28** Literature-known synthesis of Fp dimer (**156**) and FpI (**154**).<sup>[135,136]</sup>

A multilevel categorical design was chosen, with the factors ODG, substrate and catalyst being investigated at four, four and two levels, respectively. All possible combinations were examined, leading to a total of  $4 \cdot 4 \cdot 2 = 32$  reactions, which corresponded to a single overnight run in the parallel synthesizer. The design is shown in **Table 2.19**, and the structures of all reagents included in the design are given in **Figure 2.75**.

**Table 2.19** Reaction design for the investigation of Cp\*Co(CO)I<sub>2</sub> (**153**) as catalyst for C-H activation.



Factor	Levels	Settings
ODG	4	Acetyl-( <b>38</b> ), 2-Pyridyl-( <b>16</b> ), Dimethylcarbamoyl-( <b>17</b> ), 2-Oxazolinyl-( <b>47</b> )
Substrate	4	phenylethyne ( <b>30</b> ), Tolane ( <b>170</b> ), Propargyl alcohol ( <b>171</b> ), <i>N</i> -Methylmaleimide ( <b>172</b> )
Catalyst	2	Fp dimer ( <b>156</b> ), FpI ( <b>154</b> ) + AgBF <sub>4</sub>

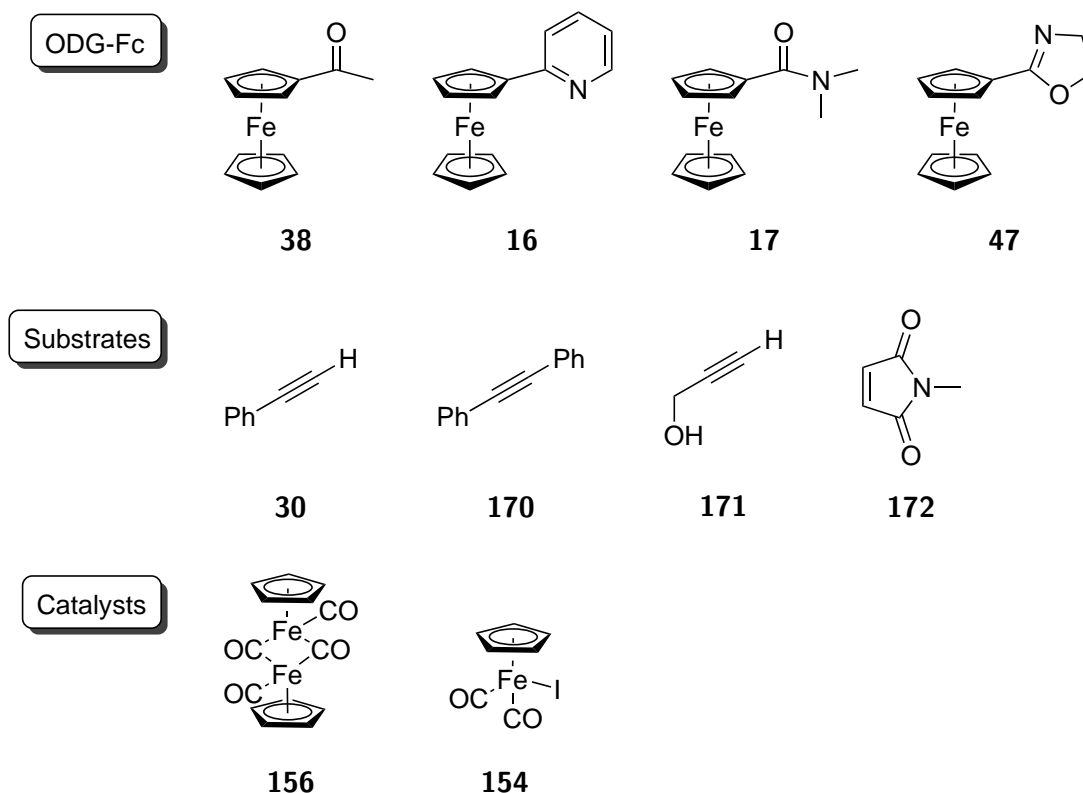
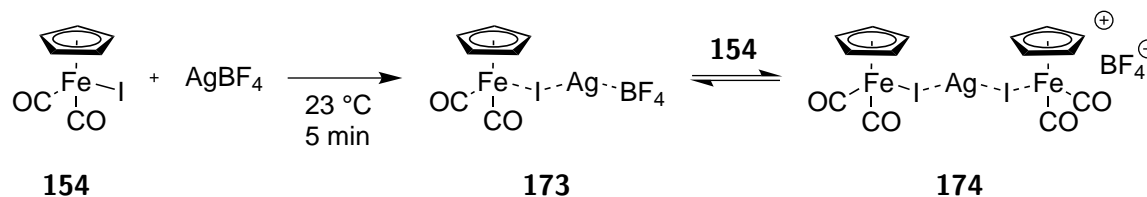


**Figure 2.75** Structures of reagents and catalysts selected for the first investigation of CpFe-based C-H activation reactivities. FpI (**154**) was used with an equimolar amount of AgBF<sub>4</sub>.

Reaction conditions strongly resembled those of typical Cp\*Co(III) reactions, using the cyclopentadienyl metal iodide in combination with a silver(I) salt to induce abstraction of iodide and freeing of the first coordination site. A short pre-conditioning time of 5 min was allocated for halide abstraction, since in cobalt-catalyzed reactions, this process was observed almost instantaneously after addition of the silver(I) salt. In Cp\*Co(III)-based catalysis cycles, the carbonyl ligand is then replaced with a pivalate group, therefore pivalic acid was provided as well. As fluorinated alcohols have shown a positive effect on C-H activation reactions,<sup>[137]</sup> 2,2,2-trifluoroethanol (TFE) was added to all reactions. 1,2-dichloroethane, a typical C-H activation solvent, was used near its boiling point, and the run was carried out over night.

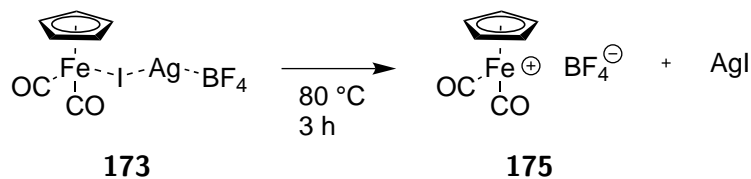
During reagent addition, some unexpected behavior was observed. After addition of AgBF<sub>4</sub> to all reactions with FpI (**154**), solutions turned from dark brown to bright orange, with no visible formation of AgI precipitate. An oxidation of the Fe(II) center to Fe(III) was considered, but should have led to a color change to greenish-blue, as known from the ferrocene-ferrocenium redox couple, as well as precipitation of elemental silver. Another explanation could be only partial halide abstraction, leading to mixed Fe(II)-Ag(I) complexes. This theory was confirmed by literature, as the metathesis reaction between FpI (**154**) and AgBF<sub>4</sub> had been mechanistically investigated before,<sup>[138]</sup> and was later applied to other combinations of metal

complex and silver(I) halide, confirming the formation of the suspected mixed complex **173** (Scheme 2.29).<sup>[139]</sup>



**Scheme 2.29** Formation of a mixed complex between FpI (**154**) and AgBF<sub>4</sub> instead of complete halide abstraction. The mixed complex **173** is in equilibrium with the dimeric form **174**.<sup>[138,139]</sup>

After subsequent addition of the ODG-bearing ferrocenes, reactions with (dimethylcarbamoyl)-ferrocene (**17**) turned green, indicating oxidation of the ferrocene Fe(II) center. This observation again pointed to unsuccessful halide abstraction by AgBF<sub>4</sub>, leaving active silver(I) in solution which is a strong oxidant. After stirring at 80 °C for several hours, however, the green color changed back to orange, and a colorless precipitate was visible in all reactions with FpI (**154**) as catalyst. Evidently, the mixed complex **173** was destroyed at elevated temperatures, leading to the originally envisioned formation of CpFe(CO)<sub>2</sub><sup>+</sup> and AgI (Scheme 2.30).



**Scheme 2.30** Formation of free Fp<sup>+</sup> **175** through complete iodide abstraction at elevated temperatures.

Automated TLC analysis was performed after 17 h of reaction time, and no clear indication was found for the formation of any of the expected C-H activation products. New, faint spots were observed in some of the reactions, but could not be definitively assigned to any single compound. For example, all reactions with the 2-oxazoliny ODG showed a new spot, a TLC-MS analysis of which pointed to some addition product between 2-oxazolinyferrocene (**47**) and either pivalic acid or TFE or both, which has been observed with carboxylic anhydrides.<sup>[140]</sup> This is highly speculative, however, and additionally, a structure with the exact *m/z* obtained could not be generated. After chromatographic purification of the combined crude reaction mixtures, no clean mass spectrum was obtained anymore, and the *m/z* peak of the starting material **47** appeared, pointing to decomposition of the presumably labile addition product on silica. Since the spots were not specific to any one reaction condition, no further effort was placed towards their identification.

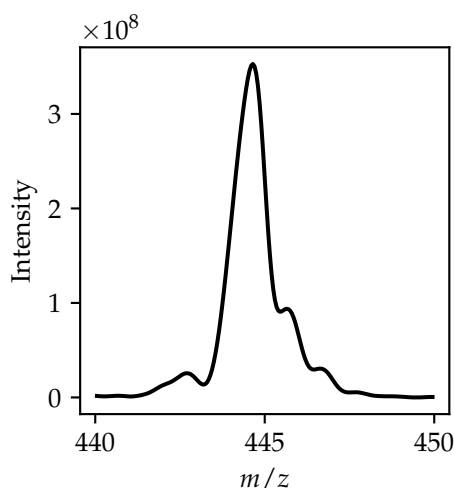
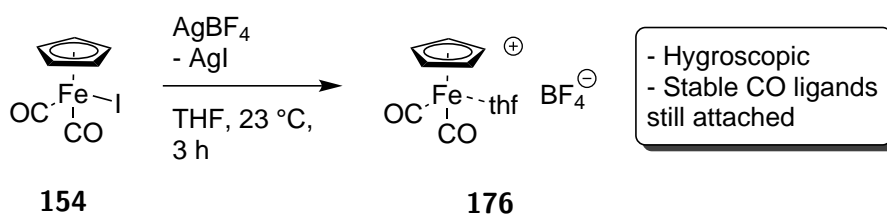


**Figure 2.76** Observed TLC-MS peak with typical ferrocene isotope pattern.

All other TLC spots were inconclusive after  $m/z$  and isotope pattern analysis, and were additionally present in such small quantities, that further investigation was not feasible.

Despite not resulting in the desired C-H activation, the experiment provided some important insight into Fp chemistry. Most notably, the abstraction of iodide from FpI (**154**) did not proceed as cleanly as envisioned, and harsher conditions were necessary. To address this, the use of the corresponding THF complex **176** was considered. It is synthesized by reacting FpI (**154**) with  $\text{AgBF}_4$  in tetrahydrofuran, which effectively outsources the halide abstraction step and provides the catalyst in a “pre-activated” form (**Scheme 2.31**).<sup>[141]</sup>



**Scheme 2.31** Attempted synthesis of  $\text{Fp}(\text{thf})\text{BF}_4$  according to COLEMAN *et al.*<sup>[141]</sup>

Product formation took place as expected, but during workup the compound proved to be highly hygroscopic, which made it somewhat unattractive as a catalyst. Furthermore, even with the halide removed, both carbonyl groups still remain attached to the iron center. It was believed that the stability of the carbonyl-iron bonds prevented the successful formation of intermediates necessary for C-H activation, and compound **176** would not alleviate this issue.

In the search for a Cp\*Fe complex with more labile ligands, inspiration was again drawn from Cp\*Co(III) chemistry, where the tris(acetonitrile) compound **177** has been used successfully in some C-H activation reactions (**Figure 2.77**).<sup>[142,143]</sup>

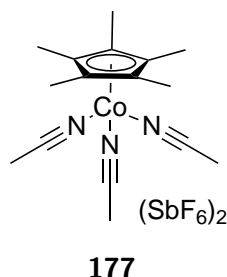
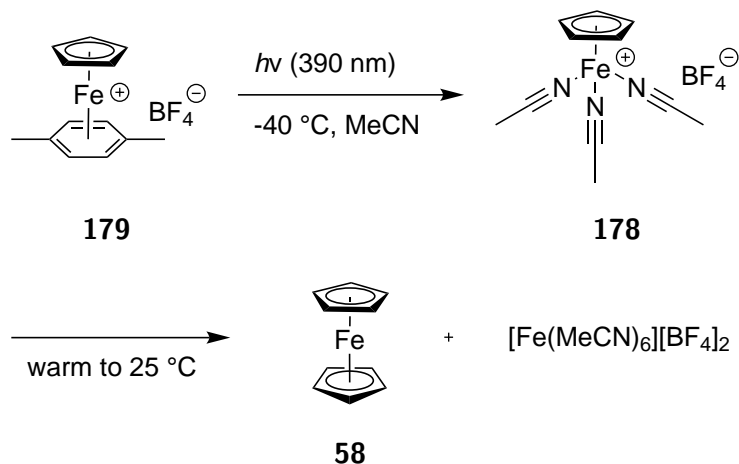


**Figure 2.77** Structure of Cp\*Co(MeCN)<sub>3</sub>(SbF<sub>6</sub>)<sub>2</sub> (**177**), a known C-H activation catalyst.<sup>[142,143]</sup>

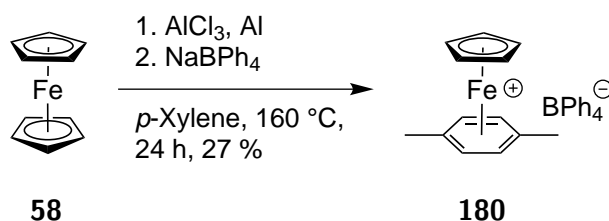
Acetonitrile complexes of transition metals are well known and have been thoroughly investigated.<sup>[144]</sup> For Cp\*Co(III) and Fp\*, complexation with acetonitrile yields thermally stable compounds,<sup>[143,145]</sup> whereas for the Fp moiety, only few literature entries exist in this regard. CpFe(MeCN)<sub>3</sub>BF<sub>4</sub> (**178**) and related compounds are reported to be unstable at ambient conditions, and they have mostly been detected as intermediates.<sup>[146]</sup> Nevertheless, CpFe(MeCN)<sub>3</sub>BF<sub>4</sub> (**178**) has been reported to be stable at -40 °C when prepared by photolysis of CpFe(*p*-Xyl)BF<sub>4</sub> (**179**), and various LEWIS-donors were successfully used to displace the acetonitrile ligands. When compound **179** is photolyzed at ambient temperatures, however, decomposition to ferrocene and inorganic hexa(acetonitrile)iron(II) occurs (**Scheme 2.32**).<sup>[147]</sup>



**Scheme 2.32** Generation of the tris(acetonitrile) species **178** by photolysis of **179** at low temperatures. Upon heating to room temperature, compound **178** decomposes to ferrocene (**58**) and inorganic iron.<sup>[147]</sup>

This behavior opened the possibility for a new catalyst system based on an *in situ* photochemical generation of species **178** from pre-catalyst **179**. The synthesis of the tetraphenylborate analogue **180** has been described by NESMEYANOV in 1963, and involves treating ferrocene (**58**)

with aluminium powder and aluminium chloride in *para*-xylene at elevated temperatures, and subsequent precipitation with sodium tetraphenylborate.<sup>[148]</sup> This synthesis was replicated with a yield of 27 % (**Scheme 2.33**)



**Scheme 2.33** Synthesis of  $\text{CpFe}(p\text{-xyl})\text{BPh}_4$  from ferrocene (**58**).<sup>[148]</sup> The oil bath temperature is given.

The wavelength for decomplexation of the *p*-xylene ligand from the hexafluorophosphate analogue of compound **179** has been given in the literature as 450 nm.<sup>[147]</sup> A UV-vis spectrum of the available compound  $\text{CpFe}(p\text{-xyl})\text{BPh}_4$  (**180**) was taken, confirming a broad absorption band in the region of  $\lambda = 350 \text{ nm} - 550 \text{ nm}$ . Since LEDs are conveniently available in this wavelength, inexpensive LED strips were purchased and their emission spectrum was taken and overlaid with the absorption spectrum of compound **180** (**Figure 2.78**).

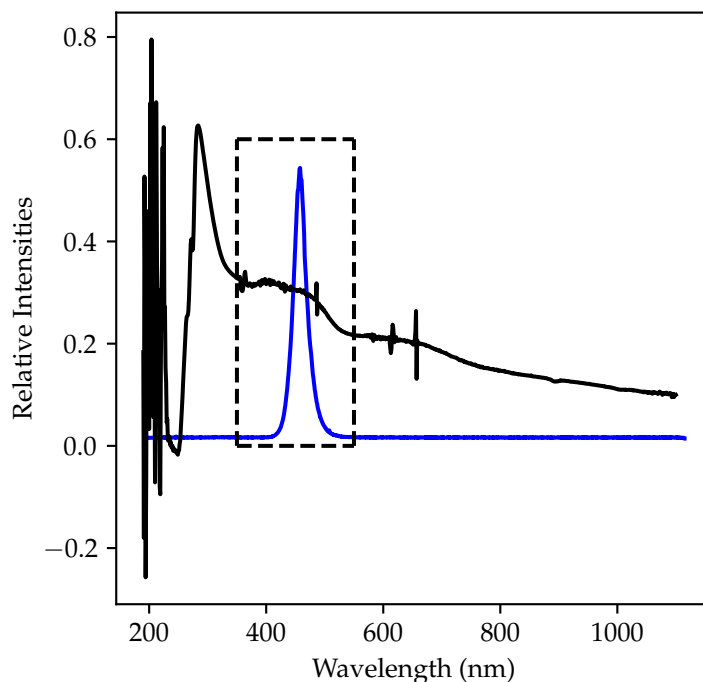


**Figure 2.78** UV-vis absorption spectrum of  $\text{CpFe}(p\text{-xyl})\text{BPh}_4$  (**180**) (black solid line), overlaid with the emission spectrum of a purchased blue LED strip (blue solid line). Black dashed box: Region of interest around  $\lambda = 350 \text{ nm} - 550 \text{ nm}$ .



To test the feasibility of the LED strip for ligand abstraction, a quick test setup was constructed. To enable irradiation of  $\text{CpFe}(p\text{-xyl})\text{BPh}_4$  (**180**) at low temperatures, a piece of LED strip was connected to a power supply and inserted into a test tube. This tube could then be inserted next to a reaction vial submerged in a dry ice/acetone bath in a DEWAR dish (**Figure 2.79**).

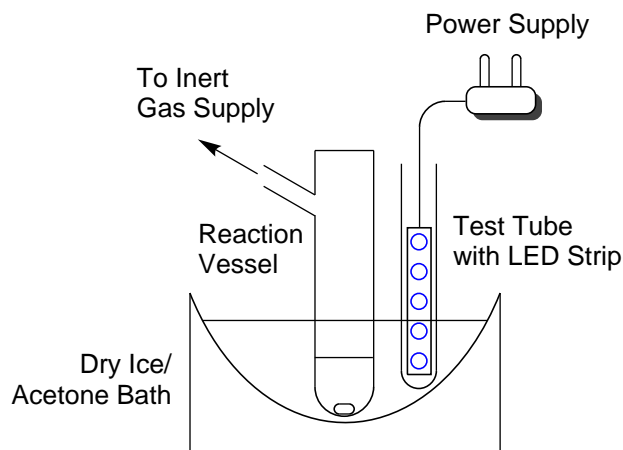
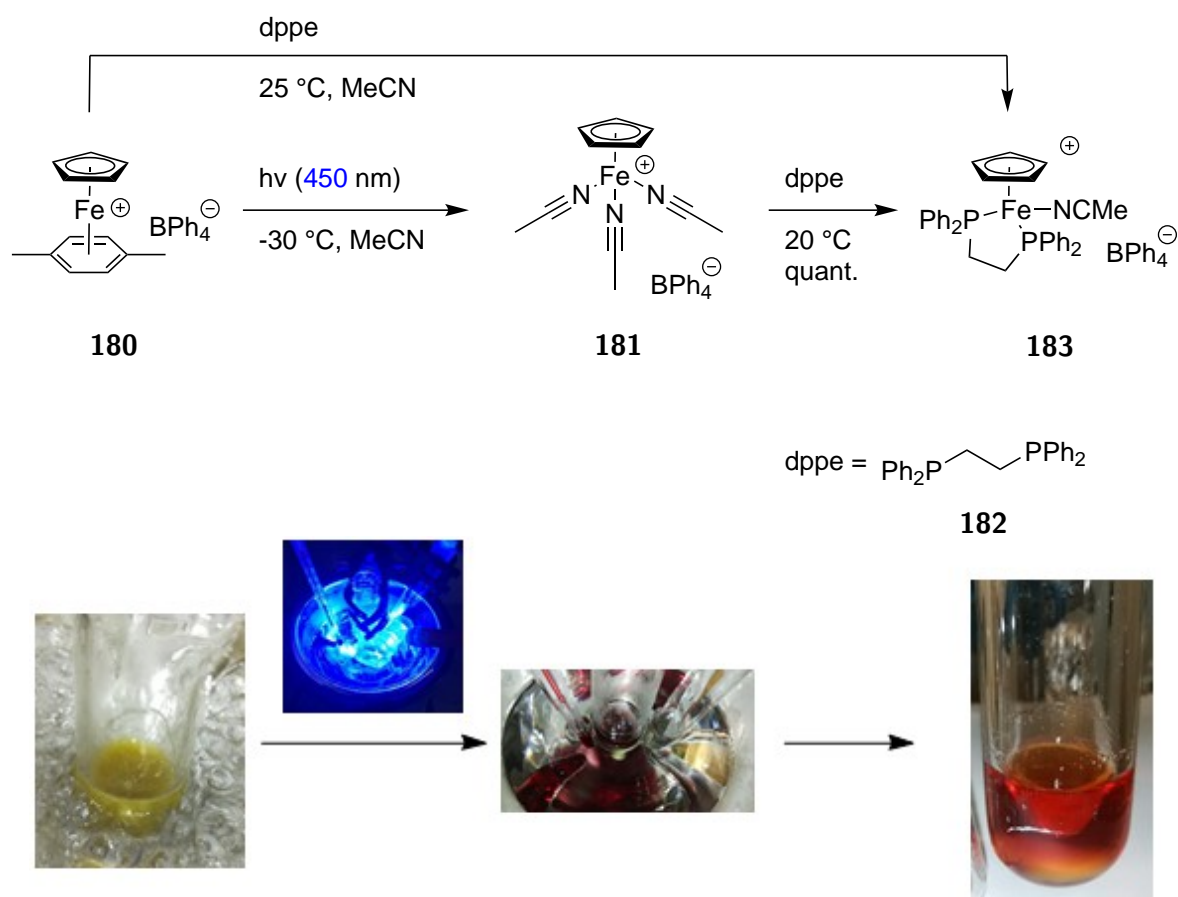


**Figure 2.79** Test setup for photochemical ligand abstraction at  $\text{CpFe}(p\text{-xyl})\text{BPh}_4$  (**180**) using blue LEDs.

Using this setup, a suspension of  $\text{CpFe}(p\text{-xyl})\text{BPh}_4$  (**180**) in acetonitrile was cooled to  $-30\text{ }^\circ\text{C}$  and irradiated with blue light. After one hour, the mixture had changed from a bright yellow suspension to a deep violet solution, indicating the successful formation of the tris(acetonitrile) complex **181**. 1,2-bis(diphenylphosphanyl)ethane (dppe, **182**) was added, and the solution was warmed to  $23\text{ }^\circ\text{C}$ , which led to a color change from violet to orange-red. The product **183** was confirmed by literature comparison of the crude  $^1\text{H-NMR}$  spectrum.<sup>[147]</sup> Color changes across the reaction sequence are visualized in **Scheme 2.34**. Notably, complex **183** is obtained directly when **180** is irradiated at  $25\text{ }^\circ\text{C}$  in the presence of acetonitrile and dppe (**182**).



**Scheme 2.34** Color changes during test reaction of  $\text{CpFe}(p\text{-xylyl})\text{BPh}_4$  (**180**) with dppe under LED irradiation.

Having established the viability of LED light sources for the *in situ* formation of the reactive intermediate **181**, two photoreactor arrays for the ASW 2000P were 3D printed and assembled with blue LEDs, enabling the simultaneous execution of 32 reactions in the parallel synthesizer. A new reaction sequence was created, involving the pre-formation of  $\text{CpFe}(\text{solvent})$  complexes under irradiation, and subsequent addition of substrates and reagents for C-H activation. The complete sequence is shown in **Figure 2.80**.

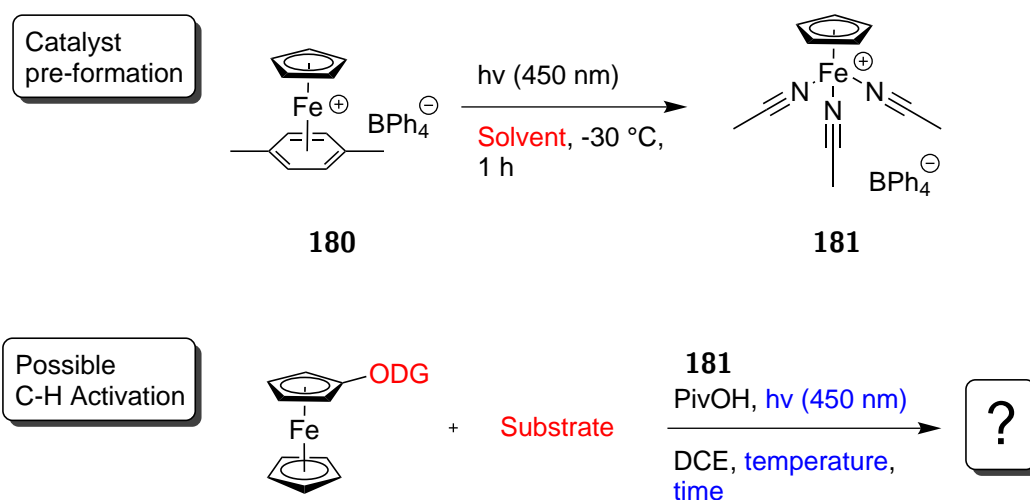


**Figure 2.80** Sequence for possible C-H activation at ODG-bearing ferrocenes using the pre-catalyst **180**. Red: Factors investigated within multilevel categorical DoE. Blue: Factors investigated through automated sampling at multiple time steps.

Factors included in the multilevel categorical DoE were solvent (4 levels), ODG (4 levels) and substrate (2 levels). Solvents and ODGs were chosen according to their respective coordination strengths, for which literature values were available.<sup>[104,149]</sup> They were selected to cover a wide range of coordination strengths, as well as to have ODG-solvent pairs of structural resemblance (e.g. the acetyl ODG in compound **38** and acetone (**185**)). (Fluorosulfonyl)ferrocene (**184**) was selected since it had shown good activity in *ortho*-lithiation reactions carried out by BOSTON.<sup>[150]</sup> Ethynylbenzene (**30**) and *N*-methylmaleimide (**172**) were used as substrates. All compounds which are factors in the DoE are given in **Figure 2.81**.

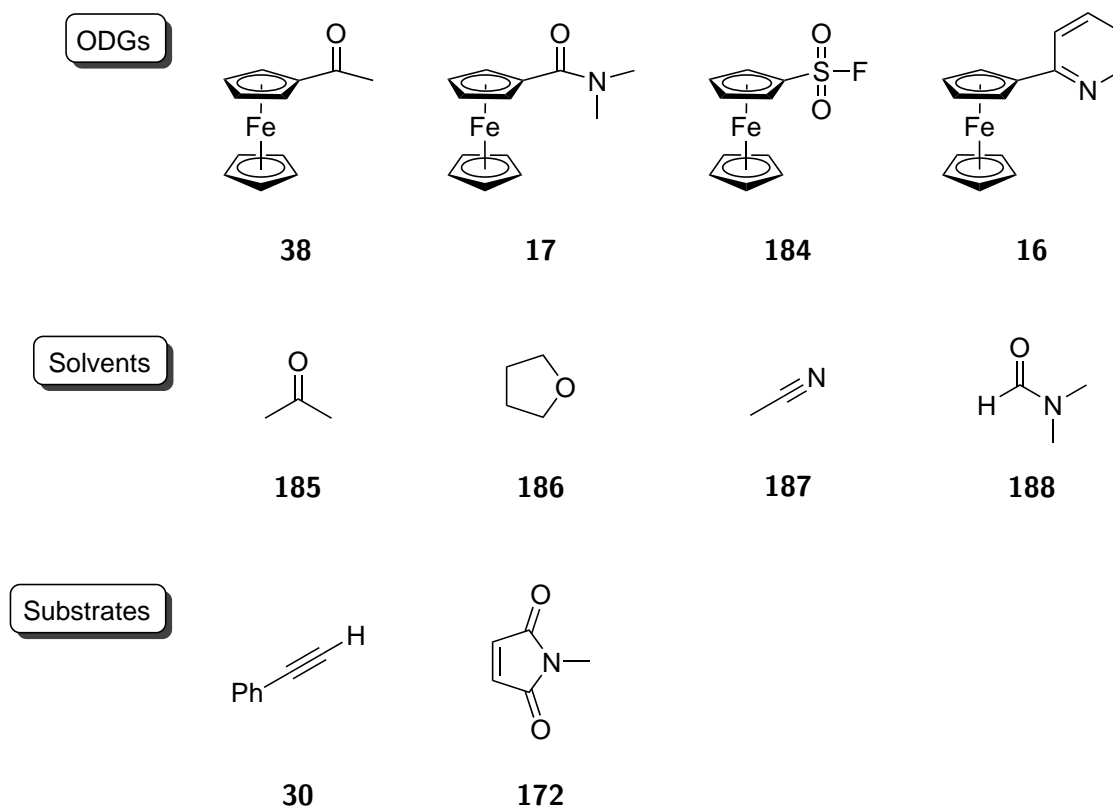


**Figure 2.81** Structures of reagents and solvents used in the investigation of CpFe(*p*-xyl)BPh<sub>4</sub> (**180**)-based C-H activation reactions.

In addition to the factors included in the pure, statistical experiment design, the influence of temperature, time, and irradiation during the C-H activation step were studied. This was achieved by taking multiple automated TLC samples at pre-defined points during the sequence. After stirring the reaction mixtures in the dark for 17 h at 0 °C (first sample), they were irradiated at the same temperature for another hour (second sample). Next, two more analyses were performed after stirring at 60 °C in the dark (third sample) and under irradiation (fourth sample), each for 1 h. The photoreactor setup proved to be mechanically stable at temperatures from -30 °C – 60 °C during vortex stirring for 17 h. Unfortunately, no formation of C-H activation products was observed again. Some decomposition of the ferrocene compounds was observed, and plotted using QTLC. For this, the integral values of the ferrocene compounds divided by that of decomposition (brown spot at baseline) was noted over the four samples per reaction. The plot of starting material decomposition for four selected reactions is shown in **Figure 2.82**.

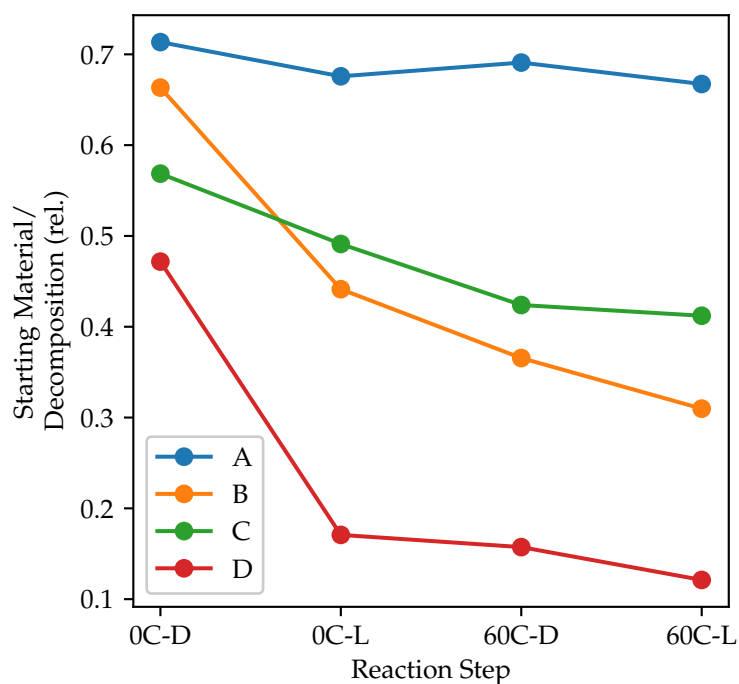
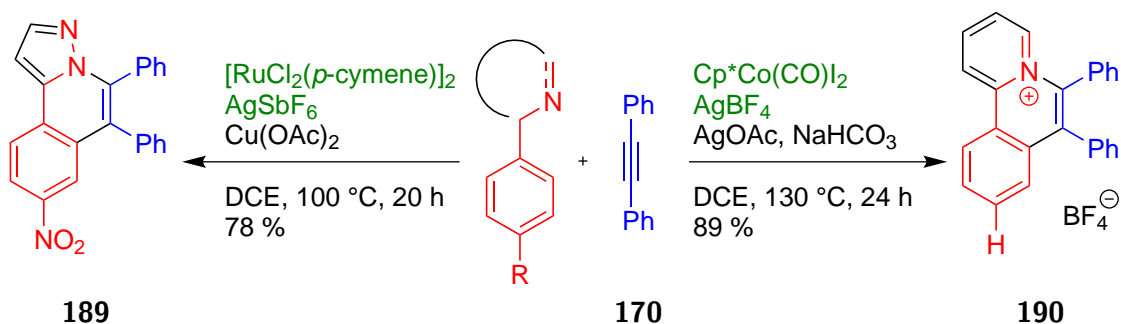


**Figure 2.82** Decomposition plots of some selected reactions during attempted C-H activation with  $\text{CpFe}(p\text{-xyl})\text{BPh}_4$  (**180**). **A**: acetylferrocene (**38**), acetone (**185**), *N*-methylmaleimide (**172**). **B**: acetylferrocene (**38**), DMF (**188**), *N*-methylmaleimide (**172**). **C**: (fluorosulfonyl)ferrocene (**184**), THF (**186**), *N*-methylmaleimide (**172**). **D**: (fluorosulfonyl)ferrocene (**184**), MeCN (**187**), ethynylbenzene (**30**).

Starting material decomposition was mostly observed with acetylferrocene (**38**) and (fluorosulfonyl)ferrocene (**184**). Acetylferrocene (**38**) was stable in some cases (**A**), but showed decomposition depending on solvent and substrate (**B**). (Fluorosulfonyl)ferrocene (**184**) showed decomposition in all cases (**C**, **D**). Strongest changes were observed after the first irradiation step at 0 °C (0C-L), which was a first indication for some of the selected ferrocenes not being stable under blue light irradiation. Besides this, no clear trends were observed.

All attempts so far were based on conditions found typically in  $\text{Cp}^*\text{Co(III)}$  catalysis. As this clearly did not lead to any promising results, the focus was shifted towards ruthenium chemistry. Ruthenium(II) compounds have recently been used extensively as C-H activation catalysts,<sup>[151]</sup> and as ruthenium sits below iron in the periodic table, similar chemical behavior was expected to some extent. Notably, some conditions reported in Ru(II)-catalyzed C-H activation were similar to those employed in  $\text{Cp}^*\text{Co(III)}$  catalysis. In particular, alkyne annulations at *N*-heterocycle-based *ortho*-directing groups using silver(I) salts for catalyst preactivation are found in both cobalt(III)- and ruthenium(II)-based examples.<sup>[152,153]</sup> **Scheme 2.35** shows such examples with pyrazolyl- and pyridyl ODGs, yielding the annulated compounds **189** and **190** from the reaction of the corresponding *N*-heterocycle with diphenylethyne (**170**).



**Scheme 2.35** Alkyne annulation at *N*-heterocyclic ODGs using both Co(III)- and Ru(II)-based catalysts.<sup>[152,153]</sup> Core structure in red, diphenylethyne motif in blue, catalytic systems in green.

The most commonly known ruthenium(II) precatalyst for C-H activation is  $[\text{RuCl}_2(p\text{-cymene})_2]$  (**191**). Structurally, the complex resembles a hybrid between  $\text{Cp}^*\text{Co}(\text{CO})\text{I}_2$  (**153**) and  $\text{CpFe}(p\text{-Xyl})\text{BF}_4$  (**179**), as it bears both halide and aryl ligands, opening it to multiple modes of activation (**Figure 2.83**).

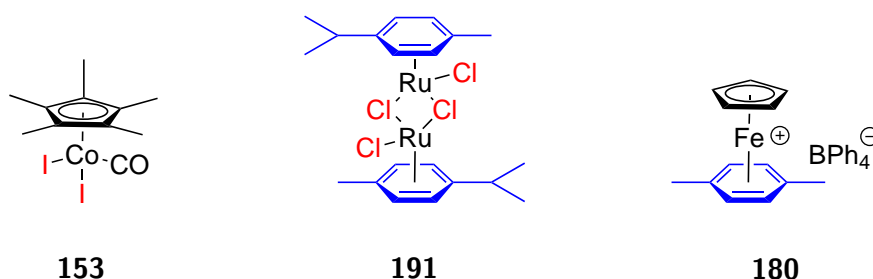
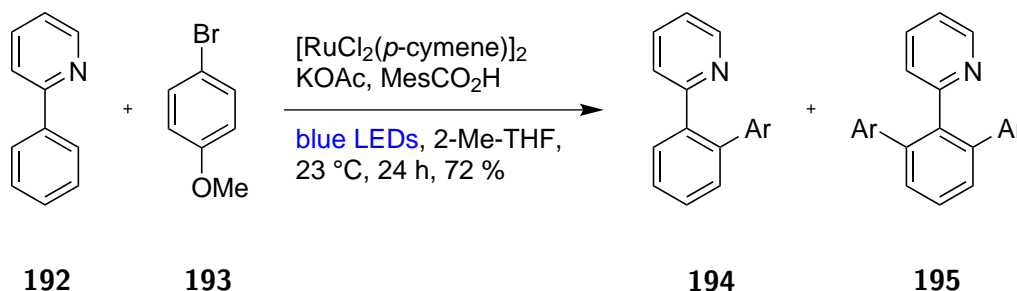


**Figure 2.83** Structure of  $[\text{RuCl}_2(p\text{-cymene})_2]$  (**191**) compared to those of  $\text{Cp}^*\text{Co}(\text{CO})\text{I}_2$  (**153**) and  $\text{CpFe}(p\text{-xyl})\text{BPh}_4$  (**180**). Halide ligands in red, neutral aryl ligands in blue.

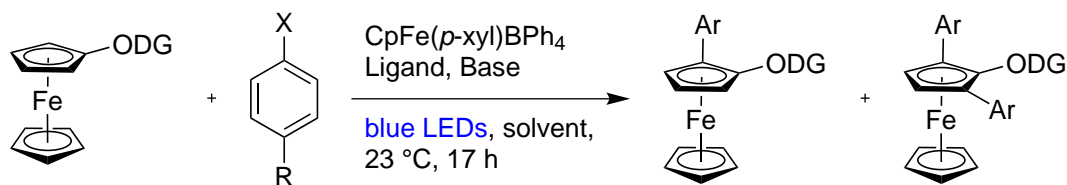
While the common activation path for  $[\text{RuCl}_2(p\text{-cymene})_2]$  (**191**) involves silver(I)-mediated halide abstraction,<sup>[154]</sup> one example of blue LED-assisted aryl decomplexation was reported by SAGADEVAN *et al.* (**Scheme 2.36**).<sup>[155]</sup> Here, 2-Phenylpyridine (**192**) is reacted with *para*-bromoanisole (**193**) to yield the mono-(**194**) and disubstituted (**195**) arylation products.



**Scheme 2.36** Ruthenium(II)-catalyzed, *ortho*-directed C-H arylation using blue LEDs for precatalyst activation.<sup>[155]</sup> The yield is reported as the combined NMR yield of compounds **194** and **195** against 1,3,5-trimethylbenzene as internal standard.

The activation of  $[\text{RuCl}_2(p\text{-cymene})_2]$  (**191**) using blue light by SAGADEVAN *et al.* resembled that of  $\text{CpFe}(p\text{-xyl})\text{BPh}_4$  (**180**) applied in this thesis. It was decided to test the reactivity of complex **180** in *ortho*-directed C-H arylations in a fractional factorial DoE. The reaction layout is shown in **Table 2.20**.

**Table 2.20** Fractional factorial design for the investigation of precatalyst  $\text{CpFe}(p\text{-xyl})\text{BPh}_4$  (**180**) in blue light-assisted, catalytic C-H arylation.



Factor	Name	Type	Low	High
A	ODG	Categoric	Acetyl-	2-Pyridyl-
B	Aryl Halide (X)	Categoric	Br	I
C	Aryl Substituent (R)	Categoric	$\text{NO}_2$	OMe
D	Ligand	Categoric	$\text{PPh}_3$	$\text{AdCO}_2\text{H}$
E	Base	Categoric	$\text{K}_2\text{CO}_3$	TMP
F	Solvent PC1	Numeric	-1	+1
G	Solvent PC2	Numeric	-1	+1

For the selection of factors and their settings, several literature examples of  $[\text{RuCl}_2(p\text{-cymene})_2]$  (**191**)-catalyzed C-H activation were reviewed, and common reagents and solvents were identified.<sup>[155–158]</sup> The final design consisted of five categoric and two numeric factors, aiming to cover a wide portion of the reaction space provided in the literature. Two *ortho*-directing groups, one carbonyl- and one *N*-heterocyclic, were investigated. Factors B and C led to four different *p*-substituted halobenzenes being included in the reaction sequence. For example, the factor combination B (Low)/C (High) encodes for *p*-Methoxybromobenzene (**193**) (**Figure 2.84**).

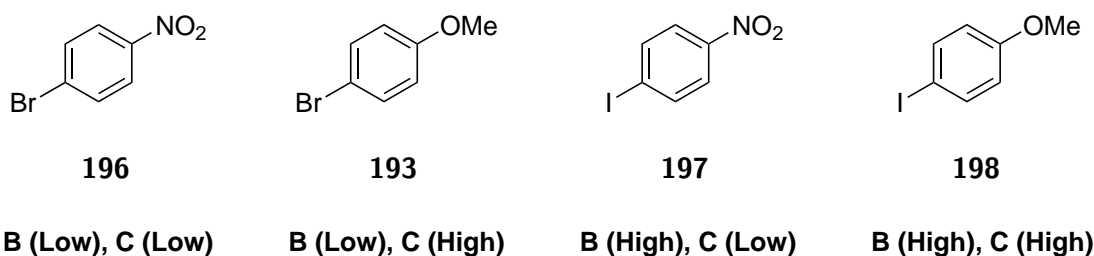


Figure 2.84 Aryl Halides and their corresponding factor settings.

Factor D describes two different ligands, a phosphine and a carboxylic acid, while Factor E contains two bases, one inorganic and one organic. Finally, four structurally diverse solvents (acetonitrile (**187**), *N*-methylpyrrolidinone (**199**), 2-methyltetrahydrofuran (**200**) and 1,2-dichloroethane (**201**)) were included through Factors F and G, which were derived from principal component analysis and encode polarity (PC1) and polarizability (PC2) (Figure 2.85).<sup>[26]</sup>

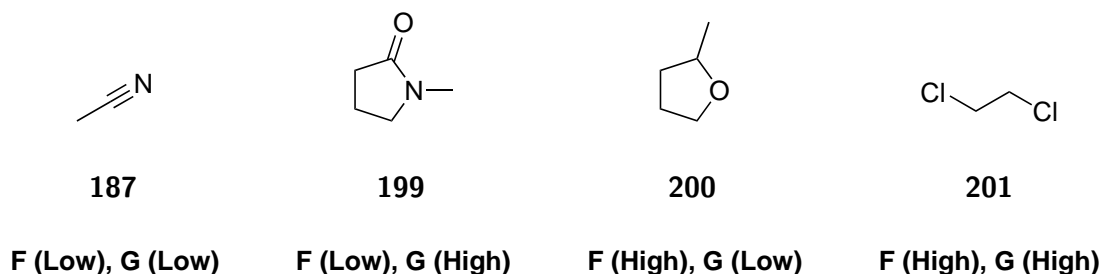


Figure 2.85 Solvents encoded by principal components.<sup>[26]</sup>

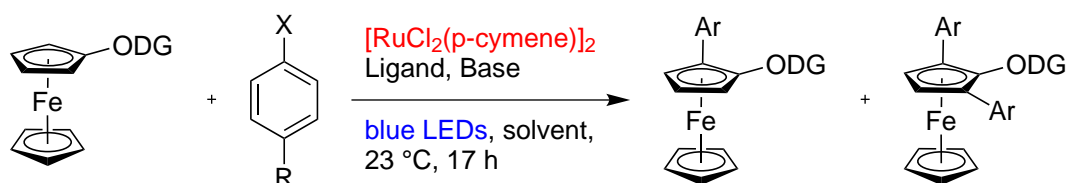
In order to maximize the usage of automated reagent addition, the addition sequence was built around the fact that potassium carbonate is insoluble in organic solvents, and the precatalyst CpFe(*p*-xyl)BPh<sub>4</sub> (**180**) is only slightly soluble in acetone. Consequently, K<sub>2</sub>CO<sub>3</sub> was added first in aqueous solution, and the evaporation of water was combined with the drying and inertization of the reactors. Subsequently, CpFe(*p*-xyl)BPh<sub>4</sub> (**180**) was added in acetone (1.4 mg mL<sup>-1</sup>) and the solvent was evaporated once again. After this, all other reagents could be added in concentrated dichloromethane solutions, as well as the actual reaction solvents. Incubation under blue light irradiation was performed, and the reaction mixtures were analyzed by automated TLC after 17 h.

Despite the large area of reaction space covered within this DoE, still no formation of product was observed, even in trace amounts. Some procedure-based sources of error are the presence of dichloromethane in all reactions, as well as the combined presence of CpFe(*p*-xyl)BPh<sub>4</sub> (**180**), acetone and K<sub>2</sub>CO<sub>3</sub> at one point. Dichloromethane might have inhibited the effects of the other solvents, while acetone and K<sub>2</sub>CO<sub>3</sub> might have led to premature ligand exchange reactions at CpFe(*p*-xyl)BPh<sub>4</sub> (**180**), although this seemed unlikely.



Besides these sources of error, two possible reasons for the lack of reactivity were considered. Firstly, the complex  $\text{CpFe}(p\text{-xyl})\text{BPh}_4$  (**180**) may simply not survive the reaction conditions. As mentioned before, the  $\text{CpFe}$  unit is not stable at ambient temperature after decomplexation of the *para*-xylenyl ligand (Scheme 2.32). While it was hypothesized that with a largely diverse set of ligands (*ortho*-directing groups, solvents, substrates) present, the catalytic cycle might have been faster than catalyst decomposition, it is certainly a reasonable source of error. Secondly, the issue might lie in ferrocene-based starting materials being combined with blue light-assisted precatalyst activation. As ferrocenes are typically orange-colored, they have significant absorption in the blue region of visible light, an indication of which was the decomposition of several ferrocene derivatives during blue LED irradiation (Figure 2.82). Additionally, the ferrocenes **38** and **16** were present in much higher concentrations than the precatalyst  $\text{CpFe}(p\text{-xyl})\text{BPh}_4$  (**180**), which might have led to photoquenching and therefore lack of precatalyst activation.

In order to test which of the aforementioned conditions were more likely to cause an absence of reactivity, the iron complex  $\text{CpFe}(p\text{-xyl})\text{BPh}_4$  (**180**) was replaced with the ruthenium compound  $[\text{RuCl}_2(p\text{-cymene})]_2$  (**191**) originally applied in the literature. To maximize efficiency, the previous DoE and reaction protocol were reused, enabling the preparation and execution of 32 ruthenium-catalyzed reactions in a single day (Scheme 2.37).



Scheme 2.37 Scheme

Once more, no reactivity was observed, despite the application of reaction conditions similar to those in the literature, except for the substrates being ferrocene- instead of phenyl-based. This strongly points to the ferrocenes absorbing most of the light, preventing precatalyst activation for both  $\text{CpFe}(p\text{-xyl})\text{BPh}_4$  (**180**) and  $[\text{RuCl}_2(p\text{-cymene})]_2$  (**191**). Since the basic chemistry of  $\text{CpFe}(p\text{-xyl})\text{BPh}_4$  (**180**) was based on blue light activation, this particular complex seemed unsuited for ferrocene chemistry. At this strategic point, the project was halted due to time constraints.

## Conclusion and Outlook

In this section, some  $\text{CpFe}$ -based complexes were investigated for their catalytic activity in *ortho*-directed C-H activation reactions. Starting from the  $\text{Cp}^*\text{Co}(\text{CO})\text{I}_2$  (**153**) analogue

CpFe(CO)<sub>2</sub>I (**154**), it was found that the carbonyl ligands likely prohibit the liberation of coordination sites necessary for reaction progression. The THF complex **176** was briefly considered, but eventually dismissed for the same reason, as well as its hygroscopic nature. Taking more inspiration from Cp\*Co(III) chemistry, the compound CpFe(MeCN)<sub>3</sub>(BF<sub>4</sub>)<sub>2</sub> (**202**) became of interest. It proved to be unstable at ambient conditions, however through light-assisted *in situ* generation from CpFe(*p*-xyl)BPh<sub>4</sub> (**180**), it is accessible at lowered temperatures. Based on complex **180**, a reaction sequence was created involving preactivation using 3D printed blue LED photoreactors, and subsequent addition of reagents. After this led to no success, conditions more akin to those found in Ru(II) chemistry were applied, still without positive results. A final DoE using [RuCl<sub>2</sub>(*p*-cymene)]<sub>2</sub> (**191**) as catalyst again gave no product, suggesting that blue light activation in combination with ferrocene substrates is not a valid strategy.

Building on these results, two different strategies are conceivable, one focussing on the ferrocene substrates, and the other focussing on the use of CpFe(*p*-xyl)BPh<sub>4</sub> (**180**) as precatalyst. As discussed above, ferrocene substrates seem incompatible with blue light precatalyst activation. Therefore, other catalyst systems than CpFe(*p*-xyl)BPh<sub>4</sub> (**180**) would be needed for further studies. An emphasis could be placed on synthesizing various CpFe complexes with different ligands such as phosphanes (**183**) or isonitriles (**203**),<sup>[147]</sup> and screening those using multilevel categorical designs. As the pentamethylcyclopentadienyl ligand has proven to be highly effective in C-H activation transformations, albeit being considerably more expensive, some corresponding Cp\*Fe complexes with labile ligands such as **204** could be tested for their catalytic activity as well (Figure 2.86).

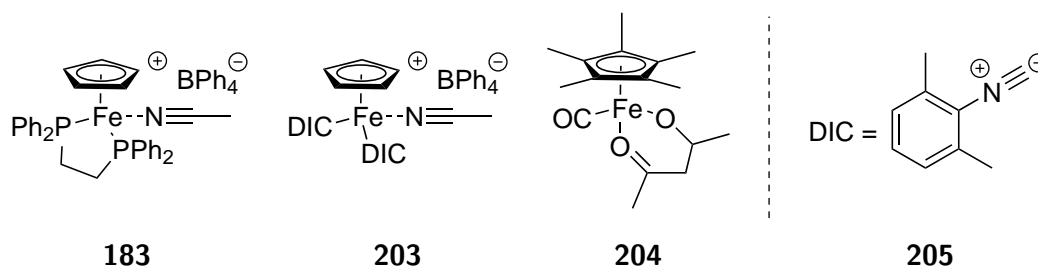
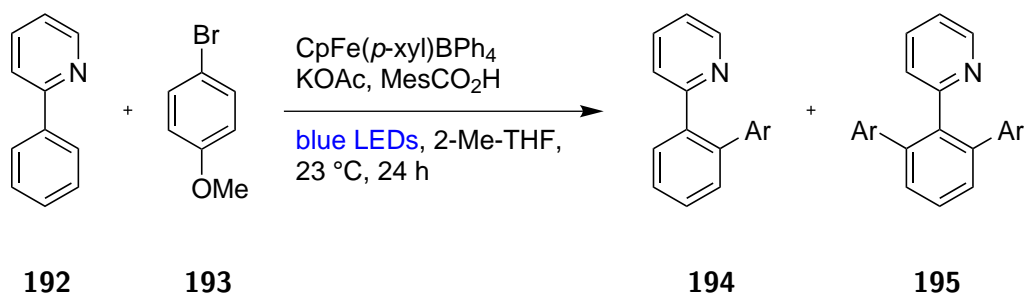


Figure 2.86 Cp and Cp\* complexes of iron possibly suitable for catalytic C-H activation.

Alternatively, the complex CpFe(*p*-xyl)BPh<sub>4</sub> (**180**) could be investigated using similar designs to those described in Table 2.20, while replacing the ferrocene-based substrates with phenyl-based ones. This could prevent the assumed photoquenching and allow for more efficient precatalyst activation, possibly yielding the desired *ortho*-functionalized products. Initial experiments could rely on the work of GREANEY *et al.* presented earlier in Scheme 2.36,<sup>[155]</sup> while replacing [RuCl<sub>2</sub>(*p*-cymene)]<sub>2</sub> (**191**) with CpFe(*p*-xyl)BPh<sub>4</sub> (**180**) (Scheme 2.38).



**Scheme 2.38** Possible initial conditions for the screening of  $\text{CpFe}(p\text{-xyl})\text{BPh}_4$  (**180**) as catalyst for *ortho*-C-H activation using non-ferrocene substrates based on the procedure of GREANEY *et al.*<sup>[155]</sup>

Using the automation/DoE approach, each new concept could be investigated directly in an extended reaction space, instead of single, isolated points. Creating these concepts became the main task, while the execution of test reactions was almost carried out “on the side”, with a typical DoE of 32 reactions being accessible within two days. Thus, most repetitive work was outsourced to automation, and even the information available through automated experimentation was optimally exploited using efficient DoE methods. Even though no positive results could be obtained, the negative results were always comprehensive and conclusive, as large areas of reasonable reaction space were covered each time, leaving little room for doubt. Excluding starting material syntheses, 128 DoE-based experiments ( $= 4 \times 32$ ) were carried out in the parallel synthesizer with minimal human intervention. Compared to the usual trial-and-error/OFAT approach, which requires constant, daily decision-making, the automated DoE approach represented a much more calm and systematic approach towards the exploration of unknown chemical behavior.

The next logical step would be to completely automate the reaction design process as well. The group of CRONIN recently presented a closed-loop, AI-based method for the semi-random exploration of reaction spaces.<sup>[2]</sup> While a custom, 6-reactor robotic platform was used here, and all reaction were carried out only in DMSO for simplicity, it is easy to imagine the neural network backbone being connected to a modern, commercial synthesis platform like the CHEMSPEED SWING using their PYTHON API. This would enable a truly high-throughput, unbiased approach towards the generation of a new, standardized reactivity database.

### 3 Conclusion and Outlook

Within this thesis, a multitude of automated devices was recommissioned, including a CHEM-SPEED ASW 2000P parallel synthesizer, a BÜCHI MPLC device and a BÜCHI Syncore parallel evaporator. These devices were made fully operational, and have been integrated into synergistic workflows, which allow the user to carry out sophisticated screening, optimization and library synthesis projects. To increase the information density of each parallel synthesizer run, DoE was implemented for the planning and analysis of automated experiments, focussing on an optimal interaction between experiment design and mechanical capabilities of the ASW 2000P.

To enhance the scope of the automated equipment even more, some knowledge in the areas of programming and data science (PYTHON, C++), electrical engineering (ARDUINO), as well as 3D modelling and -printing (AUTODESK Inventor Professional 2020, ULTIMAKER Cura) was acquired. To fully exploit the capabilities of the parallel synthesizer, a workflow for automated, quantitative thin-layer chromatography was created based again on a smartphone and a custom PYTHON script. Quantitative data for 32 reactions can now be extracted within 45 min in a fully automated way, eliminating the next bottleneck after reaction preparation. More use cases for these interdisciplinary tools were a software for automated charge calculations, a smartphone-based communication interface for the parallel synthesizer and custom photoreactors for high-throughput photochemistry. The potential of this comprehensive framework of automation and statistical Design of Experiments was demonstrated in three use cases centered around the molecule ferrocene (**58**). These use cases cover a wide variety of applications typical in chemical experimentation, namely the investigation of the influence of various factors on a known reaction, the synthesis of compound libraries, and the exploration of unknown reaction spaces.

Quinoylferrocene (**41**) has successfully been reacted with indole (**43**) to form an addition product **82** with unexpected chemoselectivity. In a fractional factorial DoE, a complex interaction between three reagents has been found, which is in accordance with the general nature of the reaction and its reactants. In this project, a self-designed, 3D-printed photoreactor array for the ASW 2000P was used.

Furthermore, a selection of 16 amines was used to synthesize a library of 16 ferrocenyl carboxamides, which then underwent a Cp\*Co(III) *ortho*-directed C-H activation with phenylethyne (**30**) to form 14 new alkenylated products. All compounds were purified automatically, and characterized spectroscopically. The 16 carboxamides were categorized into different groups based on structure, and reactivity trends could be observed across these groups.

Lastly, an attempt was made to find a CpFe-based catalyst for C-H activation reactions at ferrocenes bearing *ortho*-directing groups. Four separate runs with 32 reactions each were conducted on the parallel synthesizer, every time covering a wide range of reaction space by using either combinatorial or statistical designs. After each run, a comprehensive statement about the reactivity of the current system could be made, and the strategy could be adjusted accordingly. Although no positive result could be obtained, much knowledge on CpFe-based systems was gained during the investigation process.

Among the examples presented in this thesis, the automated methods were tested and positively evaluated with numerous collaborating partners and groups in the areas of natural product synthesis, organometallics and medicinal chemistry. Training for some long-term employees of the house was provided, which should enable the continued use of the parallel synthesis equipment as a tool for chemists to accelerate their research.

## 4 Experimentals

### 4.1 General Remarks

All reactions were carried out in inert atmosphere (argon or nitrogen) using common SCHLENK techniques. Glassware was either stored in an oven at 70 °C, or heated with a heat gun before use, while purging three times with inert gas. Syringes and cannulas were rinsed three times with inert gas before use. Reaction temperatures are given as oil bath temperatures, if not stated otherwise. If possible, solvents were purchased in dry form and stored over molecular sieves under argon. Dichloromethane was dried over calcium hydride and distilled. Diethyl ether and tetrahydrofuran were dried over sodium wire/benzophenone and distilled. Diisopropylamine, Diisopropylethylamine and Triethylamine were dried over potassium hydroxide and distilled. Technical petroleum ether for column chromatography was distilled before use.

The following compounds were synthesized according to literature procedures: (Dimethylcarbamoyl)ferrocene (**17**),<sup>[103]</sup> acetylferrocene (**38**) and 1,1'-diacetylferrocene (**39**),<sup>[159]</sup> (2-pyridyl)ferrocene (**16**),<sup>[69]</sup> (2-((*S*)-*tert*-butyl)oxazoliny)ferrocene (**18**),<sup>[160]</sup> *N*-methyl-*N*-isobutylaldehyde (**34**),<sup>[161]</sup> *N*-methyl-*N*-isobutylaldehyde (**206**),<sup>[162]</sup> pentamethylcyclopentadienyl carbonyl diiodide (**153**),<sup>[120]</sup> (2,5-dimethoxyphenyl)ferrocene (**40**),<sup>[79]</sup> quinoylferrocene (**41**),<sup>[79]</sup> 4-bromo-2,5-dimethoxyaniline (**81**),<sup>[97]</sup> 3-methyl-1,4,2-dioxazol-5-one (**60**),<sup>[163]</sup> ferrocenoyl chloride (**105**),<sup>[107]</sup> *N,N*-Diisopropylferrocenylcarboxamide (**107**),<sup>[108]</sup> cyclopentadienyliron dicarbonyl dimer (**156**),<sup>[135]</sup> cyclopentadienyliron dicarbonyl iodide (**154**),<sup>[136]</sup> (2-oxazoliny)ferrocene (**47**),<sup>[164]</sup> cyclopentadienyl-*p*-xylenyliron(II) tetraphenylborate (**180**),<sup>[148]</sup> (acetonitrile)(cyclopentadienyl)(bis-(diphenylphosphino)ethane)iron(II) tetraphenylborate (**183**).<sup>[147]</sup>

**Automated Syntheses** were carried out using a CHEMSPEED *Automated Synthesis Workstation* (ASW) 2000P. The platform was equipped with a vortexing table holding 2x8 13 mL glass reactor arrays, which were fitted with reflux condensers as well as filtration channels. The reactors were sealed using ceramic drawer tools in combination with 2/3-way valves, which were used to provide either vacuum (2-stage membrane pump, VACUUBRAND) or Argon (house line) to the reactors. Reaction temperatures were controlled by a thermo/cryostat (HUBER Unistat), which pumped a tempering fluid (HTF 190) through double jackets

built into the glass reactors. Likewise, reflux temperatures were controlled by a HUBER Ministat using Ethanol/Water (50/50). Liquid transfers were carried out by the built-in liquid handler (GILSON), which consisted of an x/y/z robotic arm with a septa-piercing, stainless steel needle attached to it. Reagent storage and sampling was done using 8 mL glass vials with pre-slit septa caps, which were provided on a suitable double-level holder. The same holder contained a rack for automated *thin-layer chromatography* (TLC) analysis, which used pre-cut plates (14x67 mm, see below). Higher quantities of solvents were added using built-in plumbing with one-way valves, which was accessed by the needle. Automated filtration was performed using a *solid phase extraction* (SPE) rack with standard 1 mL cartridges, which were filled manually with the desired filtration agent.

**<sup>1</sup>H- and <sup>13</sup>C-NMR spectra** were recorded on a BRUKER Ultrashield 400 or an Ascend 400 spectrometer (<sup>1</sup>H: 400 MHz, <sup>13</sup>C: 100 MHz). Chemical shifts ( $\delta$ ) are given in parts per million (ppm) and calibrated on the signals of the incompletely deuterated solvent as internal standard.<sup>[165]</sup> Multiplicities were noted as follows: singlet (s), doublet (d), triplet (t), quartet (q), multiplet (m), double signal (d). For conclusive signal assignment, correlation spectra (COSY, HSQC, HMBC, DEPT) were recorded.

**IR spectra** were recorded on a PERKIN-ELMER FT-1710 spectrometer. Intensities of the most diagnostic bands were given as m (medium) and s (strong).

**High-resolution mass spectra (HRMS)** were recorded on a MICROMASS LCT spectrometer (WATERS) with lock-spray unit in the ESI mode by the service department of the mass spectrometry center, Leibniz Universität Hannover.

**Analytical thin-layer chromatography** was carried out on silica-coated aluminium sheets (MERCK 60 F254). Detection was performed visually, with UV light ( $\lambda = 254$  nm) or with potassium permanganate stain.

**Reaction control** was performed using TLC in combination with mass spectrometry using an ADVION expression<sup>®</sup> CMS system (APCI+ mode) combined with a PlateExpress<sup>™</sup> module.

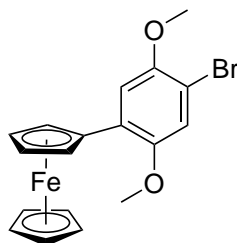
**Automated column chromatography (MPLC)** was performed using a modular system consisting of a BÜCHI Chromatography Pump B-688, a Gradient Former B-687, a Fraction Collector B-684 and a KNAUER UV detector K-2501. Empty FlashPure cartridges (BÜCHI) were equipped with a frit, loaded with silica gel (J.T. BAKER, 60  $\mu$ m) using vacuum, and sealed off with a second frit. Prior to use, the cartridge was primed circularly at high flow rates (100 mL min<sup>-1</sup>) using the respective starting gradient composition.

**X-ray crystallography** was carried out on a Smart X<sup>2</sup>S diffractometer (BRUKER).

## 4.2 Synthetic Procedures

### 4.2.1 (Methylquinoyl)ferrocene 76 and Related Compounds

#### 2-(4-bromo-2,5-dimethoxyphenyl)ferrocene (79)



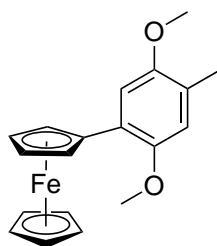
79

Concentrated hydrochloric acid (12 mL) and water (12 mL) were added to 3-bromo-2,5-dimethoxyaniline (**81**, 9.60 g, 41.39 mmol, 1.4 equiv.) and heated with a torch under stirring to solubilize most of the **81**. The suspension was cooled to (0 °C) and sodium nitrite (2.85 g, 41.39 mmol, 1.4 equiv.) in water (8 mL) were slowly added and then stirred for (1.5 h). Then, a solution of urea (530 mg, 8.87 mmol, 0.3 equiv.), ascorbic acid (2.60 g, 14.78 mmol, 0.5 equiv.) and Cetyltrimethylammonium bromide (150 mg, 0.41 mmol, 0.1 equiv.) in water (5 mL) was added. Next, a solution of ferrocene (**58**, 5.5 g, 29.56 mmol, 1.0 equiv.) in MTBE (118 mL) was slowly added to the reaction mixture through a transfer cannula. After stirring at (23 °C) for (17 h), brine (40 mL) was added and the mixture was extracted three times with MTBE (50 mL). The combined organic layers were dried over MgSO<sub>4</sub> and concentrated on silica gel. After automated column chromatography (PE/EtOAc 9:1 → 1:1), the target compound **79** was obtained as a red, crystalline solid (4.2 g, 10.47 mmol, 36 %)

<sup>1</sup>H-NMR (400 MHz, CDCl<sub>3</sub>): δ = 3.88 (s, 3H, CH<sub>3</sub>), 3.93 (s, 3H, CH<sub>3</sub>), 4.08 (s, 5H, C<sub>5</sub>H<sub>5</sub>), 4.33 (t, J = 1.9 Hz, 2H, CpH), 4.76 (t, J = 1.9 Hz, 2H, CpH), 7.09 (s, 1H, ArH), 7.12 (s, 1H, ArH) ppm. <sup>13</sup>C-NMR (100 MHz, CDCl<sub>3</sub>): δ = 56.2 (OCH<sub>3</sub>), 57.0 (OCH<sub>3</sub>), 68.7 (C<sub>Cp</sub>H), 68.8 (C<sub>Cp</sub>H), 69.6 (C<sub>5</sub>H<sub>5</sub>), 108.7 (C<sub>Ar</sub>C), 113.3 (C<sub>Ar</sub>H), 116.6 (C<sub>Ar</sub>H), 127.8 (C<sub>Ar</sub>Br), 149.9 (C<sub>Ar</sub>O), 151.3 (C<sub>Ar</sub>O) ppm. IR:  $\tilde{\nu}$  = 410 (m), 418 (m), 462 (s), 484 (s), 497 (s), 509 (s), 642 (m), 673 (m), 684 (m), 731 (s), 758 (s), 815 (s), 850 (s), 858 (s), 933 (m), 999 (s), 1016 (s), 1031 (s), 1051 (s), 1085 (s), 1103 (m), 1149 (m), 1182 (s), 1211 (s), 1236 (m), 1273 (m), 1317 (m), 1352 (m), 1367 (s), 1384 (m), 1408 (m), 1433 (s), 1446 (m), 1462 (s), 1500 (s), 1595 (m), 1685 (m), 2833 (m), 2929 (m), 2989 (m), 3076 (m), 3091 (m), 3105 (m) cm<sup>-1</sup>. HRMS (ESI): *m/z* calc. for C<sub>18</sub>H<sub>17</sub>BrFeO<sub>2</sub> [M]<sup>+</sup>: 399.9761, found: 399.9760.



### 2-(4-methyl-2,5-dimethoxyphenyl)ferrocene (80)

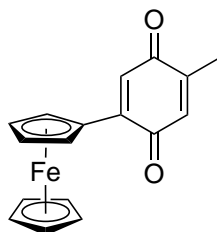


80

Methyl lithium ( $1.6 \text{ mol L}^{-1}$  in DCM, 1.8 mL, 2.88 mmol, 1.0 equiv.) was added dropwise to **79** (1.00 g, 2.49 mmol, 1.0 equiv.) and  $\text{Pd}[\text{P}(t\text{-Bu})_3]_2$  (25.00 mg, 0.05 mmol, 0.02 equiv.). The deep red solution was stirred at ( $25^\circ\text{C}$ ) for (20 min), quenched with saturated  $\text{NH}_4\text{Cl}$  (5 mL) and extracted three times with EtOAc (15 mL). The combined organic layers were dried over  $\text{MgSO}_4$  and concentrated on silica gel. After automated column chromatography (PE/EtOAc 99.4:0.6  $\rightarrow$  99.1:0.9), the target compound **80** was obtained as a red-orange solid (510 mg, 1.52 mmol, 61 %).

$^1\text{H-NMR}$  (400 MHz,  $\text{CDCl}_3$ ):  $\delta = 2.25$  (s, 3H,  $\text{CH}_3$ ), 3.86 (s, 3H,  $\text{OCH}_3$ ), 3.88 (s, 3H,  $\text{OCH}_3$ ), 4.09 (s, 5H,  $\text{C}_5\text{H}_5$ ), 4.32 - 4.26 (m, 2H, CpH), 4.78 - 4.73 (m, 2H, CpH), 6.73 (s, 1H, ArH), 7.05 (s, 1H, ArH) ppm.  $^{13}\text{C-NMR}$  (100 MHz,  $\text{CDCl}_3$ ):  $\delta = 16.2$  ( $\text{CH}_3$ ), 56.1 ( $\text{OCH}_3$ ), 56.1 ( $\text{OCH}_3$ ), 68.2 ( $\text{C}_{\text{CpH}}$ ), 68.8 ( $\text{C}_{\text{CpH}}$ ), 69.5 ( $\text{C}_5\text{H}_5$ ), 83.3 ( $\text{C}_{\text{CpC}}$ ), 111.9 ( $\text{C}_{\text{ArH}}$ ), 114.7 ( $\text{C}_{\text{ArH}}$ ), 117.1 ( $\text{C}_{\text{ArC}}$ ), 125.0 ( $\text{C}_{\text{ArC}}$ ), 150.7 ( $\text{C}_{\text{ArC}}$ ), 151.6 ( $\text{C}_{\text{ArC}}$ ) ppm. **IR**:  $\tilde{\nu} = 420$  (m), 486 (s), 590 (m), 644 (m), 678 (m), 700 (m), 713 (m), 783 (s), 813 (s), 860 (m), 881 (m), 966 (m), 999 (m), 1041 (s), 1072 (m), 1105 (m), 1149 (m), 1178 (m), 1209 (s), 1240 (m), 1278 (m), 1325 (m), 1371 (m), 1386 (m), 1398 (m), 1436 (m), 1465 (s), 1516 (m), 1614 (m), 2829 (m), 2902 (m), 2933 (m), 2991 (m), 3089 (m)  $\text{cm}^{-1}$ . **HRMS (ESI)**:  $m/z$  calc. for  $\text{C}_{19}\text{H}_{20}\text{O}_2\text{Fe}$  [ $\text{M}$ ] $^+$ : 336.0813, found: 336.0818.

### 2-(5-Methylquinoyl)ferrocene (76)



76

$\text{BBr}_3$  (10.9 mL,  $1.0 \text{ mol L}^{-1}$ , 10.89 mmol, 5.16 equiv.) was added to a solution of **80** (680 mg, 2.11 mmol, 1.0 equiv.) in DCM (8 mL) at ( $-78^\circ\text{C}$ ) under stirring. After (30 min), the reaction mixture was warmed to ( $25^\circ\text{C}$ ) and stirred for (17 h). The mixture was carefully evaporated while still under protected atmosphere, and MeOH (5 mL) and saturated  $\text{NaHCO}_3$  (5 mL) were added slowly. The mixture was extracted three times with DCM (10 mL) and the combined organic layers were concentrated to (4 mL). DDQ (620 mg, 2.74 mmol, 1.3 equiv.) was added, and the flask was agitated for (3 min). The deep green solution was filtered and the residue was washed with DCM (15 mL). The organic layer was quickly evaporated on silica gel. After automated column chromatography (PE/EtOAc 9:1  $\rightarrow$  6:4), the target compound **76** was obtained as a deep green solid (260 mg, 0.85 mmol, 40 %)

$^1\text{H-NMR}$  (400 MHz,  $\text{CDCl}_3$ ):  $\delta = 2.1$  (d,  $J = 1.6 \text{ Hz}$ , 3H,  $\text{CH}_3$ ), 4.17 (s, 5H,  $\text{C}_5\text{H}_5$ ), 4.66 - 4.60 (m, 2H, CpH), 5.00 - 4.94 (m, 2H, CpH), 6.64 - 6.58 (m, 1H, QH), 6.87 (s, 1H, QH) ppm.  $^{13}\text{C-NMR}$  (100 MHz,  $\text{CDCl}_3$ ):  $\delta = 15.4$  ( $\text{CH}_3$ ), 69.7 ( $\text{C}_{\text{CpH}}$ ), 70.5 ( $\text{C}_5\text{H}_5$ ), 72.2 ( $\text{C}_{\text{CpH}}$ ), 75.9 ( $\text{C}_{\text{CpC}}$ ), 126.9 ( $\text{C}_{\text{QH}}$ ), 134.1 ( $\text{C}_{\text{QH}}$ ), 145.5 ( $\text{C}_{\text{QC}}$ ), 148.3 ( $\text{C}_{\text{QC}}$ ), 186.7 ( $\text{C}_{\text{QC}}$ ), 187.4 ( $\text{C}_{\text{QC}}$ ) ppm. IR:  $\tilde{\nu} = 403$  (s), 414 (m), 443 (m), 474 (s), 484 (s), 497 (s), 572 (m), 623 (m), 690 (m), 709 (m), 783 (m), 819 (s), 858 (m), 877 (m), 894 (m), 927 (m), 966 (m), 1001 (m), 1037 (m), 1055 (m), 1101 (m), 1132 (m), 1195 (m), 1222 (m), 1249 (m), 1325 (m), 1363 (m), 1382 (m), 1406 (m), 1425 (m), 1456 (m), 1560 (m), 1583 (m), 1622 (m), 1641 (s), 3049 (m), 3078 (m), 3095 (m), 3115 (m)  $\text{cm}^{-1}$ . HRMS (ESI):  $m/z$  calc. for  $\text{C}_{17}\text{H}_{14}\text{O}_2\text{Fe} [\text{M}]^+$ : 306.0343, found: 306.0338.

#### 4.2.2 Fractional Factorial DoE with Quinoylferrocene **41**

The experiment was carried out in the parallel synthesizer. Before the automated run, the stock solutions in **Table 4.1** were prepared:

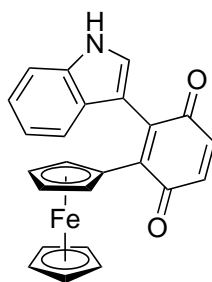
**Table 4.1** Stock solutions for the automated DoE with quinoylferrocene **41**. All solutions in dry dichloromethane, if not stated otherwise.

Identifier	Substance	Amount (mg)	Volume DCM (mL)
A	Quinoylferrocene ( <b>41</b> )	403	6.90
B	Indole ( <b>43</b> )	170	7.24
C	Silver hexafluoroantimonate	51	3.72
D	$\text{Cp}^*\text{Co}(\text{CO})\text{I}_2$ ( <b>153</b> )	36	3.72
E	2,2-Dimethylpropanoic acid	38	3.72

The Design of Experiments was carried out in STAT-EASE Design-Expert 12. The resulting layout is shown in **Table 4.2**.

All following operations were applied to the individual reactors according to **Table 4.5**. Reactions were distributed in a way that all runs with light were in one reactor block, and all runs without light in the other. Two reactor blocks were subjected to the standard drying/gas purge procedure. The reactor blocks were opened, and Ag<sub>2</sub>O (18.5 mg, 0.08 mmol, 2.0 equiv.) and NaOAc (3.3 mg, 0.04 mmol, 1.0 equiv.) were weighed manually into their respective positions. The reactors were closed, and one of them was equipped with a custom LED photoreactor array ( $\lambda = 730$  nm). All stock solutions were placed into their tray positions, and the 10 mL syringe pump was primed with acetone. Subsequently, Solution E (200  $\mu$ L, 0.02 mmol, 0.5 equiv.), Solution D (200  $\mu$ L, 4.00  $\mu$ mol, 0.1 equiv.), Solution C (200  $\mu$ L, 0.01 mmol, 0.2 equiv.), Solution B (200  $\mu$ L, 0.04 mmol, 1.0 equiv.) and Solution A (200  $\mu$ L, 0.04 mmol, 1.0 equiv.) were automatically aliquoted into their respective positions. Finally, solvent (1.6 mL) was aliquoted, the photoreactor was switched on, and reactions were incubated at 600 rpm for (17 h). Using the “wait for user input” command, automated TLC (n-Heptane/EtOAc 9:1) was carried out, and product spots were quantified using QTLC. The response for each reaction was recorded as the integral of the product **74** divided by the integral of the starting material **41**. The resulting raw responses are given in **Table 4.6**. All responses were subjected to statistical analysis in Design Expert 12. The corresponding files containing models with selected terms, error metrics and factor effect plots are part of the digital appendix of this thesis.

#### 2-(1*H*-indol-3-yl)-3-(ferrocenyl)benzoquinone (**74**)



**74**

All reactions with visible product formation were combined and evaporated with silica gel. After automated column chromatography (PE/EtOAc 9:1  $\rightarrow$  1:1), the target compound **74** was obtained as a deep purple solid (56 mg, 0.14 mmol).

<sup>1</sup>H-NMR (400 MHz, CDCl<sub>3</sub>):  $\delta$  = 4.08 (s, 4H, C<sub>5</sub>H<sub>5</sub>), 4.31 - 4.23 (m, 2H, CpH), 4.45 (s, 2H, CpH), 6.88 - 6.83 (m, 2H, QH), 7.01 - 6.88 (m, 2H, C<sub>Indole</sub>H), 7.18 - 7.09 (m, 1H, C<sub>Indole</sub>H), 7.37 - 7.31 (m,

**Table 4.2** Experiment layout for fractional factorial DoE produced by Design Expert 12.

Run	153, AgSbF <sub>6</sub>	PivOH	Ag <sub>2</sub> O	NaOAc	Light	Solvent
1	no	no	no	yes	no	pyridine
2	yes	yes	no	no	yes	2-methyl-thf
3	no	yes	yes	no	no	DCE
4	no	yes	yes	yes	no	pyridine
5	yes	yes	yes	yes	yes	DCE
6	no	yes	no	yes	no	2-methyl-thf
7	no	no	yes	yes	no	2-methyl-thf
8	no	no	yes	no	no	acetonitrile
9	yes	no	no	no	yes	pyridine
10	no	no	yes	yes	yes	DCE
11	no	no	no	no	yes	2-methyl-thf
12	yes	no	yes	yes	no	pyridine
13	yes	yes	yes	no	no	acetonitrile
14	no	yes	yes	no	yes	2-methyl-thf
15	no	no	no	no	no	DCE
16	yes	no	no	no	no	acetonitrile
17	yes	yes	yes	no	yes	pyridine
18	yes	yes	no	yes	no	pyridine
19	yes	no	yes	no	yes	2-methyl-thf
20	yes	no	no	yes	no	2-methyl-thf
21	yes	no	yes	yes	yes	acetonitrile
22	yes	yes	no	yes	yes	acetonitrile
23	yes	yes	no	no	no	DCE
24	yes	yes	yes	yes	no	2-methyl-thf
25	no	no	no	yes	yes	acetonitrile
26	no	yes	no	no	no	acetonitrile
27	yes	no	no	yes	yes	DCE
28	yes	no	yes	no	no	DCE
29	no	yes	no	no	yes	pyridine
30	no	yes	no	yes	yes	DCE
31	no	yes	yes	yes	yes	acetonitrile
32	no	no	yes	no	yes	pyridine

**Table 4.3** Responses for DoE with quinoylferrocene 41.

<b>Run</b>	<b>Response (3 h)</b>	<b>Response (35 h)</b>	<b>Response (51 h)</b>
1	0.00	0.00	0.00
2	0.12	0.45	0.52
3	0.11	0.00	0.00
4	0.00	0.00	0.00
5	0.59	0.19	0.16
6	0.00	0.00	0.00
7	0.00	0.00	0.07
8	0.00	0.96	1.76
9	–	–	–
10	0.22	0.00	0.39
11	0.00	0.00	0.00
12	–	0.00	0.00
13	0.37	0.80	0.86
14	0.00	0.85	1.38
15	0.00	0.00	0.00
16	0.00	0.00	0.00
17	0.00	0.00	0.00
18	0.00	0.00	0.00
19	0.23	0.60	0.49
20	0.00	0.00	0.00
21	0.64	1.36	0.30
22	0.00	0.00	0.00
23	0.00	0.00	0.00
24	0.58	0.50	0.78
25	0.00	0.00	0.00
26	0.00	0.00	0.00
27	0.00	0.00	0.00
28	0.11	0.51	0.79
29	–	–	–
30	0.00	0.00	0.00
31	0.41	–	0.00
32	–	–	–

1H, C<sub>Indole</sub>H), 7.43 - 7.38 (m, 1H, C<sub>Indole</sub>H), 8.48 (s, 1H, NH) ppm. <sup>13</sup>C-NMR (100 MHz, CDCl<sub>3</sub>):  $\delta$  = 70.2 (C<sub>5</sub>H<sub>5</sub>), 70.4 (C<sub>Cp</sub>H), 72.4 (C<sub>Cp</sub>H), 78.6 (C<sub>Cp</sub>C), 109.9 (C<sub>Indole</sub>C), 111.1 (C<sub>Indole</sub>H), 120.0 (C<sub>Indole</sub>H), 121.0 (C<sub>Indole</sub>H), 122.2 (C<sub>Indole</sub>H), 125.2 (C<sub>Indole</sub>C), 127.8 (C<sub>Indole</sub>H), 133.6 (C<sub>QC</sub>), 135.7 (C<sub>Indole</sub>C), 136.4 (C<sub>QH</sub>), 137.0 (C<sub>QH</sub>), 142.5 (C<sub>QC</sub>), 186.4 (C=O), 187.0 (C=O) ppm. **IR**:  $\tilde{\nu}$  = 432 (s), 443 (m), 474 (s), 486 (s), 499 (m), 534 (m), 555 (m), 592 (m), 619 (m), 661 (m), 671 (m), 686 (m), 738 (s), 761 (m), 806 (m), 840 (m), 918 (m), 987 (m), 1010 (m), 1039 (m), 1047 (m), 1085 (m), 1103 (s), 1132 (m), 1203 (m), 1230 (m), 1240 (m), 1274 (m), 1303 (s), 1336 (m), 1382 (m), 1421 (m), 1440 (m), 1456 (m), 1500 (m), 1546 (m), 1614 (m), 1641 (s), 3057 (m), 3072 (m), 3381 (m), 3396 (m) cm<sup>-1</sup>. **HRMS (ESI)**: *m/z* calc. for C<sub>24</sub>H<sub>17</sub>NO<sub>2</sub>NaFe [M+Na]<sup>+</sup>: 430.0506, found: 430.0500.

### 4.2.3 Fractional Factorial DoE with (Methylquinoyl)ferrocene 76

The experiment was carried out in the parallel synthesizer. Before the automated run, the stock solutions in **Table 4.4** were prepared:

**Table 4.4** Stock solutions for the automated DoE with (methylquinoyl)ferrocene 76. All solutions in dry dichloromethane, if not stated otherwise.

Identifier	Substance	Amount	Volume DCM
		(mg)	(mL)
A	Methylquinoylferrocene (76)	259	6.90
B	Indole (43)	104	7.24
C	Silver hexafluoroantimonate	31	3.72
D	Cp*Co(CO)I <sub>2</sub> (153)	22	3.72
E	2,2-Dimethylpropanoic acid	23	3.72

The Design of Experiments was carried out in STAT-EASE Design-Expert 12. The resulting layout is shown in **Table 4.5**.

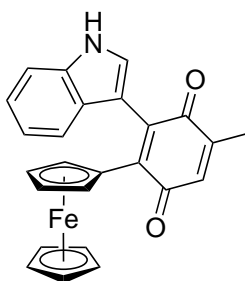
All following operations were applied to the individual reactors according to **Table 4.5**. Reactions were distributed in a way that all runs with light were in one reactor block, and all runs without light in the other. Two reactor blocks were subjected to the standard drying/gas purge procedure. The reactor blocks were opened, and Ag<sub>2</sub>O (11.4 mg, 0.05 mmol, 2.0 equiv.) and NaOAc (2.0 mg, 0.02 mmol, 1.0 equiv.) were weighed manually into their respective positions. The reactors were closed, and one of them was equipped with a custom LED photoreactor array ( $\lambda$  = 730 nm). All stock solutions were placed into their tray positions, and the 10 mL syringe pump was primed with acetone. Subsequently, Solution E (200  $\mu$ L, 0.01 mmol,

**Table 4.5** Experiment layout for fractional factorial DoE produced by Design Expert 12.

Run	153, AgSbF <sub>6</sub>	PivOH	Ag <sub>2</sub> O	NaOAc	Light	Solvent
1	no	no	no	yes	no	pyridine
2	yes	yes	no	no	yes	2-methyl-thf
3	no	yes	yes	no	no	DCE
4	no	yes	yes	yes	no	pyridine
5	yes	yes	yes	yes	yes	DCE
6	no	yes	no	yes	no	2-methyl-thf
7	no	no	yes	yes	no	2-methyl-thf
8	no	no	yes	no	no	acetonitrile
9	yes	no	no	no	yes	pyridine
10	no	no	yes	yes	yes	DCE
11	no	no	no	no	yes	2-methyl-thf
12	yes	no	yes	yes	no	pyridine
13	yes	yes	yes	no	no	acetonitrile
14	no	yes	yes	no	yes	2-methyl-thf
15	no	no	no	no	no	DCE
16	yes	no	no	no	no	acetonitrile
17	yes	yes	yes	no	yes	pyridine
18	yes	yes	no	yes	no	pyridine
19	yes	no	yes	no	yes	2-methyl-thf
20	yes	no	no	yes	no	2-methyl-thf
21	yes	no	yes	yes	yes	acetonitrile
22	yes	yes	no	yes	yes	acetonitrile
23	yes	yes	no	no	no	DCE
24	yes	yes	yes	yes	no	2-methyl-thf
25	no	no	no	yes	yes	acetonitrile
26	no	yes	no	no	no	acetonitrile
27	yes	no	no	yes	yes	DCE
28	yes	no	yes	no	no	DCE
29	no	yes	no	no	yes	pyridine
30	no	yes	no	yes	yes	DCE
31	no	yes	yes	yes	yes	acetonitrile
32	no	no	yes	no	yes	pyridine

0.5 equiv.), Solution D (200  $\mu$ L, 2.45  $\mu$ mol, 0.1 equiv.), Solution C (200  $\mu$ L, 4.90  $\mu$ mol, 0.2 equiv.), Solution B (200  $\mu$ L, 0.02 mmol, 1.0 equiv.) and Solution A (200  $\mu$ L, 0.02 mmol, 1.0 equiv.) were automatically aliquoted into their respective positions. Finally, solvent (1.6 mL) was aliquoted, the photoreactor was switched on, and reactions were incubated at 600 rpm for (3 h). Using the “wait for user input” command, automated TLC (n-Heptane/EtOAc 9:1) was carried out, and product spots were quantified using QTLC. The response for each reaction was recorded as the integral of the product **207** divided by the integral of the starting material **41**. Incubation was continued, and samples were taken again at (35 h) and (51 h). The resulting raw responses are given in **Table 4.6**. All responses were subjected to statistical analysis in Design Expert 12. The corresponding files containing models with selected terms, error metrics and factor effect plots are part of the digital appendix of this thesis.

### 2-(1*H*-indol-3-yl)-3-(ferrocenyl)-5-methylbenzoquinone (**207**)



**207**

All reactions with visible product formation were combined and evaporated with silica gel. After automated column chromatography (PE/EtOAc 9:1  $\rightarrow$  1:1), the target compound **207** was obtained as a deep purple solid (12 mg, 0.03 mmol)

**<sup>1</sup>H-NMR** (400 MHz, CDCl<sub>3</sub>):  $\delta$  = 2.17 (d,  $J$  = 1.6 Hz, 3H, CH<sub>3</sub>), 4.08 (s, 5H, C<sub>5</sub>H<sub>5</sub>), 4.27 - 4.19 (m, 2H, CpH), 4.44 (s, 2H, CpH), 6.74 - 6.68 (m, 1H, QH), 6.96 - 6.86 (m, 2H, C<sub>Indole</sub>H), 7.15 - 7.09 (m, 1H, C<sub>Indole</sub>H), 7.37 (d,  $J$  = 2.7 Hz, 1H, C<sub>Indole</sub>H), 7.45 (d,  $J$  = 8.0 Hz, 1H, C<sub>Indole</sub>H), 8.48 (s, 1H, NH) ppm. **<sup>13</sup>C-NMR** (100 MHz, CDCl<sub>3</sub>):  $\delta$  = 16.1 (CH<sub>3</sub>), 70.1 (C<sub>5</sub>H<sub>5</sub>), 70.2 (C<sub>Cp</sub>H), 72.3 (C<sub>Cp</sub>H), 78.5 (C<sub>Cp</sub>C), 110.2 (C<sub>Indole</sub>C), 111.0 (C<sub>Indole</sub>H), 118.6 (C<sub>Indole</sub>H), 119.9 (C<sub>Indole</sub>H), 120.9 (C<sub>Indole</sub>C), 121.3 (C<sub>Indole</sub>H), 122.1 (C<sub>Indole</sub>C), 127.5 (C<sub>Indole</sub>H), 134.0 (C<sub>QH</sub>), 135.7 (C<sub>QC</sub>), 142.4 (C<sub>QC</sub>), 145.2 (C<sub>QC</sub>), 186.9 (C=O), 187.1 (C=O) ppm. **IR**:  $\tilde{\nu}$  = 401 (m), 430 (m), 453 (m), 482 (m), 503 (m), 561 (m), 607 (m), 624 (m), 646 (m), 661 (m), 709 (m), 740 (s), 765 (m), 819 (m), 844 (m), 891 (m), 908 (m), 972 (m), 995 (m), 1012 (m), 1035 (m), 1053 (m), 1103 (m), 1122 (m), 1159 (m), 1197 (m), 1215 (m), 1251 (m), 1303 (m), 1357 (m), 1379 (m), 1425 (m), 1438 (m), 1458 (m), 1490



**Table 4.6** Responses for DoE with (methylquinoyl)ferrocene **76**.

<b>Run</b>	<b>Response (3 h)</b>
1	0.00
2	0.43
3	0.32
4	0.00
5	0.33
6	0.00
7	0.14
8	0.43
9	0.00
10	1.17
11	0.00
12	0.00
13	0.57
14	0.59
15	0.00
16	0.00
17	0.00
18	0.00
19	0.36
20	0.21
21	1.54
22	0.00
23	1.05
24	–
25	0.00
26	0.00
27	0.19
28	0.80
29	0.00
30	0.00
31	1.03
32	0.00

(m), 1508 (m), 1560 (m), 1618 (m), 1629 (m), 1639 (m), 2918 (m), 2926 (m), 2960 (m), 3367 (m)  $\text{cm}^{-1}$ . HRMS (ESI):  $m/z$  calc. for  $\text{C}_{25}\text{H}_{19}\text{NO}_2\text{NaFe}$   $[\text{M}+\text{Na}]^+$ : 444.0663, found: 444.0669.

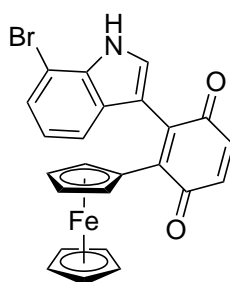
#### 4.2.4 ((Indolyl)quinoyl)ferrocene Library

##### General Procedure 1 (GP 1)

The experiment was carried out in the parallel synthesizer. Before the automated run, stock solutions of quinoylferrocene (Solution A, **41**, 1145 mg in 2-methyl-THF (29.4 mL)) and (methylquinoyl)ferrocene (Solution B, **76**, 527 mg in 2-methyl-THF ((12.9 mL))) were prepared.

A single reactor block was subjected to the standard drying/gas purge procedure. The block was disassembled, and  $\text{Ag}_2\text{O}$  (93 mg, 0.40 mmol, 1.0 equiv.), NaOAc (33 mg, 0.40 mmol, 1.0 equiv.) were added to eleven reactors in total. Indoles **83**, **84**, **85**, **86**, **87**, **88**, **89** and **90** (0.40 mmol, 1.0 equiv.) were added to reactors 1 – 8, and indoles **83**, **85** and **86** (0.40 mmol, 1.0 equiv.) were added to reactors 9 – 11. The reactor block was closed and equipped with a custom LED photoreactor array ( $\lambda = 730 \text{ nm}$ ). Solution A (3000  $\mu\text{L}$ , 0.40 mmol, 1.0 equiv.) was automatically aliquoted to reactors 1 – 8, and Solution B (3000  $\mu\text{L}$ , 0.40 mmol, 1.0 equiv.) was aliquoted to reactors 9 – 11. All stock solutions were placed into their tray positions, and the 10 mL syringe pump was primed with acetone. The photoreactor was switched on, and all samples were incubated at (600 rpm, 17 h). Reaction progress was monitored using automated TLC-MS, and reactions with visible product formation were automatically collected and concentrated to dryness.

##### 2-(7-bromo-1H-indol-3-yl)-3-(ferrocenyl)benzoquinone (**91**)

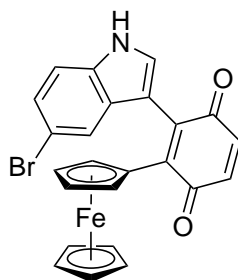


**91**

GP 1, reactor 1, indole **83** (78 mg, 0.40 mmol, 1.0 equiv.). After automated column chromatography (PE/EtOAc 9:1 → 1:1), the target compound **91** was obtained as a deep purple oil (19 mg, 0.04 mmol, 10%).

<sup>1</sup>H-NMR (400 MHz, CDCl<sub>3</sub>): δ = 4.1 (s, 5H, C<sub>5</sub>H<sub>5</sub>), 4.34 - 4.27 (m, 2H, CpH), 4.45 - 4.38 (m, 2H, CpH), 6.86 (s, 2H, QH), 7.11 (d, *J* = 0.8 Hz, 1H, C<sub>Indole</sub>H), 7.2 (d, *J* = 1.2 Hz, 2H, C<sub>Indole</sub>H), 7.38 (d, *J* = 2.6 Hz, 1H, C<sub>Indole</sub>H), 8.49 (s, 1H, NH) ppm. <sup>13</sup>C-NMR (100 MHz, CDCl<sub>3</sub>): δ = 70.3 (C<sub>5</sub>H<sub>5</sub>), 70.6 (C<sub>Cp</sub>H), 72.3 (C<sub>Cp</sub>H), 78.3 (C<sub>Cp</sub>C), 109.6 (C<sub>Indole</sub>Br), 112.5 (C<sub>Indole</sub>H), 113.3 (C<sub>Indole</sub>H), 123.7 (C<sub>Indole</sub>H), 125.1 (C<sub>Indole</sub>H), 127.0 (C<sub>Indole</sub>C), 128.7 (C<sub>Indole</sub>H), 133.1 (C<sub>QC</sub>), 134.3 (C<sub>Indole</sub>C), 136.4 (C<sub>QH</sub>), 137.1 (C<sub>QH</sub>), 143.1 (C<sub>QC</sub>), 186.1 (C=O), 186.7 (C=O) ppm. IR:  $\tilde{\nu}$  = 424 (m), 449 (m), 466 (s), 476 (s), 584 (m), 605 (m), 630 (m), 669 (m), 698 (m), 746 (m), 775 (m), 794 (m), 817 (m), 840 (m), 864 (m), 885 (m), 918 (m), 987 (m), 1001 (m), 1043 (m), 1055 (m), 1087 (m), 1105 (m), 1138 (m), 1203 (m), 1213 (m), 1232 (m), 1261 (m), 1286 (m), 1303 (m), 1340 (m), 1381 (m), 1411 (m), 1446 (m), 1502 (m), 1550 (m), 1560 (m), 1612 (m), 1643 (s), 1697 (m), 1701 (m), 2968 (m), 3342 (m) cm<sup>-1</sup>. MS (APCI): *m/z* calc. for C<sub>24</sub>H<sub>16</sub>BrFeNO<sub>2</sub> [M+H]<sup>+</sup>: 486.0, found: 486.2.

## 2-(5-bromo-1*H*-indol-3-yl)-3-(ferrocenyl)benzoquinone (**92**)



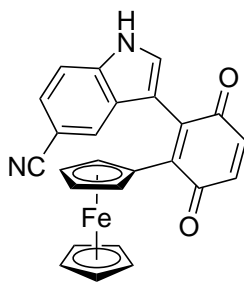
**92**

GP 1, reactor 3, indole **85** (78 mg, 0.40 mmol, 1.0 equiv.). After automated column chromatography (PE/EtOAc 9:1 → 1:1), the target compound **92** was obtained as a deep purple oil (21 mg, 0.04 mmol, 11%).

<sup>1</sup>H-NMR (400 MHz, CDCl<sub>3</sub>): δ = 4.09 (s, 5H, C<sub>5</sub>H<sub>5</sub>), 4.29 (t, *J* = 2.0 Hz, 2H, CpH), 4.43 (s, 2H, CpH), 7.04 - 6.71 (m, 2H, C<sub>Indole</sub>H), 6.86 (d, *J* = 0.7 Hz, 2H, QH), 7.30 - 7.20 (m, 1H, C<sub>Indole</sub>H), 7.48 (d, *J* = 2.6 Hz, 1H, C<sub>Indole</sub>H), 8.62 (s, 1H, NH) ppm. <sup>13</sup>C-NMR (100 MHz, CDCl<sub>3</sub>): δ = 70.3 (C<sub>5</sub>H<sub>5</sub>), 70.7 (C<sub>Cp</sub>H), 72.4 (C<sub>Cp</sub>H), 78.2 (C<sub>Cp</sub>C), 104.6 (C<sub>Indole</sub>Br), 111.1 (C<sub>Indole</sub>H), 120.2 (C<sub>Indole</sub>H), 121.1 (C<sub>Indole</sub>H), 124.6 (C<sub>Indole</sub>H), 126.4 (C<sub>Indole</sub>C), 128.1 (C<sub>Indole</sub>H), 132.9 (C<sub>QC</sub>), 134.4 (C<sub>Indole</sub>C), 136.4 (C<sub>QH</sub>), 137.0 (C<sub>QH</sub>), 143.2 (C<sub>QC</sub>), 186.0 (C=O), 186.8 (C=O) ppm. IR:  $\tilde{\nu}$  = 412 (m), 447 (s), 470 (s), 487 (s), 499 (s), 549 (m), 559 (m), 570 (m), 611 (s), 626 (m), 634 (m), 671 (m), 698 (m), 738 (m), 775 (s), 812 (s), 842 (m), 867 (m), 885 (m), 918 (m), 954 (m), 985 (m), 1001 (m),

1037 (m), 1049 (s), 1087 (s), 1105 (s), 1159 (m), 1199 (s), 1232 (m), 1276 (s), 1290 (m), 1303 (m), 1332 (m), 1342 (m), 1369 (m), 1382 (m), 1415 (m), 1433 (m), 1442 (m), 1490 (m), 1498 (s), 1546 (m), 1560 (m), 1614 (m), 1643 (s), 1718 (m), 1724 (m), 2850 (m), 2920 (m), 2953 (m), 3350 (m)  $\text{cm}^{-1}$ . **MS (APCI):**  $m/z$  calc. for  $\text{C}_{24}\text{H}_{16}\text{BrFeNO}_2$   $[\text{M}+\text{H}]^+$ : 486.0, found: 486.2.

### 2-(5-cyano-1H-indol-3-yl)-3-(ferrocenyl)benzoquinone (93)

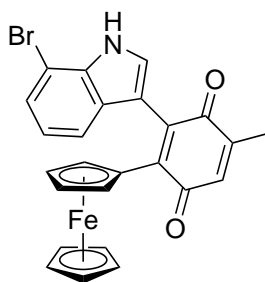


93

GP 1, reactor 4, indole **86** (57 mg, 0.40 mmol, 1.0 equiv.). After automated column chromatography (PE/EtOAc 9:1  $\rightarrow$  1:1), the target compound **93** was obtained as a deep purple oil (18 mg, 0.04 mmol, 11 %).

**$^1\text{H-NMR}$**  (400 MHz,  $\text{CDCl}_3$ ):  $\delta$  = 4.1 (s, 5H,  $\text{C}_5\text{H}_5$ ), 4.32 (d,  $J$  = 1.9 Hz, 2H, CpH), 4.39 (s, 2H, CpH), 6.88 (s, 2H, QH), 7.33 - 7.31 (m, 1H,  $\text{C}_{\text{IndoleH}}$ ), 7.35 (dd,  $J$  = 1.5, 8.4 Hz, 1H,  $\text{C}_{\text{IndoleH}}$ ), 7.4 (dd,  $J$  = 0.8, 8.5 Hz, 1H,  $\text{C}_{\text{IndoleH}}$ ), 7.54 (d,  $J$  = 2.6 Hz, 1H,  $\text{C}_{\text{IndoleH}}$ ), 8.77 (s, 1H, NH) ppm.  
 **$^{13}\text{C-NMR}$**  (100 MHz,  $\text{CDCl}_3$ ):  $\delta$  = 70.4 ( $\text{C}_5\text{H}_5$ ), 70.9 ( $\text{C}_{\text{CpH}}$ ), 72.4 ( $\text{C}_{\text{CpH}}$ ), 78.0 ( $\text{C}_{\text{CpC}}$ ), 103.3 ( $\text{C}_{\text{IndoleC}}$ ), 110.7 ( $\text{C}_{\text{IndoleH}}$ ), 112.1 ( $\text{C}_{\text{CyanoN}}$ ), 120.3 ( $\text{C}_{\text{IndoleH}}$ ), 125.0 ( $\text{C}_{\text{IndoleH}}$ ), 125.2 ( $\text{C}_{\text{IndoleH}}$ ), 126.6 ( $\text{C}_{\text{IndoleC}}$ ), 129.6 ( $\text{C}_{\text{IndoleH}}$ ), 132.2 ( $\text{C}_{\text{QC}}$ ), 136.4 ( $\text{C}_{\text{IndoleC}}$ ), 137.1 ( $\text{C}_{\text{QH}}$ ), 137.3 ( $\text{C}_{\text{QH}}$ ), 143.8 ( $\text{C}_{\text{QC}}$ ), 185.8 (C=O), 186.4 (C=O) ppm. **IR:**  $\tilde{\nu}$  = 422 (m), 447 (m), 462 (m), 474 (m), 493 (m), 509 (m), 578 (m), 588 (m), 642 (m), 671 (m), 686 (m), 731 (m), 758 (m), 786 (m), 813 (s), 829 (m), 842 (m), 869 (m), 885 (m), 916 (m), 985 (m), 1001 (m), 1037 (m), 1047 (m), 1078 (m), 1097 (m), 1105 (m), 1178 (m), 1205 (m), 1213 (m), 1234 (m), 1247 (m), 1278 (m), 1296 (m), 1321 (m), 1352 (m), 1371 (m), 1382 (m), 1396 (m), 1438 (m), 1458 (m), 1469 (m), 1502 (m), 1554 (m), 1577 (m), 1610 (m), 1641 (m), 1697 (m), 1701 (m), 2220 (m), 3323 (m)  $\text{cm}^{-1}$ . **MS (APCI):**  $m/z$  calc. for  $\text{C}_{25}\text{H}_{16}\text{FeN}_2\text{O}_2$   $[\text{M}+\text{H}]^+$ : 433.1, found: 432.7.

## 2-(7-bromo-1*H*-indol-3-yl)-3-(ferrocenyl)-5-methylbenzoquinone (**98**)



**98**

GP 1, reactor 9, indole **83** (78 mg, 0.40 mmol, 1.0 equiv.). After automated column chromatography (PE/EtOAc 9:1 → 1:1), the target compound **98** was obtained as a deep purple oil (12 mg, 0.02 mmol, 7%)

**<sup>1</sup>H-NMR** (400 MHz, CDCl<sub>3</sub>): δ = 2.17 (d, *J* = 1.6 Hz, 3H, CH<sub>3</sub>), 4.09 (s, 4H, C<sub>5</sub>H<sub>5</sub>), 4.32 - 4.23 (m, 2H, CpH), 4.39 (s, 2H, CpH), 6.71 (d, *J* = 1.6 Hz, 1H, QH), 7.16 - 7.10 (m, 1H, C<sub>Indole</sub>H), 7.25 - 7.19 (m, 2H, C<sub>Indole</sub>H), 7.37 (d, *J* = 2.6 Hz, 1H, C<sub>Indole</sub>H), 8.44 (s, 1H, NH) ppm. **<sup>13</sup>C-NMR** (100 MHz, CDCl<sub>3</sub>): δ = 70.2 (C<sub>5</sub>H<sub>5</sub>), 70.4 (C<sub>Cp</sub>H), 72.3 (C<sub>Cp</sub>H), 78.2 (C<sub>Cp</sub>C), 110.0 (C<sub>Indole</sub>C), 112.4 (C<sub>Indole</sub>H), 113.3 (C<sub>Indole</sub>H), 123.6 (C<sub>Indole</sub>H), 125.1 (C<sub>Indole</sub>H), 127.2 (C<sub>Indole</sub>C), 128.3 (C<sub>Indole</sub>H), 133.2 (C<sub>QC</sub>), 134.1 (C<sub>Indole</sub>C), 134.2 (C<sub>QH</sub>), 143.0 (C<sub>QH</sub>), 145.2 (C<sub>QC</sub>), 186.5 (C=O), 186.8 (C=O) ppm. **MS (APCI)**: *m/z* calc. for C<sub>25</sub>H<sub>18</sub>BrFeNO<sub>2</sub> [M+H]<sup>+</sup>: 500.0, found: 500.2.

### 4.2.5 Ferrocenylcarboxamide Library

#### General Procedure 2 (GP 2)

The experiment was carried out in the parallel synthesizer. Before the automated run, the stock solutions in **Table 4.7** were prepared:

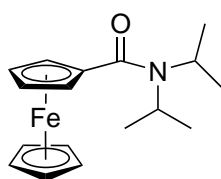
**Table 4.7** Stock solutions for the automated synthesis of ferrocenylcarboxamides. All solutions in dry dichloromethane, if not stated otherwise.

Identifier	Substance	Amount (mg)	Volume DCM (mL)
A	Ferrocenoyl Chloride ( <b>105</b> )	1750.3	35.0
B	Triethylamine	2474.7	0 (neat)
C	2-aminoethanol ( <b>109</b> )	72.8	1.5
D	Diisopropylamine ( <b>108</b> )	126.9	1.5
E	Weinreb amine ( <b>110</b> )	55.3	1.5
F	(S)-(+)-2-(Methoxymethyl)pyrrolidine ( <b>111</b> )	104.3	1.5
G	1-Methylpiperazine ( <b>112</b> )	90.7	1.5
H	Pyrazole ( <b>113</b> )	61.7	1.5
I	N-methyl-2-phenylethan-1-amine ( <b>114</b> )	122.4	1.5
J	2-(Isopropyl)-5-methylcyclohexylamine ( <b>115</b> )	140.6	1.5
K	pyridin-2-ylmethanamine ( <b>116</b> )	97.9	1.5
L	Tricyclo(3.3.1.1 <sup>3,7</sup> )dec-1-ylmethanamine ( <b>117</b> )	149.7	1.5
M	8-aminoquinoline ( <b>118</b> )	130.6	1.5
N	2,4-Dichlorobenzylamine ( <b>119</b> )	159.4	1.5
O	3-Nitrobenzylamine ( <b>120</b> )	137.8	1.5
P	Diethylamine ( <b>121</b> )	93.7	1.5
Q	2-Butanamine, (S)- ( <b>122</b> )	66.2	1.5
R	Bis(alpha-methylbenzyl)amine, (+)- ( <b>123</b> )	204.1	1.5

A single reactor block was subjected to the standard drying/gas purge procedure. All Stock solutions were placed into their tray positions, and the 10 mL syringe pump was primed with acetone. Solution A (2000  $\mu\text{L}$ , 0.4 mmol, 1.0 equiv.) was aliquoted to reactors 1 – 16. The reactor block was cooled to 0 °C, and stirred at 600 rpm. Solution B (112  $\mu\text{L}$ , 0.81 mmol, 2.0 equiv.) was aliquoted to reactors 1 – 16, and subsequently Solutions C – R (1000  $\mu\text{L}$ , 0.60 mmol, 1.5 equiv.) were dispensed to one reactor each (1 – 16). The reactor block was warmed to 23 °C, and stirring was continued for 16 h using the “wait for user input” command. Automated TLC (n-Heptane/EtOAc 9:1, then 4:1) was carried out, and product spots were identified using TLC-MS. All reactions were evaporated to dryness, and fresh dichloromethane (2.0 mL) and aqueous HCl (1 mol L<sup>-1</sup>, 2.0 mL) were aliquoted to all reactors. The reactor block was stirred vigorously

at 1000 rpm for 1 min, and the aqueous layers were discarded using a preset needle aspiration height. This cycle was repeated with saturated aqueous NaHCO<sub>3</sub> (2.0 mL), and finally with saturated aqueous NaCl (2.0 mL). One SPE cartridge per reaction was equipped with a filter frit and MgSO<sub>4</sub> (300 mg), and preconditioned with DCM (1.0 mL), and all organic phases were dispensed slowly onto their respective SPE cartridge. Each filtrate was evaporated manually with silica (1 g), and sequentially subjected to automated column chromatography (PE/EtOAc 9:1 → 1:1 ("non-polar gradient") or 4:1 → 1:1 ("polar gradient")). Product fractions were each concentrated on the rotary evaporator, and finally evaporated to dryness simultaneously on a BUECHI Syncore parallel evaporator.

***N,N*-Diisopropylferrocenylcarboxamide (107)**<sup>[166]</sup>

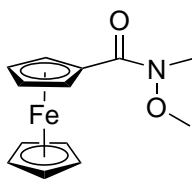


**107**

GP 2, Solution D, non-polar gradient. The product **107** was obtained as an orange oil (15 mg, 0.05 mmol, 12%). Identification through spectral comparison.<sup>[166]</sup>

<sup>1</sup>H-NMR (400 MHz, CDCl<sub>3</sub>):  $\delta$  = 1.27 (bs, 6H, CH<sub>3</sub>), 1.47 (bs, 6H, CH<sub>3</sub>), 3.43 (bs, 1H, CH), 4.23 (s, 5H, C<sub>5</sub>H<sub>5</sub>), 4.27 (t,  $J$  = 2.0 Hz, 2H, CpH), 4.56 (t,  $J$  = 2.0 Hz, 2H, CpH), 4.61 (bs, 1H, CH) ppm.

***N*-Methoxy-*N*-methylferrocenylcarboxamide (19)**

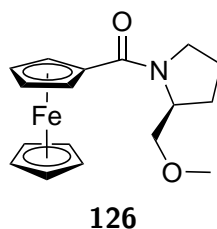


**19**

GP 2, Solution E, non-polar gradient. The product **19** was obtained as an orange oil (20 mg, 0.07 mmol, 18%). Identification through spectral comparison.<sup>[112]</sup>

<sup>1</sup>H-NMR (400 MHz, CDCl<sub>3</sub>):  $\delta$  = 3.33 (s, 3H, NCH<sub>3</sub>), 3.76 (s, 3H, OCH<sub>3</sub>), 4.23 (s, 5H, C<sub>5</sub>H<sub>5</sub>), 4.4 (t,  $J$  = 2.0 Hz, 2H, CpH), 4.93 (t,  $J$  = 2.0 Hz, 2H, CpH) ppm.

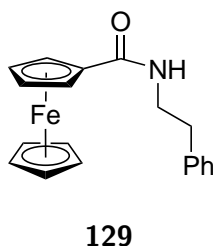
**(S)-2-(2-(methoxymethyl)pyrrolidin-1-yl)(ferrocenyl)methanone (126)**



GP 2, Solution F, non-polar gradient. The product **126** was obtained as an orange-brown solid (65 mg, 0.20 mmol, 50 %).

<sup>1</sup>H-NMR (400 MHz, CDCl<sub>3</sub>):  $\delta$  = 2.09 - 1.82 (m, 5H, CH<sub>2</sub>), 3.38 (s, 3H, CH<sub>2</sub>), 3.73 - 3.53 (m, 3H, OCH<sub>3</sub>), 3.83 (s, 1H, CH), 4.2 (s, 5H, C<sub>5</sub>H<sub>5</sub>), 4.40 - 4.29 (m, 1H, CpH), 4.43 (s, 1H, CpH), 4.71 (s, 1H, CpH), 4.79 (s, 1H, CpH) ppm. <sup>13</sup>C-NMR (100 MHz, CDCl<sub>3</sub>):  $\delta$  = 25.4 (CH<sub>2</sub>), 27.4 (CH<sub>2</sub>), 49.0 (CH<sub>2</sub>), 57.7 (CH<sub>2</sub>), 59.2 (OCH<sub>3</sub>), 70.2 (C<sub>5</sub>H<sub>5</sub>), 70.2 (CpH), 71.5 (CpH), 72.7 (CH), 69.8 (CpH), 70.5 (CpH), 169.6 (C=O) ppm. IR:  $\tilde{\nu}$  = 428.2 (m), 441.7 (s), 480.28 (s), 497.63 (s), 549.71 (m), 570.93 (m), 594.08 (m), 619.15 (m), 686.66 (m), 761.88 (m), 775.38 (m), 798.53 (m), 808.17 (m), 835.18 (s), 869.9 (m), 898.83 (m), 921.97 (m), 974.05 (m), 997.2 (m), 1020.34 (m), 1031.92 (m), 1055.06 (m), 1068.56 (s), 1101.35 (s), 1109.07 (s), 1165.0 (m), 1184.29 (m), 1201.65 (m), 1220.94 (m), 1253.73 (m), 1296.16 (m), 1334.74 (m), 1371.39 (s), 1381.03 (s), 1402.25 (s), 1458.18 (s), 1535.34 (m), 1602.85 (s), 1654.92 (m), 1683.86 (m), 2808.36 (m), 2827.64 (m), 2868.15 (m), 2891.3 (m), 2937.59 (m), 2960.73 (m), 2978.09 (m), 3091.89 (m), 3111.18 (m) cm<sup>-1</sup>. HRMS (ESI): *m/z* calc. for C<sub>17</sub>H<sub>21</sub>FeNO [M+Na]<sup>+</sup>: 350.0817, found: 350.0810.

**N-Phenethylferrocenylcarboxamide (129)**

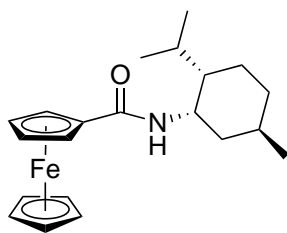


GP 2, Solution I, non-polar gradient. The product **129** was obtained as an orange-brown solid (53 mg, 0.15 mmol, 38 %). Identification through spectral comparison.<sup>[114]</sup>

<sup>1</sup>H-NMR (400 MHz, CDCl<sub>3</sub>):  $\delta$  = 3.04 - 2.84 (m, 2H, CH<sub>2</sub>), 3.1 (bs, 2H, CpH), 3.79 - 3.66 (m, 2H, CH<sub>2</sub>), 4.22 (s, 5H, C<sub>5</sub>H<sub>5</sub>), 4.35 - 4.28 (m, 1H, NH), 4.6 (s, 2H, CpH), 7.41 - 7.18 (m, 5H, C<sub>Ph</sub>) ppm.



***N*-((1*S*,2*S*,5*R*)-2-isopropyl-5-methylcyclohexyl)ferrocenylcarboxamide (130)**

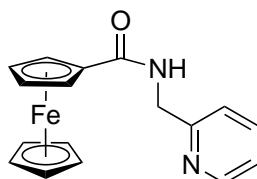


**130**

GP 2, Solution J, non-polar gradient. The product **130** was obtained as an orange-brown solid (38 mg, 0.10 mmol, 26 %).

<sup>1</sup>H-NMR (400 MHz, CDCl<sub>3</sub>): δ (ppm) = 0.97 - 0.85 (m, 11H, CH<sub>2</sub>, CH<sub>3</sub>), 1.23 - 1.09 (m, 2H, CH, CH<sub>2</sub>), 1.62 - 1.37 (m, 1H, CH), 1.86 - 1.68 (m, 2H, CH<sub>2</sub>), 2.24 - 1.86 (m, 2H, CH, CH<sub>2</sub>), 3.92 (tdd, *J* = 4.1, 9.6, 11.0 Hz, 1H, C<sub>*i*</sub>PrH), 4.19 (s, 5H, C<sub>5</sub>H<sub>5</sub>), 4.33 (ddt, *J* = 0.7, 1.5, 2.2 Hz, 2H, CpH), 4.65 (ddt, *J* = 1.5, 2.2, 17.9 Hz, 2H, CpH), 5.32 (d, *J* = 9.6 Hz, 1H, NH). <sup>13</sup>C-NMR (100 MHz, CDCl<sub>3</sub>): δ (ppm) = 16.5 (CH<sub>3</sub>), 21.4 (CH<sub>3</sub>), 22.4 (CH<sub>3</sub>), 24.0 (CH<sub>2</sub>), 27.2 (CH<sub>2</sub>), 32.1 (CH), 34.7 (CH<sub>2</sub>), 43.6 (CH<sub>2</sub>), 48.7 (CH), 49.9 (C<sub>*i*</sub>Pr), 67.8 (C<sub>Cp</sub>H), 68.4 (C<sub>Cp</sub>H), 69.8 (C<sub>5</sub>H<sub>5</sub>), 70.4 (C<sub>Cp</sub>H), 70.4 (C<sub>Cp</sub>H), 76.8 (C<sub>Cp</sub>C), 169.3 (C=O). IR:  $\tilde{\nu}$  = 430.13 (w), 447.49 (w), 482.2 (s), 495.71 (s), 513.07 (m), 574.79 (w), 586.36 (w), 601.79 (w), 684.73 (w), 732.95 (w), 759.95 (w), 773.46 (w), 815.89 (m), 833.25 (w), 842.89 (w), 867.97 (w), 881.47 (w), 923.9 (w), 970.19 (w), 1006.84 (m), 1028.06 (w), 1045.42 (w), 1058.92 (w), 1109.07 (m), 1147.65 (w), 1176.58 (w), 1224.8 (w), 1236.37 (w), 1263.37 (w), 1294.24 (m), 1303.88 (m), 1336.67 (w), 1357.89 (w), 1382.96 (m), 1415.75 (w), 1452.4 (w), 1531.48 (s), 1618.28 (s), 2866.22 (w), 2924.09 (m), 2947.23 (w), 3084.18 (w), 3099.61 (w), 3107.32 (w), 3300.2 (w) cm<sup>-1</sup>. HRMS (ESI): *m/z* calc. for C<sub>21</sub>H<sub>29</sub>FeNO [M+Na]<sup>+</sup>: 390.1496, found: 390.1499.

***N*-(Pyridin-2-ylmethyl)ferrocenylcarboxamide (131)**

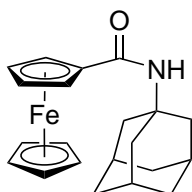


**131**

GP1, Solution K, non-polar gradient. The product **131** was obtained as an orange-brown solid (17 mg, 0.05 mmol, 13 %). Identification through spectral comparison.<sup>[115]</sup>

**<sup>1</sup>H-NMR** (400 MHz, CDCl<sub>3</sub>):  $\delta$  = 4.17 (s, 5H, C<sub>5</sub>H<sub>5</sub>), 4.38 - 4.30 (m, 2H, CpH), 4.67 (d,  $J$  = 5.1 Hz, 2H, CH<sub>2</sub>), 4.80 - 4.71 (m, 2H, CpH), 7.0 (s, 1H, PyH), 7.25 - 7.19 (m, 1H, PyH), 7.35 (dt,  $J$  = 0.8, 7.8 Hz, 1H, PyH), 7.69 (td,  $J$  = 1.8, 7.8 Hz, 1H, PyH), 8.58 (ddd,  $J$  = 0.8, 1.8, 5.1 Hz, 1H, PyH) ppm.

***N*-((3*s*,5*s*,7*s*)-adamantan-1-yl)ferrocenylcarboxamide (132)**

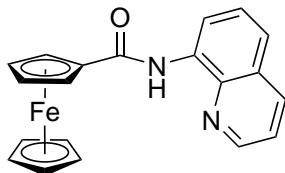


**132**

GP 2, Solution L, polar gradient. The product **132** was obtained as an orange-brown solid (53 mg, 0.14 mmol, 34 %). Identification through spectral comparison.<sup>[116]</sup>

**<sup>1</sup>H-NMR** (400 MHz, DMSO-d<sub>6</sub>):  $\delta$  = 1.52 (s, 6H, C<sub>Adamantyl</sub>H<sub>2</sub>), 1.76 - 1.57 (m, 6H, C<sub>Adamantyl</sub>H<sub>2</sub>), 1.96 (s, 3H, C<sub>Adamantyl</sub>H), 4.19 (s, 5H, C<sub>5</sub>H<sub>5</sub>), 4.34 (s, 2H, CpH), 4.84 (s, 2H, CpH), 6.77 - 6.31 (m, 1H, NH) ppm.

***N*-(quinolin-8-yl)ferrocenylcarboxamide (102)**

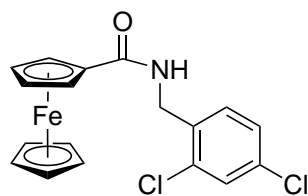


**102**

GP 2, Solution M, polar gradient. The product **102** was obtained as an orange-brown oil (58 mg, 0.16 mmol, 41 %). Identification through spectral comparison.<sup>[102]</sup>

**<sup>1</sup>H-NMR** (400 MHz, CDCl<sub>3</sub>):  $\delta$  = 7.57 - 7.49 (m, 2H, C<sub>Cp</sub>H), 4.32 (s, 5H, C<sub>5</sub>H<sub>5</sub>), 4.56 - 4.40 (m, 2H, C<sub>Cp</sub>H), 5.08 - 4.92 (m, 2H, NCHCH, NHCCHCH), 7.64 - 7.58 (m, 1H, NHCCH), 8.22 (dd,  $J$  = 1.7, 8.3 Hz, 1H, NHCCCCH), 8.83 (dd,  $J$  = 1.4, 7.6 Hz, 1H, NCHCHCH), 8.92 (dd,  $J$  = 1.7, 4.2 Hz, 1H, NCH), 10.32 (s, 1H, NH) ppm.

### N-(2,4-dichlorobenzyl)ferrocenylcarboxamide (133)

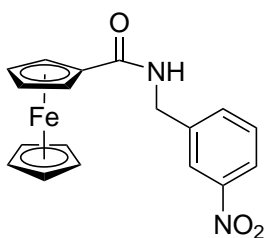


133

GP 2, Solution N, non-polar gradient. The product **133** was obtained as an orange-brown solid (54 mg, 0.14 mmol, 35 %).

$^1\text{H-NMR}$  (400 MHz,  $\text{CDCl}_3$ ):  $\delta$  (ppm) = 4.1 (s, 5H,  $\text{C}_5\text{H}_5$ ), 4.40 - 4.33 (m, 2H, CpH), 4.6 (d,  $J = 6.2$  Hz, 2H,  $\text{CH}_2$ ), 4.70 - 4.64 (m, 2H, CpH), 6.27 - 6.08 (m, 1H, NH), 7.3 (dd,  $J = 8.2, 2.1$  Hz, 1H, ArH), 7.4 (d,  $J = 2.1$  Hz, 1H, ArH), 7.5 (d,  $J = 8.2$  Hz, 1H, ArH).  $^{13}\text{C-NMR}$  (100 MHz,  $\text{CDCl}_3$ ):  $\delta$  (ppm) = 41.4 ( $\text{CH}_2$ ), 68.3 ( $\text{C}_{\text{CpH}}$ ), 69.8 ( $\text{C}_5\text{H}_5$ ), 70.8 ( $\text{C}_{\text{CpH}}$ ), 75.5 ( $\text{C}_{\text{CpC}}$ ), 127.6 ( $\text{C}_{\text{ArH}}$ ), 129.5 ( $\text{C}_{\text{ArH}}$ ), 131.9 ( $\text{C}_{\text{ArH}}$ ), 133.0 ( $\text{C}_{\text{ArC}}$ ), 134.3 ( $\text{C}_{\text{ArCl}}$ ), 134.9 ( $\text{C}_{\text{ArCl}}$ ), 170.5 ( $\text{C}=\text{O}$ ). IR:  $\tilde{\nu} = 420.48$  (m), 432.05 (m), 459.06 (s), 486.06 (s), 501.49 (s), 520.78 (m), 534.28 (m), 545.85 (w), 570.93 (w), 588.29 (m), 601.79 (w), 655.8 (m), 688.59 (s), 748.38 (s), 779.24 (m), 810.1 (m), 827.46 (s), 860.25 (m), 902.69 (w), 948.98 (m), 991.41 (m), 1001.06 (m), 1024.2 (m), 1037.7 (m), 1045.42 (m), 1068.56 (m), 1103.28 (m), 1176.58 (w), 1201.65 (m), 1224.8 (w), 1257.59 (m), 1269.16 (m), 1301.95 (s), 1375.25 (m), 1417.68 (m), 1440.83 (m), 1446.61 (m), 1467.83 (m), 1487.12 (m), 1537.27 (s), 1560.41 (w), 1591.27 (w), 1627.92 (s), 2852.72 (w), 2922.16 (w), 3030.17 (w), 3080.32 (w), 3307.92 (w)  $\text{cm}^{-1}$ . HRMS (ESI):  $m/z$  calc. for  $\text{C}_{18}\text{H}_{15}\text{Cl}_2\text{FeNO}$  [ $\text{M}+\text{Na}$ ] $^+$ : 409.9778, found: 409.9778.

### N-(3-nitrobenzyl)ferrocenylcarboxamide (134)

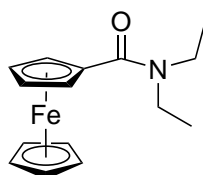


134

GP 2, Solution O, polar gradient. The product **134** was obtained as a brown solid (32 mg, 0.09 mmol, 22 %).

**<sup>1</sup>H-NMR** (400 MHz, CDCl<sub>3</sub>): δ (ppm) = 4.2 (s, 5H, C<sub>5</sub>H<sub>5</sub>), 4.45 - 4.34 (m, 2H, CpH), 4.69 - 4.65 (m, 2H, CH<sub>2</sub>), 4.76 - 4.64 (m, 2H, CpH), 6.2 (s, 1H, NH), 7.53 (t, *J* = 7.8, 7.8 Hz, 1H, ArH), 7.73 (d, *J* = 7.8 Hz, 1H, ArH), 8.15 (dd, *J* = 7.8, 2.1 Hz, 1H, ArH), 8.23 (s, 1H, ArH). **<sup>13</sup>C-NMR** (100 MHz, CDCl<sub>3</sub>): δ (ppm) = 42.9 (CH<sub>2</sub>), 68.3 (C<sub>5</sub>H<sub>5</sub>), 69.9 (C<sub>Cp</sub>H), 70.9 (C<sub>Cp</sub>H), 75.5 (C<sub>Cp</sub>C), 122.4 (C<sub>Ar</sub>H), 122.6 (C<sub>Ar</sub>H), 129.8 (C<sub>Ar</sub>H), 134.0 (C<sub>Ar</sub>H), 141.6 (C<sub>Ar</sub>C), 148.9 (C<sub>Ar</sub>NO<sub>2</sub>), 171.2 (C=O). **IR**:  $\tilde{\nu}$  = 406.98 (w), 426.27 (w), 480.28 (s), 509.21 (m), 563.21 (w), 597.93 (w), 644.22 (w), 669.3 (w), 692.44 (w), 727.16 (w), 738.74 (w), 783.1 (w), 823.6 (m), 914.26 (w), 1002.98 (w), 1028.06 (w), 1053.13 (w), 1107.14 (w), 1157.29 (m), 1195.87 (w), 1219.01 (w), 1280.73 (m), 1346.31 (m), 1413.82 (w), 1473.62 (m), 1527.62 (m), 1560.41 (w), 1649.14 (m), 1654.92 (m), 1701.22 (w), 2852.72 (w), 2922.16 (w), 3076.46 (w) cm<sup>-1</sup>. **HRMS (ESI)**: *m/z* calc. for C<sub>18</sub>H<sub>16</sub>FeN<sub>2</sub>O<sub>3</sub> [M+Na]<sup>+</sup>: 387.0406, found: 387.0399.

#### *N,N*-diethylferrocenylcarboxamide (**135**)

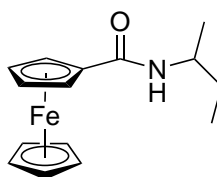


**135**

GP 2, Solution P, non-polar gradient. The product **135** was obtained as an orange-brown solid (60 mg, 0.21 mmol, 53 %). Identification through spectral comparison.<sup>[117]</sup>

**<sup>1</sup>H-NMR** (400 MHz, CDCl<sub>3</sub>): δ = 1.22 (t, *J* = 7.1 Hz, 6H, CH<sub>3</sub>), 3.51 (s, 4H, CH<sub>2</sub>), 4.22 (s, 5H, C<sub>5</sub>H<sub>5</sub>), 4.29 (t, *J* = 2.0 Hz, 2H, C<sub>Cp</sub>H), 4.62 (t, *J* = 2.0 Hz, 2H, C<sub>Cp</sub>H) ppm.

#### *N*-(*sec*-butyl)ferrocenylcarboxamide (**136**)

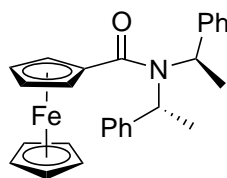


**136**

GP 2, Solution Q, polar gradient. The product **136** was obtained as a brown solid (63 mg, 0.22 mmol, 55 %).

**<sup>1</sup>H-NMR** (400 MHz, CDCl<sub>3</sub>): δ (ppm) = 0.98 (t, *J* = 7.4 Hz, 3H, CH<sub>3</sub>), 1.2 (d, *J* = 6.6 Hz, 3H, CH<sub>3</sub>), 1.61 - 1.49 (m, 2H, CH<sub>2</sub>), 4.07 (dq, *J* = 8.6, 6.6, 6.6 Hz, 1H, CH), 4.2 (s, 5H, C<sub>5</sub>H<sub>5</sub>), 4.33 (dd, *J* = 1.6, 2.2 Hz, 2H, CpH), 4.63 (dt, *J* = 1.6, 2.2 Hz, 1H, CpH), 4.66 (dt, *J* = 1.6, 2.2 Hz, 1H, CpH), 5.4 (d, *J* = 8.6 Hz, 1H, NH). **<sup>13</sup>C-NMR** (100 MHz, CDCl<sub>3</sub>): δ (ppm) = 10.6 (CH<sub>3</sub>), 21.0 (CH<sub>3</sub>), 30.0 (CH<sub>2</sub>), 46.7 (CH), 68.0 (C<sub>Cp</sub>H), 68.3 (C<sub>Cp</sub>H), 69.8 (C<sub>5</sub>H<sub>5</sub>), 70.4 (C<sub>Cp</sub>H), 70.4 (C<sub>Cp</sub>H), 76.7 (C<sub>Cp</sub>C), 169.5 (C=O). **IR:**  $\tilde{\nu}$  = 401.19 (w), 416.62 (w), 430.13 (w), 466.77 (m), 482.2 (s), 495.71 (s), 540.07 (w), 549.71 (w), 592.15 (w), 601.79 (w), 661.58 (w), 771.53 (w), 783.1 (w), 794.67 (w), 823.6 (s), 918.12 (w), 935.48 (w), 1004.91 (w), 1014.56 (w), 1031.92 (w), 1051.2 (w), 1105.21 (m), 1128.36 (w), 1149.57 (w), 1180.44 (m), 1220.94 (w), 1257.59 (w), 1294.24 (m), 1301.95 (m), 1340.53 (w), 1354.03 (w), 1379.1 (w), 1411.89 (w), 1442.75 (w), 1458.18 (w), 1533.41 (s), 1620.21 (s), 2873.94 (w), 2927.94 (w), 2964.59 (w), 3076.46 (w), 3304.06 (w) cm<sup>-1</sup>. **HRMS (ESI):** *m/z* calc. for C<sub>11</sub>H<sub>15</sub>NO [M+Na]<sup>+</sup>: 308.0714, found: 308.0714.

***N,N*-bis((*R*)-1-phenylethyl)ferrocenylcarboxamide (137)**



**137**

GP 2, Solution R, non-polar gradient. The product **137** was obtained as an orange oil with a ferrocene-based impurity in a ratio of 1:6 (97 mg, 0.22 mmol, corrected yield 55 %).

**<sup>1</sup>H-NMR** (400 MHz, CDCl<sub>3</sub>): δ (ppm) = 1.35 - 1.30 (m, 2H, CH), 1.81 (d, *J* = 6.96 Hz, 6H, CH<sub>3</sub>), 4.23 (s, 5H, C<sub>5</sub>H<sub>5</sub>), 4.3 (td, *J* = 1.33, 2.53 Hz, 1H, CpH), 4.32 (td, *J* = 1.33, 2.53 Hz, 1H, CpH), 4.69 (td, *J* = 1.33, 2.53 Hz, 1H, CpH), 4.73 (dt, *J* = 1.33, 2.53 Hz, 1H, CpH), 7.27 - 7.20 (m, 10H, PhH). **<sup>13</sup>C-NMR** (100 MHz, CDCl<sub>3</sub>): δ (ppm) = 19.3 (CH<sub>3</sub>), 24.9 (CH), 69.0 (C<sub>Cp</sub>H), 69.1 (C<sub>Cp</sub>H), 69.9 (C<sub>5</sub>H<sub>5</sub>), 70.2 (C<sub>Cp</sub>H), 70.2 (C<sub>Cp</sub>H), 81.0 (C<sub>Cp</sub>C), 127.9 (C<sub>Ph</sub>H), 128.0 (C<sub>Ph</sub>H), 128.4 (C<sub>Ph</sub>H), 141.2 (C<sub>Ph</sub>C), 170.2 (C=O). **IR:**  $\tilde{\nu}$  = 482.2 (s), 543.93 (m), 605.65 (w), 644.22 (w), 665.44 (w), 696.3 (s), 729.09 (s), 748.38 (m), 792.74 (m), 819.75 (m), 908.47 (w), 966.34 (w), 1001.06 (m), 1024.2 (m), 1043.49 (w), 1066.64 (w), 1095.57 (w), 1105.21 (w), 1161.15 (w), 1182.36 (w), 1205.51 (w), 1244.09 (w), 1298.09 (m), 1357.89 (w), 1375.25 (w), 1413.82 (w), 1446.61 (m), 1494.83 (w), 1618.28 (m), 1712.79 (w), 1768.72 (w), 2237.43 (w), 2927.94 (w), 2970.38 (w), 3028.24 (w), 3059.1 (w), 3088.03 (w) cm<sup>-1</sup>. **HRMS (ESI):** *m/z* calc. for C<sub>27</sub>H<sub>27</sub>FeNO [M+Na]<sup>+</sup>: 460.1338, found: 460.1326.

## 4.2.6 C-H Activation Library

### General Procedure 3 (GP 3)

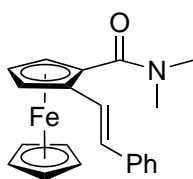
The experiment was carried out in the parallel synthesizer. Before the automated run, the stock solutions in **Table 4.8** were prepared:

**Table 4.8** Stock solutions for automated C-H activation at compounds from the ferrocenylcarboxamide library. All solutions in dry 1,2-dichloroethane, if not stated otherwise.

Identifier	Substance	Amount (mg)	Volume 1,2-DCE (mL)
A	carboxamide <b>17</b>	70.0	2.0
B	carboxamide <b>107</b>	12.2	2.0
C	carboxamide <b>19</b>	22.9	2.0
D	carboxamide <b>126</b>	70.4	2.0
E	carboxamide <b>127</b>	24.7	2.0
F	carboxamide <b>128</b>	61.5	2.0
G	carboxamide <b>129</b>	50.4	2.0
H	carboxamide <b>130</b>	40.9	2.0
I	carboxamide <b>131</b>	16.3	2.0
J	carboxamide <b>132</b>	55.8	2.0
K	carboxamide <b>102</b>	54.2	2.0
L	carboxamide <b>133</b>	54.6	2.0
M	carboxamide <b>134</b>	31.5	2.0
N	carboxamide <b>135</b>	74.4	2.0
O	carboxamide <b>136</b>	63.7	2.0
P	carboxamide <b>137</b>	104.8	2.0
Q	Cp*Co(CO)I <sub>2</sub> ( <b>153</b> )	114.4	6.6
R	AgSbF <sub>6</sub>	124.0	6.6
S	PivOH	165.2	6.6
T	PhCCH ( <b>30</b> )	613.9	6.6

A single reactor block was subjected to the standard drying/gas purge procedure. Carboxamide stock solutions were prepared automatically by placing vials with the respective masses into the parallel synthesizer, and automatically aliquoting 1,2-dichloroethane (2.0 mL) in two steps. Undissolved material was treated manually in an ultrasonic bath. All stock solutions were placed into their tray positions, and the 10 mL syringe pump was primed with acetone. Cp\*Co(CO)I<sub>2</sub> (**153**, 0.13 equiv.), PivOH (0.67 equiv.) and AgSbF<sub>6</sub> (0.26 equiv.) were aliquoted to all 16 reactors and stirred for 5 min at 600 rpm. All carboxamides (1.0 equiv.) were dispensed into one reactor each, followed by the addition of PhCCH (**30**, 3.3 equiv.) to all 16 reactors. After equilibrating the reflux circuit to 5 °C, the reactor temperature was set to 85 °C, and all reactions were stirred at 600 rpm for 27 h. After cooling to 23 °C, automated TLC (n-Heptane/EtOAc 4:1) was carried out, and product spots were identified using TLC-MS. Each reaction mixture was evaporated manually with silica (1 g), and sequentially subjected to automated column chromatography (PE/EtOAc 9:1 → 1:1). Product fractions were each concentrated on the rotary evaporator, and finally evaporated to dryness simultaneously on a BUECHI Syncore parallel evaporator.

***rac*-(E)-N,N-Dimethyl-2-styrylferrocenylcarboxamide (*rac*-31)**

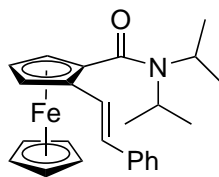


***rac*-31**

GP 3, Stock solutions Q (679 μL, 27.2 μmol, 0.13 equiv.), R (679 μL, 136.1 μmol, 0.67 equiv.), S (679 μL, 54.5 μmol, 0.27 equiv.), A (1500 μL, 272.3 μmol, 1.0 equiv.), T (679 μL, 680.6 μmol, 3.33 equiv.). After automated column chromatography (PE/EtOAc 9:1 → 1:1), the target compound *rac*-31 was obtained as an orange solid (57 mg, 0.16 mmol, 79%). Identification through spectral comparison.<sup>[37]</sup>

<sup>1</sup>H-NMR (400 MHz, CDCl<sub>3</sub>): δ = 2.96 (d, *J* = 38.2 Hz, 6H, CH<sub>3</sub>), 4.26 (s, 5H, C<sub>5</sub>H<sub>5</sub>), 4.34 (td, *J* = 0.5, 2.5, 2.5 Hz, 1H, CpH), 4.48 (dd, *J* = 1.4, 2.5 Hz, 1H, CpH), 4.65 (ddd, *J* = 0.5, 1.3, 2.5 Hz, 1H, CpH), 6.74 (d, *J* = 16.2 Hz, 1H, CHPh), 7.13 (d, *J* = 16.2 Hz, 1H, CHCHPh), 7.26 - 7.19 (m, 1H, ArH), 7.36 - 7.27 (m, 2H, ArH), 7.49 - 7.43 (m, 2H, ArH) ppm.

***rac*-(E)-N,N-Diisopropyl-2-styrylferrocenylcarboxamide (*rac*-138)**

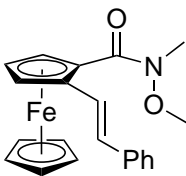


***rac*-138**

GP 3, Stock solutions Q (97  $\mu$ L, 3.9  $\mu$ mol, 0.13 equiv.), R (97  $\mu$ L, 19.5  $\mu$ mol, 0.67 equiv.), S (97  $\mu$ L, 7.8  $\mu$ mol, 0.27 equiv.), B (1500  $\mu$ L, 39.0  $\mu$ mol, 1.0 equiv.), T (97  $\mu$ L, 97.4  $\mu$ mol, 3.33 equiv.). After automated column chromatography (PE/EtOAc 9:1  $\rightarrow$  1:1), the target compound *rac*-138 was obtained as an orange oil (6 mg, 0.02 mmol, 51 %).

**$^1\text{H-NMR}$**  (400 MHz,  $\text{CDCl}_3$ ):  $\delta$  = 1.02 (s, 6H,  $\text{CH}_3$ ), 1.55 (s, 6H,  $\text{CH}_3$ ), 3.42 (s, 1H, NCH), 3.83 (s, 1H, NCH), 4.28 (td,  $J$  = 0.5, 2.5, 2.5 Hz, 1H, CpH), 4.29 (s, 5H,  $\text{C}_5\text{H}_5$ ), 4.39 (dd,  $J$  = 1.4, 2.5 Hz, 1H, CpH), 4.56 (ddd,  $J$  = 0.5, 1.4, 2.5 Hz, 1H, CpH), 6.75 (d,  $J$  = 16.3 Hz, 1H, =CH), 7.0 (d,  $J$  = 16.3 Hz, 1H, =CH), 7.27 - 7.18 (m, 1H, ArH), 7.37 - 7.28 (m, 2H, ArH), 7.46 - 7.39 (m, 2H, ArH) ppm.  **$^{13}\text{C-NMR}$**  (100 MHz,  $\text{CDCl}_3$ ):  $\delta$  = 20.9 ( $\text{CH}_3$ ), 21.1 ( $\text{CH}_3$ ), 29.4 (NCH), 53.9 (NCH), 64.4 ( $\text{C}_{\text{CpH}}$ ), 67.3 ( $\text{C}_{\text{CpH}}$ ), 68.7 ( $\text{C}_{\text{CpH}}$ ), 71.2 ( $\text{C}_5\text{H}_5$ ), 82.6 ( $\text{C}_{\text{CpC}}$ ), 88.1 ( $\text{C}_{\text{CpC}}$ ), 125.3 (=CH), 126.0 ( $\text{C}_{\text{PhH}}$ ), 127.1 ( $\text{C}_{\text{PhH}}$ ), 127.1 (=CH), 128.8 ( $\text{C}_{\text{PhH}}$ ), 137.9 ( $\text{C}_{\text{PhC}}$ ), 168.0 (C=O) ppm. **IR**:  $\tilde{\nu}$  = 443 (m), 459 (m), 489 (s), 518 (m), 540 (m), 619 (m), 698 (s), 740 (m), 752 (s), 817 (s), 844 (m), 875 (m), 912 (m), 954 (m), 964 (m), 997 (m), 1004 (m), 1039 (m), 1072 (m), 1105 (m), 1124 (m), 1155 (m), 1193 (m), 1211 (m), 1251 (m), 1261 (m), 1290 (m), 1323 (s), 1346 (m), 1357 (m), 1367 (m), 1415 (m), 1448 (m), 1458 (m), 1496 (m), 1597 (m), 1625 (s), 2872 (m), 2927 (m), 2960 (m), 2993 (m), 3082 (m)  $\text{cm}^{-1}$ . **HRMS (ESI)**:  $m/z$  calc. for  $\text{C}_{25}\text{H}_{29}\text{FeNO}$  [ $\text{M}+\text{Na}$ ] $^+$ : 483.1470, found: 483.1475.

***rac*-(E)-N-Methoxy-N-methyl-2-styrylferrocenylcarboxamide (*rac*-139)**



***rac*-139**

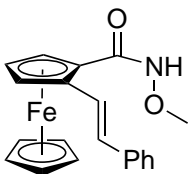
GP 3, Stock solutions Q (209  $\mu$ L, 8.4  $\mu$ mol, 0.13 equiv.), R (209  $\mu$ L, 41.9  $\mu$ mol, 0.67 equiv.), S (209  $\mu$ L, 16.8  $\mu$ mol, 0.27 equiv.), C (1500  $\mu$ L, 83.8  $\mu$ mol, 1.0 equiv.), T (209 mg, 209.6 mmol,



3.33 equiv.). After automated column chromatography (PE/EtOAc 9:1 → 1:1), the target compound *rac*-**139** was obtained as an orange oil (10 mg, 0.03 mmol, 45 %).

<sup>1</sup>H-NMR (400 MHz, CDCl<sub>3</sub>): δ = 3.3 (s, 3H, NCH<sub>3</sub>), 3.6 (s, 3H, OCH<sub>3</sub>), 4.22 (s, 5H, C<sub>5</sub>H<sub>5</sub>), 4.52 - 4.37 (m, 1H, CpH), 4.79 (s, 1H, CpH), 4.8 (s, 1H, CpH), 6.77 (d, *J* = 16.4 Hz, 1H, =CH), 7.25 - 7.18 (m, 1H, ArH), 7.36 - 7.29 (m, 2H, ArH), 7.53 - 7.46 (m, 2H, ArH), 7.61 (d, *J* = 16.4 Hz, 1H, =CH) ppm. <sup>13</sup>C-NMR (100 MHz, CDCl<sub>3</sub>): δ = 33.9 (NCH<sub>3</sub>), 61.0 (OCH<sub>3</sub>), 66.2 (CpH), 69.4 (CpH), 70.5 (CpH), 71.2 (C<sub>5</sub>H<sub>5</sub>), 75.0 (C<sub>Cp</sub>C), 86.5 (C<sub>Cp</sub>C), 126.1 (=CH), 126.2 (C<sub>Ph</sub>H), 127.0 (C<sub>Ph</sub>H), 127.3 (=CH), 128.6 (C<sub>Ph</sub>H), 137.9 (C<sub>Ph</sub>C), 170.6 (C=O) ppm.  $\tilde{\nu}$  = 439 (m), 459 (s), 482 (s), 551 (m), 605 (m), 640 (m), 692 (s), 750 (m), 817 (m), 848 (m), 889 (m), 966 (m), 1001 (m), 1072 (m), 1105 (m), 1157 (m), 1209 (m), 1261 (m), 1288 (m), 1363 (m), 1423 (m), 1483 (m), 1581 (m), 1597 (m), 1629 (m), 2852 (m), 2926 (m), 2958 (m), 3057 (m), 3082 (m) cm<sup>-1</sup>. HRMS (ESI): *m/z* calc. for C<sub>21</sub>H<sub>21</sub>FeNO<sub>2</sub> [M+Na]<sup>+</sup>: 398.0819, found: 398.0821.

#### *rac*-(*E*)-*N*-Methoxy-2-styrylferrocenylcarboxamide (**140**)



**140**

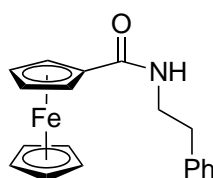
GP 3, Stock solutions Q (209 μL, 8.4 μmol, 0.13 equiv.), R (209 μL, 41.9 μmol, 0.67 equiv.), S (209 μL, 16.8 μmol, 0.27 equiv.), C (1500 μL, 83.8 μmol, 1.0 equiv.), T (209 mg, 209.6 mmol, 3.33 equiv.). After automated column chromatography (PE/EtOAc 9:1 → 1:1), the target compound **140** was obtained as an orange oil (2 mg, 0.01 mmol, 9 %).

<sup>1</sup>H-NMR (400 MHz, CDCl<sub>3</sub>): δ = 2.96 (d, *J* = 4.9 Hz, 3H, OCH<sub>3</sub>), 4.19 (s, 5H, C<sub>5</sub>H<sub>5</sub>), 4.4 (td, *J* = 0.5, 2.6, 2.6 Hz, 1H, CpH), 4.56 (dd, *J* = 1.4, 2.6 Hz, 1H, CpH), 4.78 (ddd, *J* = 0.5, 1.4, 2.6 Hz, 1H, CpH), 5.77 (s, 1H, NH), 6.8 (d, *J* = 16.4 Hz, 1H, =CH), 7.28 - 7.19 (m, 1H, ArH), 7.40 - 7.30 (m, 2H, ArH), 7.59 - 7.47 (m, 2H, ArH), 7.69 (d, *J* = 16.4 Hz, 1H, =CH) ppm. <sup>13</sup>C-NMR (100 MHz, CDCl<sub>3</sub>): δ = 26.5 (OCH<sub>3</sub>), 67.4 (C<sub>Cp</sub>H), 68.6 (C<sub>Cp</sub>H), 69.3 (C<sub>Cp</sub>H), 70.9 (C<sub>5</sub>H<sub>5</sub>), 75.6 (C<sub>Cp</sub>C), 84.8 (C<sub>Cp</sub>C), 125.4 (=CH), 126.2 (C<sub>Ph</sub>H), 127.1 (C<sub>Ph</sub>H), 128.3 (=CH), 128.6 (C<sub>Ph</sub>H), 137.7 (C<sub>Ph</sub>C), 171.2 (C=O) ppm. IR:  $\tilde{\nu}$  = 405 (m), 445 (s), 466 (s), 486 (s), 542 (m), 580 (m), 605 (m), 692 (s), 736 (m), 752 (m), 775 (m), 810 (m), 910 (m), 964 (m), 1001 (m), 1026 (m), 1070 (m), 1105 (m), 1153 (m), 1186 (m), 1213 (m), 1242 (m), 1257 (m), 1286 (m), 1300 (m), 1363 (m), 1408 (m), 1436 (m), 1452 (m), 1492 (m), 1529 (m), 1533 (m), 1635 (m), 1701 (m), 2852 (m), 2924 (m), 2958 (m), 3057



**<sup>1</sup>H-NMR** (400 MHz, CDCl<sub>3</sub>):  $\delta$  = 1.26 (d,  $J$  = 0.7 Hz, 1H, CH<sub>2</sub>), 2.01 - 1.80 (m, 3H, CH<sub>2</sub>), 3.78 - 3.12 (m, 7H, CH<sub>2</sub>), 4.26 (s, 5H, C<sub>5</sub>H<sub>5</sub>), 4.35 (t,  $J$  = 2.4, 2.4 Hz, 1H, CpH), 4.4 (s, 1H, CH), 4.59 (d,  $J$  = 2.4 Hz, 1H, CpH), 4.64 (s, 1H, CpH), 6.74 (d,  $J$  = 16.3 Hz, 1H, =CH), 7.12 (d,  $J$  = 16 Hz, 1H, =CH), 7.29 - 7.19 (m, 1H, ArH), 7.38 - 7.30 (m, 2H, ArH), 7.46 (d,  $J$  = 7.7 Hz, 2H, ArH) ppm. **<sup>13</sup>C-NMR** (100 MHz, CDCl<sub>3</sub>):  $\delta$  = 29.3 (CH<sub>2</sub>), 53.8 (CH<sub>2</sub>), 56.8 (NCH), 59.1 (CH<sub>2</sub>), 64.9 (C<sub>Cp</sub>H), 68.4 (C<sub>Cp</sub>H), 71.0 (C<sub>Cp</sub>H), 71.1 (C<sub>5</sub>H<sub>5</sub>), 72.5 (CH<sub>2</sub>), 82.0 (C<sub>Cp</sub>C), 125.8 (=CH), 126.0 (C<sub>Ph</sub>H), 126.6 (=CH), 127.0 (C<sub>Ph</sub>H), 128.7 (C<sub>Ph</sub>H), 137.8 (C<sub>Ph</sub>C), 168.5 (C=O) ppm. **IR**:  $\tilde{\nu}$  = 435 (m), 460 (m), 486 (s), 526 (m), 561 (m), 692 (s), 731 (m), 750 (m), 815 (m), 889 (m), 912 (m), 962 (m), 1001 (m), 1055 (m), 1072 (m), 1105 (s), 1157 (m), 1197 (m), 1257 (m), 1286 (m), 1375 (m), 1446 (s), 1608 (m), 1701 (m), 2873 (m), 2924 (m), 2962 (m), 3028 (m), 3057 (m), 3082 (m) cm<sup>-1</sup>. **HRMS (ESI)**:  $m/z$  calc. for C<sub>20</sub>H<sub>25</sub>FeNO<sub>2</sub> [M+Na]<sup>+</sup>: 452.1287, found: 452.1284.

***rac*-(E)-N-methyl-N-phenethyl-2-styrylferrocenylcarboxamide (*rac*-143)**



***rac*-143**

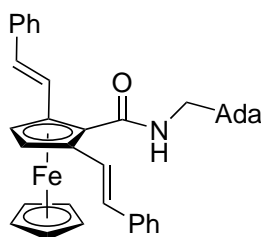
GP 3, Stock solutions Q (362  $\mu$ L, 14.5  $\mu$ mol, 0.13 equiv.), R (362  $\mu$ L, 72.6  $\mu$ mol, 0.67 equiv.), S (362  $\mu$ L, 29.0  $\mu$ mol, 0.27 equiv.), G (1500  $\mu$ L, 145.1  $\mu$ mol, 1.0 equiv.), T (362  $\mu$ L, 362.9  $\mu$ mol, 3.33 equiv.). After automated column chromatography (PE/EtOAc 9:1  $\rightarrow$  1:1), the target compound *rac*-143 was obtained as an orange oil (24 mg, 0.05 mmol, 48 %).

**<sup>1</sup>H-NMR** (400 MHz, CDCl<sub>3</sub>):  $\delta$  = 3.01 (d,  $J$  = 41.8 Hz, 2H, CH<sub>2</sub>), 3.57 (d,  $J$  = 134.2 Hz, 2H, CH<sub>2</sub>), 4.25 (s, 5H, C<sub>5</sub>H<sub>5</sub>), 4.32 (t,  $J$  = 2.5, 2.5 Hz, 1H, CpH), 4.41 (s, 1H, CpH), 4.68 - 4.61 (m, 1H, CpH), 6.73 (d,  $J$  = 16.2 Hz, 1H, =CH), 7.06 - 6.92 (m, 1H, =CH), 7.25 - 7.18 (m, 1H, ArH), 7.32 (t,  $J$  = 7.5, 7.5 Hz, 2H, ArH), 7.49 - 7.40 (m, 2H, ArH) ppm. **<sup>13</sup>C-NMR** (100 MHz, CDCl<sub>3</sub>):  $\delta$  = 49.6 (CH<sub>2</sub>), 52.7 (CH<sub>2</sub>), 64.6 (C<sub>Cp</sub>H), 67.9 (C<sub>Cp</sub>H), 69.6 (C<sub>Cp</sub>H), 70.0 (C<sub>Cp</sub>C), 71.2 (C<sub>5</sub>H<sub>5</sub>), 83.6 (C<sub>Cp</sub>C), 126.0 (=CH), 126.4 (C<sub>Ph</sub>H), 127.0 (C<sub>Ph</sub>H), 128.5 (=CH), 128.7 (C<sub>Ph</sub>H), 137.7 (C<sub>Ph</sub>C), 169.6 (C=O) ppm. **IR**:  $\tilde{\nu}$  = 430 (m), 459 (s), 486 (s), 545 (m), 572 (m), 605 (m), 646 (m), 694 (s), 746 (s), 815 (m), 908 (m), 960 (m), 1001 (m), 1029 (m), 1064 (m), 1105 (m), 1153 (m), 1207 (m), 1249 (m), 1286 (m), 1359 (m), 1390 (m), 1419 (m), 1452 (m), 1485 (m), 1620 (m), 1701 (m), 1716 (m), 2862 (m), 2926 (m), 3024 (m), 3057 (m), 3082 (m) cm<sup>-1</sup>. **HRMS (ESI)**:  $m/z$  calc. for C<sub>27</sub>H<sub>25</sub>FeNO [M+Na]<sup>+</sup>: 472.1340, found: 472.1341.



CH<sub>2</sub>), 2.14 - 1.95 (m, 1H, CH, CH<sub>2</sub>), 3.96 (qd, *J* = 3.9, 10.8 Hz, 1H, C<sub>iPr</sub>H), 4.18 (s, 5H, C<sub>5</sub>H<sub>5</sub>), 4.4 (td, *J* = 0.5, 2.7 Hz, 1H, CpH), 4.6 (dd, *J* = 1.4, 2.7 Hz, 1H, CpH), 4.77 (ddd, *J* = 0.5, 1.4, 2.7 Hz, 1H, CpH), 5.48 (d, *J* = 9.4 Hz, 1H, NH), 6.79 (d, *J* = 16.4 Hz, 1H, =CH), 7.26 - 7.19 (m, 1H, ArH), 7.42 - 7.29 (m, 2H, ArH), 7.54 - 7.46 (m, 2H, ArH), 7.67 (d, *J* = 16.4 Hz, 1H, =CH) ppm. <sup>13</sup>C-NMR (100 MHz, CDCl<sub>3</sub>): δ = 16.4 (CH<sub>3</sub>), 21.4 (CH<sub>3</sub>), 22.4 (CH<sub>3</sub>), 24.0 (CH<sub>2</sub>), 29.4 (CH), 32.1 (CH), 34.7 (CH<sub>2</sub>), 43.7 (CH<sub>2</sub>), 48.6 (CH), 50.1 (C<sub>iPr</sub>H), 67.6 (C<sub>Cp</sub>H), 69.3 (C<sub>Cp</sub>H), 69.5 (C<sub>Cp</sub>H), 71.1 (C<sub>5</sub>H<sub>5</sub>), 75.9 (C<sub>Cp</sub>C), 84.5 (C<sub>Cp</sub>C), 125.6 (=CH), 126.3 (C<sub>Ph</sub>H), 127.3 (C<sub>Ph</sub>H), 128.4 (=CH), 128.8 (C<sub>Ph</sub>H), 137.8 (C<sub>Ph</sub>C), 169.7 (C=O) ppm. IR:  $\tilde{\nu}$  = 474 (s), 484 (s), 597 (m), 617 (m), 692 (m), 736 (m), 750 (m), 771 (m), 817 (m), 891 (m), 920 (m), 964 (m), 1001 (m), 1028 (m), 1053 (m), 1072 (m), 1105 (m), 1176 (m), 1226 (m), 1240 (m), 1261 (m), 1288 (m), 1330 (m), 1367 (m), 1454 (m), 1508 (m), 1517 (m), 1521 (m), 1624 (m), 1629 (m), 1697 (m), 1701 (m), 2866 (m), 2922 (m), 2953 (m), 3057 (m), 3082 (m), 3354 (m) cm<sup>-1</sup>. HRMS (ESI): *m/z* calc. for C<sub>29</sub>H<sub>35</sub>FeNO [M+Na]<sup>+</sup>: 492.1966, found: 492.1961.

***N*-(((3*r*,5*r*,7*r*)-adamantan-1-yl)methyl)-2,6-di(*E*-styryl)ferrocenylcarboxamide (145)**

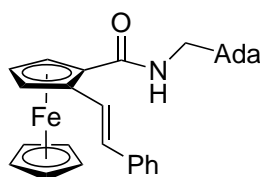


**145**

GP 3, Stock solutions Q (369 μL, 14.8 μmol, 0.13 equiv.), R (369 μL, 73.9 μmol, 0.67 equiv.), S (369 μL, 29.6 μmol, 0.27 equiv.), J (1500 μL, 147.9 μmol, 1.0 equiv.), T (369 μL, 369.7 μmol, 3.33 equiv.). After automated column chromatography (PE/EtOAc 9:1 → 1:1), the target compound **145** was obtained as an orange oil (1 mg, 2.29 μmol, 2 %).

<sup>1</sup>H-NMR (400 MHz, CDCl<sub>3</sub>): δ = 1.72 (d, *J* = 12.8 Hz, 6H, C<sub>Adamantyl</sub>H<sub>2</sub>), 1.97 (s, 3H, C<sub>Adamantyl</sub>H), 2.26 - 2.14 (m, 3H, C<sub>Adamantyl</sub>H<sub>2</sub>), 2.71 - 2.58 (m, 3H, C<sub>Adamantyl</sub>H<sub>2</sub>), 3.20 - 3.10 (m, 2H, NCH<sub>2</sub>), 3.77 - 3.72 (m, 1H, CpH), 4.21 (s, 5H, C<sub>5</sub>H<sub>5</sub>), 4.81 (s, 2H, CpH), 6.81 (d, *J* = 16.4 Hz, 2H, =CH), 7.36 - 7.30 (m, 7H, ArH), 7.53 - 7.44 (m, 4H, ArH, =CH), 8.1 (s, 1H, NH) ppm.

*rac*-*N*-(((3*r*,5*r*,7*r*)-adamantan-1-yl)methyl)-2-((*E*)-styryl)ferrocenylcarboxamide (*rac*-146)

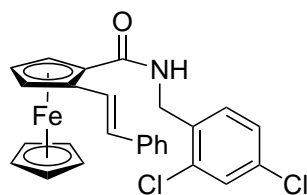


*rac*-146

GP 3, Stock solutions Q (369  $\mu$ L, 14.8  $\mu$ mol, 0.13 equiv.), R (369  $\mu$ L, 73.9  $\mu$ mol, 0.67 equiv.), S (369  $\mu$ L, 29.6  $\mu$ mol, 0.27 equiv.), J (1500  $\mu$ L, 147.9  $\mu$ mol, 1.0 equiv.), T (369  $\mu$ L, 369.7  $\mu$ mol, 3.33 equiv.). After automated column chromatography (PE/EtOAc 9:1  $\rightarrow$  1:1), the target compound *rac*-146 was obtained as an orange oil (8 mg, 0.02 mmol, 16 %).

$^1\text{H-NMR}$  (400 MHz,  $\text{CDCl}_3$ ):  $\delta$  = 1.58 (d,  $J$  = 2.9 Hz, 6H,  $\text{C}_{\text{AdamantaneH}_2}$ ), 1.83 - 1.62 (m, 6H,  $\text{C}_{\text{AdamantaneH}_2}$ ), 2.02 (d,  $J$  = 4.2 Hz, 3H,  $\text{C}_{\text{AdamantaneH}}$ ), 3.26 - 2.97 (m, 2H,  $\text{NCH}_2$ ), 4.2 (s, 5H,  $\text{C}_5\text{H}_5$ ), 4.4 (td,  $J$  = 0.5, 2.6, 2.6 Hz, 1H, CpH), 4.63 (dd,  $J$  = 1.5, 2.6 Hz, 1H, CpH), 4.77 (ddd,  $J$  = 0.5, 1.5, 2.6 Hz, 1H, CpH), 5.87 (s, 1H, NH), 6.81 (d,  $J$  = 16.3 Hz, 1H, =CH), 7.26 - 7.19 (m, 1H, ArH), 7.39 - 7.28 (m, 2H, ArH), 7.55 - 7.47 (m, 2H, ArH), 7.68 (d,  $J$  = 16.3 Hz, 1H, =CH) ppm.  $^{13}\text{C-NMR}$  (100 MHz,  $\text{CDCl}_3$ ):  $\delta$  = 28.3 ( $\text{C}_{\text{AdamantylH}}$ ), 33.9 ( $\text{C}_{\text{AdamantylC}}$ ), 37.0 ( $\text{C}_{\text{AdamantylH}_2}$ ), 40.5 ( $\text{C}_{\text{AdamantylH}_2}$ ), 51.0 ( $\text{CH}_2$ ), 67.5 ( $\text{C}_{\text{CpH}}$ ), 68.9 ( $\text{C}_{\text{CpH}}$ ), 69.2 ( $\text{C}_{\text{CpH}}$ ), 71.0 ( $\text{C}_5\text{H}_5$ ), 76.2 ( $\text{C}_{\text{CpC}}$ ), 84.7 ( $\text{C}_{\text{CpC}}$ ), 125.4 (=CH), 126.2 ( $\text{C}_{\text{PhH}}$ ), 127.2 ( $\text{C}_{\text{PhH}}$ ), 128.6 (=CH), 128.6 ( $\text{C}_{\text{PhH}}$ ), 137.6 ( $\text{C}_{\text{PhC}}$ ), 170.5 (C=O) ppm. IR:  $\tilde{\nu}$  = 420 (m), 445 (m), 466 (m), 486 (s), 501 (m), 551 (m), 569 (m), 601 (m), 623 (m), 690 (m), 734 (m), 750 (m), 773 (m), 815 (m), 902 (m), 966 (m), 981 (m), 1001 (m), 1039 (m), 1105 (m), 1186 (m), 1238 (m), 1284 (m), 1309 (m), 1346 (m), 1363 (m), 1423 (m), 1448 (m), 1529 (m), 1597 (m), 1635 (m), 2845 (m), 2899 (m), 3053 (m), 3082 (m), 3342 (m)  $\text{cm}^{-1}$ . HRMS (ESI):  $m/z$  calc. for  $\text{C}_{29}\text{H}_{31}\text{FeNO}$  [ $\text{M}+\text{Na}$ ] $^+$ : 502.1809, found: 502.1809.

*rac*-(*E*)-*N*-(2,4-dichlorobenzyl)-2-styrylferrocenylcarboxamide (*rac*-147)



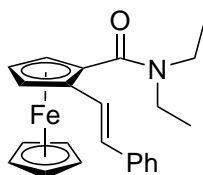
*rac*-147

GP 3, Stock solutions Q (351  $\mu$ L, 14.1  $\mu$ mol, 0.13 equiv.), R (351  $\mu$ L, 70.3  $\mu$ mol, 0.67 equiv.), S (351  $\mu$ L, 28.1  $\mu$ mol, 0.27 equiv.), L (1500  $\mu$ L, 140.7  $\mu$ mol, 1.0 equiv.), T (351  $\mu$ L, 351.7  $\mu$ mol,

3.33 equiv.). After automated column chromatography, the target compound *rac*-**147** was obtained as an orange oil (3 mg, 0.01 mmol, 5 %).

**<sup>1</sup>H-NMR** (400 MHz, CDCl<sub>3</sub>):  $\delta$  = 4.14 (s, 5H, C<sub>5</sub>H<sub>5</sub>), 4.38 (s, 2H, CpH), 4.61 (d,  $J$  = 6.3 Hz, 2H, CH<sub>2</sub>), 4.7 (s, 1H, CpH), 6.28 (d,  $J$  = 6.3 Hz, 1H, NH), 6.42 (d,  $J$  = 16.2 Hz, 1H, =CH), 7.08 (d,  $J$  = 16.2 Hz, 1H, =CH), 7.63 - 7.22 (m, 8H, ArH) ppm. **<sup>13</sup>C-NMR** (100 MHz, CDCl<sub>3</sub>):  $\delta$  = 41.2 (CH<sub>2</sub>), 68.2 (C<sub>Cp</sub>H), 69.7 (C<sub>5</sub>H<sub>5</sub>), 70.7 (C<sub>Cp</sub>H), 88.9 (C<sub>Cp</sub>C), 91.8 (C<sub>Cp</sub>C), 108.2 (=CH), 123.4 (C<sub>Ar</sub>C), 126.3 (C<sub>Ar</sub>H), 127.4 (C<sub>Ar</sub>H), 128.4 (C<sub>Ar</sub>H), 128.8 (C<sub>Ar</sub>H), 129.3 (C<sub>Ar</sub>H), 131.5 (C<sub>Ar</sub>H), 134.1 (C<sub>Ar</sub>C), 134.8 (C<sub>Ar</sub>C), 136.3 (C<sub>Ar</sub>C), 141.3 (=CH), 170.4 (C=O) ppm. **IR**:  $\tilde{\nu}$  = 445 (m), 520 (m), 578 (m), 653 (s), 696 (m), 761 (m), 802 (m), 918 (m), 968 (m), 1020 (m), 1076 (m), 1222 (m), 1259 (m), 1377 (m), 1446 (m), 1490 (m), 1558 (m), 1597 (m), 1683 (m), 2852 (m), 2924 (m), 2958 (m) cm<sup>-1</sup>.

#### (*E*)-*N,N*-diethyl-2-styrylferrocenylcarboxamide (*rac*-**148**)



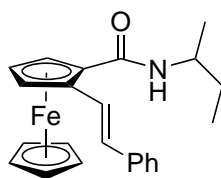
*rac*-**148**

GP 3, Stock solutions Q (521  $\mu$ L, 20.9  $\mu$ mol, 0.13 equiv.), R (521  $\mu$ L, 104.4  $\mu$ mol, 0.67 equiv.), S (521  $\mu$ L, 41.8  $\mu$ mol, 0.27 equiv.), N (1500  $\mu$ L, 208.9  $\mu$ mol, 1.0 equiv.), T (521  $\mu$ L, 522.2  $\mu$ mol, 3.33 equiv.). After automated column chromatography (PE/EtOAc 9:1  $\rightarrow$  1:1), the target compound *rac*-**148** was obtained as an orange oil (64 mg, 0.17 mmol, 85 %).

**<sup>1</sup>H-NMR** (400 MHz, CDCl<sub>3</sub>):  $\delta$  = 1.44 - 0.89 (m, 6H, CH<sub>3</sub>), 3.71 - 3.01 (m, 4H, CH<sub>2</sub>), 4.28 (s, 5H, C<sub>5</sub>H<sub>5</sub>), 4.31 (td,  $J$  = 0.5, 2.5 Hz, 1H, CpH), 4.45 (dd,  $J$  = 1.4, 2.5 Hz, 1H, CpH), 4.61 (dd,  $J$  = 1.4, 2.5 Hz, 1H, CpH), 6.73 (d,  $J$  = 16.3 Hz, 1H, =CH), 7.05 (d,  $J$  = 16.3 Hz, 1H, =CH), 7.25 - 7.18 (m, 1H, ArH), 7.35 - 7.28 (m, 2H, ArH), 7.51 - 7.41 (m, 2H, ArH) ppm. **<sup>13</sup>C-NMR** (100 MHz, CDCl<sub>3</sub>):  $\delta$  = 14.3 (CH<sub>3</sub>), 21.1 (CH<sub>3</sub>), 29.4 (CH), 31.8 (CH), 64.6 (C<sub>Cp</sub>H), 67.7 (C<sub>Cp</sub>H), 69.2 (C<sub>Cp</sub>H), 71.2 (C<sub>5</sub>H<sub>5</sub>), 83.2 (C<sub>Cp</sub>C), 84.8 (C<sub>Cp</sub>C), 125.3 (=CH), 126.0 (C<sub>Ph</sub>H), 127.1 (C<sub>Ph</sub>H), 127.1 (=CH), 128.8 (C<sub>Ph</sub>H), 137.8 (C<sub>Ph</sub>C), 168.7 (C=O) ppm. **IR**:  $\tilde{\nu}$  = 403 (m), 453 (s), 462 (s), 487 (s), 520 (m), 551 (m), 609 (m), 646 (m), 696 (s), 740 (s), 754 (s), 781 (m), 819 (s), 844 (m), 883 (m), 896 (m), 912 (m), 964 (m), 977 (m), 1002 (m), 1026 (m), 1037 (m), 1074 (m), 1087 (m), 1105 (m), 1132 (m), 1176 (m), 1219 (m), 1247 (m), 1265 (m), 1286 (m), 1315 (m), 1346 (m), 1361 (m), 1377 (m), 1406 (m), 1431 (m), 1448 (m), 1477 (s), 1595 (m), 1616 (s), 1625 (s), 1701 (m), 2872 (m), 2931 (m), 2972 (m),

3057 (m), 3076 (m)  $\text{cm}^{-1}$ . **HRMS (ESI):**  $m/z$  calc. for  $\text{C}_{23}\text{H}_{25}\text{FeNO}$   $[\text{M}+\text{Na}]^+$ : 410.1183, found: 410.1184.

**(E)-N-(sec-butyl)-2-styrylferrocenylcarboxamide (*rac*-149)**



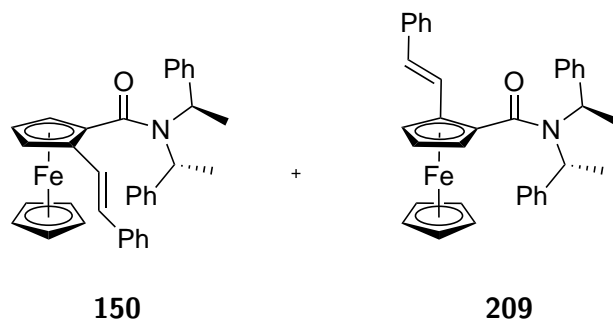
*rac*-149

GP 3, Stock solutions Q (410  $\mu\text{L}$ , 16.4  $\mu\text{mol}$ , 0.13 equiv.), R (410  $\mu\text{L}$ , 82.1  $\mu\text{mol}$ , 0.67 equiv.), S (410  $\mu\text{L}$ , 32.8  $\mu\text{mol}$ , 0.27 equiv.), O (1500  $\mu\text{L}$ , 164.1  $\mu\text{mol}$ , 1.0 equiv.), T (410  $\mu\text{L}$ , 410.4  $\mu\text{mol}$ , 3.33 equiv.). After automated column chromatography (PE/EtOAc 9:1  $\rightarrow$  1:1), the target compound *rac*-149 was obtained as an orange oil (13 mg, 0.03 mmol, 21 %).

**$^1\text{H-NMR}$**  (400 MHz,  $\text{CDCl}_3$ ):  $\delta$  = 1.07 - 0.81 (m, 3H,  $\text{CH}_2\text{CH}_3$ ), 1.30 - 1.16 (m, 3H,  $\text{CHCH}_3$ ), 1.78 - 1.44 (m, 2H,  $\text{CH}_2$ ), 4.17 - 4.04 (m, 1H, NCH), 4.18 (d,  $J$  = 0.7 Hz, 5H,  $\text{C}_5\text{H}_5$ ), 4.39 (t,  $J$  = 2.8 Hz, 1H,  $\text{C}_p\text{H}$ ), 4.57 (ddd,  $J$  = 1.4, 2.8, 10.1 Hz, 1H,  $\text{C}_p\text{H}$ ), 4.77 (td,  $J$  = 1.4, 2.8 Hz, 1H,  $\text{C}_p\text{H}$ ), 5.70 - 5.53 (m, 1H, NH), 6.8 (d,  $J$  = 16.4 Hz, 1H, =CH), 7.26 - 7.19 (m, 1H, ArH), 7.40 - 7.28 (m, 2H, ArH), 7.57 - 7.46 (m, 2H, ArH), 7.71 (dd,  $J$  = 16.4, 19.0 Hz, 1H, =CH) ppm.  **$^{13}\text{C-NMR}$**  (100 MHz,  $\text{CDCl}_3$ ):  $\delta$  = 10.5 ( $\text{CH}_2\text{CH}_3$ ), 20.8 ( $\text{CHCH}_3$ ), 29.9 ( $\text{CH}_2$ ), 46.6 (CH), 67.5 ( $\text{C}_{\text{CpH}}$ ), 68.4 ( $\text{C}_{\text{CpH}}$ ), 68.9 ( $\text{C}_{\text{CpH}}$ ), 69.3 ( $\text{C}_5\text{H}_5$ ), 84.7 ( $\text{C}_{\text{CpC}}$ ), 85.0 ( $\text{C}_{\text{CpC}}$ ), 125.5 (=CH), 126.2 ( $\text{C}_{\text{PhH}}$ ), 127.1 ( $\text{C}_{\text{PhH}}$ ), 128.3 (=CH), 128.6 ( $\text{C}_{\text{PhH}}$ ), 137.7 ( $\text{C}_{\text{PhC}}$ ), 169.8 (C=O) ppm. **IR:**  $\tilde{\nu}$  = 455 (s), 466 (s), 480 (s), 524 (m), 538 (m), 580 (m), 607 (m), 634 (m), 669 (m), 688 (s), 740 (m), 748 (m), 779 (m), 806 (m), 817 (m), 833 (m), 891 (m), 908 (m), 964 (m), 975 (m), 1001 (m), 1028 (m), 1047 (m), 1072 (m), 1109 (m), 1153 (m), 1186 (m), 1234 (m), 1259 (m), 1284 (m), 1300 (m), 1365 (m), 1379 (m), 1425 (m), 1448 (m), 1483 (m), 1494 (m), 1523 (s), 1597 (m), 1618 (m), 1629 (m), 1701 (m), 2872 (m), 2927 (m), 2964 (m), 3022 (m), 3057 (m), 3082 (m), 3309 (m)  $\text{cm}^{-1}$ . **HRMS (ESI):**  $m/z$  calc. for  $\text{C}_{23}\text{H}_{25}\text{FeNO}$   $[\text{M}+\text{Na}]^+$ : 410.1183, found: 410.1190.



*R<sub>p</sub>*-*N,N*-bis((*R*)-1-phenylethyl)-2-((*E*)-styryl)ferrocenylcarboxamide **150** and  
*S<sub>p</sub>*-*N,N*-bis((*R*)-1-phenylethyl)-2-((*E*)-styryl)ferrocenylcarboxamide **209**



GP 3, Stock solutions Q (718  $\mu$ L, 28.8  $\mu$ mol, 0.13 equiv.), R (718  $\mu$ L, 143.9  $\mu$ mol, 0.67 equiv.), S (718  $\mu$ L, 57.6  $\mu$ mol, 0.27 equiv.), P (1500  $\mu$ L, 287.8  $\mu$ mol, 1.0 equiv.), T (718  $\mu$ L, 719.4  $\mu$ mol, 3.33 equiv.). After automated column chromatography (PE/EtOAc 9:1  $\rightarrow$  1:1), the target compounds **150** and **209** were obtained as an orange oil (mixture of diastereomers, *d.r.* =  $2.0 \pm 0.1$  : 1 20 mg, 0.04 mmol, 21 %).

**<sup>1</sup>H-NMR** (400 MHz, CDCl<sub>3</sub>):  $\delta$  = 1.26 (s, 6H, CH<sub>3</sub>), 2.25 - 2.16 (m, 2H, CH), 4.3 (s, 5H, C<sub>5</sub>H<sub>5</sub>), 4.33 - 4.31 (m, 1H, CpH), 4.47 (dd, *J* = 1.3, 2.5 Hz, 1H, CpH), 4.64 (ddd, *J* = 0.4, 1.3, 2.5 Hz, 1H, CpH), 6.76 (d, *J* = 16.3 Hz, 1H, =CH), 6.93 (d, *J* = 16.3 Hz, 1H, =CH), 7.15 - 6.97 (m, 7H, ArH), 7.28 - 7.22 (m, 2H, ArH), 7.32 (d, *J* = 4.3 Hz, 4H, ArH), 7.55 - 7.33 (m, 2H, ArH) ppm. **<sup>13</sup>C-NMR** (100 MHz, CDCl<sub>3</sub>):  $\delta$  = 29.3 (CH<sub>3</sub>), 30.9 (CH), 31.8 (CH), 63.9 (C<sub>Cp</sub>H), 67.3 (C<sub>Cp</sub>H), 67.7 (C<sub>Cp</sub>H), 71.1 (C<sub>5</sub>H<sub>5</sub>), 83.5 (C<sub>Cp</sub>C), 88.2 (C<sub>Cp</sub>C), 125.0 (C<sub>Ph</sub>H), 125.3 (=CH), 125.9 (C<sub>Ph</sub>H), 126.0 (C<sub>Ph</sub>H), 127.0 (C<sub>Ph</sub>H), 127.4 (=CH), 127.9 (C<sub>Ph</sub>H), 128.3 (C<sub>Ph</sub>H), 128.4 (C<sub>Ph</sub>H), 128.6 (C<sub>Ph</sub>H), 128.8 (C<sub>Ph</sub>C), 131.5 (C<sub>Ph</sub>C), 137.7 (C<sub>Ph</sub>C), 167.8 (C=O) ppm. **IR**:  $\tilde{\nu}$  = 445 (m), 464 (m), 484 (s), 513 (m), 543 (m), 576 (m), 609 (m), 619 (m), 659 (m), 692 (s), 750 (s), 792 (m), 817 (m), 846 (m), 912 (m), 960 (m), 1001 (m), 1024 (m), 1072 (m), 1087 (m), 1107 (m), 1157 (m), 1184 (m), 1203 (m), 1244 (m), 1269 (m), 1288 (m), 1307 (m), 1357 (m), 1375 (m), 1408 (m), 1444 (m), 1494 (m), 1597 (m), 1635 (m), 2927 (m), 2970 (m), 3028 (m), 3057 (m), 3086 (m) cm<sup>-1</sup>. **HRMS (ESI)**: *m/z* calc. for C<sub>35</sub>H<sub>33</sub>FeNO [M+H]<sup>+</sup>: 540.1990, found: 540.1993.

## References

- [1] E. S. Isbrandt, R. J. Sullivan, S. G. Newman, *Angew. Chemie* **2019**, *131*, 7254–7267.
- [2] D. Caramelli, J. M. Granda, S. H. M. Mehr, D. Cambié, A. B. Henson, L. Cronin, *ACS Cent. Sci.* **2021**, *7*, 1821–1830.
- [3] R. Mandal, B. Emayavaramban, B. Sundararaju, *Org. Lett.* **2018**, *20*, 2835–2838.
- [4] P. M. Murray, S. N. Tyler, J. D. Moseley, *Org. Process Res. Dev.* **2013**, *17*, 40–46.
- [5] R. Carlson, J. E. Carlson, *Design and optimization in organic synthesis*, 2nd ed., Elsevier B.V., Amsterdam, **2005**.
- [6] J. Ružička, E. H. Hansen, *Anal. Chim. Acta* **1975**, *78*, 145–157.
- [7] M. B. Plutschack, B. Pieber, K. Gilmore, P. H. Seeberger, *Chem. Rev.* **2017**, *117*, 11796–11893.
- [8] Z. Amara, E. S. Streng, R. A. Skilton, J. Jin, M. W. George, M. Poliakoff, *European J. Org. Chem.* **2015**, *2015*, 6141–6145.
- [9] B. P. MacLeod, F. G. L. Parlane, T. D. Morrissey, F. Häse, L. M. Roch, K. E. Dettelbach, R. Moreira, L. P. E. Yunker, M. B. Rooney, J. R. Deeth, V. Lai, G. J. Ng, H. Situ, R. H. Zhang, M. S. Elliott, T. H. Haley, D. J. Dvorak, A. Aspuru-Guzik, J. E. Hein, C. P. Berlinguette, *Sci. Adv.* **2020**, *6*, DOI 10.1126/sciadv.aaz8867.
- [10] B. Burger, P. M. Maffettone, V. V. Gusev, C. M. Aitchison, Y. Bai, X. Wang, X. Li, B. M. Alston, B. Li, R. Clowes, N. Rankin, B. Harris, R. S. Sprick, A. I. Cooper, *Nature* **2020**, *583*, 237–241.
- [11] F. Häse, L. M. Roch, C. Kreisbeck, A. Aspuru-Guzik, *ACS Cent. Sci.* **2018**, *4*, 1134–1145.
- [12] S. Steiner, J. Wolf, S. Glatzel, A. Andreou, J. M. Granda, G. Keenan, T. Hinkley, G. Aragon-Camarasa, P. J. Kitson, D. Angelone, L. Cronin, *Science (80-. )*. **2019**, *363*, DOI 10.1126/science.aav2211.
- [13] L. Cronin, Home | Chemify.
- [14] L. A. Thompson, J. A. Ellman, *Chem. Rev.* **1996**, *96*, 555–600.

- [15] L. M. Roch, F. Häse, C. Kreisbeck, T. Tamayo-Mendoza, L. P. Yunker, J. E. Hein, A. Aspuru-Guzik, *PLoS One* **2020**, *15*, 1–18.
- [16] M. Christensen, F. Adedeji, S. Grosser, K. Zawatzky, Y. Ji, J. Liu, J. A. Jurica, J. R. Naber, J. E. Hein, *React. Chem. Eng.* **2019**, 1–4.
- [17] A. C. Vaucher, P. Schwaller, J. Geluykens, V. H. Nair, A. Iuliano, T. Laino, *Nat. Commun.* **2021**, *12*, DOI 10.1038/s41467-021-22951-1.
- [18] M. Christensen, L. P. E. Yunker, P. Shiri, T. Zepel, P. L. Prieto, S. Grunert, F. Bork, J. E. Hein, *Chem. Sci.* **2021**, *12*, 15473–15490.
- [19] S. A. Weissman, N. G. Anderson, *Org. Process Res. Dev.* **2015**, *19*, 1605–1633.
- [20] I. Surowiec, L. Vikström, G. Hector, E. Johansson, C. Vikström, J. Trygg, *Anal. Chem.* **2017**, *89*, 6491–6497.
- [21] V. Rosso, J. Albrecht, F. Roberts, J. M. Janey, *React. Chem. Eng.* **2019**, *4*, 1646–1657.
- [22] O. W. Gooding, *Curr. Opin. Chem. Biol.* **2004**, *8*, 297–304.
- [23] Y. Liu, F. Xie, A. Q. Jia, X. Li, *Chem. Commun.* **2018**, *54*, 4345–4348.
- [24] V. W. Rosso, J. L. Pazdan, J. J. Venit, *Org. Process Res. Dev.* **2001**, *5*, 294–298.
- [25] R. Carlson, J. E. Carlson, *Org. Process Res. Dev.* **2005**, *9*, 680–689.
- [26] P. M. Murray, F. Bellany, L. Benhamou, D.-K. Bučar, A. B. Tabor, T. D. Sheppard, *Org. Biomol. Chem.* **2016**, *14*, 2373–2384.
- [27] J. D. Moseley, P. M. Murray, *J. Chem. Technol. Biotechnol.* **2014**, *89*, 623–632.
- [28] N. Fey, M. F. Haddow, J. N. Harvey, C. L. McMullin, A. G. Orpen, *J. Chem. Soc. Dalton Trans.* **2009**, 8183–8196.
- [29] R. Carlson, M. P. Prochazka, T. Lundstedt, K. Westlid, H. Lönnberg, J.-E. Berg, M. Bartók, I. Pelczer, G. Dombi, *Acta Chem. Scand.* **1988**, *42b*, 157–165.
- [30] B. Skagerberg, D. Bonelli, S. Clementi, G. Cruciani, C. Ebert, *Quant. Struct. Relationships* **1989**, *8*, 32–38.
- [31] F. P. Ballistreri, C. G. Fortuna, G. Musumarra, D. Pavone, S. Scirè, *Arkivoc* **2002**, *2002*, 54–64.
- [32] J. A. Selekmán, J. Qiu, K. Tran, J. Stevens, V. Rosso, E. Simmons, Y. Xiao, J. Janey, *Annu. Rev. Chem. Biomol. Eng.* **2017**, *8*, 525–547.
- [33] C. Nunn, A. Dipietro, N. Hodnett, P. Sun, K. M. Wells, *Org. Process Res. Dev.* **2018**, *22*, 54–61.

- [34] M. Christensen, L. P. E. Yunker, P. Shiri, T. Zepel, P. L. Prieto, S. Grunert, F. Bork, J. E. Hein, *Chem. Sci.* **2021**, *12*, 15473–15490.
- [35] P. G. Chirila, C. J. Whiteoak, *Dalt. Trans.* **2017**, 9721–9739.
- [36] J. G. Gerstenberger, B. Sc. Thesis, Leibniz Universität Hannover, **2019**.
- [37] D. Schmiel, R. Gathy, H. Butenschön, *Organometallics* **2018**, *2*, acs.organomet.8b00243.
- [38] J. Sherwood, *Angew. Chemie* **2018**, *130*, 14482–14486.
- [39] M. Scholl, S. Ding, C. W. Lee, R. H. Grubbs, *Org. Lett.* **1999**, *1*, 953–956.
- [40] V. Lavallo, Y. Canac, C. Präsang, B. Donnadieu, G. Bertrand, *Angew. Chemie - Int. Ed.* **2005**, *44*, 5705–5709.
- [41] M. Melaimi, R. Jazzar, M. Soleilhavoup, G. Bertrand, *Angew. Chemie - Int. Ed.* **2017**, *56*, 10046–10068.
- [42] B. Spangenberg, C. Poole, C. Weins, *Quantitative Thin-Layer Chromatography: A Practical Survey*, Springer Berlin Heidelberg, **2011**.
- [43] J. G. Kirchner, J. M. Miller, R. G. Rice, *J. Agric. Food Chem.* **1954**, *2*, 1031–1033.
- [44] F. Hefendehl, *Planta Med.* **1960**, *8*, 65–70.
- [45] J. Sherma, G. Morlock, *J. Planar Chromatogr. - Mod. TLC* **2008**, *21*, 471–477.
- [46] F. Lundh, A. Clark, Pillow (PIL Fork) Documentation, **2015**.
- [47] P. Virtanen, R. Gommers, T. E. Oliphant, M. Haberland, T. Reddy, D. Cournapeau, E. Burovski, P. Peterson, W. Weckesser, J. Bright, S. J. van der Walt, M. Brett, J. Wilson, K. J. Millman, N. Mayorov, A. R. Nelson, E. Jones, R. Kern, E. Larson, C. J. Carey, Í. Polat, Y. Feng, E. W. Moore, J. VanderPlas, D. Laxalde, J. Perktold, R. Cimrman, I. Henriksen, E. A. Quintero, C. R. Harris, A. M. Archibald, A. H. Ribeiro, F. Pedregosa, P. van Mulbregt, A. Vijaykumar, A. P. Bardelli, A. Rothberg, A. Hilboll, A. Kloeckner, A. Scopatz, A. Lee, A. Rokem, C. N. Woods, C. Fulton, C. Masson, C. Häggström, C. Fitzgerald, D. A. Nicholson, D. R. Hagen, D. V. Pasechnik, E. Olivetti, E. Martin, E. Wieser, F. Silva, F. Lenders, F. Wilhelm, G. Young, G. A. Price, G. L. Ingold, G. E. Allen, G. R. Lee, H. Audren, I. Probst, J. P. Dietrich, J. Silterra, J. T. Webber, J. Slavič, J. Nothman, J. Buchner, J. Kulick, J. L. Schönberger, J. V. de Miranda Cardoso, J. Reimer, J. Harrington, J. L. C. Rodríguez, J. Nunez-Iglesias, J. Kuczynski, K. Tritz, M. Thoma, M. Neville, M. Kümmerer, M. Bolingbroke, M. Tartre, M. Pak, N. J. Smith, N. Nowaczyk, N. Shebanov, O. Pavlyk, P. A. Brodtkorb, P. Lee, R. T. McGibbon, R. Feldbauer, S. Lewis, S. Tygier, S. Sievert, S. Vigna, S. Peterson, S. More, T. Pudlik, T. Oshima, T. J. Pingel, T. P. Robitaille, T. Spura, T. R. Jones, T. Cera, T. Leslie, T. Zito, T. Krauss, U. Upadhyay, Y. O. Halchenko, Y. Vázquez-Baeza, *Nat. Methods* **2020**, *17*, 261–272.

- [48] L. H. Negri, PeakUtils 1.3.3 documentation, **2014**.
- [49] L. D. Asnin, *TrAC - Trends Anal. Chem.* **2016**, *81*, 51–62.
- [50] B. J. Asher, L. A. D'Agostino, J. D. Way, C. S. Wong, J. J. Harynuk, *Chemosphere* **2009**, *75*, 1042–1048.
- [51] Y. Vanderheyden, K. Broeckhoven, G. Desmet, *J. Chromatogr. A* **2014**, *1364*, 140–150.
- [52] A. D. Melnikov, Y. P. Tsentelovich, V. V. Yanshole, *Anal. Chem.* **2020**, *92*, 588–592.
- [53] K. Levenberg, *Q. Appl. Math.* **1944**, *2*, 164–168.
- [54] D. W. Marquardt, *J. Soc. Ind. Appl. Math.* **1963**, *11*, 431–441.
- [55] G. Huang, B. Li, W. Liu, L. Shi, Y. Ma, *J. Chem. Res. - Part S* **2000**, 491.
- [56] S. Hessam, M. Craven, A. I. Leonov, G. Keenan, L. Cronin, *Science (80-. )*. **2020**, *370*, 101–108.
- [57] CWA GmbH, DaMaRIS Gefahrstoffverzeichnis.
- [58] N. A. Romero, D. A. Nicewicz, *Chem. Rev.* **2016**, *116*, 10075–10166.
- [59] K. Hölz, J. Lietard, M. M. Somoza, *ACS Sustain. Chem. Eng.* **2017**, *5*, 828–834.
- [60] H. E. Bonfield, T. Knauber, F. Lévesque, E. G. Moschetta, F. Susanne, L. J. Edwards, *Nat. Commun.* **2020**, *11*, 2–5.
- [61] M. W. Logan, S. Ayad, J. D. Adamson, T. Dilbeck, K. Hanson, F. J. Uribe-Romo, *J. Mater. Chem. A* **2017**, *5*, 11854–11863.
- [62] D. Astruc, *Eur. J. Inorg. Chem.* **2017**, *2017*, 6–29.
- [63] G. Noirbent, D. Brunel, T. T. Bui, S. Péralta, P. H. Aubert, D. Gigmes, F. Dumur, *New J. Chem.* **2021**, *45*, 13475–13498.
- [64] S. Prabu, E. David, T. Viswanathan, K. Thirumoorthy, T. Panda, C. Dragonetti, A. Colombo, D. Marinotto, S. Righetto, D. Roberto, N. Palanisami, *Dalt. Trans.* **2020**, *49*, 1854–1863.
- [65] N. Krauß, H. Butenschön, *Eur. J. Org. Chem.* **2014**, 6686–6695.
- [66] H. Chen, S. Schlecht, T. C. Semple, J. F. Hartwig, *Science (80-. )*. **2000**, *287*, 1995–1997.
- [67] C. Sambigao, D. Schönbauer, R. Blicck, T. Dao-Huy, G. Pototschnig, P. Schaaf, T. Wiesinger, M. F. Zia, J. Wencel-Delord, T. Besset, B. U. W. Maes, M. Schnürch, *Chem. Soc. Rev.* **2018**, *47*, 6603–6743.
- [68] S.-B. Wang, Q. Gu, S.-L. You, *J. Catal.* **2018**, *361*, 393–397.
- [69] D. Schmiel, H. Butenschön, *Eur. J. Org. Chem.* **2017**, 3041–3048.

- [70] F. Bureš, *RSC Adv.* **2014**, *4*, 58826–58851.
- [71] Y. Masuda, N. Ishida, M. Murakami, *Chem. - An Asian J.* **2019**, *14*, 403–406.
- [72] K. Schlögl, **1984**, 27–62.
- [73] A. Togni, *Angew. Chemie Int. Ed. English* **1996**, *35*, 1475–1477.
- [74] D. Schaarschmidt, H. Lang, *Organometallics* **2013**, *32*, 5668–5704.
- [75] O. Riant, G. Argouarch, D. Guillaneux, O. Samuel, H. B. Kagan, *J. Org. Chem.* **1998**, *63*, 3511–3514.
- [76] C. Pi, X. Cui, X. Liu, M. Guo, H. Zhang, Y. Wu, *Org. Lett.* **2014**, *16*, 5164–5167.
- [77] T. Kawasaki, M. Sato, S. Ishiguro, T. Saito, Y. Morishita, I. Sato, H. Nishino, Y. Inoue, K. Soai, *J. Am. Chem. Soc.* **2005**, *127*, 3274–3275.
- [78] W. L. Noorduin, A. A. C. Bode, M. van der Meijden, H. Meekes, A. F. van Etteger, W. J. P. van Enckevort, P. C. M. Christianen, B. Kaptein, R. M. Kellogg, T. Rasing, E. Vlieg, *Nat. Chem.* **2009**, *1*, 729–732.
- [79] S. B. Colbran, S. T. Lee, D. G. Lonnon, F. J. Maharaj, A. M. McDonagh, K. A. Walker, R. D. Young, *Organometallics* **2006**, *25*, 2216–2224.
- [80] J. R. Beadle, S. H. Korzeniowski, D. E. Rosenberg, B. J. Garcia-Slanga, G. W. Gokel, *J. Org. Chem.* **1984**, *49*, 1594–1603.
- [81] Y. Suzuki, B. Sun, T. Yoshino, M. Kanai, S. Matsunaga, *Tetrahedron* **2015**, *71*, 4552–4556.
- [82] Y. Zhu, F. Chen, X. Zhao, D. Yan, W. Yong, J. Zhao, *Org. Lett.* **2019**, *21*, 5884–5888.
- [83] X. Zhou, Y. Luo, L. Kong, Y. Xu, G. Zheng, Y. Lan, X. Li, *ACS Catal.* **2017**, *7*, 7296–7304.
- [84] T. Li, Y. Yang, B. Li, P. Yang, *Chem. Commun.* **2019**, *55*, 353–356.
- [85] M. Sen, N. Rajesh, B. Emayavaramban, J. R. Premkumar, B. Sundararaju, *Chem. - A Eur. J.* **2018**, *24*, 342–346.
- [86] M. R. Sk, S. S. Bera, M. S. Maji, *Org. Lett.* **2018**, *20*, 134–137.
- [87] R. Möhlau, A. Redlich, *Berichte der Dtsch. Chem. Gesellschaft* **1911**, *44*, 3605–3618.
- [88] J. S. Yadav, B. V. Subba Reddy, K. Shiva Shankar, T. Swamy, K. Premalatha, *Bull. Korean Chem. Soc.* **2008**, *29*, 1418–1420.
- [89] J. S. Yadav, B. V. Reddy, T. Swamy, *Synthesis (Stuttg.)*. **2004**, *44*, 106–110.
- [90] S. B. Kamble, P. P. Vyas, R. V. Jayaram, C. V. Rode, *ACS Omega* **2017**, *2*, 2238–2247.
- [91] Y. Yamamoto, K. Nishimura, N. Kiriya, *Chem. Pharm. Bull.* **1976**, *24*, 1853–1859.
- [92] S. Shimizu, Y. Yamamoto, S. Koshimura, *Chem. Pharm. Bull.* **1982**, *30*, 1896–1899.

- [93] M. Patra, G. Gasser, *Nat. Rev. Chem.* **2017**, *1*, 0066.
- [94] N. Metzler-Nolte, M. Salmann in *Ferrocenes Ligands, Mater. Biomol. Vol. 47*, **2008**, pp. 499–639.
- [95] J. A. Jurica, J. P. McMullen, *Org. Process Res. Dev.* **2021**, *25*, 282–291.
- [96] C. Georgakis, *Ind. Eng. Chem. Res.* **2013**, *52*, 12369–12382.
- [97] J. Guo, I. N. Kiran, J. Gao, R. S. Reddy, Y. He, *Tetrahedron Lett.* **2016**, *57*, 3481–3484.
- [98] E. B. Pinxterhuis, M. Giannerini, V. Hornillos, B. L. Feringa, *Nat. Commun.* **2016**, *7*, 1–7.
- [99] P. Friedländer, *Berichte der Dtsch. Chem. Gesellschaft* **1909**, *42*, 765–770.
- [100] R. S. Monson in *Adv. Org. Synth.* Elsevier, **1971**, pp. 54–67.
- [101] S. R. De, *Asian J. Org. Chem.* **2021**, *10*, 980–1011.
- [102] D. Schmiel, H. Butenschön, *Organometallics* **2017**, *36*, 4979–4989.
- [103] M. Tazi, W. Erb, Y. S. Halauko, O. A. Ivashkevich, V. E. Matulis, T. Roisnel, V. Dorcet, F. Mongin, *Organometallics* **2017**, *36*, 4770–4778.
- [104] A. Tomberg, M. É. Muratore, M. J. Johansson, I. Terstiege, C. Sköld, P. O. Norrby, *iScience* **2019**, *20*, 373–391.
- [105] D. Wang, X. Yu, X. Xu, B. Ge, X. Wang, Y. Zhang, *Chem. - A Eur. J.* **2016**, *22*, 8663–8668.
- [106] R. Tanaka, H. Ikemoto, M. Kanai, T. Yoshino, S. Matsunaga, *Org. Lett.* **2016**, *18*, 5732–5735.
- [107] J. Lopic, V. Havaic, D. Šakic, K. Sankovic, S. Djakovic, V. Vrček, *European J. Org. Chem.* **2015**, *2015*, 5424–5431.
- [108] R. S. Laufer, G. I. Dmitrienko, *J. Am. Chem. Soc.* **2002**, *124*, 1854–1855.
- [109] X. Wu, K. Yang, Y. Zhao, H. Sun, G. Li, H. Ge, *Nat. Commun.* **2015**, *6*, 6462.
- [110] K. Kawai, Y. Bunno, T. Yoshino, S. Matsunaga, *Chem. - A Eur. J.* **2018**, *24*, 10231–10237.
- [111] M. Tsukazaki, M. Tinkl, A. Roglans, B. J. Chapell, N. J. Taylor, V. Snieckus, *J. Am. Chem. Soc.* **1996**, *118*, 685–686.
- [112] S. Masi, S. Top, L. Boubekour, G. Jaouen, S. Mundwiler, B. Spingler, R. Alberto, *Eur. J. Inorg. Chem.* **2004**, *3*, 2013–2017.
- [113] A. S. Tompa, *Thermochim. Acta* **1984**, *77*, 133–150.
- [114] I. Lavastre, J. Besancon, *Bull. Soc. Chim. Fr.* **1995**, *132*, 188–195.
- [115] M. Sattar, Praveen, C. Durga Prasad, A. Verma, S. Kumar, S. Kumar, *Adv. Synth. Catal.* **2016**, *358*, 240–253.

- [116] Y. Qiu, S. Yi, A. E. Kaifer, *J. Org. Chem.* **2012**, *77*, 4622–4627.
- [117] D.-y. Huang, Q.-j. Yao, S. Zhang, X.-t. Xu, K. Zhang, B.-f. Shi, *Org. Lett.* **2019**, *21*, 951–954.
- [118] P. Gandeepan, T. Müller, D. Zell, G. Cera, S. Warratz, L. Ackermann, *Chem. Rev.* **2018**, DOI 10.1021/acs.chemrev.8b00507.
- [119] P. Chirik, R. Morris, *Acc. Chem. Res.* **2015**, *48*, 2495.
- [120] B. Sun, T. Yoshino, S. Matsunaga, M. Kanai, *Adv. Synth. Catal.* **2014**, *356*, 1491–1495.
- [121] J. Silver, *Chemistry of Iron*, (Ed.: J. Silver), Springer Netherlands, Dordrecht, **1993**.
- [122] V. Artero, M. Fontecave, *Comptes Rendus Chim.* **2008**, *11*, 926–931.
- [123] K. Sakata, M. Eda, Y. Kitaoka, T. Yoshino, S. Matsunaga, *J. Org. Chem.* **2017**, *82*, 7379–7387.
- [124] D. Catheline, D. Astruc, *Organometallics* **1984**, *3*, 1094–1100.
- [125] S. L. Gipson, L. K. Liu, R. U. Soliz, *J. Organomet. Chem.* **1996**, *526*, 393–395.
- [126] W. E. Williams, F. J. Lalor, *J. Chem. Soc. Dalt. Trans.* **1973**, 1329–1332.
- [127] K. Ferré, L. Toupet, V. Guerschais, *Organometallics* **2002**, *21*, 2578–2580.
- [128] Y. Xie, C. Wu, C. Jia, C. H. Tung, W. Wang, *Org. Chem. Front.* **2020**, *7*, 2196–2201.
- [129] R. Shang, L. Ilies, E. Nakamura, *Chem. Rev.* **2017**, *117*, 9086–9139.
- [130] R. Shang, L. Ilies, E. Nakamura, *J. Am. Chem. Soc.* **2016**, *138*, 10132–10135.
- [131] G. Cerveau, E. Colomer, R. Corriu, *J. Organomet. Chem.* **1977**, *136*, 349–353.
- [132] Y. Ohki, T. Hatanaka, K. Tatsumi, *J. Am. Chem. Soc.* **2008**, *130*, 17174–17186.
- [133] Y. Wang, J. Zhu, A. C. Durham, H. Lindberg, Y. M. Wang, *J. Am. Chem. Soc.* **2020**, *141*, 19594–19599.
- [134] Y. Wang, J. Zhu, R. Guo, H. Lindberg, Y.-M. Wang, *Chem. Sci.* **2020**, *11*, 12316–12322.
- [135] J. Ou, W. Zheng, Z. Xiao, Y. Yan, X. Jiang, Y. Dou, R. Jiang, X. Liu, *J. Mater. Chem. B* **2017**, *5*, 8161–8168.
- [136] S. Yasuda, H. Yorimitsu, K. Oshima, *Organometallics* **2008**, *27*, 4025–4027.
- [137] J. Wencel-Delord, F. Colobert, *Org. Chem. Front.* **2016**, *3*, 394–400.
- [138] B. M. Mattson, W. A. Graham, *Inorg. Chem.* **1981**, *20*, 3186–3189.
- [139] D. J. Liston, C. A. Reed, Y. J. Lee, W. R. Scheidt, *J. Am. Chem. Soc.* **1989**, *111*, 6643–6648.
- [140] S. Kobayashi, M. Isobe, T. Saegusa, *Bull. Chem. Soc. Jpn.* **1982**, *55*, 1921–1925.



- [141] D. Reger, C. Coleman, *J. Organomet. Chem.* **1977**, *131*, 153–162.
- [142] S. Ji, K. Yan, B. Li, B. Wang, *Org. Lett.* **2018**, *acs.orglett.8b02796*.
- [143] D. G. Yu, T. Gensch, F. De Azambuja, S. Vásquez-Céspedes, F. Glorius, *J. Am. Chem. Soc.* **2014**, *136*, 17722–17725.
- [144] S. F. Rach, F. E. Kuhn, *Chem. Rev.* **2009**, *109*, 2061–2080.
- [145] D. Catheline, D. Astruc, *J. Organomet. Chem.* **1983**, *248*, 12–15.
- [146] D. C. Boyd, D. A. Bohling, K. R. Mann, *J. Am. Chem. Soc.* **1985**, *107*, 1641–1644.
- [147] T. P. Gill, K. R. Mann, *Inorg. Chem.* **1983**, *22*, 1986–1991.
- [148] A. N. Nesmeyanov, N. A. Vol'kenay, I. N. Bolesova, *Dokl. Akad. Nauk SSSR* **1963**, *149*, 615–618.
- [149] S. Brook, *Inorg. Chem.* **1985**, *24*, 1638–1643.
- [150] G. M. Boston, H. M. Philipp, H. Butenschön, *Eur. J. Inorg. Chem.* **2021**, *2021*, 4903–4914.
- [151] G. Duarah, P. P. Kaishap, T. Begum, S. Gogoi, *Adv. Synth. Catal.* **2019**, *361*, 654–672.
- [152] S. Prakash, K. Muralirajan, C. H. Cheng, *Angew. Chemie - Int. Ed.* **2016**, *55*, 1844–1848.
- [153] S. I. Kozhushkov, L. Ackermann, *Chem. Sci.* **2013**, *4*, 886–896.
- [154] K. S. Singh, P. H. Dixneuf, *Organometallics* **2012**, *31*, 7320–7323.
- [155] A. Sagadevan, A. Charitou, F. Wang, M. Ivanova, M. Vuagnat, M. F. Greaney, *Chem. Sci.* **2020**, *11*, 4439–4443.
- [156] S. Oi, E. Aizawa, Y. Ogino, Y. Inoue, *J. Org. Chem.* **2005**, *70*, 3113–3119.
- [157] P. Gandeepan, J. Koeller, K. Korvorapun, J. Mohr, L. Ackermann, *Angew. Chemie - Int. Ed.* **2019**, *58*, 9820–9825.
- [158] A. Sagadevan, M. F. Greaney, *Angew. Chemie - Int. Ed.* **2019**, *58*, 9826–9830.
- [159] J. Davis, D. Huw Vaughan, M. F. Cardosi, *J. Chem. Educ.* **1995**, *72*, 266–267.
- [160] S. A. Herbert, D. C. Castell, J. Clayden, G. E. Arnott, *Org. Lett.* **2013**, *15*, 3334–3337.
- [161] M. A. Shaik, H. Oelschläger, *Arch. Pharm. (Weinheim)*. **1984**, *317*, 214–219.
- [162] B. Capon, Z. P. Wu, *J. Org. Chem.* **1990**, *55*, 2317–2324.
- [163] V. Bizet, L. Buglioni, C. Bolm, *Angew. Chemie - Int. Ed.* **2014**, *53*, 5639–5642.
- [164] D. A. Loginov, A. A. Pronin, Z. A. Starikova, P. V. Petrovskii, A. R. Kudinov, *Mendeleev Commun.* **2010**, *20*, 271–272.

- [165] G. R. Fulmer, A. J. Miller, N. H. Sherden, H. E. Gottlieb, A. Nudelman, B. M. Stoltz, J. E. Bercaw, K. I. Goldberg, *Organometallics* **2010**, *29*, 2176–2179.
- [166] M. Tsukazaki, M. Tinkl, A. Roglans, B. J. Chapell, N. J. Taylor, V. Snieckus, *J. Am. Chem. Soc.* **1996**, *118*, 685–686.

# Curriculum Vitae

## Personal Information

Name	Robert Gathy
Date of Birth	18.12.1989
Place of Birth	Gehrden, Germany

## Education

2018 – present	Doctoral Thesis, Institute of Organic Chemistry, Leibniz University Hannover
2015 – 2018	M. Sc. Natural Product Chemistry, Institute of Organic Chemistry, Leibniz University Hannover (1.5)
2012 – 2015	B. Sc. Biochemistry, Leibniz University Hannover (1.9)
2011	University Entrance Qualification, IGS Mühlenberg (1.3)

## Internships

03/2017 – 06/2017	Honeywell Specialty Chemicals Seelze GmbH – Synthetic and methodological work with Luminous Organic Dyes
-------------------	--

## List of Publications

[1]	D. Schmiel, R. Gathy, H. Butenschön, <i>Organometallics</i> 2018, 37, 2095–2110.
-----	--